

marine reSEARCH@CNR.it

Risks



National Research Council of Italy

Risks

The Detection of Marine Oil Slicks in VNIR Satellite Images: the Role of Sunglint

G. De Carolis¹, M. Adamo³, V. De Pasquale², G. Pasquariello³

1, Institute for Electromagnetic Sensing of the Environment, CNR, Milano, Italy

2, Planetek Italia S.r.l., Bari, Italy

3, Institute of Intelligent Systems for Automation, CNR, Bari, Italy

decarolis@ba.issia.cnr.it

Abstract

This paper deals with the capability of spaceborne visible and near infrared (VNIR) imaging sensors to detect oil films floating on the sea surface. In particular, the use of the VNIR bands of MODIS and MERIS sensors is investigated. It is shown that the underlying physical mechanism that enables oil slick detection is based on the alteration of the wind-roughened sea surface slopes produced by the presence of the floating mineral oils. The role of specular reflection (sunglint) is recognized and assessed as the chief mechanism that allow VNIR wavelengths to image floating patches of oil. To accomplish the task, case studies of oil pollution from the disaster occurred in front of the Lebanon shoreline during the summer 2006 were selected. High rate of MODIS and MERIS acquisitions with significant percentage of imagery affected by sunglint occur in low-latitude seas like the Mediterranean. As a result, VNIR images can notably contribute to improve the actual oil slick monitoring capability offered by a single spaceborne synthetic aperture radar (SAR) system. A simulation study specific for the Mediterranean Sea was carried out in order to demonstrate the effectiveness of such approach supporting SAR observations. The unprecedented temporal capability offered by the combination of SAR and VNIR observations thus becomes of crucial importance for the tight monitoring of oil drift as required during the first hours after the spillage.

1 Introduction

Oil spills are among the major threats that can affect the marine environment. Effective near real time intervention not only requires knowledge of how the oil has been actually dispersed, but also does need accurate predictions of its evolution and thickness spatial distribution in the next hours. Synthetic Aperture Radar (SAR) has been demonstrated as the best remote sensor able to detect oil patches on the sea surface independent of solar illumina-

tion, cloud coverage and atmospheric conditions. Therefore, spaceborne SAR images taken by the several sensors installed on the orbiting platforms (ERS, RADARSAT, ENVISAT and the recent TerraSAR and Cosmo-SkyMed) are being extensively used to provide worldwide distribution of surface oil pollution for wind regimes in the 2-12 m·s⁻¹ range [1, 2, 3, 4]. As the microwave probe is sensitive to the modified sea surface roughness, the main drawback of SAR systems is the inability to discriminate between oil/no-oil

slicks. In contrast to the massive use of SAR products, the exploitation of visible and near infrared (VNIR) imagery gathered by spaceborne sensors has not been sufficiently developed. Indeed, the presently orbiting imaging sensors gather VNIR images at moderate spatial resolution that is suitable for oil slick discrimination, thus opening new perspectives for its utilization. Such sensors are the MODerate Resolution Imaging Spectroradiometer (MODIS) on Aqua/Terra platforms and the MEDium Resolution Imaging Spectrometer Instrument (MERIS) on ENVISAT satellite. At nadir, MODIS can acquire images with 250 m resolution in the red (band 1: 620-670 nm) and NIR (band 2: 841-876 nm) wavelengths, while MERIS instrument acquires images with 300 m resolution for 15 bands over the 390-1040 nm. Although in the optical range there are “no specific characteristics that distinguish oil from the background” [5], efforts aimed at demonstrating the potential of VNIR imaging sensors for oil spill detection have been documented in the scientific literature (see e.g. [6]). Physical models that predict the water leaving radiance of oil polluted sea surface have been developed. Depending on the observational geometry and wind speed, a contrast, either positive or negative, with the clean sea surface reflectance was predicted for $\lambda=550$ nm [7, 8]. In addition, because models predict decreasing contrast with increasing wavelengths up to $\lambda=700$ nm, care should be taken in selecting viewing angles that are “far from the direction where there is a high probability of sun glitter occurrence” [9]. The latter is a very tight requirement because the specular reflection over the oceans is actually widely observed in satellite VNIR imagery [10, 11]. Partial confirmation of the above theoretical predictions was provided with MODIS obser-

vations of oil slicks in the Lake Maracaibo [12], where oil patches under sunglint were also reported. MISR observations of the same oil spills confirmed the slick visibility under sunglint collected by the quasi-nadir oriented cameras [13]. In addition, MERIS sunglint VNIR observations of oil slicks were reported in occasion of the Chinese freighter “Fu Shan Hai” disaster occurred offshore Sweden coasts on May 2003 [14]. This paper is aimed at assessing the ambient and solar/sensor geometric conditions that allow the exploitation of the VNIR bands of MODIS and MERIS for oil slick detection. Besides, it will be shown that satellite VNIR imagery can suitably support SAR observations in the Mediterranean Sea as a result of the high temporal rate of image acquisition (nearly one per day per sensor) and the high probability to acquire in sunglint conditions.

2 The sea surface reflectance

The direct specular reflection of the solar radiation over the ocean waves (sunglint) can be described on a statistical basis. By representing the clean sea surface as a collection of small, mirror-like planar facets each with a characteristic slope, Cox and Munk [15, 16] showed that the statistical distribution of the facets’ slope is a function of the horizontal wind vector and is well approximated by a skewed Gaussian distribution with principal axes in the up- and cross-wind directions. Measurements of wave slopes carried out on an oil-covered surface further indicated that the oil slick smoothed out the capillary waves, leaving only waves greater than 30 cm, and eliminated the up-wind skewness

| | $\sigma_c (\times 10^{+3})$ | $\sigma_u (\times 10^{+3})$ | $C_{21} (\times 10^{+2})$ | $C_{03} (\times 10^{+2})$ | C_{40} | C_{22} | C_{04} |
|--------------------|-----------------------------|-----------------------------|---------------------------|---------------------------|----------|----------|----------|
| Clean Water | 3.00+1.92 W | 3.16W | 1.00- 0.86W | 4.00- 3.30W | 0.40 | 0.12 | 0.23 |
| Oil Slick | 3.00+0.84 W | 5.00+0.78W | 0.00 | 0.20 | 0.36 | 0.10 | 0.26 |

Table 1: Dependence of the Cox and Munk parameters on wind speed (W) measured at 12.5 m·s⁻¹ and oil slick contamination. All other c_{ij} terms can be neglected provided that the probability distribution is close to Gaussian and large values of c_{ij} are excluded.

of the distribution. The following expression of the surface wave slopes pdf, known as Gram-Charlier series, is valid for both clean and oil polluted sea surfaces [15]:

$$P(z_c, z_u) = \frac{\exp\left[-\frac{1}{2}\left(\frac{z_c^2}{\sigma_c^2} + \frac{z_u^2}{\sigma_u^2}\right)\right]}{2\pi\sigma_u\sigma_c} \cdot \quad (1)$$

$$\cdot \left[1 + \sum_{i=0}^{\infty} \sum_{j=0}^{\infty} c_{ij} H_i\left(\frac{z_c}{\sigma_c}\right) H_j\left(\frac{z_u}{\sigma_u}\right) \right],$$

where z_c and z_u are the cross-wind and up-wind slope components of the facets, H_n is the n^{th} Hermite polynomial; the parameters $\sigma_c, \sigma_u, c_{ij}$ linearly depend on the wind speed with coefficients that take different numerical values for clean sea surface and oil contaminated sea surface. Their values are reported in Table 1. The sunglint reflectance just above the sea surface can thus be computed for both clean and oil polluted surfaces by summing the elementary reflectance contributions coming from the facets oriented as a mirror with respect to the Sun and the sensor location [15]:

$$\rho_G \lambda = \frac{\pi}{4} \frac{r(\omega, \lambda)}{\cos\theta_s \cos\theta_v \cos^4\beta} P(z_c, z_u) \quad (2)$$

where ω is the specular reflection angle; θ_s and θ_v are the sun and sensor zenith angles; β is the angle formed by the normal of the facet with the up-ward vertical axis perpendicular to the wind reference system. The angles ω and β are defined as follows:

$$\cos 2\omega = \cos\theta_s \cos\theta_v + \sin\theta_s \sin\theta_v \cos\Delta\phi, \quad (3)$$

$$\cos\beta = \frac{\cos\theta_s + \cos\theta_v}{\sqrt{2 + 2\cos^2 2\omega}}, \quad (4)$$

where $\Delta\phi = \phi_s - \phi_v$, ϕ being the solar (s) and view (v) azimuth angle. $r(\omega, \lambda)$ is the Fresnel reflection coefficient of the surface for radiation of wavelength λ . In VNIR the clean waters exhibit a Fresnel reflection coefficient which is almost constant for incidence angles from 0 to 40 degrees. In contrast, for an oil-water system the Fresnel reflection coefficient depends on the type and thickness of the oil along with the incidence angle and the wavelength of the impinging radiation [17]. As the specular reflection from the oil/water system is the overall result of both the Fresnel reflection coefficient and the probability of reflection, oil films may be imaged either brighter [18, 13] or darker [12, 19, 20] than the neighbouring clean sea surface.

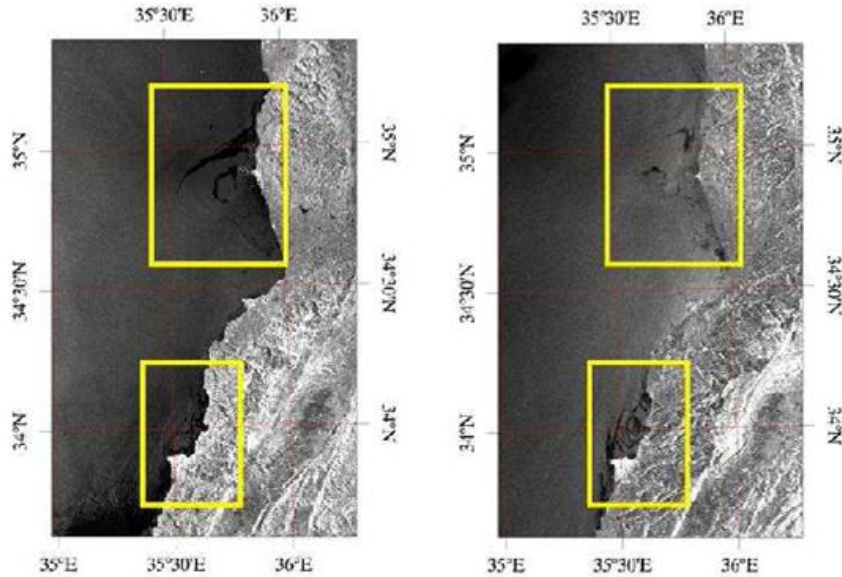


Figure 1: Portion of the ASAR images acquired on (left) August 5 at 19:30 and (right) on August 6 at 07:45. Times are UTC. The yellow frames contain the observed oil slicks.

3 Case studies

A number of MODIS and MERIS images were considered as case studies to assess the VNIR visibility conditions of oil slicks. SAR images were also considered to validate VNIR oil slick observations. The selected cases are relevant to the major oil pollution that affected the Lebanon shoreline after the Israeli attack against the Jiyeh power station on 14-15 July 2006. Up to 16,000 tons of heavy fuel were estimated to have been released. The consequent oil spill threatened marine life for about 170 Km of coast North reaching Syria. We will focus on two consecutive dates, August 5 and August 6, because of the unique availability of MODIS, MERIS and ENVISAT ASAR images. Table 2 includes the

list of the VNIR images utilized. Figure 1 shows the ASAR WS images gathered on August 5 at 19:30 and on August 6 at 07:45, respectively. Both images include two patterns of oil slicks: the northern slick, centered at about (35.0°N,35.75°E), develops higher variability by becoming less evident the day after; the southern slick (34.0°N,35.5°E) occupies almost the same area on both the images. The MERIS image acquired on August 5 about 13 hours before ASAR includes both slicks (Figure 2). The northern slick has a wider extension with respect to the one detected by ASAR. This is in accordance to the ASAR observation of the next day that reports a further decreased extent. The southern slick shows instead an extension comparable with the one reported by ASAR. It is

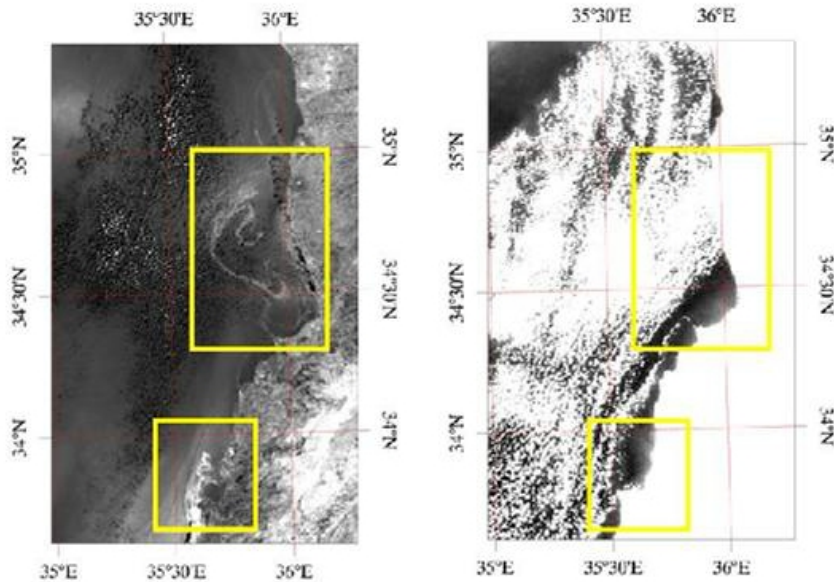


Figure 2: Band 13 of the MERIS image acquired on (left) August 5 at 08:16 and (right) on August 6 at 07:45. The yellow frames contain the observed oil slicks. On the image of August 5 slicks appear brighter than the surrounding waters.

worth to note that both slicks appear bright with respect to the neighbouring clean sea because the area has been imaged with solar/sensor geometry typical of full glint. Unfortunately, the MERIS image of the next day includes a large portion of cloud coverage that hampers the possibility to image the slicks. Of considerable interest is instead the fact that the MODIS/Terra image acquired on August 5 at 08:05, that is 11 minutes before the MERIS acquisition, does not show any slicks (Figure 3); instead, the MODIS/Terra of the next day includes oil pattern consistent with those observed on the other images. The southern slick is still visible, while the northern one is completely disappeared confirming the trend of progressive reduction of its extension already documented on the pre-

vious imagery. The same considerations can be made for the MODIS/Aqua (Figure 4): slicks are apparent only on the MODIS/Aqua of August 6, in accordance to the sunglint conditions relevant to the two images. It is worth noting that the slicks imaged by MODIS appear all darker than the neighbouring sea. It can be concluded that there is a strong relation between the slick visibility and the sunglint reflectance. The simulated sunglint values are reported in Table 2. It can be recognized that where the slicks are not visible, the simulated reflectance of the clean sea surface is not higher than $\sim 10^{-8}$. Similar results were found after analyzing other cases of imaged oil slicks [20]. The available imagery allowed to estimate the value of sunglint reflectance at $\sim 10^{-4}$ as the

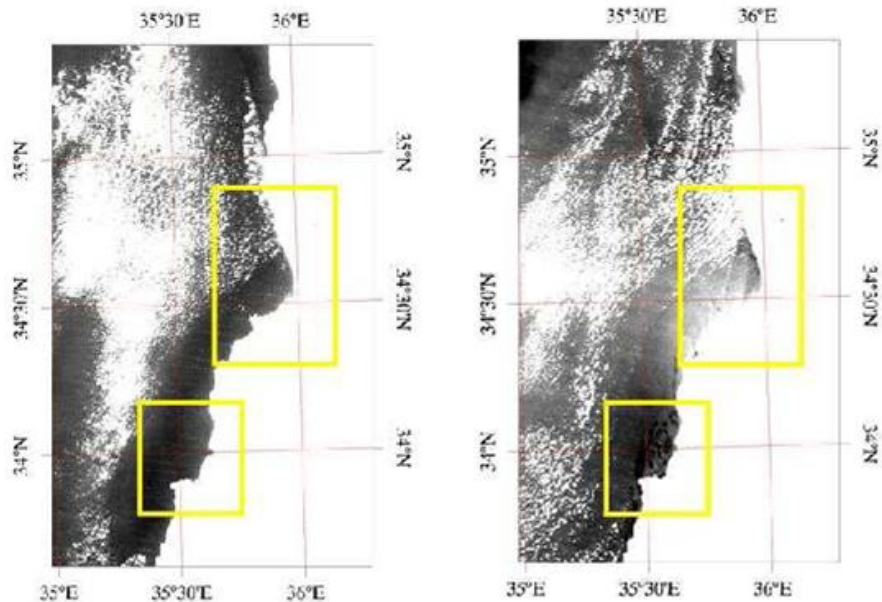


Figure 3: Band 2 of the MODIS Terra image acquired on (left) August 5 at 08:05 and (right) on August 6 at 08:50. The yellow frames contain the observed oil slicks.

lower limit value for oil slick visibility in red-NIR. An oil slick brighter appearance than the neighboring sea can be explained by the occurrence of specular reflection conditions at the sea surface resulting from the oil layer.

4 The NIR imaging of the Mediterranean Sea

The Mediterranean Sea is an area characterized by intense marine traffic with high risk of oil pollution [21]. Therefore, it would be of interest to assess the feasibility of NIR imagery to support SAR observations for oil slick detection in terms of spatial and temporal distribution. We report the results of a study performed for year

2007, that can be considered, in the average, representative of any temporal period [20]. The threshold value of reflectance beyond which there is a finite probability to detect an oil slick of given type and thickness can be estimated assuming the following simplifying assumptions:

- In the NIR region of the e.m. spectrum, the radiance emerging from the water body (water leaving radiance) is negligible for both clean sea and oil patches. Although the approximation strictly holds for case I waters, contribution from case II waters could still be neglected provided that the sunglint contamination is strong enough, as it is required for successful oil slick detection;
- Reflectance due to whitecaps can be always neglected within both oil patches

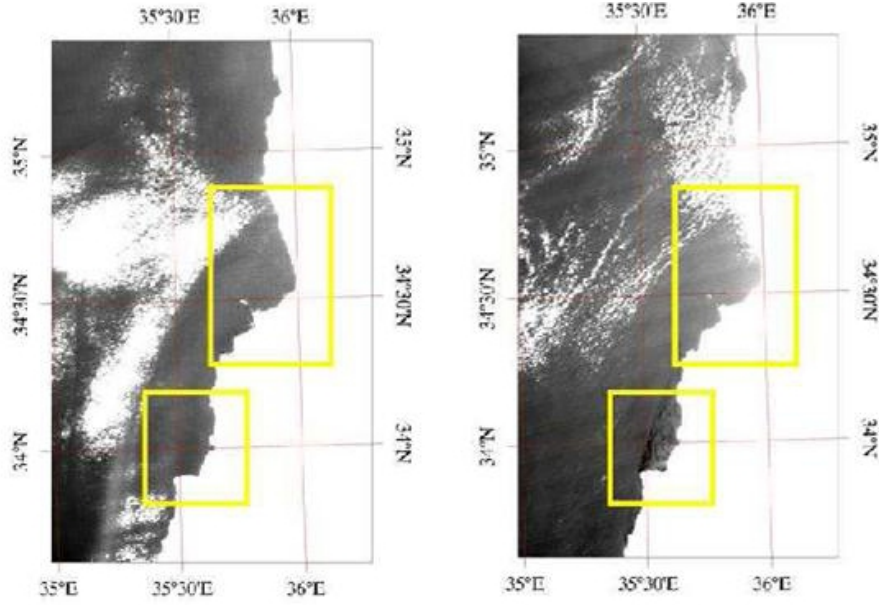


Figure 4: Band 2 of the MODIS Aqua image acquired on (left) August 5 at 11:20 and (right) on August 6 at 10:25. The yellow frames contain the observed oil slicks.

and clean sea surfaces for wind speeds up to about $14 \text{ m}\cdot\text{s}^{-1}$ as well. According to Koepke [22], whitecap reflectance is almost null for wind speeds less than $7 \text{ m}\cdot\text{s}^{-1}$. For higher wind speeds not exceeding $14 \text{ m}\cdot\text{s}^{-1}$ the upwelling irradiance is not higher than the 0.5% of the incident irradiance. As reliable oil slick detection can be performed for moderate wind speed regimes, whitecap contribution can be ruled out in the overall reflectance computation;

- The atmosphere contributes equally to the TOA reflectance measured on oil polluted pixels and neighbouring clean sea pixels.

By adopting the above approximations, the quantity $\Delta\rho_{TOA} = |\rho_{oil}^{TOA} - \rho_{clean}^{TOA}|$, which

denotes the absolute difference of TOA reflectance between an oil patch and the surrounding clean sea, can be expressed as the corresponding glint reflectance difference, as follows:

$$|\rho_{oil}^G - \rho_{clean}^G| \approx \frac{\Delta\rho_{TOA}}{T} \quad (5)$$

where T is the direct atmospheric transmittances [20].

Furthermore, considering the minimum difference in reflectance measurable by the sensor, $\Delta\rho$, which depends on the characteristics of S/N ratio and sensitivity of the sensor itself, the above condition to be satisfied for oil slick visibility becomes:

$$|\rho_{oil}^G - \rho_{clean}^G| > \frac{\Delta\rho}{T} \quad (6)$$

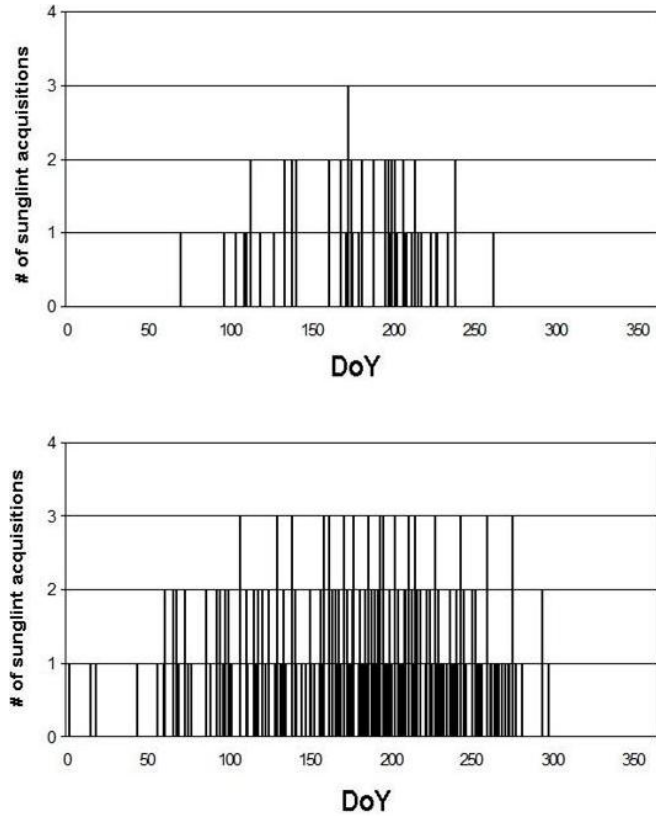


Figure 5: Minimum (top) and maximum (bottom) number of useful optical acquisitions of the Northern Adriatic Sea and offshore Crete Island, respectively.

It should be pointed out that the ratio $\Delta\rho/T$ ($\text{m}\cdot\text{s}^{-1}$) not only depends on the wavelength, but also on the solar illumination and imaging geometry. Sunlint reflectance for clean and oil polluted sea surfaces were computed using expression (2) for the NIR bands of MERIS and MODIS. Oil patches $5\ \mu\text{m}$ thick with average absorbing properties in the NIR ($n=1.47-8.00\times 10^{-6}i$, $i=\sqrt{-1}$) were supposed to be imaged [17]. The simulations were performed on grids 1° wide in lat/lon coordinates and considering the 10 m ECMWF wind speed (≤ 14 $\text{m}\cdot\text{s}^{-1}$) and direction at the closest time of each satellite overpass during the year 2007. Standard atmosphere with maritime aerosols of AOT=0.2 was considered to compute the direct transmittance function. Finally, the presence of clouds was also considered. The total cloud index (TCI) predicted by ECMWF atmospheric model was employed as parameter: only those acquisitions for which $\text{TCI}<2/10$ were considered for further computations. An upper value of $2/10$ was arbitrarily selected as cloud cover above which sea surface

was not visible to the sensor. On average, 150 images, i.e. about 16.1% of the total acquisitions, were available over the Mediterranean Sea to detect oil slick signatures; the maximum number of 243 images (26.4%) were of the area surrounding Crete Island and the minimum number of 62 images (5.6%) were of the area located in the Northern Adriatic Sea. In order to investigate how the number of images useful for oil slick detection are distributed throughout the year, we focus on the less favourable and most favourable areas of the Mediterranean Sea, namely the point located in the Northern Adriatic Sea and offshore Crete, respectively. Figure 5 shows the number of useful sunglint acquisitions and the corresponding expected reflectance. It results that winter time is the less favourable period to detect oil slicks on NIR images due to the lower sun elevation. In general, the results show a reduced capability to detect an oil spill while moving toward North. Finally, the cloud cover is an important limiting factor for the point in the North Adriatic sea, mainly in the winter, being however almost negligible in the Eastern Mediterranean offshore Crete area.

5 Conclusions

A method that extends the SAR capability to detect marine oil slicks using VNIR imagery collected by MERIS and MODIS sensors under sunglint imaging

conditions has been developed. The procedure was applied to oil slicks detected in the Mediterranean Sea offshore the Lebanon shoreline in August 2006. Discrimination of the oil slick from clean sea surface in presence of sun glitter and as a function of the VNIR wavelengths has been reported. Discrimination of the oil slick from clean sea surface in presence of sun glitter and as a function of the VNIR wavelengths has been reported. The seas located in low to mid latitudes geographical sites are the most favoured for sunglint imaging. The present work indicates that the spring to early in autumn period affords full exploitation of the NIR imagery in detecting the oil slicks of the Mediterranean Sea.

6 Acknowledgements

The ENVISAT ASAR and MERIS images used for this study were provided by ESA within the CAT-1 project 3506 "Exploitation of MERIS images for oil spill detection". MODIS images were freely downloaded from the NASA archive available at <http://ladsweb.nascom.nasa.gov/index.html>. This work has been carried out in the framework of the project IMCA (Integrated Monitoring of Coastal Areas) funded by the Italian Ministry of University and Scientific Research grant MIUR PON D.M. 593/00.

| SENSOR | MODIS Terra | MERIS | MODIS Aqua | MERIS | MODIS Aqua | MERIS | MODIS Terra | MODIS Aqua |
|---|--|-----------------------|------------------------|-----------------------|------------------------|-----------------------|-----------------------|-----------------------|
| ORBIT | D | D | A | D | A | D | D | A |
| DATE (dd/mm/yy) | 05/08/06 | 05/08/06 | 05/08/06 | 06/08/06 | 05/08/06 | 06/08/06 | 06/08/06 | 06/08/06 |
| UTC TIME (hh:mm) | 08:05 | 08:16 | 11:20 | 07:45 | 11:20 | 08:50 | 08:50 | 10:25 |
| WIND VECTOR (m·s⁻¹/deg) | 3.1/45 | | 4.1/52 | 4.9/37 | 4.1/52 | 5.2/41 | 5.2/41 | 5.6/44 |
| SOLAR ZENITH ANGLE (deg) | 27.2 | 26.0 | 28.7 | 31.4 | 28.7 | 21.0 | 21.0 | 20.0 |
| SENSOR ZENITH ANGLE (deg) | 36.3 | 28.0 | 52.8 | 25.0 | 52.8 | 39.0 | 39.0 | 38.5 |
| SOLAR AZIMUTH ANGLE (deg) | 98.0 | 126.5 | 238.7 | 116.6 | 238.7 | 143.0 | 143.0 | 213.0 |
| SENSOR AZIMUTH ANGLE (deg) | 123.4 | 285.8 | 264.8 | 101.6 | 264.8 | 283.0 | 283.0 | 77.0 |
| RED GLINT REFLECTANCE (*) | 4.08×10 ⁻⁸ | 2.49×10 ⁻¹ | 3.49×10 ⁻¹¹ | 4.26×10 ⁻⁵ | 3.49×10 ⁻¹¹ | 3.81×10 ⁻² | 3.81×10 ⁻² | 2.35×10 ⁻² |
| NIR GLINT REFLECTANCE (**) | 4.03×10 ⁻⁸ | 2.46×10 ⁻¹ | 3.44×10 ⁻¹¹ | 4.21×10 ⁻⁵ | 3.44×10 ⁻¹¹ | 3.76×10 ⁻² | 3.76×10 ⁻² | 2.32×10 ⁻² |
| OIL SLICK VISIBILITY | N | Y | N | ? | N | Y | Y | Y |
| (*) | band 1 [620-670] nm for MODIS; band 8 [673.75-688.75] nm for MERIS | | | | | | | |
| (**) | band 2 [841-876] nm for MODIS; band 13 [845-885] nm for MERIS | | | | | | | |

Table 2: Summary of the imaging and solar illumination geometry, the Skiron wind vector, the expected sunglint reflectance at the water level on clear sea and flag of oil slick visibility for the analyzed MODIS and MERIS images. Azimuth and wind angles are measured clockwise from N. Wind direction is “going to”. Question mark denotes no slick detection because of cloud hindering.

References

- [1] B. Fiscella, A. Giancaspro, F. Nirchio, P. Pavese, and P. Trivero. Oil spill detection using marine SAR images. *International Journal of Remote Sensing*, 21:3561–3566, 2000.
- [2] B. Jones. A comparison of visual observations of surface oil with synthetic aperture radar imagery of the Sea Empress oil spill. *International Journal of Remote Sensing*, 22:1619–1638, 2001.
- [3] C. Brekke and H.S. Solberg. Oil spill detection by satellite remote sensing. *Remote Sensing of Environment*, 95:1–13, 2005.
- [4] F. Nirchio, M. Sorgente, A. Giancaspro, W. Biamino, et al. Automatic detection of oil spills from SAR images. *International Journal of Remote Sensing*, 26:1157–1174, 2005.
- [5] M.F. Fingas and C.E. Brown. Review of oil spill remote sensing. *Spill Science and Technology Bulletin*, 4:199–208, 1997.
- [6] V. Byfield. Optical remote sensing of oil in the marine environment. *Ph.D. dissertation, University of Southampton*, 1998.
- [7] Z. Otremba and J. Piskozub. Modelling of the optical contrast of an a sea surface. *Optics Express*, 9:411–415, 2001.
- [8] Z. Otremba and J. Piskozub. Modeling the remotely sensed optical contrast caused by oil suspended in the sea water column. *Optics Express*, 11:2–6, 2003.
- [9] Z. Otremba and J. Piskozub. Modelling the bidirectional reflectance distribution function (BRDF) of seawater polluted by an oil film. *Optics Express*, 12:1671–1676, 2004.
- [10] S. Khattak, R.A. Vaughan, and A.P. Cracknell. Sun glint and its observation in AVHRR data. *Remote Sensing of Environment*, 37:101–116, 1991.
- [11] A. Morel. Open ocean monitoring with MERIS. *Proceedings MERIS – (A)ATSR workshop, ESA, Frascati (Italy)*, 2005.
- [12] C. Hu, F. Muller-Karger, C.J. Taylor, D. Myhre, et al. MODIS detects oil spills in Lake Maracaibo, Venezuela. *Eos, Transactions of the American Geophysical Union*, 84:313–319, 2003.
- [13] G. Chust and Y. Sagarminaga. The multi-angle view of MISR detects oil slicks under sun glitter conditions. *Remote Sensing of Environment*, pages 232–239, 2007.
- [14] O.F. d’Andon, A. Mangin, S. Bélanger, P. Garnesson, et al. Optical remote sensing of the Chinese freighter accident on 31st May 2003 in the Baltic Sea. *COAST-WATCH Investigative Monitoring Report*, 2003.

- [15] C. Cox and W. Munk. The measurement of the roughness of the sea surface from photographs of the sun's glitter. *Journal of the Optical Society of America*, 44:838–850, 1954.
- [16] C. Cox and W. Munk. Slopes of the sea surface deduced from photographs of sun glitter. *Bulletin of the Scripps Institution of Oceanography of the University of California*, 6:401–488, 1956.
- [17] H. Arst. Optical properties and remote sensing of multicomponential water bodies. 2003.
- [18] Q. Zheng, Yan X., W.T. Liu, V. Klemas, and D. Sun. Space shuttle observations of open ocean oil slicks. *Remote Sensing of Environment*, 76:49–56, 2001.
- [19] M. Adamo, G. De Carolis, V. De Pasquale, and G. Pasquariello. Combined use of SAR and MODIS imagery to detect marine oil spills. *Proceedings of SPIE Vol. 5980*, 59800I, 10.1117/12. 627505, 2005.
- [20] M. Adamo, G. De Carolis, V. De Pasquale, and G. Pasquariello. Detection and tracking of oil slicks on sun-glittered visible and near infrared satellite imagery. *International Journal of Remote Sensing*, 30:6403–6427, 2009.
- [21] G. Ferraro, A. Bernardini, M. David, S. Meyer-Roux, et al. Towards an operational use of space imagery for oil pollution in the Mediterranean basin: A demonstration in the Adriatic Sea. *Marine Pollution Bulletin*, 54:403–422, 2007.
- [22] P. Koepke. Effective reflectance of oceanic whitecaps. *Applied Optics*, 23:1816–1824, 1984.

Submarine Earthquake Geology: Active Faults, Slip Rates and the Recurrence Time of Major Catastrophic Events at Sea

A. Polonia

Institute of Marine Sciences, CNR, Bologna, Italy
alina.polonia@ismar.cnr.it

Abstract

Seismic risk assessment in densely populated coastal regions such as southern Italy or many other mega-cities all around the world, necessarily has to include seismogenic faults at sea where they are often associated with a tsunamigenic potential. Innovative techniques in the field of marine geology make now earthquake geology feasible at sea. These techniques will be briefly described together with some results obtained from the study of submarine faults in two different geodynamic settings.

1 Submarine earthquake geology

Paleoseismology is the investigation of the timing, location and size of individual earthquakes from their geological signatures such as those produced directly along the rupture plane, and those produced indirectly (landslides and mass wasting deposits) in the vicinity of faults. It focuses in particular on the almost instantaneous deformation of landforms and sediments during individual earthquakes. While paleoseismology has become a primary tool for seismic hazard evaluation on land, only few paleoseismological studies have been attempted on submarine fault systems mainly because of the limited resolution of the available geophysical techniques used at sea. Technological advances in the field of marine geology, such as accuracy of positioning and new generations of sonar systems led to carry out paleoseismological studies in submerged ar-

reas even though resolution is comparable but lower than that attained during direct observations onland. For this reason the study of the history, effects, and mechanics of earthquakes occurring in the submarine environment is here referred to as the “submarine earthquake geology” approach. One of the main advantages of conducting earthquake geological studies in the marine environment is that submarine geophysical data provide complete spatial coverage of fault structures, both horizontally and vertically. Moreover, sedimentation is more continuous and sedimentation rates are generally higher than in onshore alluvial/fluviol settings, which are commonly characterized by hiatuses. This allows for regional stratigraphic correlations, a clear advantage for assessing the geological effects of each earthquake in an entire region. Furthermore, the absence of obstacles such as buildings and dense vegetation allow the acquisition of dense grids of regularly spaced geophysi-

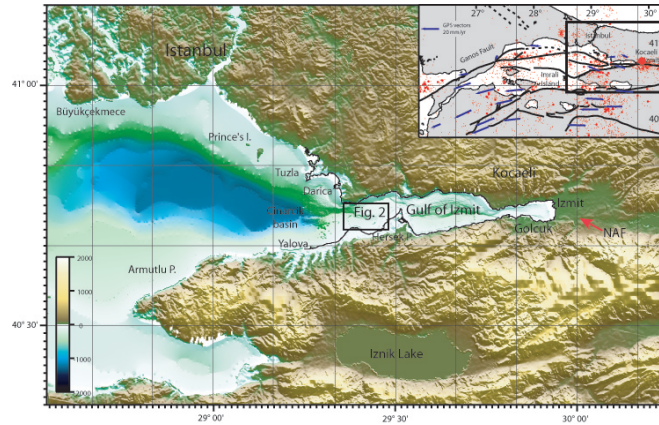


Figure 1: Shaded relief map of the Marmara regions (modified from [1]) that combine (A) the Odin Finder and Urania 20 m resolution DTM (Digital Terrain Model: SIMRAD EM-300 for water depth greater than 100 m and SIMRAD-3000 for water depth shallower than 100 m and ecosounder 12 KHz deso25) , (B) data acquired by SHOD (Seyir Hidrografi ve Oşinografi Dairesi) of Turkish Navy in 1999 (ELAC-SEABAM 50 KHz multibeam data) and (C) International Bathymetric Chart of the Mediterranean data (IBCM), with (D) on-land ERS (European Research Satellite) SAR interferometric DEM (Digital Elevation Model). The map clearly shows the NAF entering the gulf of Izmit from western Turkey (red arrow). The epicenter of the M7,4 17-aug-1999 Kocaeli earthquake is represented by the largest red circle in the inset map. The tectonic model used in the inset map is taken from Okay et al.[2].

cal data necessary for 3-D reconstructions. The objectives of each earthquake geological study are mainly related to (i) reconstructing location, geometry and kinematics of active faults; (ii) estimating slip rates on single fault strands; (iii) reconstructing recurrence time of major seismic events and (iv) estimating the likely tectonic movements that are expected to occur within a future time span. For active faults at sea, these objectives may be addressed through an integrated/multi-scale marine geological/geophysical approach that involves the combined analysis of geological (sediment samples) and geophysical data that allow observations in a scale range spanning from tens of

km (Multichannel Seismic profiles) to centimetres (CHIRP sub-bottom data and high resolution morpho-bathymetric images of the seafloor). As in the sub-aerial environment, major submarine seismic events may trigger mass wasting and gravity flows that accumulate at the base of submarine slopes, and, potentially, some tsunami deposits along the shorelines. As for land paleoseismology, a careful stratigraphic analysis is critical. Radiocarbon ages can be obtained from monospecific planktonic foraminiferal samples above and beneath suspected seismic related deposits such as large-scale resedimented units (mass wasting deposits, gravity flows, turbidities) and small-scale features (sand-injections, car-

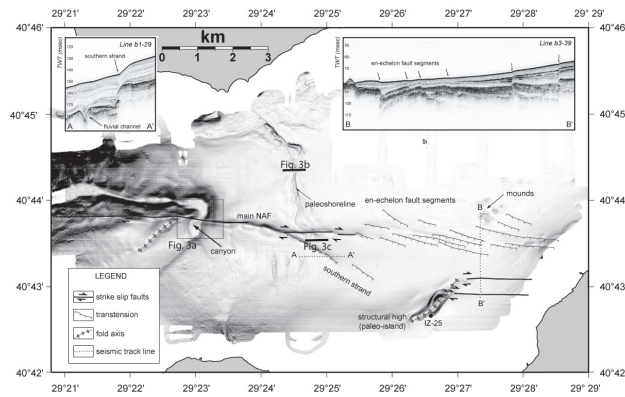


Figure 2: Shaded relief map of the western basin with structural interpretation derived from the analysis of multibeam and seismic data. The canyon is offset right-laterally by about 100 m along the E-W main branch of the NAF. A-A': E/W oriented CHIRP profile across the southern strand of the NAF. A fluvial channel is well imaged below 15 m of Holocene sediments. B-B': N/S oriented CHIRP profile across the wide and diffuse NAF displacement zone to the east. Deformation in this area is accommodated by short, en-echelon and south-dipping fault to the north, and vertical strike-slip segments to the south (modified from [1]).

bonate crusts). Correlation with earthquake catalogues is essential to understand if the high energy events observed are related to seismic activity. In the recent past ISMAR projects have started to apply earthquake geology in two different geodynamic settings: the Marmara Sea [3, 1, 4] on the North Anatolian Fault (NAF) and the Calabrian Arc in the Ionian Sea [5]. I'll briefly summarize in this paper major results obtained in these two key areas focusing in particular on those general aspects that may be applied to any seismogenic fault at sea.

2 The North Anatolian Fault in the Marmara Sea

The 1999 earthquakes of Izmit and Duzce (Duzce, Mw 7.1; Izmit Mw 7.4) gave impulse to multidisciplinary studies in north-western Turkey to fill major uncertainties regarding, geometry, kinematics and slip-rates of major fault branches affecting the accuracy of seismic risk assessment in this highly populated coastal region, which includes Istanbul with its 15 million inhabitants. These uncertainties were mainly related to the submerged portion of the NAF in the Marmara Sea where high resolution seismo-acoustic images have become available only after the earthquakes. The Marmara Sea (Figure 1 represents an ex-

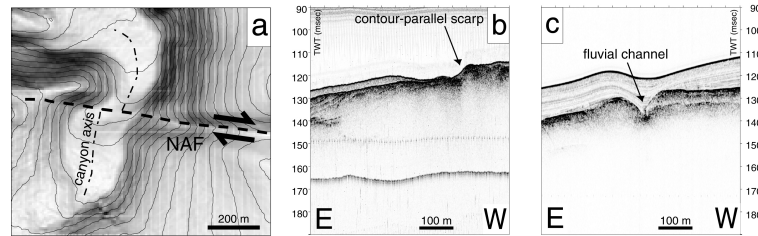


Figure 3: (a) This multibeam map shows the region where the canyon is offset right-laterally by about 100 m along the east-west main branch of the North Anatolian Fault (see Figure 2 for its location). Figures 3b and 3c are two CHIRP profiles collected across the paleo-shoreline and the fluvial channel (see Figure 2 for their location). Modified from [3].

ceptional area for conducting submarine earthquake geology. There exist well-documented records of large earthquakes dating back 2000 years [6]. Strike-slip motion across the plate boundary reaches $22\text{--}24\text{ mm}\cdot\text{yr}^{-1}$ [7] and may offset Holocene structures by as much as several tens of meters across the main fault strands. Sedimentation rates are high enough to allow the recognition of individual seismic events in the sediment column. Three marine geological/geophysical cruises have been carried out [3, 1, 8] in coastal areas of the Marmara Sea (Figure 1), that were considered key regions for identifying the seismogenic segments of the NAF and for making quantitative estimates on their displacements. An integrated geological/geophysical approach, that involved the analysis of high resolution geophysical data (multibeam, chirp, side scan sonar, multichannel seismic reflection) and well targeted sediment cores has been applied with the main purpose to gather new insights on the behaviour of active faults averaged over geological times. Collected geophysical data allowed us to obtain very high-resolution images of the seafloor (Fig-

ure 2) and 3D or pseudo-3D reconstruction of key stratigraphic levels in the recent sediment column, with a vertical resolution of a few cm. Recognition of piercing lines such as submarine canyons (Figure 3a), submerged paleo-shorelines (Figure 3b) and river channels (Figure 3c) displaced along the fault strands represented an important tool to estimate deformation rates along single fault strands. An east-west-trending submarine canyon connects the western Gulf of İzmit continental shelf to the Çınarcık deep basin (Figures 2 and 3a). The east-west-trending canyon bends sharply to the south of 90° and is offset by the E-W-trending NAF (Figure 3a). We used multibeam bathymetry and sub-bottom CHIRP profiles to image morphology and acoustically identify different sea bottom domains. Based on acoustic reflectivity, i.e., on physical properties of the sediments, we matched similar patterns on opposite sides of the faults. Comparing reflectivity profiles collected N and S of the main fault track, as well as reflectivity patterns superimposed on bathymetry (Figure 4), we estimated a $\sim 100\text{ m}$ dextral strike-slip displacement of the canyon

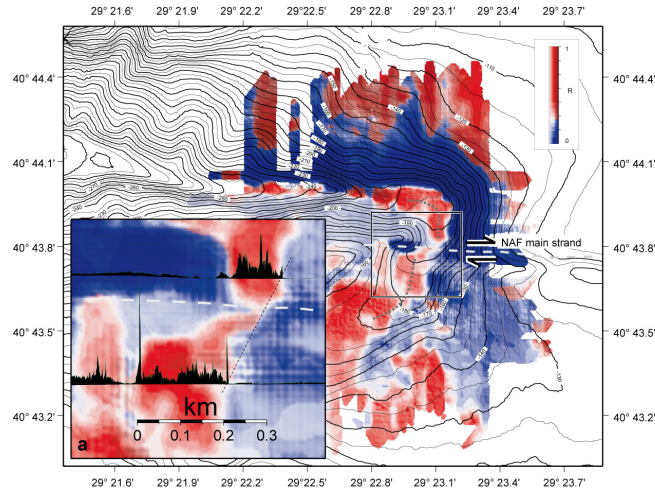


Figure 4: Shaded relief multibeam bathymetric map (contour each 5 m, illumination from NE) draped by sea-floor reflectivity from CHIRP sonar data (red to blue colour scale). Red colour indicate high reflectivity while blue colour is related to low-reflectivity. The flat bottomed canyon is displaced by the main NAF strand. a: two reflectivity profiles outside the displacement zone have been chosen in order to correlate zones of similar reflectivity pattern north and south of the fault zone. This allow us to estimate a horizontal displacements of about 100 m since the canyon became inactive after the last episode of sea-level rise. Modified from [1].

head along the fault track. Considering that the submarine canyon became inactive during the last episode of transgression dated 11000-10000 years b.p. the slip rate along this NAF branch is about $10 \text{ mm}\cdot\text{yr}^{-1}$. A second piercing line has been discovered through the interpretation of high-resolution bathymetry and sub-bottom CHIRP profiles that revealed a prominent contour-parallel scarp at a depth of approximately 85 m (Figures 2, 3b). The integrated analyses of sediment cores, including facies analysis and quantitative assessment of foraminiferal and ostracod distribution, provides invaluable paleodepth information, leading to refined identification of a paleoshoreline at ~ 85 m below the present day sea level [1]. Immediately

E of the paleo-shoreline, CHIRP records show the presence of a V-shaped erosional channel (Figure 3c). This channel is now inactive, having been partially buried by a thick (up to 20 ms TWT) transparent unit, that hampers its recognition from morphobathymetric data alone (Figure 5a). A close-spaced grid of CHIRP profiles was acquired where the buried channel intersects the NAF displacement zone (Figure 5). The analysis of this tight grid of profiles has been performed in order to reconstruct and map the subbottom topography of this area (Figure 5b) that predates the last episode of sea level rise by picking the erosional base of the Holocene mud deposits within each single CHIRP profile. The map shows a channel meander-

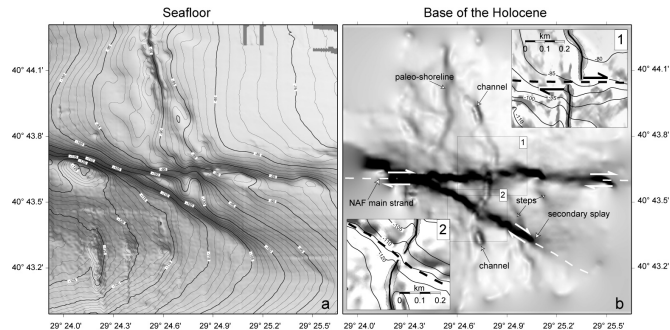


Figure 5: a: shaded relief multibeam bathymetric map (contour each 1 m, illumination from NE). b: gradient map of the base of the Holocene sediments obtained through a semi-automatic picking of CHIRP-subbottom profiles. It images sedimentary and tectonic features below the Holocenic drape. The topographic gradient map of the Holocene base shows the meandering river channel which is displaced along the NAF fault strands (insets 1 and 2). We calculate an offsets of ~ 80 and ~ 10 m in the main and secondary strands respectively. Modified from [1].

ing landward of the -85 m paleo-shoreline within a coastal plain: as it approaches the NAF displacement zone it is displaced by the main fault track and by the secondary splay to the S. A close-up view indicates right-lateral displacements of the channel of about 80 m along the main fault (Figure 5b inset 1), and of about 10 m along the secondary splay (Figure 5b inset 2). Channel abandonment due to rising sea-level is documented by the onset of a marine fauna, and radiocarbon dates obtained from organic material suggest a 10.200 ± 50 yr BP age for the paleoshoreline. The offsets measured at the canyon and at the fluvial channel are similar in length, and give an average rate of $10 \pm 1.5 \text{ mm}\cdot\text{yr}^{-1}$ for the right-lateral motion along this major strand of the NAF during the Holocene (i.e., the last 10,000 years). Sediment cores collected in the tectonically controlled sedimentary basins have been analyzed to learn more about the seismic and tectonic history of single fault strands. The approach

was to test whether the depocenters of the larger basins contain a record of all historic $M_s > 7$ earthquakes within the Marmara Sea region. Evidence of earthquakes in the subsurface (Figure 6) has been found and correlated with historic events in 181 AD, 740 AD, 1063 AD, 1343 AD, 1509 AD, 1766 AD, 1894 AD and 1912 AD. The geologic evidence comes primarily from those basins adjacent to the rupture as inferred from historic data. This suggests that coseismic deformation of the sea floor along the rupture is a critical factor in the sedimentary record [4].

3 The Calabrian Arc subduction complex

The Calabrian Arc (CA) subduction complex connects the E-W trending Sicilian Maghrebic belt with the NW-SE trending Southern Apennines and develops along the African-Eurasian plate boundary in the

Ionian Sea (Figure 7). At the toe of the CA, the thick sedimentary section of the African plate has been scraped off and piled up along thrust faults. This contributed to emplace a thick and about 200 km wide subduction complex represented by a well developed accretionary wedge, multiple slope sedimentary basins and a seaward dipping continental basement [9]. The Calabrian Arc (CA) is part of the most active seismic belt in Italy and it has been struck repeatedly by very strong historical earthquakes often associated with destructive tsunamies. Although the regional architecture of the margin geometry has been described through the analysis of high penetration seismic data [10, 11, 12, 13, 14], some major questions remains unanswered: 1) is the Calabria subduction zone still active? 2) What is location, geometry and kinematics of active faults absorbing plate motion? 3) Is there evidence of the geological record of past catastrophic events in the subsurface? In order to address these issues we have analysed in detail the structure and the evolution of the external CA, through a multi-scale approach addressing tectonics, kinematics and mass balancing in the accretionary complex [9]. The regional architecture of the subduction complex has been reconstructed through the analysis of deep penetration seismic profiles belonging to the CROP dataset that has been reprocessed through the application of the pre-stack depth migration (Figure 8) that allows to obtain depth sections well representing the real geometries of the geological structures [5]. Single fault strands have been analysed with higher resolution Sparker data belonging to the J dataset collected by ISMAR during 70's [10]. These seismic data have lower penetration than MCS data but are characterized by higher resolution, which

is necessary in order to address recent evolutionary processes and relationships between tectonics and sedimentation [5]. Once the regional geodynamic framework has been focused, high resolution geophysical data (MCS and CHIRP profiles) have been acquired in key areas, selected in order to address in more detail single fault strands, to learn more about subduction activity and to study active deformation along the African/Eurasian plate boundary. CHIRP sub-bottom profiles acquired at the transition between the flat-lying Ionian abyssal plain and the outermost accretionary wedge reveal active deformation at the seafloor (Figure 9). In the abyssal plain the recent sedimentary pile resting on the incoming African plate includes well layered clastic sediments and more transparent units possibly corresponding to megaturbidites. In particular, the recent-most one corresponds to the so called "Homogenite" [15]. Since its discovery, this deposit was interpreted as a megaturbidite triggered by a tsunami wave induced by the collapse of the Santorini caldera, after the Minoan eruption about 3500 years BP [15, 16]. Even if there is a general agreement on its catastrophic origin, there's still an open debate on the possible triggering mechanism that generated the turbidite. Recently Pareschi et al. [17] suggested that the homogenite was generated by a major tsunami triggered by the collapse of the eastern flank of the Etna Volcano that subsequently formed the Valle del Bove (7.600 ± 130 yr B.P.) but this reconstruction received strong criticism since homogenite's stratigraphic position suggest that it has to be younger than sapropel S1 i.e. younger than 5700 yr b.p. [18]. A second megaturbidite is widespread in the abyssal plain and present also in the perched basins between the folds within the

accretionary wedge. The detailed analysis of the areal distribution of these sedimentary units and the study of their geometries relative to the tectonic structures will be carried out in order to understand likely relationships between tectonics and sedimentation to reconstruct deformation rates of single tectonic structures. The folding of the uppermost transparent layer, identified as the 3500 BP Augias Turbidite, indicates active shortening at the toe of the wedge implying that accretion and shortening processes are still going on, thus confirming the activity of convergence processes. Sediment cores collected in the Ionian abyssal plain (3800 m water depth) as well as other deep marine basins adjacent to inner deformation fronts and transverse faults, have sampled turbidite sequences interbedded within a well understood chronology of sapropel units, tephra and hemipelagic deposits. We recognised at least 7 cycles of turbidites which likely contain a record of the great earthquakes in the region. Radiocarbon ages will be obtained from monospecific planktonic foraminiferal samples above and beneath deposits suspected to be related to seismic events, while Pb210 and Cs137 radiocarbon dating will be applied to selected cores to resolve seismites associated with some recent 19th and 20th century seismic events. We will compare the record of anomalous sedimentary events found in the cores with the paleoseismic catalogue of the region, and we will try to push the record of paleo-earthquakes back in time, to understand which is the recurrence time of major events, if it is constant or not and which portions of the subduction complex could have experienced great earthquakes in the past.

4 Conclusions

The North Anatolian Fault in the Marmara Sea, active faults of the Calabrian Arc subduction system, and other tectonic features offshore the coasts of southern Italy, as well as in many locations in Greece (e.g. the Gulf of Corinth) represent ideal areas for conducting research on submarine earthquake geology, since long-term geological studies and a unique record of large historical earthquakes/tsunamis dating back to 2000 years BP are available. Moreover, these areas are located along major plate boundaries, are characterized by the presence of large scale tectonic features and relative high strain rates and prone to seismic and tsunami hazards. Results from the marine geological studies carried out in the Sea of Marmara and recently in the Calabrian Arc, are promising and suggest the feasibility of the earthquake geological studies in the submarine environment since we were able to: 1) map the fault pattern, discriminating between active and inactive faults; 2) address their geometry and kinematics; 3) estimate slip-rates over geological time along single fault strands; 4) describe and date the past earthquakes in the sedimentary sequence; 5) recognize the submarine extent of recent ruptures. Geophysical high-resolution images, coupled with accurate paleoceanographic/stratigraphic reconstructions allowed for unprecedented quantitative estimate of seismogenic fault behaviour over geological times. These data are important to infer the fault behaviour over geological time scales (10,000 years). Long-term slip rate estimates from geological reconstructions can be used to test the significance of geodetic, short-term measurements, and analyse permanent deformation (co-seismic + post-seismic) along sin-

gle fault segments. Sediment samples collected in several basins of different size in the Marmara Sea have shown that: (1) the depocenters of the larger basins preserve a record of major historic earthquakes; (2) dip-slip and strike-slip Holocene deformation can be quantified; and (3) the effects of an earthquake include both primary structural features due to rupture of the sea floor - strata offset, scarps and tilting - as well as secondary effects due to shaking, such as mass-wasting and gravitational flows. The effects of these anomalous geological events are evident not only in shallow water environments such as the Izmit gulf, but rather, they are very well preserved in "low-energy" environments, such as the deep-sea basins of the Ionian Sea, where we observe the destruction of the continuous, generally fine-grained sedimentary record by the coarse signature of the direct or indirect effect of the catastrophic processes. For this reason the deep sea environment represents a natural catalogue of anomalous geological major events that can be decoded more easily than in shallow water environments. The surveying techniques and approaches used have therefore the potential of documenting earthquake ruptures of fault segments and to extend the earthquake record far

before the known history, thus improving hazard evaluations and the fundamental understanding of earthquake processes. We further stress the importance of a multidisciplinary/multiscale approach that involves the fine scale reconstruction of single fault strand dynamics with the study of regional tectonics, paleoceanography, stratigraphy and ultimately basin evolution.

5 Acknowledgements

This review is a summary of the results obtained from scientific projects among different cooperations between ISMAR and other institutions (L-DEO, ITU, TUBITAK, IFREMER, UBO, NATO, MIUR, University of Parma). The work developed among these projects has been possible thanks to the contribute of many colleagues from ISMAR (Bellucci L.G., Bonatti E., Bortoluzzi G., D'Orlando F., Ferrante V., Gasperini L., Ligi M., Marozzi G., Panieri G., Riminucci F., Stanghellini G.). This work has been developed among different projects: Progetto Strategico CNR, CNR-RSTL, INGV-DPC Project S1, Topomed. Structural mapping and CHIRP data processing has been performed with the SeisPrho software [19].

References

- [1] A. Polonia et al. Holocene Slip rate of the North Anatolian Fault beneath the Sea of Marmara. *Earth and Planetary Science Letters*, 427:411–426, 2004.
- [2] A. Morelli and E. Barrier. Commission for the geological Map of the World, coord. by Cadet J.-P. and Funicello R. Okay, A.I., A. Kaslilar-Özcan, C. Imren, A. Boztepe-Güney, E. Demirbag, and I. Kusçu, 2000. Active faults and evolving strike-slip basins in the Marmara Sea, northwest Turkey: a multichannel seismic reflection study. *Tectonophysics*, 321:189–218, 2004.
- [3] A. Polonia et al. EOS Transactions AGU. 83:229 and 235–236, 2002.

- [4] C.M.G. McHugh, L. Seeber, M.-H. Cormier, J. Dutton, et al. Submarine earthquake geology along the North Anatolia Fault in the Marmara Sea, Turkey: A model for transform basin sedimentation. *Journal Earth and Planetary Science Letters*, 248(3-4):661–684, 2006.
- [5] A. Polonia, L. Torelli, P. Mussoni, L. Gasperini, A. Artoni, and D. Klaeschen. The Calabrian Arc Subduction Complex in the Ionian Sea: Regional Architecture, Active Deformation and Seismic Hazard. *Tectonics*, accepted pending revision.
- [6] N.N. Ambraseys and J.A. Jackson. Seismicity of the Sea of Marmara (Turkey) since. *Geophysical Journal International*, 141:F1–F6, 2000.
- [7] S. McClusky et al. Global Positioning system constraints on plate kinematics and dynamics in the eastern Mediterranean and Caucasus. *Journal of Geophysical Research*, 105((B3)):5695–5719, 2000.
- [8] L. Gasperini, A. Polonia, G. Bortoluzzi, P. Henry, et al. How far did the surface rupture of the 1999 İzmit earthquake reach in Sea of Marmara? *Tectonics TC1010*, doi:10.1029/2010TC002726, 30, 2011.
- [9] A. Polonia, L. Torelli, R. Capozzi, F. Riminucci, et al. African/Eurasian plate boundary in the ionian sea: shortening and strike slip deformation in the outer calabrian arc accretionary wedge. *GNGTS meeting*, 2008.
- [10] S. Rossi and R. Sartori. A seismic reflection study of the External Calabrian Arc in the Northern Ionian Sea (Eastern Mediterranean). *Marine Geoph. Res.*, 4:403–426, 1981.
- [11] I. Finetti. Structure, stratigraphy and evolution of Central Mediterranean. *Bollettino di Geofisica Teorica ed Applicata*, XXIV:247–312, 1982.
- [12] L. Cernobori et al. Crustal image of the Ionian basin and its Calabrian margins. *Tectonophysics*, 264:175–189, 1996.
- [13] C. Doglioni et al. Foredeep geometries at the front of the Apennines in the Ionian Sea (central Mediterranean). *Earth and Planetary Science Letters*, 168:243–254, 1999.
- [14] L. Minelli and C. Faccenna. Evolution of the Calabrian Accretionary wedge (Central Mediterranean). *Tectonics TC4004*, doi:10.1029/2009TC002562, 29, 2010.
- [15] K.A. Kastens and M.B. Cita. Tsunami induced sediment transport in the abyssal Mediterranean Sea. *Geol. Soc. Am. Bull.*, 89:591–604, 1981.
- [16] W. Hieke. A thick holocene homogenite from the Ionian abyssal plain (Eastern Mediterranean). *Mar. Geol.*, 55:63–78, 1984.
- [17] M.T. Pareschi, E. Boschi, and M. Favalli. Lost tsunamis. *Geophys. Res. Lett.*, page 33, 2006.

- [18] L. Vigliotti. Comment on “Lost tsunami” by Maria Teresa Pareschi and others. *Geophys. Res. Lett.*, 35, 2008.
- [19] L. Gasperini and G. Stanghellini. SeisPrho: An interactive computer program for processing and interpretation of high-resolution seismic reflection profiles. *Computers & Geosciences*, 35(7):1497–1507, 2009.

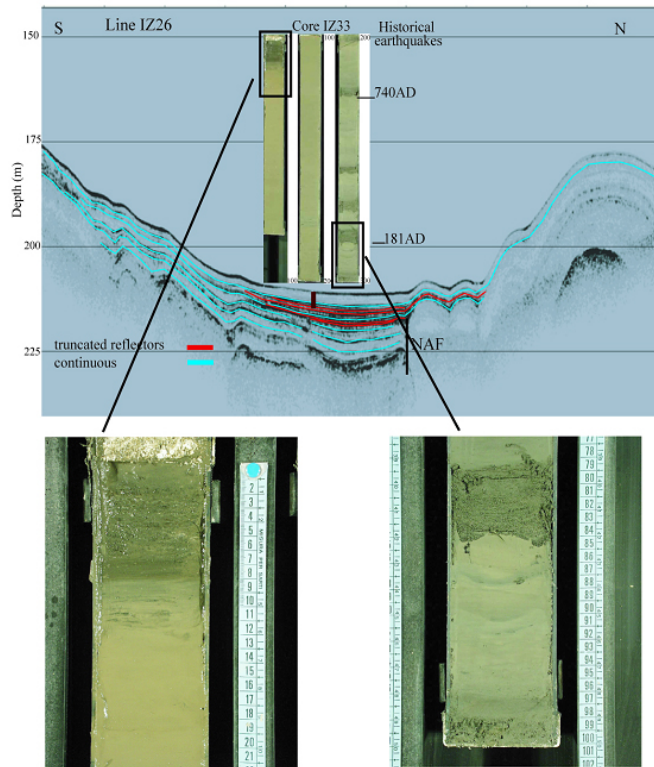


Figure 6: Subbottom profile Line IZ26 across Izmit Gulf and gravity core IZ33 collected in the basin d eposcenter. Integrated analysis of the coarser sand beds outlined that they are related to earthquake events that led to scour of the basin floor. 14C chronology linked two of the analysed sand beds to the 181 AD and 740 AD earthquake events. Stratigraphic relations suggest that the event at the top of the core may be that occurred in 1999 (Modified from [4]).

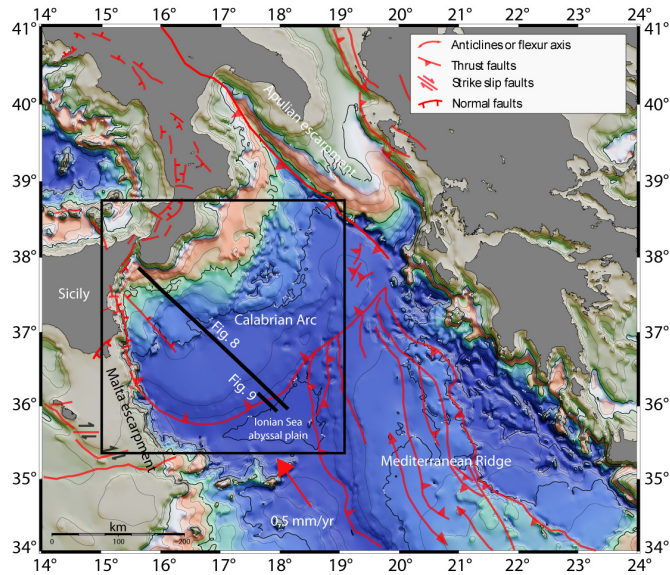


Figure 7: Simplified tectonic map of the central Mediterranean Sea. Tectonic model modified from Morelli and Barrier [2]. Seafloor bathymetry GEBCO 1 min.

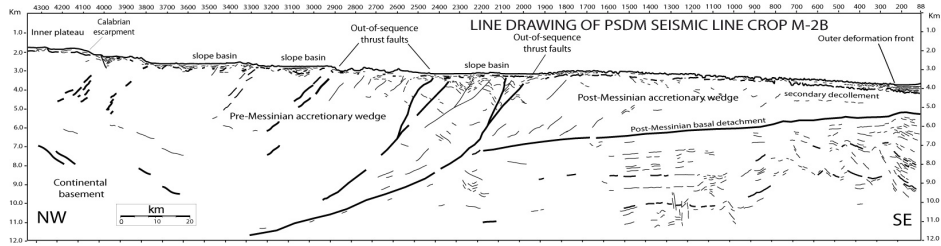


Figure 8: Line drawing of pre-stack depth migrated 36 fold MCS line CROP M-2B. Location of seismic profile is shown in Figure 7. The post-Messinian accretionary complex at the toe of the continental margin is made primarily of Messinian salt. The salt bearing complex lies above the basal detachment represented by the base of the Messinian evaporites, while the well layered Tertiary and Mesozoic African plate sediments are coupled with the lower plate and moves towards NW.

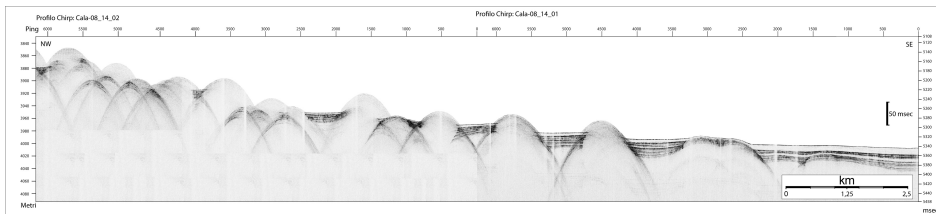


Figure 9: CHIRP sonar sub-bottom profile acquired across the deformation front of the subduction system (see Figure 7 for its location). This profile clearly shows active deformation at the seafloor related to folding and thrusting. In particular, deformation of the uppermost transparent layer suggests that shortening is active at the toe of the wedge. Moving towards NW, deformation rate and fold amplitude increase, while fold wavelength progressively decreases. The rough morphology of the outer accretionary wedge is known as “cobblestone topography” and is related to tectonic processes possibly driving salt dissolution (modified from [5]).

Predicting the Fate of Oil Spill at Sea, the Bonifacio Strait Study Case

A. Cucco, A. Ribotti, A. Olita, R. Sorgente, L. Fazioli, B. Sorgente, A. Perilli

Institute for Coastal Marine Environment, CNR, Oristano, Italy
andrea.cucco@cnr.it

Abstract

In the western Mediterranean, the Bonifacio Mouths are a wide strait between Sardinia and Corsica, with several small islands, rocks, and banks. The area has a high environmental and economical importance being also included in the plan area of international cooperation Franco-Italian-Monegasque RAMOGEPOL. Despite this importance, several accidents have occurred during the years involving both large vessels and small yachts, with a consequence increase the danger for the marine environment. In order to facilitate the rapid planning and coordination of operations of the marine authorities to tackle pollution during oil spill emergencies, an innovative forecasting system of the coastal marine circulation was developed through a numerical approach. In particular, the system is based on a high resolution 3D hydrodynamic numerical model coupled with a wind wave model both based on the finite element method and applied to the coastal area of the Bonifacio Strait. This is able to predict the currents and wave fields in the area and the trajectories followed by hydrocarbons dispersed on the sea surface. The system has been used to create "scenarios and risk maps" to quickly identify the most sensitive areas to oil-spill pollution in relationship to the oil tanks traffic.

1 Introduction

In the western Mediterranean, the Bonifacio Mouths are a wide strait between Sardinia and Corsica. Inside their eastern part, La Maddalena Archipelago is composed by several small islands, rocks, and banks. The area has a high environmental importance with two marine national parks, one Italian since 1994 and a second French since 1999, and it has been part of the International Sanctuary for the Protection of Marine Mammals in the Mediterranean since 2001. Despite this importance, several accidents have occurred during the years involving both large vessels

and small yachts, with a consequence increase of the danger for the marine environment mainly due to high current fields crossing the area particularly during strong Mistral (north western) or Greco (north eastern) wind events causing high waves. But hydrocarbons pollution at sea and coastline is also determined by what is called "operational pollution" of ships. Unfortunately, some ships tend to deliberately and illegally download their "dirty waters" (cleaning of tanks, bilges and ballasts) that lead to the formation of oil spills. In order to facilitate the rapid planning and coordination of operations of the marine authorities to tackle pollution during oil spill

emergencies, an innovative monitoring and forecasting system of the coastal marine circulation was developed through a numerical approach and in the framework of a 2-years project named "SOS-Bonifacio". The system allows to obtain simulations in real time to predict the fate of oils at sea and forecasts of their spread in the marine environment. The main objective is therefore the prevention and/or limitation of damages, for the conservation of marine resources in coastal waters, especially the most vulnerable areas of high environmental value typical of this area. Then, this system allows to limit an area of probability from which pollution was generated (backward investigation). In this paper the numerical system, named Bonifacio Oil spill Operational numerical Model "BOOM", is described and some "scenarios" and "risk maps" resulting from numerical runs are shown. The creation of "scenarios and risk maps" is very important as they will quickly identify the most appropriate intervention strategies, given the high variability of possible events, to be taken during an environmental emergency.

2 The boom system

The fate of oil at sea is determined by environmental conditions as well as by physicochemical properties of the oil. In particular, the main processes governing the fate of an oil slick at sea, are the mechanical transport induced by water currents and wind, and the "weathering" processes. The former are mass conservative whereas the latter, which are the spreading, evaporation, dispersion, emulsification, sedimentation and biodegradation, lead to reduce the mass of hydrocarbons at sea. Both transport and weathering processes are under-

stood with different levels of confidence and can be described by numerical models. The Bonifacio Oil spill Operational Model (BOOM) is composed of different numerical models and facilities aimed to provide a prognostic tool for managing oil spill emergencies in the strait of Bonifacio area. In particular, the core of the BOOM system consists of a set of finite element numerical model with a 3D hydrodynamic model (SHYFEM), a phase averaging wind-wave model (WWM), a Lagrangian trajectory module and a "weathering" module coupled one to each other. The SHYFEM hydrodynamic model [1] resolves the shallow water equations in their formulations with water levels and transport. Vertical integration is performed on a set of finite difference layers whereas it uses finite elements for horizontal integration and a semi-implicit algorithm for integration in time. The horizontal diffusion, the baroclinic pressure gradient and the advective terms in the momentum equation are fully explicitly treated. The Coriolis force and the barotropic pressure gradient terms in the momentum equation and the divergence term in the continuity equation are semi implicitly treated. The friction term is treated fully implicitly for stability reasons. The discretization chosen let the model be unconditionally stable for what concerns the effects of fast gravity waves, of the bottom friction and of Coriolis acceleration [2]. For the computation of the vertical diffusivities and viscosities a turbulence closure scheme has been used. This scheme is an adaptation of the k- module of GOTM (General Ocean Turbulence Model) described in [3]. The WWM wind wave model [4] is a phase averaging numerical model which solves the Wave Action Equations (WAE) by means of finite element integration method. The model de-

scribes the growth, decay, advection, refraction and diffraction of wind waves due to wind action, depth gradient and coasts geometrical features. The coupling of the wave and the current models is realized using the wave induced surface stresses computed with the aid of the radiation stress theory of [5] as formulated by [6]. The hydro-wave numerical model is coupled with a tool for reproducing Lagrangian trajectories generated by both staggered current and wave fields. Finally, a module for reproducing the main weathering processes affecting the oil spill at sea is including, taking into account for evaporation emulsification and mechanical spreading of different type of fuel oil and crude oil. The adopted algorithms have been found in bibliography [7]. The integrated set of numerical tools are applied over the same numerical domain constituted by a staggered finite element grid which reproduces the main geometrical and morphological features of the Bonifacio Strait with a spatial resolution ranging between few kilometers and few meters, as reported in Figure 1. The system is also connected to an interface for managing forcing and boundary data in real time which allows, daily, to receive both high resolution atmospheric data and hydrological data along the domain borders. Both are predicted for the next 5 days by SKIRON model from Athens University and by WMED circulation regional model from IAMC-CNR in Oristano, respectively. Therefore, every day, operationally, wind and wave fields, 3D water circulation and water temperature and salinity are provided hourly by the BOOM system for the interested area with a forecasting time lag of 5 days.

3 Applications

The BOOM system is going to be totally operational in the early 2011 at the Coast Guard offices of the La Maddalena Island. Up to now it has been used to provide scenarios analysis and to evaluate the risk induced by the hypothetical impact of hydrocarbons in the coastal areas of the La Maddalena Archipelago. Furthermore, the system has been applied to develop a technique for tracking back in time the path followed by oil dispersed in the sea. The adopted method known as “backward investigation” allows to identify the most probable initial hydrocarbons spilling area. In the following, the results obtained by a selected scenario simulation, by the risk analysis and by an example of backward investigation are reported and discussed.

3.1 Oil spill scenarios

A series of numerical simulations have been carried out in order to reproduce the most probable pollutant scenarios affecting the Bonifacio Mouth area. In particular meteo-marine forcing, type and quantity of dispersed hydrocarbons and spilling area have been selected considering the climate, the maritime traffic features and the historical maritime incidents occurred in the area. Six main macro-scenarios have been defined differing one from the other in relationship to the spilling area and the type and quantity of hydrocarbons released. For each macro-scenario, 8 simulations have been carried out in order to consider the seasonal variability of wind regime and water temperature. For all the simulations, stationary open boundary conditions and wind forcing have been defined and a spin-up time of 3 days have been selected to damp out the noises generated by the im-

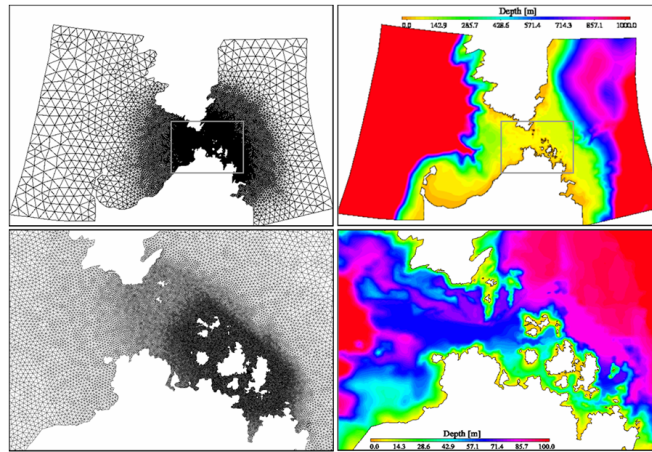


Figure 1: Finite element grid and bathymetry of the Bonifacio Strait area (upper panels) and zoom for the La Maddalena Archipelagos (lower panels).

posed initial condition. Wind wave propagation and the three dimensional water circulation have been reproduced for the interested area. For each macro-scenario, a defined quantity of numerical particles have been initialised in the selected spilling area. Each particle represents a quantity of oil released in the water with an associated density depending on the type of oil simulated. Simulations considered oil quantity released varying between 1000 m^3 and 10 m^3 with an oil density range representative of fuel oil, marine diesel and crude oil. About 50 scenarios have been considered and several types of results have been provided:

- wave and surface current velocity fields ;
- hourly field of oil slick depth ;
- hourly field of Lagrangian particle position and oil impact areas on the shore;
- time series of oil quantity dispersed on sea or beached.

In the following, the results obtained for a scenario consisting on the impact on the Baretini shoal ($41^\circ 16.8' \text{ N}$, $009^\circ 24.1'$

E, Figure 2) of a cruise ship on the route Livorno-Barcellona are reported. The hypothetical maritime incident has been settled in the spring period during an high intense mistral wind storm. A 30 m^3 fuel oil has been set as the initial quantity of oil released. In Figure 2 the surface water circulation computed by the model is reported. The intense mistral wind ($13 \text{ m}\cdot\text{s}^{-1}$), generates an eastward water circulation with currents velocities up to $1 \text{ m}\cdot\text{s}^{-1}$. The Lagrangian particles released are quickly transported eastward from the combined effect of wave, water currents and wind drift. In Figure 3, three snapshots representing the particles distribution in the water as computed by the model are reported. After 10 hours from the moment of the release all the particles are beached. In particular, the area mostly interested by the oil impact is the Caprera Island (see green dots in Figure 3). In Figure 4 the temporal variation of the total amount of the oil, as shared between quantity dispersed in the water and quantity beached, is shown. The

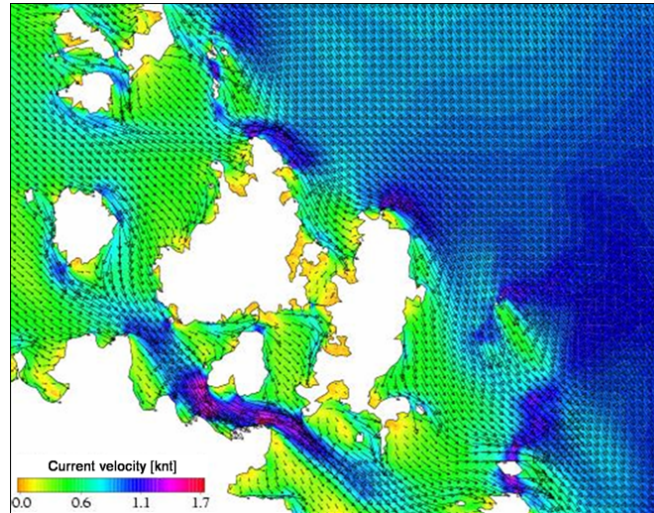


Figure 2: Surface water circulation induced by a $13 \text{ m}\cdot\text{s}^{-1}$ Mistral wind.

oil mass dispersed in the water (red curve in Figure 4) decreases fast in the first 3-4 hours due to the evaporative processes. Then, the reduction is due to the impact on the shore, which is well evidenced by the increasing of the green curve in Figure 4. After all the oil is beached, the total quantity is still diminishing because of the evaporative and emulsification processes which occur on the part of oil re-dispersed on the sea by the wind wave impact on the shore. The obtained results allow the local Coast Guard to have an accurate view above the evolution of the most probable oil spill events in the area. In particular, the hourly maps of oil slick position and the information about areas of oil impact in relationship to the different meteorological conditions provide a useful tool to manage oil spill emergencies.

3.2 Risk analysis

Several numerical simulations have been conducted with the BOOM in order to produce probabilistic estimates of the oil impacts on the coast in relationship different oil spills. In particular, three different categories of oil spills events have been chosen:

- release of hydrocarbons from oil-tank vessels;
- release of hydrocarbons from cruise-ships;
- release of hydrocarbons from ferry-boats.

For all these cases, the quantity of oil considered during each experiment corresponds to the average volumes contained in the bunkers of the different ships. For each category, an one year simulation have been carried out forcing the hydrodynamic and wave model with wind and open boundary data provided by meteorological and open ocean operational model. Each simulation is initialised with an amount of par-

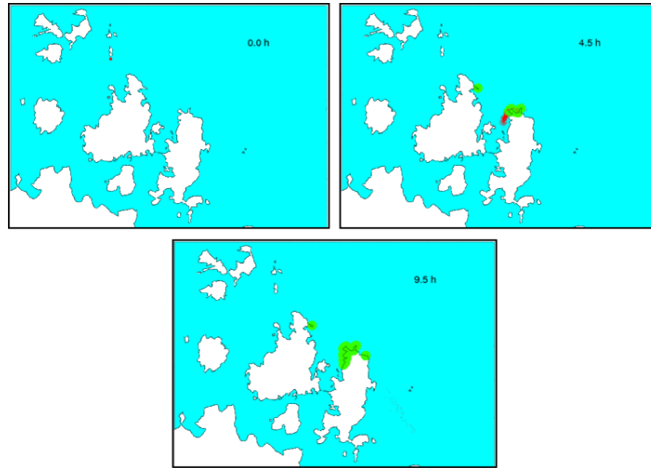


Figure 3: Snapshots of oil particles distribution dispersed in the water (red dots) and beached on the shore (green dots).

ticles statistically enough to cover the paths corresponding to the maritime traffic routes followed by the considered ship category. The particle “seeding” is repeated daily in order to take into account the influence of the meteorological variability on the Lagrangian transport. Each particle represents a possible spilling event of a defined quantity and type of oil which can occur along the whole maritime route and at any time of the year. The computed water currents, wave propagation and wind drift, transport and diffuse all the particles within the numerical domain. Each particle is also subjected to the weathering and stranding processes which led to reduce the oil quantity on the sea. After the end of each model run, the quantity and number of oil particles beached on the coast has been computed. The coastline has been subdivided into cells of 200 meters size and, for each cell, the total amount of oil beached during each month of the simulated year has been calculated. Then, the cell values have

been normalized to the maximum quantity of oil beached on a cell during the considered month. Therefore, for each category, 12 maps consisting on the distribution of a relative risk index, ranging between 0 and 1, have been produced. The so-derived risk index aims to describe, in a probabilistic way, the risk that the spilled oil will contact the coast as a function of geophysical forcing only. Neither vulnerability aspects (biological resources, environmental value, anthropic value etc.) nor accessibility of the coast have been considered. In Figure 5 the monthly map of risk induced by the impact of oil on the coast as released by ferry-boats connecting Palau to La Maddalena harbours is reported as computed for January. The maximum risk of impact is found in two landing areas (Palau and Maddalena harbours) and between La Maddalena island and Sardinia, whereas, it decreases eastward and westward along the coastline. The obtained results allow the local Coast Guard to have a tool for eval-

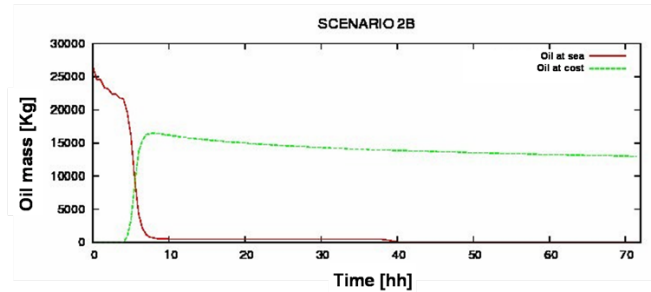


Figure 4: Temporal variation of the total amount of oil quantity dispersed in the water column (red curve) and beached on the shore (green curve).

uating the most exposed areas to the risk of oil impact on the coast in relationship to the period of the year. Such information are very useful in order to define the proper location along the coast to place the instruments and resources need to intervene in the case of oil spill pollution.

3.3 Backward investigation

When a major oil spill happens in the sea, most marine pollution authorities are usually quick to respond and to identify the responsible. Nevertheless, specially in coastal waters, most of the oil spill events are due to the common illegal practice of refuelling or pumping oily bilge water overboard. Even if they constitutes small spills, their high frequency can have significant negative effects on the marine environments. In this case, the identification and the quantification of the responsibilities is very difficult and quite impossible. In order to provide a support to the Coast Guard for detecting the responsibilities in oil spill pollution events, a numerical tool for carrying out the so-called “backward investigation” has been developed. The system based on the BOOM aims to track in the past the paths followed by the oil dis-

persed in the water which constitutes the pollutant event. The method consists on performing a sequential run of 2 simulations, a “forward” and a “backward” one. In the first, the hydrodynamic and wave models reproduce the water circulation and wave field during a selected period (TI), before a time TF when the oil slick has been detected in position XF. The results are stored in external files and processed to invert both the temporal order of the fields sequence and the current and wave propagation directions. Then, the “backward” run is performed and the Lagrangian advection model only is used to transport and diffuse a quantity of particles representing the amount of oil spill detected in the final position XF at time TF for a time lag corresponding to TI. The simulation uses as input data the stored and processed current and wave data obtained by the forward run. The results provide, therefore, a tracking of the detected oil spill from moment TF and final position XF back in time to TI and to initial most probable position XI. In Figure 6 an example of a backward analysis carried out to backtrack an oil slick of about 30 m³ detected in XF at the 12:00 of the 27/08/2008 is shown. The first frame refers to the moment TI whereas the last

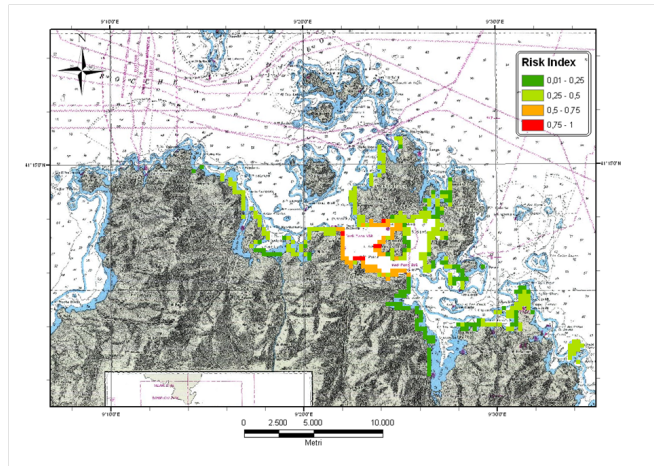


Figure 5: Risk map of oil impact on the coast released from ferry-boats connecting Palau to La Maddalena computed for January.

frame is referring to 6 days before the time TI when the position of the slick is in correspondence to the main maritime traffic route (XI). Here the release probably occurred. The method cannot individuate the exact initial position of the oil spill but it reveals the most probable path followed by the oil slick in the water. Therefore, such numerical tool constitutes a useful instrument to facilitate the detection of responsibility in case of oil pollution events.

4 Conclusions

The Bonifacio Oil spill Operational Model (BOOM) constitutes the core of an operational system developed to support the La Maddalena Island Coast Guard to manage oil-spill emergencies occurring in the coastal area of the Bonifacio Mouth. The BOOM is an integrated numerical tool constituted by a 3D hydrodynamic model and by a wind wave model both based on the finite element method and coupled alto-

gether. The system is also coupled with a Lagrangian trajectory model and a module for reproducing the main weathering processes that interests the oil slick on the sea. The system will be fully operational on the early 2010 at the La Maddalena Coast Guard and will allow to predict, in real time, the fate of oil spills in the investigated area. Up to now it has been used to investigate the consequences induced by selected hypothetical oil-spills events, to produce maps of risk due to the potential oil slicks impact on the coasts and to provide a tool for tracking back the paths followed by oil slick on the sea surface. The obtained results provide to the local Coast Guard an accurate view above the evolution of the most probable oil spill events in the area and a tool for evaluating the most exposed areas to the risk of oil impact on the coast in relationship both to the period of the year and to the type and quantity of spilled oil.

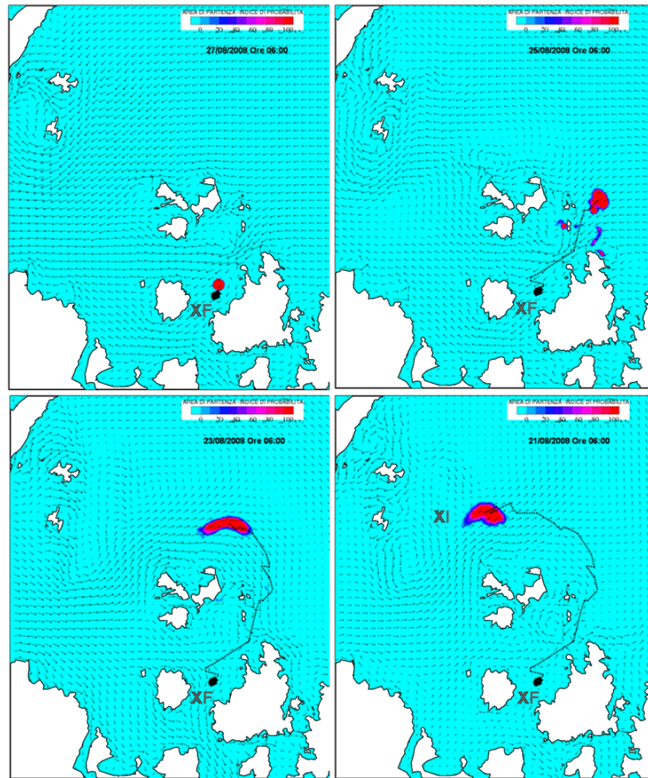


Figure 6: Backward investigation results. XF and XI are the final position at time TF and the most probable initial position at time TI, which corresponds to 6 days before TF.

5 Acknowledgements

A special thank to the CF (CP) Commander Rodolfo Giovannini of the La Maddalena Harbour Office for his support to opera-

tions. This work is part of the project SOS-BONIFACIO (contract DEC/DPN 2291 of 19/12/2008) funded by the Directorate General for Nature Protection of the Italian Ministry for Environment, Land and Sea.

References

- [1] G. Umgiesser, D. Melaku Canu, A. Cucco, and C. Solidoro. A finite element model for the Venice Lagoon. Development, set up, calibration and validation. *Journal of Marine Systems*, 51:123–145, 2004.
- [2] G. Umgiesser and A. Bergamasco. Outline of a Primitive Equations Finite Element Model. 1995.

- [3] H. Burchard and O. Petersen. Models of turbulence in the marine environment - a comparative study of two equation turbulence models. *Journal of Marine Systems*, 21:29–53, 1999.
- [4] A. Roland, A. Cucco, C. Ferrarin, T.W. Hsu, J.M. Liao, G. Umgiesser, and U. Zanke. On the development and verification of a 2d coupled wave-current model on unstructured meshes. *Journal of Marine Systems*, 78:244–254, 2009.
- [5] M.S. Longuet-Higgins and R.W. Stewart. Radiation stress in water waves: a physical discussion with applications. *Deep Sea Research*, 11:529–562, 1964.
- [6] X. Huayong, X. Zongwan, and Z. Liangsheng. Vertical variation in radiation stress and wave-induced current. *Coastal Engineering*, 51:309–32, 2004.
- [7] D. Mackay, F. Buist, R. Mascarenhas, and S. Paterson. *Oil Spill Processes and Models*. 1980.

Coastal and Offshore Geohazard in the Bays of Napoli and Salerno (Campania, Southern Italy)

C. Violante, G. de Alteriis, E. Esposito, F. Molisso, S. Porfido, M. Sacchi
Institute for Coastal Marine Environment, CNR, Napoli, Italy
crescenzo.violante@iamc.cnr.it

Abstract

In the Bays of Naples and Salerno major hazard-related seafloor features strictly correlate with episodes of intense coastal erosion driven by volcano-tectonic activity and hydrological events. Debris aprons and seafloor hummocks off Ischia volcanic island and Somma-Vesuvio indicate the presence of catastrophic landslide events with high tsunamigenic potential. These deposits partly associate with underwater failure areas, but the occurrence of a subaerial amphitheatre scarps clearly suggest a terrestrial initiation of the landslide phenomena. Other volcanic-dominated seafloor and coastal slope instabilities associate with dispersal of pyroclastic fall-out deposits following the great AD 79 Vesuvius eruption. The plinian event have accumulated huge amount of loose pyroclastic material over large marine and coastal areas thus creating favorable conditions for volcanoclastic mass flows and rapid sediment transfer. As a consequence coastal fan deltas fed by alluvial fans developed at mouth of main streams that flow into the Napoli and Salerno Bays. Moreover, wavy and lobate seafloor morphologies resulting from creep deformations and slumps of the AD 79 air-fall tephra occur off the Sarno River and in the Salerno Bay. Such hazard-related features have been detected by marine and on-land geological investigations and reported in geohazard maps with the aim to recognize, compare and classify hazard bearing coastal processes.

1 Introduction

The study coastal area includes among the most active volcanoes, namely: Somma-Vesuvius, Campi Flegrei, Ischia, and Procida (Figure 1). The volcanic activity started about 300-400 ka in the Vesuvian area [3] and about 150 ka at Ischia Island [4]. Oldest volcanic products in the Campi Flegrei area date back to 60 ka [5]. In the Pozzuoli area major periods of volcanic activity occurred from 10.0 to 8.0 ky B.P [6] and 4.5 to 3.7 ky B.P. [7] with two main plinian events: the Aganano Pomici Principali and the Agnano

Monte Spina eruption. The intensive volcanic activity shaped the coastal morphology and provided a large amount of volcanoclastic material with significant geomorphic implications. The rapid emplacement of volcanoclastic material significantly controlled the hazard related seafloor and coastal features resulting from geophysical and geological investigations carried out both on land and at sea.

Large aprons of avalanche deposits off the Somma-Vesuvius and the Ischia island (Figure 2 and Figure 6) clearly indicate catastrophic coastal failures able to trigger tsunami events as the displaced

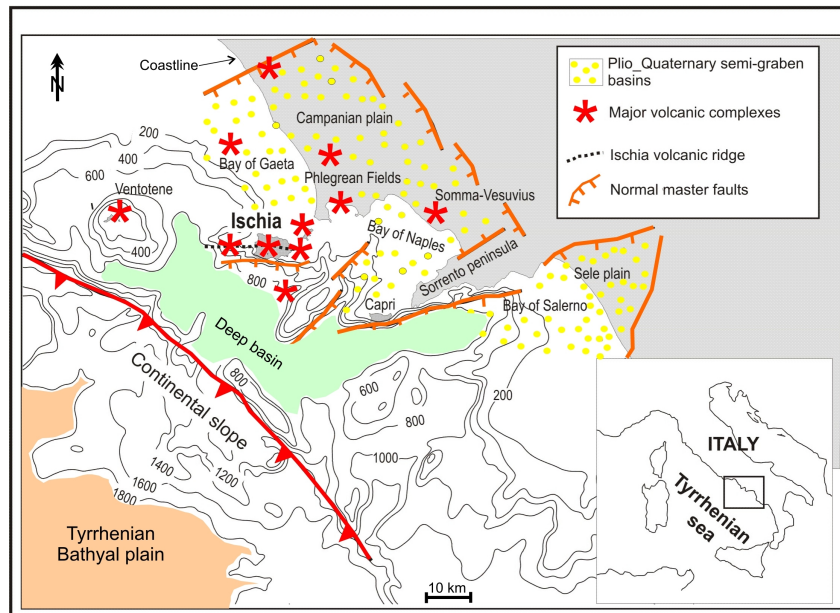


Figure 1: Location of the study area. Modified from de Alteriis and Violante [1].

material enter into the sea. These deposits well correlate with slope instabilities affecting the volcanic structures on-shore, suggesting a terrestrial initiation of the landslide phenomena [8, 9, 10, 1]. Volcanic induced geohazard processes are also claimed by spread of pyroclastic fallout deposits, mostly produced by the famous AD 79 Somma-Vesuvius eruption, now forming unstable sedimentary covers on top of steep coastal slopes and weak layers in the marine sedimentary record. A pyroclastic level found in core samples and traced in seismic profiles [2] has been recognized as the 79 AD tephra (Figure 3). It is buried at various depths below seafloor and appears to act as a “decollément layer” for several instability phenomena denoted by lobate morphologies in the shelf areas (Figure 4) and by arcuate failure scarps in deep sea areas (see Figure 9). In the bay of

Pozzuoli these features are associated with local tephra layers and triggered by intracaldera resurgence.

On the Amalfi and Sorrento rocky coasts catastrophic stream-flows occurred soon after the Pompei eruption burying the Roman maritime villas of Positano, Amalfi and Marina di Equa with a significant costal progradation of some hundred meters [11, 12, 13, 14]. In these areas severe alluvial crisis induced by volcanic watershed disturbance following the AD 79 Somma- Vesuvio fall-out event deposited a large amount of pyroclastics in the form of fan deltas and coarse clinofolds at the mouth of major coastal streams. In the last four centuries similar phenomena caused heavy damages and many casualties to the coastal communities, historically located at river mouths or along the paths of the flowing waters [15, 16, 13, 17]. Other signif-

icant offshore geohazard features relate to the Magnaghi and Dohrn canyons that originate from the shelf break of the Napoli Bay off the Campi Flegrei volcanic complex. It is a fossil drainage system, likely controlled by morphostructural lineaments i. e. the Banco di Fuori and Capri structural highs with retreating heads and erosional walls as testified by several scars and sliding phenomena. Arcuate lineaments at canyon heads often associated with rills and channels in the mid-upper slope commonly develop at shelf break suggesting incipient retrogressive failures. Erosional processes also occur along the canyon axes mostly as slump phenomena [18, 19, 20]. The main aim of this paper is to document the influence of volcanic activity on the stability of Napoli and Salerno coastal geomorphic system. For this purpose the most significant examples based on marine geophysical investigations are herein reported and discussed. The collected data and information have been mapped with the aim to recognize, compare and classify hazard bearing coastal processes: a basic approach for assessing and managing risk related to geological processes.

2 Data and methods

The dataset used in this study includes partially published swath bathymetric data, acoustic imagery from side-scan sonar records, and high resolution seismic and sub-bottom acoustic profiles. The bathymetric data have been collected in several multibeam sonar surveys over a wide depth range, with different spatial resolutions [18, 21]. The merging of these surveys with the on-land topography resulted in a 20 m x 20 m digital elevation model (DEM). This DEM allows us to recog-

nize large-scale features and sea-floor fabric with a spatial resolution of some meters, which is sufficient to detect most of the hazard-related features described below. Side-scan sonar data were acquired with a 100 kHz Edgetech DF1000 tow fish and processed through the Isis-Delph Map (TM) software package for navigational errors and slant-range correction. Processing and mosaicking of the sonar records resulted in backscatter maps with sub-meter resolution.

Seismic single-channel data include some digital and analogue records both acquired with a 1-4 kJ sparker source. Digital records were processed in the 200-1500 Hz frequency range after de-bias, filtering, time variant gain, automatic gain control and muting. The seismic data include also subbottom Chirp profiles and a grid of more than 100 km of very high-resolution single channel (uniboom) reflection profiles acquired using the IKB-Seistec profiler off the Amalfi shelf. This latter has been designed specifically for collecting very high-resolution data in shallow-water environments. Ground truth was provided by detailed analysis of gravity-cores and grab samples. By integrating these datasets large portions of the seafloor has been mapped for geological purpose and hazard assessment.

3 The Campi Flegrei coastal area

The Campi Flegrei (i.e. “burning plains”) are located north of Naples, an area characterized by active tectonics and volcanism since the Pleistocene. It is a densely urbanized coastal zone, including the bay of Pozzuoli, Procida and Ischia islands, where

documented human activities have been developing for more than two thousand years. In the Pozzuoli area two major periods of eruptive volcanic activity occurred from 10.0 to 8.0 ky B.P. and 4.5 to 3.7 ky B.P. These periods were followed by the September 1538 Monte Nuovo eruption. Numerous monogenic volcanoes formed close to the shoreline and volcanic debris interpreted as submarine counterpart of subaerial flow and surge, has been detected offshore [19, 12]. On Ischia Island the most recent volcanic activity starts around 10.0 ky B.P. [22] to which associates several eruptive centers mostly located in the western sector. The last eruption dates back to Arso flow in 1302. Nevertheless the landscape of Ischia is dominated by Mount Epomeo in the central part of the island, which is the highest peak (788 m). It is a volcano-tectonic structure that raised above sea level between 33 and 28 ka BP, due to the intrusion of magma at shallow depth [23, 24]. In the Campi Flegrei, magma related activity is testified by extensive hydrothermalism, and recent episodes (1883 on Ischia, and 1970-71 and 1982-84 on Pozzuoli coast) of shallow seismicity and ground deformation, exceeding rates of 100 cm/year in the years 1983-1984. Volcanic and volcano-tectonic activity mainly associate with a resurgent calderas [6, 25] whose uplift have caused mass wasting phenomena, faulting and erosional activity both on land and at sea. Major geohazard features resulting from marine geophysical and sedimentological investigations (Figure 5) include (1) extensive landslide deposits and associated hummocky topographies off Ischia volcanic island, (2) seafloor instabilities in the form of creep/slump, channeled sediment flow and deep sedimentary fan (3) superficial faulting (i.e. displacing the seafloor) in the bay

of Pozzuoli and (4) erosional morphologies and forms at the canyon heads and the shelf break. Moreover, numerous volcanic bank and pyroclastic structures have been detected off the bay of Pozzuoli and Ischia Island, both in the shelf area and deeper waters [21, 25, 26].

4 The Somma-Vesuvius coastal district

This coastal district includes two small alluvial plains: the Sebeto plain and the Sarno plain developing immediately to the north and to the south of the Somma-Vesuvius volcanic structure respectively. It is a coastal area located in between the Campi Flegrei and the Sorrento Peninsula characterized by a wide continental shelf mostly formed by volcanoclastic and prodelta deposits. The shelf depositional system off the Somma-Vesuvius is controlled by the occurrence of two small deltas, formed by the Sebeto and Sarno rivers separated by an irregular relief south of Vesuvius, down to a depth of 100 m, associated with volcanic debris avalanches (Figure 6).

Wavy seafloor structures occur both off the Herculaneum archaeological site immediately south of the Sebeto delta area (Figure 6) and off the Sarno prodelta (Figure 4). In the first case such bedforms are induced by pyroclastic current derived deposits associated with the AD 79 eruption. Wavy facies correspond to dunes showing smaller size and dimension in the distal area of the subaqueous density flow suggesting a gradual decrease in grain size toward the sea [10]. In the Sarno marine area, seafloor undulations document extensive creep involving the whole post-79 AD succession. Seismic interpretation showed that slump-

ing of semi-consolidated strata occur over a basal surface represented by the lithologic discontinuity between the base of the 79 AD tephra deposits and the underlying hemipelagite (Figure 4, [2]). In particular, the geological evolution of the Sarno coastal area has been strongly influenced by Somma-Vesuvius activity. The AD 79 eruption produced about 10 km^3 of pyroclastic material [27] that buried the Roman cities of Pompeii, Herculaneum, and Stabiae and promoted a sudden progradation of the Sarno delta system with a seaward shift of the local shoreline of about 1 km [28].

5 The Sorrento-Amalfi coastal area

The Sorrento Peninsula is a major Quaternary morpho-structural unit of the western flank of the Southern Apennines consisting of a narrow and elevated mountain range (up to 1444 m) that separates the two bays of Naples and Salerno (Figure 1). It is mostly formed by a pile of Mesozoic carbonate rocks, covered by Tertiary to Quaternary siliciclastic and pyroclastic units, and is deeply cut by a complex pattern of bedrock rivers and channels characterized by small catchment areas that are very high relative to the base level. These rivers show a distinct seasonality and torrential behavior, with main delivery areas into the adjacent marine shelf [15, 16, 29, 19, 13, 14]. This area is located about 20 km south of the Somma-Vesuvius and has been repeatedly mantled during the last millennia by the pyroclastic products of the volcano. The most recent explosive eruptions of Vesuvius, particularly the AD 79 Plinian event, have accumulated loose pyroclas-

tic material over the steep coastal slopes thus creating favorable conditions for volcaniclastic debris to generate mass flows and flash floods in concomitance with rainy periods. In particular, during the Plinian eruption in AD 79, the study area was covered by up to 2 m of pyroclastic air-fall tephra [27, 30] now partly occurring as weathered levels up to a few meters thick or as deeply incised stream-flow deposits (locally called Durece) up to 30 m thick along the stream valleys [11]) and mostly stored as small coastal fan deltas fed by alluvial fans at the mouth of the main streams (Figure 7, [19, 20, 12, 13, 14].

Seismic profiles (Figure 8) show that the individual deltaic bodies are about 1 km^2 wide and a few tens of meters thick. They display a generally conical morphology with a delta front slope of approx. 20° and foresets inclination ranging from 15° to 30° . The pattern of seismic reflectors indicates that the stratigraphic architecture of the deltaic wedge is characterized by an average increase coupled with significant variations of progradation rates in the delta foresets. These variations are particularly evident in the delta front area. It can also be observed from the seismic record that gravity flows locally form debris-flow units and/or turbidite lobes with a thickness of a few meters and width of a few tens of meters (Figure 8b). Fine-grained turbidites are found above the AD 79 tephra layer, as suggested by the internal seismic facies and the external geometry of the deposits. Evidence of gravity-driven instability is common at various stratigraphic levels in the front of the delta system, particularly at the base of the prograding foresets.

The prominent gravity-driven instability and deformation of sediments detected at various stratigraphic levels within the delta slopes suggest that the stratal geometry of

the fan deltas was dominantly dictated by the effective transfer of sediments by hyperpycnal (e.g. inertia, turbidity) flows directly fed by river floods. This implies a primary control by stream-flow episodes that have provided conspicuous sediment yields to the coastal area, concomitant with the famous AD 79 Somma- Vesuvius eruption.

6 The Salerno Valley

The Salerno Valley is a wide morphostructural depression oriented NW-SE occurring off Salerno city up to a depth of about 900 m (see Figure 7). It is characterized by an asymmetric transversal profile with the northern flank coincident with the steep slope of the Capri-Amalfi fault and the southern one composed of gentle slope clinofolds of the Sele River prodelta. In the northern side the major hazard-related seafloor features are associated with talus and stream-born deposits occurring at the base of the Amalfi shelf-break. This latter is indented by numerous canyon heads, arcuate scarps and rills denoting incipient retrogressive failures. Deep sedimentary fans characterize both valley sides, while several debris slides (Figure 9) and channeled sediment flows, partly due to rapid accumulation of volcanoclastic material, occur along the southern side up to a depth of 500/600 m [19, 20, 13].

7 Conclusions

Marine geophysical surveys and a wide range of sea-bottom observations and sampling coupled with analysis of historical sources and sea-land correlations clearly indicate the influence of volcanic activity on the stability of Napoli and Salerno coastal geomorphic systems. In these areas episodes of coastal and seafloor instabilities are mainly driven by volcano-tectonic activity and associate with rapid deposition of pyroclastic fall-out deposits following explosive eruptions. On the base of the above investigations major geohazard features have been characterized and mapped. In the marine areas main hazard-related structures includes:

1. volcanic debris avalanches off Ischia Island and Somma-Vesuvius;
2. superficial faulting (i.e. displacing the seafloor) in the bay of Pozzuoli;
3. volcanic banks and pyroclastic structures off the bay of Pozzuoli and Ischia Island;
4. widespread seafloor deformations in the form of creep/slump, debris slide, channeled sediment flow and deep sedimentary fan;
5. coarse fan-deltas at mouth of main streams and small rivers;
6. erosional morphologies and forms at the canyon heads and the shelf break.

The collected data and information allowed us to recognize, compare and classify hazard bearing coastal processes providing tools for assessing and managing risk related to geological processes in coastal areas.

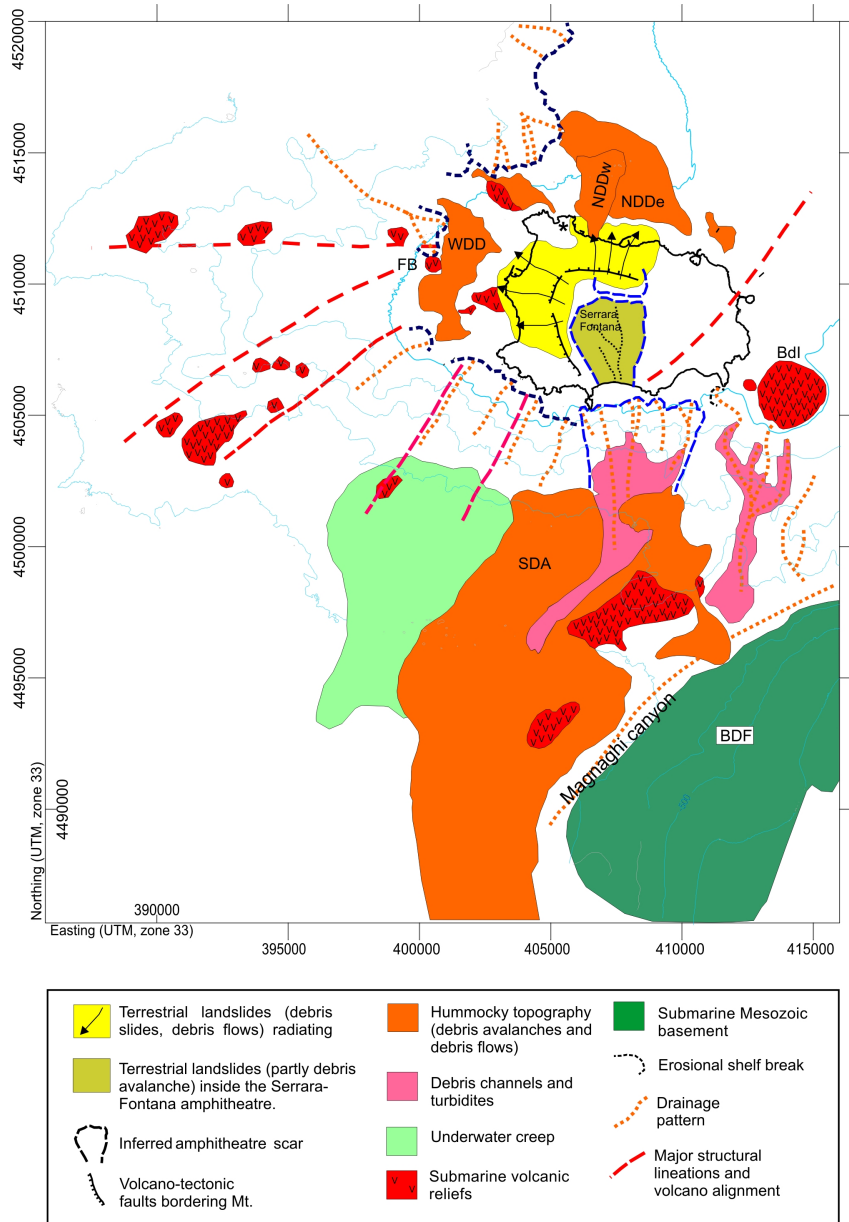


Figure 2: Interpretative geomorphological map of Ischia volcanic island and its offshore. SDA: southern debris avalanche; WDD western debris deposits; NDDE: northern debris deposits; NDDW: northern debris deposits (latest event); BDF: Banco di fuori; BDI: Banco d'Ischia; FB: Banco di Forio. Thin lines are the bathymetry contour. Modified from de Alteriis and Violante [1].

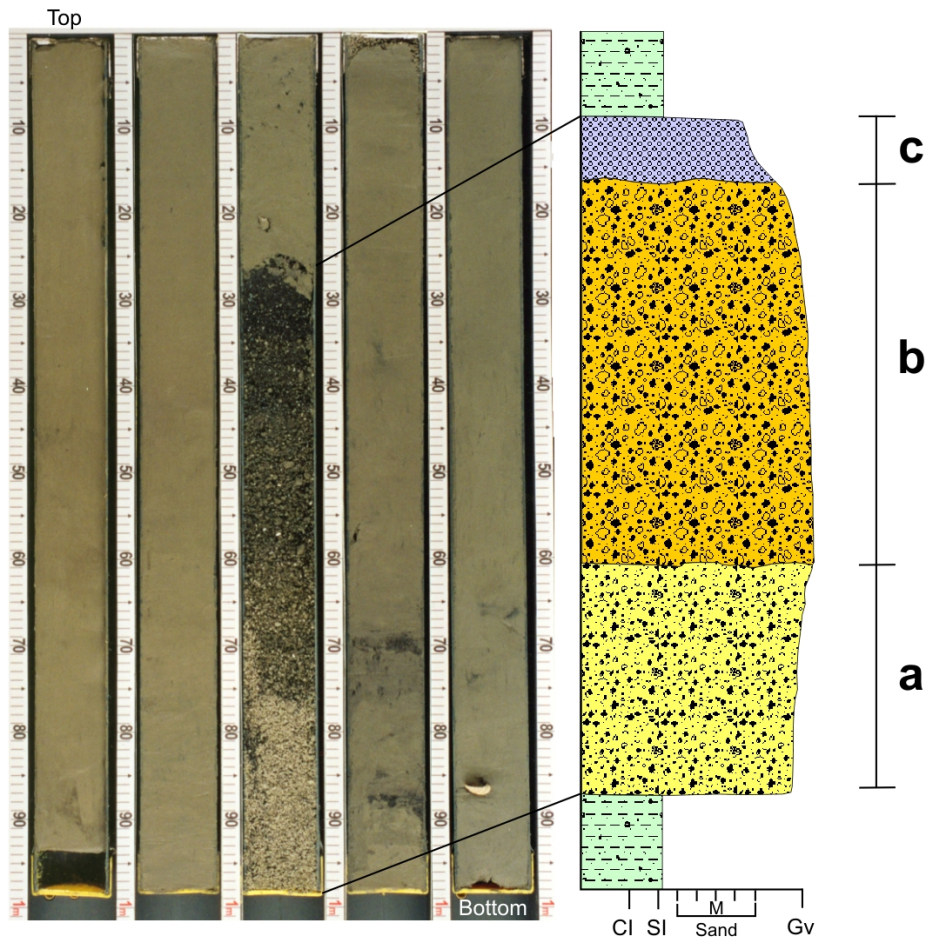


Figure 3: Core sample of the 79 AD tephra collected off Amalfi coast. The tephra consists of: (a) 25-cm-thick, reversely graded, subrounded, white pumice and lapilli; (b) 45-cm-thick, normally graded, sub-angular, coarse grey pumice lapilli and lithics and (c) 10-cm-thick, parallel-laminated coarse pumiceous and scoriaceous lapilli.

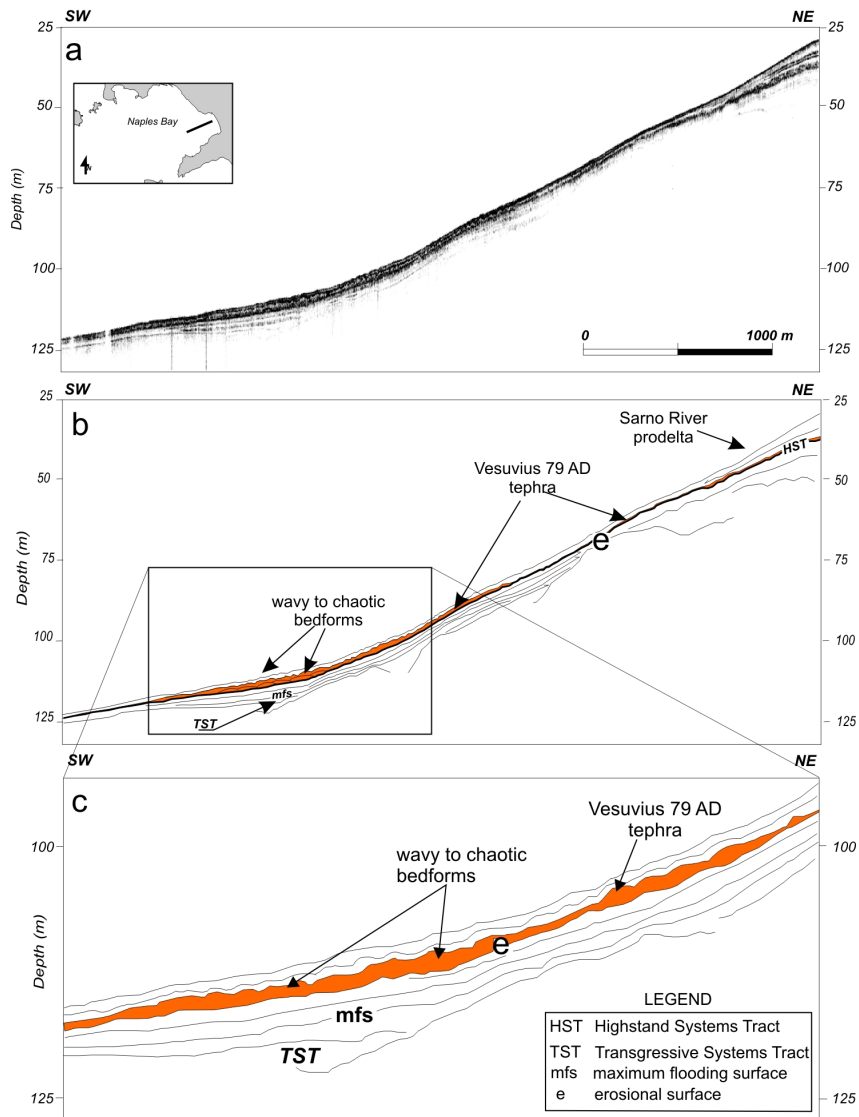


Figure 4: (a) Sub-bottom Chirp profile CsC-18 off the Sarno river mouth and (b) relative interpretation. (c) Note the remarkable erosive character of the base of the 79 AD tephra layer (e) down to 50-60 m water depth and the wavy to chaotic reflections within the post-79 AD deposits between 100 and 120 m water depth. See inset map in (a) for location. Modified from Sacchi et al. [2].

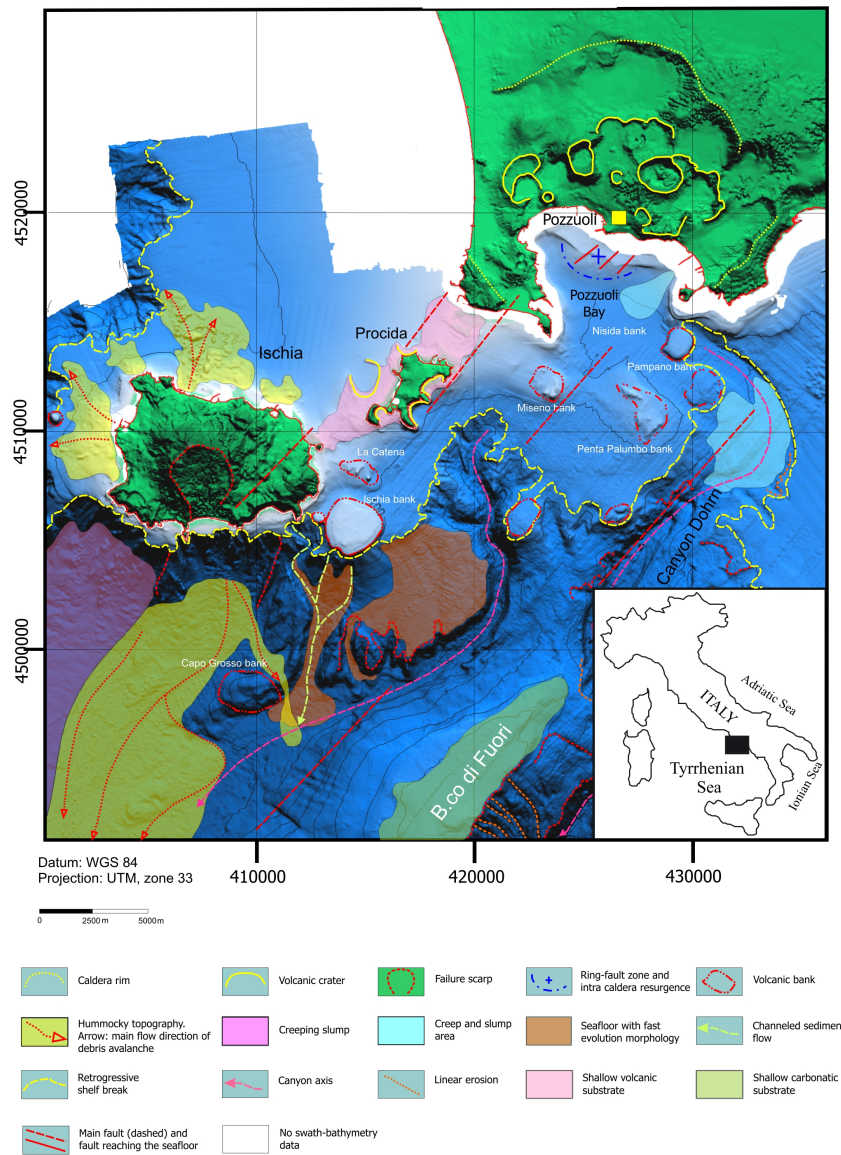


Figure 5: Geohazard map of the Campi Flegrei coastal area based on marine and on-land investigations including multibeam bathymetry, seismic stratigraphy, sea-floor imaging by side-scan sonar, sea-floor grab and core sampling, coastal geomorphology and aerial photographs. Modified from Violante[13].

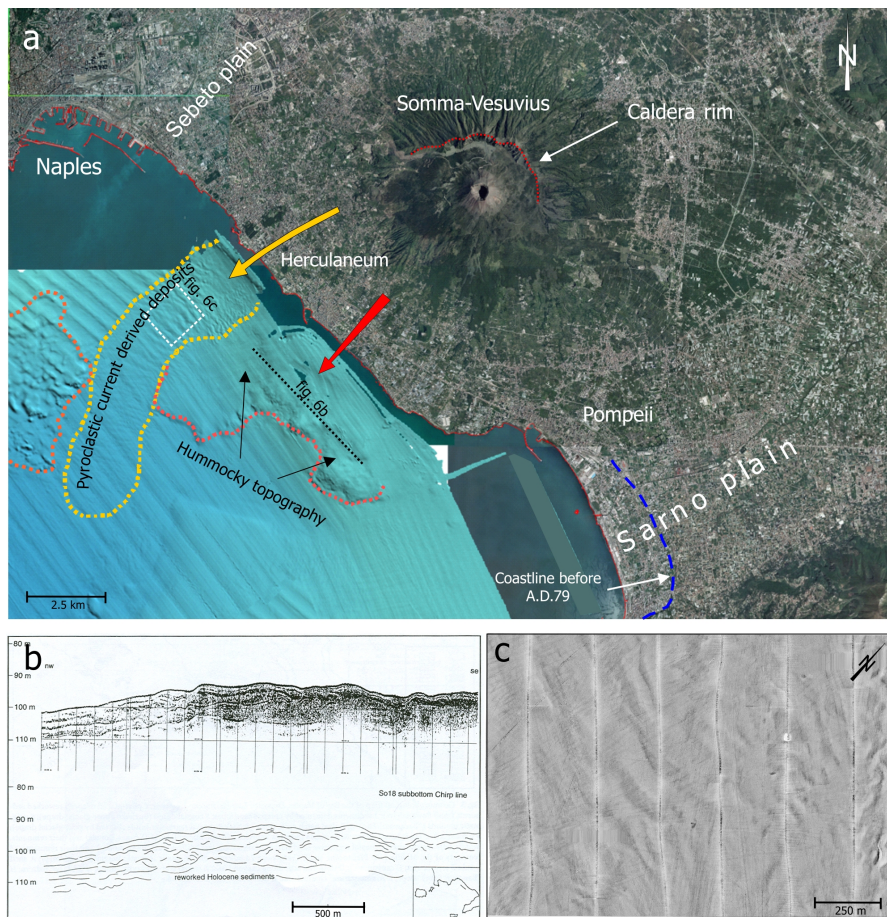


Figure 6: The Somma-Vesuvius coastal area. a - Example of the main hazard-related coastal and seafloor features obtained by merging swath bathymetry data and terrestrial elevation/aerial photographic data. b - Sub-bottom Chirp profile So18 showing the internal organization of the hummocky deposits. c - 100 kHz side-scan sonar image surveyed off Herculaneum with seafloor undulations.

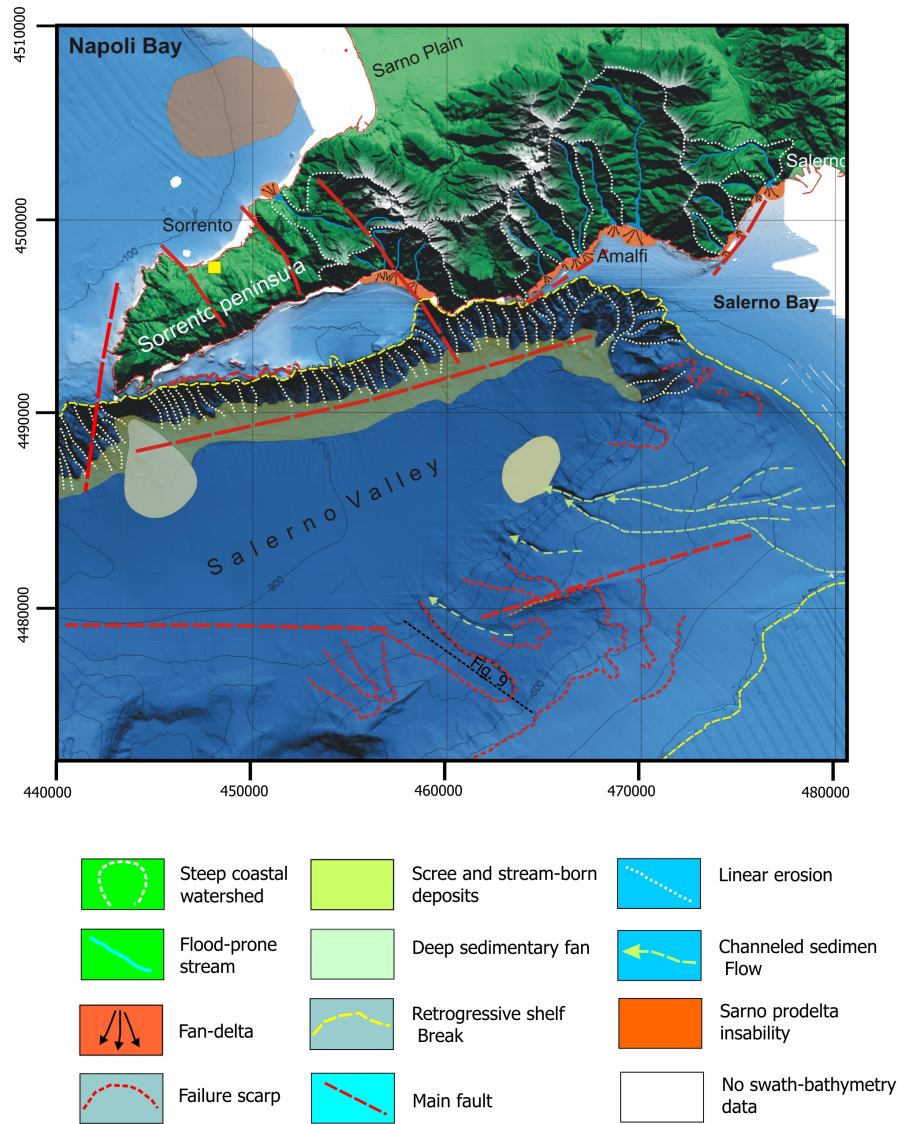


Figure 7: Geohazard map of the Sorrento Peninsula coastal and offshore area obtained by merging swath bathymetry data and terrestrial elevation data. Modified from Violante [13].

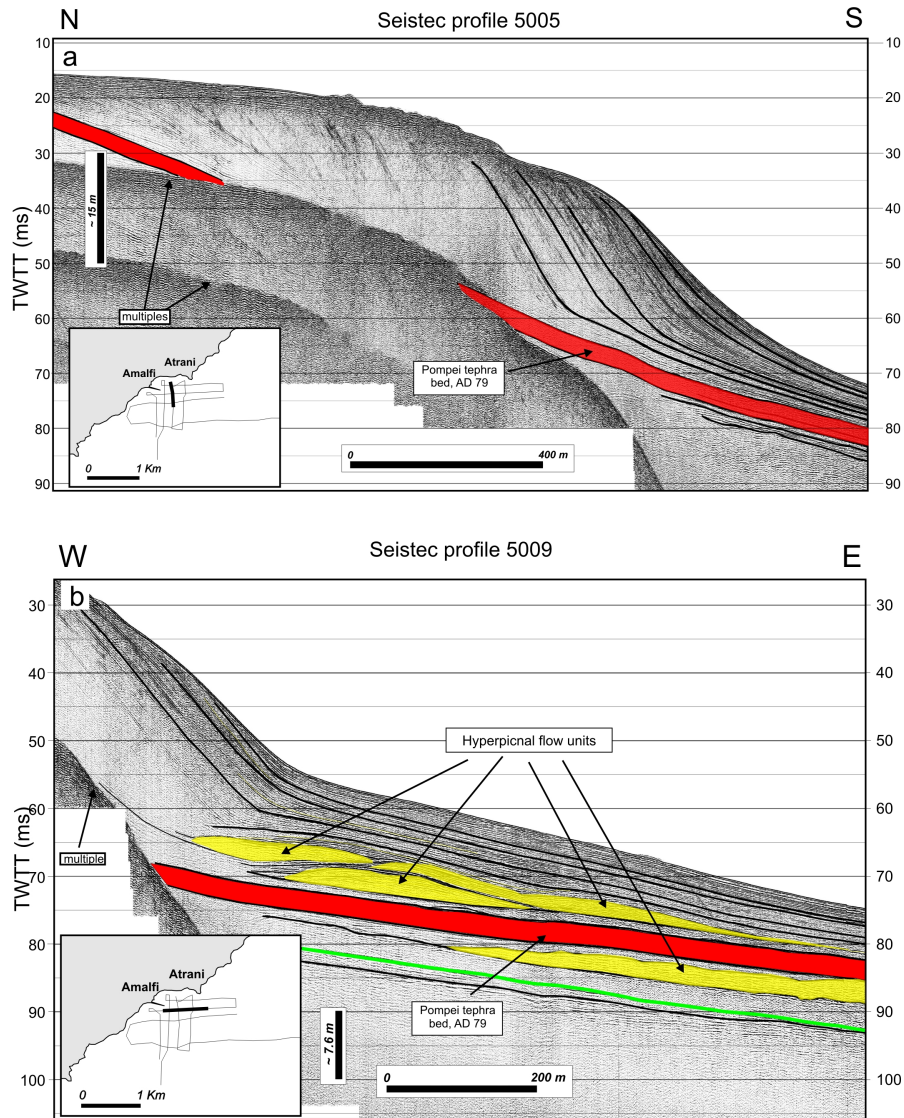


Figure 8: Main features of Amalfi fan delta based on very high resolution (IKB-Seitec) seismic profiles. Black lines are different tephra layers. The green line correspond to the maximum flooding surface. Insets show location of profiles. See text for further explanation. Redrawn from Sacchi et al. [12].

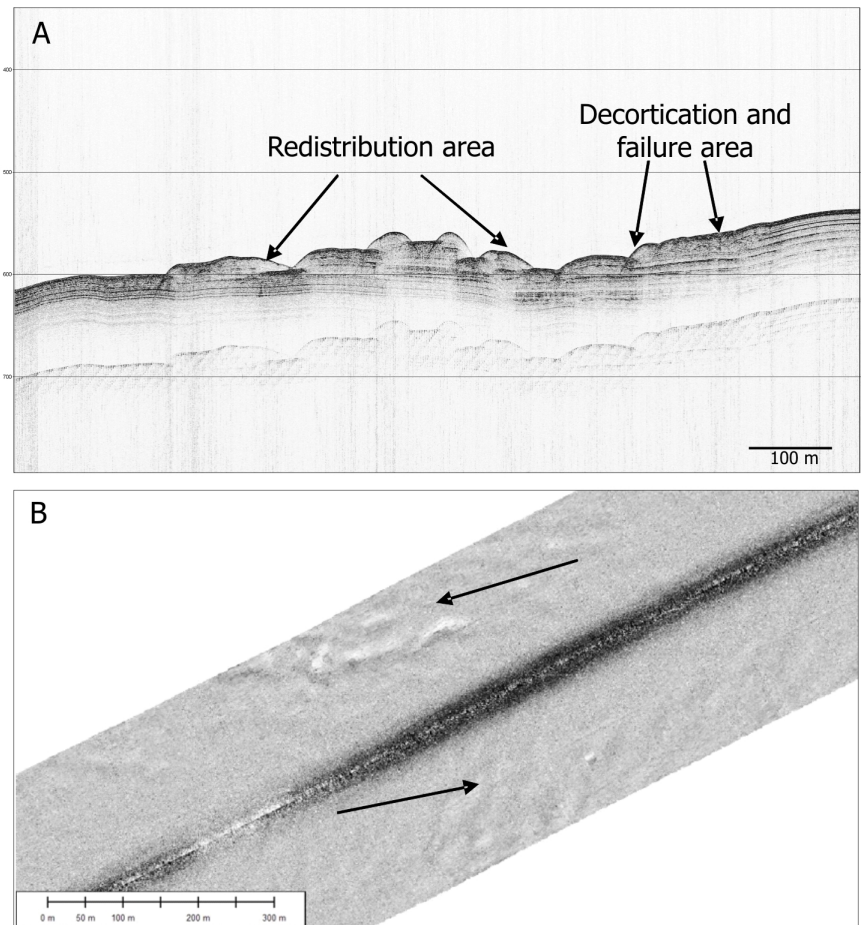


Figure 9: (a) Sub-bottom Chirp profile and (b) sidescan sonar image showing seafloor instability occurring along the southern flank of the Salerno Valley. See Figure 7 for location.

References

- [1] G. de Alteriis and C. Violante. Catastrophic landslides off Ischia volcanic island (Italy) during pre-history. *Special Publication, Geological Society of London*, 322:73–104, 2009.
- [2] M. Sacchi, D. Insinga, A. Milia, F. Molisso, et al. Stratigraphic signature of the Vesuvius 79 AD event off the Sarno prodelta system, Naples Bay. *Marine Geology*, 222-223:443–469, 2005.
- [3] D. Bocchini, C. Principe, D. Castradori, M.A. Laurenzi, and L. Gorla. Quaternary evolution of the southern sector of the Campanian Plain and early Somma-Vesuvius activity: insights from the Trecase 1 well. *Mineral. Petrol.*, 73:67–91, 2001.
- [4] S. Poli, S. Chiesa, P.Y. Gillot, and F. Guichard. Chemistry versus time in the volcanic complex of Ischia (Gulf of Naples, Italy): Evidence of successive magmatic cycles. *Contrib. Min. Petrol.*, 95:322–335, 1987.
- [5] L. Pappalardo, L. Civetta, S. de Vita, M.A. Di Vito, et al. Timing of magma extraction during the Campanian Ignimbrite eruption (Campi Flegrei caldera). *J. Volcanol. Geotherm. Res.*, 114:479–497, 2002.
- [6] M. Rosi and A. (eds) Sbrana. Phlegraean Fields. CNR, *Quaderni della Ricerca Scientifica*, 114(8):175 pp, 1987.
- [7] M.A. Di Vito, R. Isaia, G. Orsi, J. Southon, et al. Volcanism and deformation since 12,000 years at the Campi Flegrei caldera (Italy). *J. Volcanol. Geotherm. Res.*, 91:221–246, 1999.
- [8] C. Violante, F. Budillon, E. Esposito, S. Porfido, and E. Vittori. Submerged hummocky topographies and relations with landslides on the northwestern flank of Ischia island, southern Italy. In: L. Picarelli, *Proc. of Int. Conference on*.
- [9] F.L. Chiocci and G. de Alteriis. The Ischia debris avalanche. First clear submarine evidence in the Mediterranean of a volcanic island pre-historic collapse. *Terra Nova*, 18:202–209, 2006.
- [10] A. Milia, F. Molisso, A. Raspini, M. Sacchi, and M. Torrente. Syneruptive features and sedimentary processes associated with pyroclastic currents entering the sea: the AD 79 eruption of Vesuvius, Bay of Naples, Italy. *Journal of the Geological Society, London*, 165:839–848, 2008.
- [11] A. Cinque and G. Robustelli. Alluvial and coastal hazards caused by long-range effects of Plinian eruptions: the case of the Lattari Mts. After the AD 79 eruption of Vesuvius. *Geological Society, London, Special Publications*, 322:155–171, 2009.

- [12] M. Sacchi, F. Molisso, C. Violante, E. Esposito, D. Insigna, et al. Insights into flood-dominated fan-deltas: very high-resolution seismic examples off the Amalfi cliffed coasts, Eastern Tyrrhenian Sea. *In: Violante C. Geohazard in rocky coastal areas, Special Publication, Geological Society of London*, 322:33–71, 2009.
- [13] C. Violante. Rocky coast: geological constraints for hazard assessment. *In: Violante C. Geohazard in rocky coastal areas, Special Publication, Geological Society of London*, 322:1–31, 2009.
- [14] C. Violante, C. Biscarini, E. Esposito, F. Molisso, et al. The consequences of hydrologic events on steep coastal watersheds: the Costa d'Amalfi, eastern Tyrrhenian sea. *In: Liebsher, H.J. and others IAHS Publ., Red Book*, 327:102–113, 2009.
- [15] E. Esposito, S. Porfido, and C. Violante (eds). Il Nubifragio dell'Ottobre 1954 a Vietri sul Mare, Costa d'Amalfi, Salerno. Scenario ed effetti di una piena fluviale catastrofica in un'area di costa rocciosa. *Pubblicazione Gruppo Nazionale per la Difesa dalle Catastrofi Idrogeologiche*, 2870:381, 2004.
- [16] E. Esposito, S. Porfido, C. Violante, C. Biscarini, et al. Water events and historical flood recurrences in the Vietri sul Mare coastal area (Costiera Amalfitana, southern Italy). *In: Rodda, G. and Ubertini, L. (eds), The Basis of Civilization-Water Science? International Association of Hydrological Sciences*, 286:95–106, 2004.
- [17] S. Porfido, E. Esposito, F. Alaia, F. Molisso, and M. Sacchi. The use of documentary sources for reconstructing flood chronologies on the Amalfi rocky coast (southern Italy). *In: Violante, C. (ed.) Geohazard in Rocky Coastal Areas. Geological Society, London, Special Publications*, 322:173–187, 2009.
- [18] B. D'Argenio et al. Digital Elevation Model of the Bay of Naples and adjacent areas (Eastern Tyrrhenian Sea). *In: Pasquarè, G. & Venturini, C. (eds) Mapping Geology in Italy APAT-Dipartimento Difesa del Suolo Monography, Firenze*, pages 21–28, 2004.
- [19] C. Violante, G. de Alteriis, and E. Esposito. Seafloor base maps, geological features and hazard assessment in marine coastal areas. Example from the Bay of Naples, Campania, Southern Italy. *Proc. Of 5th European Congress on Geoscientific Cartography and Information Systems. Barcellona. Ist. Geo. Catalonia*, 1:534–537, 2006.
- [20] C. Violante, G. de Alteriis, and M. Sacchi. Marine geohazards in the Bays of Napoli and Salerno, eastern Tyrrhenian sea. *Società Geologica Italiana*, vol. 3:777–778, 2008.
- [21] G. de Alteriis, R. Tonielli, S. Passaro, and M. De Lauro. Isole Flegree (Ischia e Procida). *Serie: Batimetria dei fondali marini della Campania. Liguori, Napoli*, 1:55, 2007.

- [22] L. Vezzoli. Island of Ischia. *Quaderni de 'La Ricerca Scientifica' Progetto finalizzato 'Geodinamica', CNR Monografie finali*, page 67, 1988.
- [23] G. Buchner, A. Italiano, and C. Vita-Finzi. Recent uplift of Ischia, Southern Italy. In: *Mc Guire, W. J. and Jones, A.P. and Neuberg, J. (eds), Geological Society, London, Special Publications*, 110:249–252., 1996.
- [24] R.J. Brown, G. Orsi, and S. De Vita. New insights into Late Pleistocene explosive volcanic activity and caldera formation on Ischia (southern Italy). *Bulletin of Volcanology*, 70:583–603, 2008.
- [25] M. Sacchi, G. Alessio, I. Aquino, E. Esposito, et al. Risultati preliminari della campagna oceanografica CAFE-07 Leg-3 nei Golfi di Napoli e Pozzuoli, Mar Tirreno Orientale. *Quaderni di Geofisica*, 64:1–23, 2009.
- [26] A. Milia. The stratigraphic signature of volcanism off Campi Flegrei (Bay of Naples, Italy). *Doi: 10.1130/2010.2464(08), GSA Special Papers*, 464:155–170, 2010.
- [27] H. Sigurdsson, S. Carey, W. Cornell, and T. Pescatore. The eruption of Vesuvius in AD 79. *Nat. Geogr. Res.*, 1:332–387, 1985.
- [28] T. Pescatore, M.R. Senatore, G. Capretto, and G. Lerro. Holocene coastal environments near Pompeii before the AD 79 eruption of Mount Vesuvius, Italy. *Quaternary Research*, 55:77–85, 2001.
- [29] F. Budillon, C. Violante, A. Conforti, E. Esposito, et al. Event beds in the recent prodelta stratigraphic record of the small flood-prone Bonea Stream (Amalfi Coast, Southern Italy). *Marine Geology*, 222-223:419–441, 2005.
- [30] R. Cioni, R. Santacroce, and A. Sbrana. Pyroclastic deposits as a guide for reconstructing the multi-stage evolution of the Somma-Vesuvius caldera. *Bulletin of Volcanology*, 60:207–222, 1999.

Submarine Geohazard Assessment Based on Regional Seafloor Mapping. Example from the Italian Project MAGIC (Marine Geohazards along the Italian Coasts)

D. Ridente¹, A. Bosman¹, A. Sposato¹, D. Casalbore¹, A. Scalzo², C. Cristiani², V. Bosi², F.L. Chiocci^{3,1}

1, Institute of Environmental Geology and Geoengineering, CNR, Roma, Italy

2, Civil Protection Department, Roma, Italy

3, Department of Earth Sciences, University of Roma "La Sapienza", Roma, Italy
domenico.ridente@igag.cnr.it

Abstract

Recent developments in seafloor imaging and mapping techniques greatly improved our capability of identifying marine geohazards affecting the continental margins. Geological processes ranging from volcanic activity to active faulting, from slope instability to bedform migration, are well documented on Italian continental margins and are potential geohazards for human settlements and infrastructures on the coast and offshore. A number of geomorphic features can be detected by high-resolution multibeam imaging and regarded as geohazard indicators the most common include slide scarps and deposits, canyon headscarps and steep erosional canyon flanks, fault-related seafloor relief, mud volcanoes, pockmarks, gravity flow deposits, erosional scours and bedforms indicating sediment mobility at different temporal/spatial scale. We discuss some of the most frequent problems dealing with reconnaissance, interpretation and cartographic representation of geohazard-related submarine geomorphic features, with special reference to the National Mapping Project MAGIC (Marine Geohazards along the Italian Coasts).

1 Introduction

In very recent times, the impact of catastrophic events at global (e.g. Indonesia earthquake and tsunami, 2004 Samoa Islands earthquake and tsunami, 2009) and regional scale (e.g. Stromboli slide and tsunami, 2002) has made evident the necessity of knowing the worldwide distribution of submarine geological structures responsible for their generation, with particular reference to seismogenic faults, vol-

canic activity, submarine and coastal landslides. More in general, marine geohazards derive from a vast variety of geological processes reflecting the recent/modern seafloor morpho-dynamics, as well as the long-term tectono-sedimentary evolution of continental margins.

The capability to identify and characterize marine geohazards significantly improved because of the recent developments in seafloor imaging and mapping techniques. As a consequence, many research

programs specifically designed for defining marine geohazards rely on extensive (regional) seafloor mapping. Marine geohazards can be defined at different scales and level of detail and accuracy. As a starting point, geohazard mapping relies on the reconnaissance of the geohazard-related geological features, and is essentially regarded as the detection of their presence/absence and state of activity. In this view, the Italian Civil Protection Department promoted the national project MAGIC (Marine Geohazards along the Italian Coasts), aimed at acquiring multibeam morpho-bathymetry along the most geologically active margins of Italy the acquired dataset will then be the basis for interpreting geomorphic features and identifying potential geohazards.

In the following discussion we take into account some general aspects of geohazard reconnaissance and cartographic criteria relative to regional scale geohazard mapping, based on the experience arising from the Italian project MAGIC. In particular, we discuss some of the main conceptual and practical problems that arise when attempting geohazard identification based on multibeam imaging.

2 Multibeam Sonar acquisition

Sonar systems based on acoustic energy (echosounding) are the main instrument for exploring the sea. The term "SONAR" (SOund Navigation And Ranging) was first used referring to the underwater acoustic devices developed for submarine target location during wartimes. Since then, scientific institutions have been developing echosounder technology to allow increasingly detailed and accurate mapping of the

seafloor. This has brought to the evolution of bathymetry mapping into morpho-bathymetry mapping, including qualitative information on the nature and geology of the sea floor. Such advance in acquisition and mapping technology coincides with the advent of multibeam systems in place of the conventional single beam ecosounding systems.

The conventional single beam Sonar system is based on the emission of a single pulse acoustic energy (beam) from a transducer and directed to the sea floor directly beneath the ship (Figure 1A). After emitting, the transducer "listens" for the returning energy from the seafloor that is reflected from a single point. When the reflection is received, the water depth can be calculated by using the travel time of the emitted acoustic pulse from the transducer to the sea floor and back (i.e. two-way travel time). Interpolation and contouring of every individual depth value allows to generate bathymetric maps the detail of which increases with the number (density) of the measured depth points.

With Multibeam sonar systems, a fan of pulses (multibeam) is generated in the across-track direction (Figure 1B); each individual beam hits the seafloor along a line of soundings perpendicular to the track line. As the vessel moves forward, the multibeam acoustic soundings "sweep" an area of the seafloor, producing a sweep of depth measurement known as a "swath". The acquisition of contiguous swaths allows 100% coverage of the survey area, with a detail depending on the resolution (number and density of reflecting depth points). All other parameters being equal (pulse energy and frequency, number of beams, seafloor morphology, etc.) the greater the depth, the less the resolution (Figure 2).

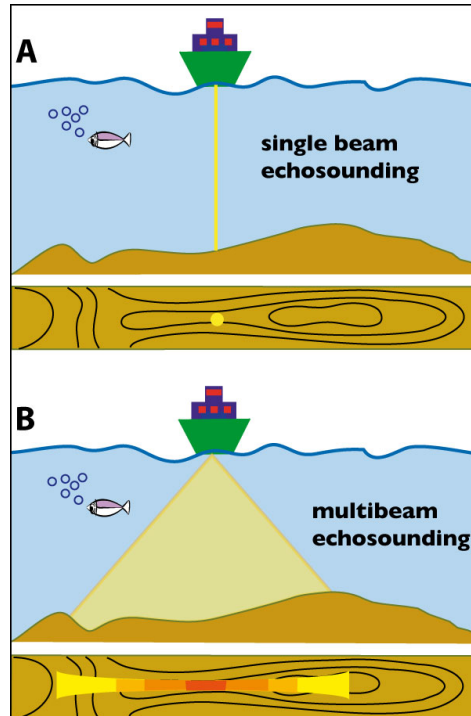


Figure 1: A. Standard single beam acquisition system. Bathymetry is the result of interpolation and contouring of every individual depth value. The detail of bathymetric maps increases with the number and density of the measured depth points. B. Multibeam acquisition system. Bathymetry is obtained as a swath of measured points. Resolution decreases from red to yellow, also depending on the energy and frequency of the acoustic pulse and on seafloor depth and roughness.

3 The geomorphic expression of marine geohazards

The identification of marine geohazards deals with our capability to investigate the marine environment, as well as with the variety of expression and manifesting of geohazards. Geohazards consists of geological processes that have the potential to generate events that impact human life or infrastructures, thus leading to a situation of risk.

Where these processes have occurred more frequently in the past, they are more likely preserved in the geological record and their identification and correct interpretation are essential for defining future geohazard.

Geohazard-related features are commonly the result of seafloor mobilisation and remoulding by different processes (Figure 3): active faults may generate earthquakes and they can affect the seafloor or remain buried at variable depth deep-seated deformation (both faults and folds) may pro-

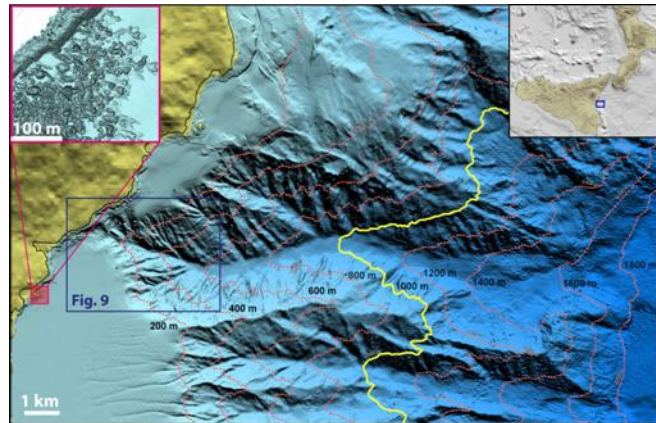


Figure 2: Example of Multiberam morpho-bathymetry from the continental margin off-shore Catania, eastern Sicily. The shelf is deeply incised by a complex network of channels producing a submarine canyon system. Where the shelf is preserved from landward canyon incision (lower left) the presence of shallow, sub-parallel linear troughs indicates erosion by smaller channels (gullies) connecting seaward directly to the canyon headscarp. The headscarp region and the steep flanks of canyons are frequently affected by sediment failure at variable scale. The red box is a detail at higher resolution showing the presence in very shallow water of a lava flow deposited from the onshore. The area in the blue box is shown in detail in Figure9.

duce fluid overpressure resulting in the upward migration and emission at the seafloor of fluids (pockmarks and fluid escape features) or of mixed sediment and fluids (mud volcanoes). These processes destroy the stratigraphic structure of sediments and weaken mechanical properties of soils, thus pre-disposing sediment to instability and failure. Instability causes sediment deformation down-slope producing shallow, rootless faults and folds that may in turn enhance failure with generation of a slide deposit. Slide deposits may evolve distally into turbidity currents, which can also form independently from sediment failure [1, 2]. Turbidity currents travel on long distances (up to hundreds or even thousands of kilometres) at high velocity (up to tens of meters per second)

depending on their density and slope gradients sediment is deposited progressively as velocity decreases and, finally, accumulates as lobes and fans in the deeper part of the basin [3]. Here, strong water mass circulation known as contour currents may rework sediment creating wave-like deposits and large sediment mounds (sediment waves and contourites) that alternate with zones of scouring and erosion of the seafloor [4].

Intense erosion and sediment transport and mass failure are among the most common agents shaping submarine landscape these processes may variously interact giving rise to remarkable geomorphic features, as for instance submarine canyons [5, 6, 7, 8, 9]. Submarine canyons (e.g. Figure 2) are large-scale incisions (hundreds of me-

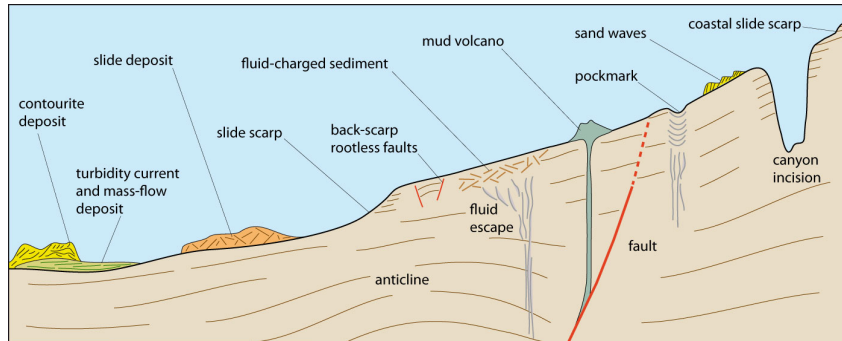


Figure 3: Simplified cartoon reporting some geological features and processes (both at seafloor and in the subsurface) typically responsible for the most frequent marine geohazards. These include seafloor displacement and shaking by faults and earthquakes; sediment failure creating slide scarps and deposits; high-energy depositional/erosional events (turbidity currents), strong sediment transport and erosion (bottom currents), abrupt fluid and sediment emission (pock marks and mud volcanoes).

ters deep, up to several kilometres wide and hundreds of kilometres long) on the shelf and slope of continental margins and represent preferential pathways to the deepest part of sedimentary basins for both river- and shelf-borne sediment [10, 8]. The headscarp and the steep flanks of canyons are frequently affected by sediment failure at variable scale, typically with a back-stepping (retrogressive) pattern that determines the progressive landward migration of the canyon head.

Geomorphic features resulting from each of the above mentioned processes bring specific problems concerning their identification, related hazard evaluation and cartographic representation.

4 Defining marine geohazard: conceptual and practical aspects

By definition, the hazard concept requires the identification of a process and the evaluation of the probability of occurrence of a dangerous event, whereas risk assessment descends from the calculation of the impact on human life and infrastructures. Concerning the issue of submarine geohazard definition, main problems descend from the difficulty of determining the age of geological features in order to evaluate both their state of activity and probability of occurrence of a dangerous event within human-scale time intervals. Age determination and state of activity of geohazard-related processes and features are among the most challenging tasks essentially because: 1) age definition of geological features is time-consuming, economically demanding and in many cases methodologi-

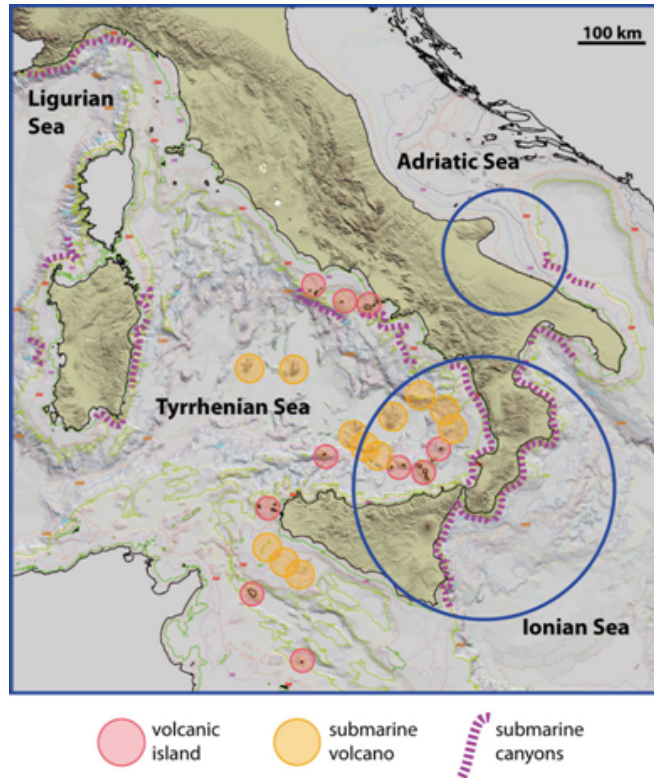


Figure 4: Distribution of major structural and geomorphic features bearing marine geohazards on the Italian continental margins. Blue circles encompass coastal areas hit by tsunami in recent and/or historical times.

cally not possible or unreliable; 2) whereas the recent occurrence of a given process is an indicator of the state of activity, the frequency of many geological processes yielding geohazard is very low, implying that a relatively non-recent age is not synonymous to “inactive”; indeed, geological processes may persist through long intervals (hundreds of thousands or even millions of years) though exhibiting relatively short-lived, low-frequency manifestations. Therefore, geological features yielding an age not apparently recent and/or low-frequency of occurrence can be overlooked

in terms of geohazard potential, specially if not evaluated within the broader geological context. Similarly, marine geohazards may intuitively result unlikely from the point of view of commonly adopted probabilistic analyses. This means that in many instances the state of activity of geological processes and features should be determined independently of their age as well, their probability of occurrence in the near future should not rely too much on their frequency in the past, since the geological context and the intervening controlling factors relative to geomorphic shap-

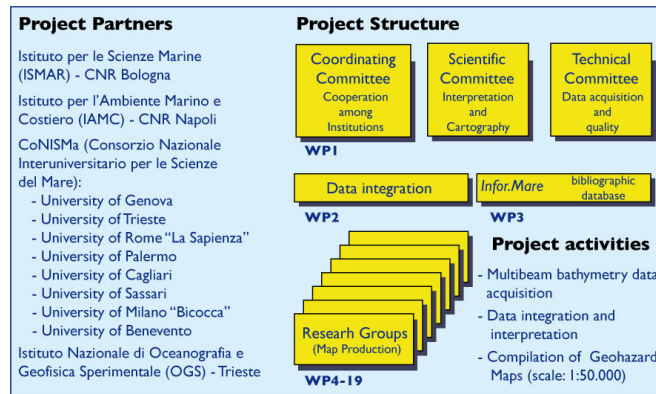


Figure 5: Partners and structure of MAGIC Project showing the workpackages (WP) and the activities to which they are dedicated.

ing of continental margins are continuously evolving.

5 Large-scale mapping of geohazard-related features

5.1 Structure and objectives of MAGIC

The continental margins of Italy are affected by seismicity and volcanic activity capable of generating significant tsunami impacting the coastal zones (Figure 4). The Tyrrhenian Sea is characterised by rifted margins affected by intense volcanic activity producing coastal, insular and submarine edifices [11, 12, 13, 14]. The Ionian margins are part of the accretionary prism relative to the subduction along the Calabrian Arc, and encompass the lithospheric discontinuity extending from the Malta Escarpment to the Etna Volcano [15, 16]. The Adriatic margin is part of a foreland dissected by regional fault systems that bear

significant seismicity [17, 18]. Finally, the Ligurian and Sardinia margins are tectonically active and/or deeply cut by submarine canyons [19]. All the Italian coasts along these margins experienced severe earthquakes and tsunami in historical and modern times [20], and the continental shelf and slope of the surrounding seas show diffused erosional scarps, deeply-incised shelf-indented canyons and countless slide scarps and deposits [21, 11, 22, 23, 24]. Altogether, these features indicate that geomorphic and destabilizing processes are frequent. The Italian project MAGIC (Marine Geohazards along the Italian Coasts) is a 5-year project (December 2007- December 2012) funded by the Italian Civil Protection Department as a national-scale and multitask effort aimed at investigating geohazards on the Italian continental margins. This main issue is pursued through the acquisition of high-resolution multibeam bathymetry and the production of maps of the geohazard-related geomorphic features of most of the Italian continental margins ("Map of Geohazard-related Features of the Italian Seas"). More than

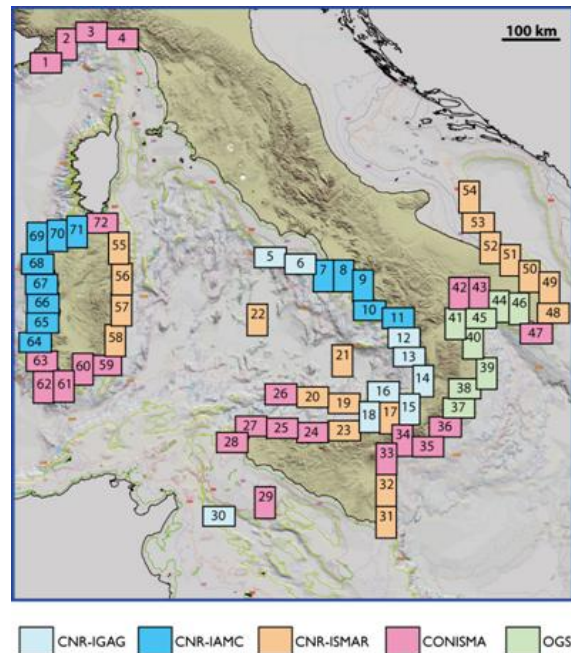


Figure 6: Location of the 72 sheets of the “Map of Geohazard-related Features of the Italian Seas”. Different colours refer to the institution responsible for the acquisition and production of each sheet (see Figure 5).

60.000 nautical miles of multibeam data will be analyzed and interpreted, of which ca. 40.000 will be acquired during the project life-time. The acquisition and interpretation issues are sustained by the participation of the entire scientific community currently active in the field of marine geology within the main Italian Research Centres (Figure 5). The “Map of Geohazard-related Features of the Italian Seas” will consist of 72 sheets (Figure 6), each including 4 Levels of representation and detailed descriptive notes. Level 2 and 3 (see § 5.3) are the core of the Map and are represented at scale 1:50.000. In addition to the multibeam database, also an updated archive of the existing literature on the con-

tinental margins of Italy will be constructed (Infor.Mare database).

5.2 Cartographic criteria for regional mapping of geohazard-related geomorphic features

Since the beginning of the project it was clear the need of standardizing not only acquisition procedures but also interpretative and cartographic principles. When mapping at a regional scale, we deal with a very broad spectrum of geological settings to account for, as well as a high variability within individual geomorphic features of the same type (i.e. generated by the same

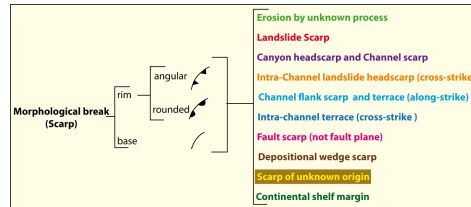


Figure 7: Graphic symbol and colour code combination for representing the different genesis of a same type of Morpho-bathymetric Element. Note that unknown (yellow) or very general (green) interpretative options are available in order to account for most problematic cases.

kind of process or event). The high variability of genetically-equivalent geomorphic features imposes the entire variability range to be taken into account by general definitions and symbols. Criteria fulfilling these methodological constraints typically require a high degree of applicability and thus retain a low specificity.

Within MAGIC, the main constraint relative to methodological and conceptual issues descends from the fact that the identification and representation of geohazard-related features rely essentially on multi-beam morpho-bathymetry. Additional data can be used when available to support interpretation nevertheless, all the features represented should be readily evident from the morpho-bathymetry data, properly interpreted according to the selected cartographic standards and criteria. In this respect, it is important that complementary data be described in detail (using specific descriptive notes) in order to account for the difference in density, quality and variety of datasets used for interpreting and compiling each sheet of the Map of Geohazard-related Features of the Italian Seas.

With the above limitation, establishing objective criteria for homogeneous interpreta-

tion/representation of morpho-bathymetric features yielding geohazard potential requires to separate morphological (objective) and genetic (interpretative) aspects, allowing at first morphological features to be mapped independently of their nature and geohazard potential. Defining the geohazard potential of geomorphic features is an interpretative issue that can be accomplished when the relationship between the geomorphic feature and its genetic process can be established confidently.

5.3 The Map of Geohazard-related Features of the Italian Seas

The Map of Geohazard-related Features of the Italian Seas is composed by 72 sheets (42x60 km), each being a digital multi-level cartographic file supported by Descriptive Notes and tables. Individual sheets are made up by the following four cartographic levels, with increasing detail:

- Level 1 – Physiographic Domains (PD scale 1:250.000);
- Level 2 – Morphological Units (MU scale 1:50.000);
- Level 3 – Morpho-bathymetric Elements (ME scale 1:50.000);

- Level 4 – Critical Zones (CZ detailed highlights at various scale).

From an operational and more practical perspective, mapping is achieved first by compiling Level 3 and then by defining the more general Level 2 and Level 1; Level 4 is a scale-independent level.

Level 3 (ME). The detailed mapping of seafloor morphology is accomplished by identifying and tracing all geomorphic features of the seafloor using a lower dimensional limit of ca. 100 m. These features are termed Morpho-bathymetric Elements (ME) for the sake of simplicity, ME are grouped into 4 main types (1: morphological breaks or scarps; 2: bedforms; 3: event-related deposits; 4: irregular and/or deformed seafloor). When possible, ME of the same type (e.g. morphological scarps) are imaged by the same graphic symbol (e.g. line patterns) but by different colour depending on their specific genesis and related processes such as tectonics, sediment failure, canyon incision, unknown, etc. (Figure 7). ME constitute the basic level of information relative to geohazard features and processes and are represented in 1:50.000 maps (Figures 8B and 9).

Level 2 (MU). The envelope of broad, sub-regional areas dominated by a characterizing assemblage of ME is termed Morphological Unit (MU) and is mapped (using a distinctive transparent colour) at scale 1:50.000 (Figure 8C). Each MU is the object of specific morphometric measurement and classification that allow an association with attributes and tables in GIS environment.

Level 1 (PD). At a larger scale, Physiographic Domains include regional or sub-regional features represented at scale 1:250.000 such as continental shelf, continental slope, intra-slope and bathial basins, intra-slope relief and seamounts, volca-

noes, regional-wide erosional areas (Figure 10).

Level 4 (CZ). Because of the civil protection purposes of the project, we include a further level aimed at highlighting specific situations, defined as Critical Zones (CZ), where geohazard-related features deserve special attention due to their close location to human settlements and infrastructures (e.g. shelf-indenting canyon heads, shallow-water incipient instability signs, etc.), assuming that their impact in case of generating a dangerous event would be higher. CZ are highlighted within Level 3 by red rectangles (Figure 9) and are documented individually using descriptive notes and cartography at any appropriate scale, based on all available data.

6 Discussion and Conclusions

The exploitation of multibeam morpho-bathymetry as a basic tool for defining and mapping geohazard-related features is one of the main issues in the field of marine geology. In this view, the national project MAGIC is a multi-task effort for acquiring multibeam morpho-bathymetry and defining geohazards along the most geologically active margins of Italy. The Italian continental margins display a large number of geohazards and are characterized by having tsunami-generating sources within a small geographical area and relatively confined seas. Moderate earthquakes can destabilize the continental slope where it is steeper or affected by thick, unstable deposits and dissected by canyon headscarps. In addition, active volcanic islands and underwater volcanic activity may periodically generate landslides that cause local but

still dangerous tsunami (e.g., the Stromboli 2002 event). The coasts of Italy experienced severe earthquakes and tsunami also in historical time some of the most remarkable events are: the 1627 Gargano Promontory earthquake and tsunami, in southern Adriatic the 1693 Catania earthquake and tsunami, in eastern Sicily the 1783 Scilla earthquake sequence and associated rock avalanche and tsunami, in Tyrrhenian Calabria the 1908 Reggio and Messina earthquake and tsunami, in Calabria and Sicily. Multibeam high-resolution seafloor mapping has greatly improved the knowledge on the mechanisms, distribution and frequency of marine geohazards, leading to a growing attention, on one hand, on the risk from major catastrophic events (like tsunami) and, on the other hand, also on the possible impact of smaller but more frequent tectonic and sedimentary events. For instance, new light is being shed on the role of small-scale instability that appears to affect continental margins with unexpected high frequency. Data that are being collected within MAGIC indicate that small-scale slide scars and deposits are very frequent on the Italian margins and display two main distributional patterns: 1) one in which sediment failure is pervasive and affects the continental margin on a regional scale; 2) one in which failure concentrates within submarine canyon heads indenting the continental shelf. In this latter case, retrogressive erosion of the canyon head is enhanced and the process by which canyon erosion progressively cannibalizes the shelf results significantly accelerated. As a consequence, canyon heads step back and move very close to the coastal area where anthropogenic infrastructures are present. The process may be particularly rapid in areas where the continental shelf rims steep/deep

tectonically-controlled basins and is therefore very narrow. In addition, the development of infrastructures in the coastal zones has significantly increased the risk related both to natural events and human impact. Indeed, human activity and settlements amplify natural phenomena potentially catastrophic and, in some cases, directly induce catastrophic phenomena. Most impressive examples of such kind of disaster derive from slope failure caused by harbours built in very narrow continental shelf settings, with a shelf margin only few hundred meters from the coast and a steep slope deeply incised by canyons, as described above. In these cases the induced landslide may seriously destabilize harbours and related infrastructures or even cause local tsunami that impact on the nearby coasts. For instance, a slide undermined the harbour of Gioia Tauro (Tyrrhenian Calabria) in 1977 and a small tsunami impacted on the nearby coasts only few years later (1979), during the construction of a harbour within the new airport of Nizza (Ligurian continental margin), a failure of the seafloor destroyed the harbour and generated a local tsunami few meters in height in Antibes, some 10 km away from the building site. The results from MAGIC project indicate that similar human-induced disasters can be easily avoided with the aid of detailed morpho-bathymetric maps aimed at defining geohazard-related features at regional scale along coasts densely inhabited and settled by infrastructures. With the development of standard interpretative cartographic criteria, these maps will also provide a prompt and basic tool for addressing more specific and detailed investigation of geohazard and risk assessment, also fulfilling the more practical requirements of industry and oil companies.

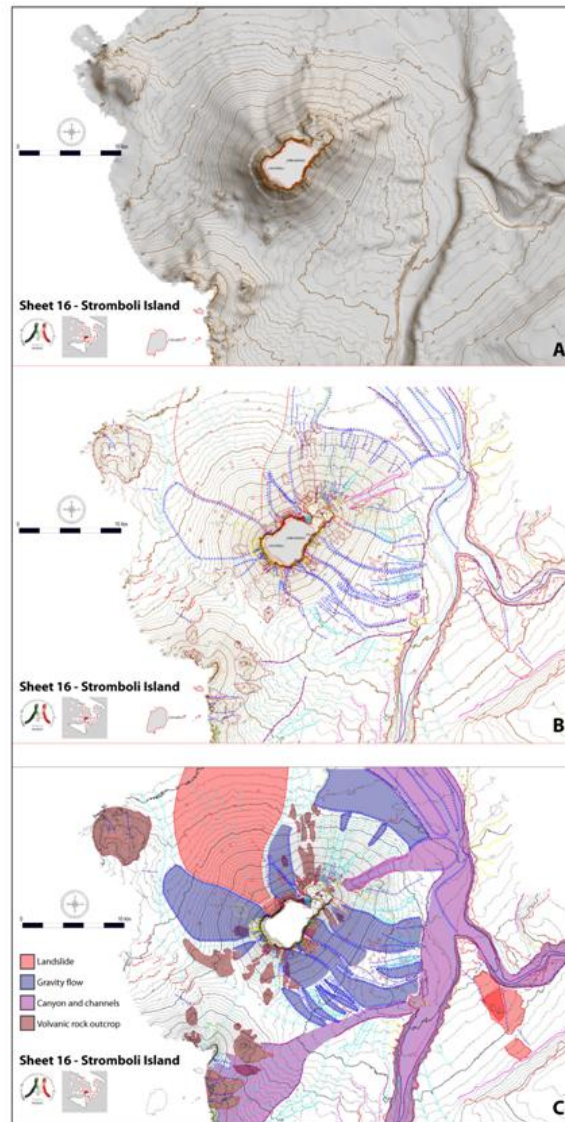


Figure 8: Shaded relief (A) of the submarine volcanic edifice of Stromboli Island (southern Tyrrhenian Sea) and detailed mapping of the Morpho-bathymetric Elements (ME) of Level 3 (B) and of the Morphological Units (MU) of Level 2 (C). The representation of ME is accomplished through more than 50 graphic symbols accounting for most of the seafloor geomorphic features detectable through multibeam mapping (see detail in Figure 9); MU are coloured areas superimposed on Level 3; Both Level 2 and 3 are represented at scale 1:50.000.

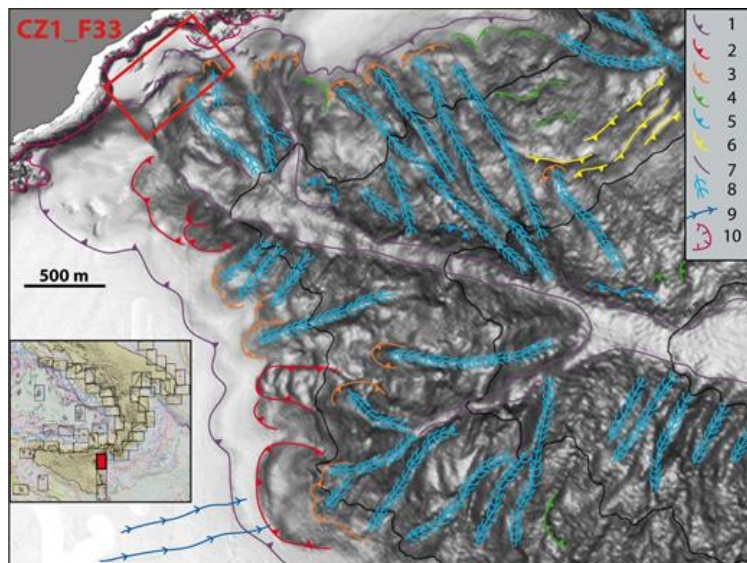


Figure 9: Portion of MaGIC Sheet 33 – Catania. The mapping Level 3 (Morphobathymetric Elements) is accomplished through more than 50 graphic symbols accounting for most of the seafloor geomorphic features detectable in multibeam data. Red box labelled CZ1_F33 indicates a Critical Zone (mapping Level 4) where a canyon headscarp deeply indents the shelf and the coastline. Legend 1: canyon headscarp; 2: slide scarp; 3: intra-channel slide scarp; 4: erosion by unknown process (e.g. by “normal” erosion or mass failure); 5: channel-flank scarp and terrace; 6: scarp of unknown origin (e.g. either by erosion, mass failure or tectonics); 7: base of canyon scarp; 8: secondary channel (rim and base of scarp not traceable); 9: gully; 10: lava flow. A broader part of this area is shown in Figure 2.

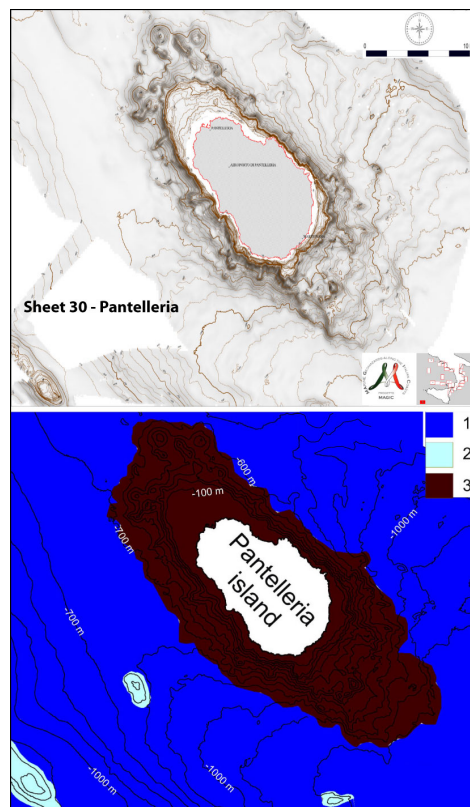


Figure 10: MaGIC Sheet 30 – Pantelleria. Upper: Multibeam shaded relief and contour. Lower: Example of Level 1 to be represented at 1:250.000 scale. 1: intra-slope and bathial basin; 2: intra-slope relief and seamounts; 3: volcanic edifice.

References

- [1] D.J.W. Piper, P. Cochonat, and M.L. Morrison. The sequence of events around the epicentre of the 1929 Great Banks earthquake: initiation of debris flows and turbidity current inferred from sidescan sonar. *Sedimentology*, 46:79–97, 1999.
- [2] D.J.W. Piper and W.R. Normark. Processes that initiate turbidity currents and their influence on turbidites: a marine geology perspective. *Journal Sedimentary Research*, 79:347–362, 2009.
- [3] E. Mutti, D. Bernoulli, F. Ricci Lucchi, and R. Tinterri. Turbidites and turbidity currents from Alpine ‘flysch’ to the exploration of continental margins. *Sedimentology*, 55:267–318, 2009.
- [4] A.R. Viana, J.C. Faugères, and D.A.V. Stow. Bottom-current-controlled sand deposits – a review of modern shallow- to deep-water environments. *Sedimentology*, 115:53–80, 1998.
- [5] D.C. Twichel and D. Roberts. Morphology, distribution, and development of submarine canyons on the United States Atlantic continental slope between Hudson and Baltimore Canyons. *Geology*, 10:408–412, 1982.
- [6] L.F. Pratson, W.B.F. Ryan, G.S. Mountain, and D.C. Twichell. Submarine canyon initiation by downslope-eroding sediment flows: evidence in late Cenozoic strata on the New Jersey continental slope. *GSA Bulletin*, 106:395–412, 1994.
- [7] D.L. Orange, B.G. McAdoo, J.C. Moore, H. Tobin, E. Screaton, H. Chezar, H., Lee, M. Reid, and R. Vail. Headless submarine canyons and fluid flow on the toe of the Cascadia accretionary complex. *Basin Research*, 9:303–312, 1997.
- [8] M. Canals, J.L. Casamor, G. Lastras, A. Monaco, J. Acosta, S. Berné, B. Loubrieu, P.P.E. Weaver, A. Grehan, and B. Dennielou. The role of Canyons on strata formation. *Oceanography*, 17(4):80–91, 2004.
- [9] J. Baztan, S. Berne, J. Olivet, M. Rabineau, D. Aslanian, M. Gaudin, J.P. Rehault, and M. Canals. Axial incision the key to understand submarine canyon evolution (in the western Gulf of Lion). *Marine and Petroleum Geology*, 22:805–826, 2005.
- [10] B.L. Mullenbach and C.A. Nittrouer. Rapid deposition of fluvial sediment in the Eel Canyon, northern California. *Continental Shelf Research*, 20, 2191–2212, 20:2191–2212, 2000.
- [11] F. Gamberi and M. Marani. Downstream evolution of the Stromboli Slope Valley (southeastern Tyrrhenian Sea). *Marine Geology*, 243:180–199, 2007.
- [12] T. Trua, G. Serri, M. Marani, A. Tenzulli, and F. Gamberi. Volcanological and petrological evolution of Marsili Seamount (southern Tyrrhenian Sea). *Journal of Volcanology and Geothermal Research*, 114:441–464, 2002.

- [13] A. Milia, M.M. Torrente, M. Russo, and A. Zuppetta. Tectonics and crustal structure of the Campania continental margin: relationships with volcanism. *Mineralogy and Petrology*, 79:33–47, 2003.
- [14] F.L. Chiocci and G. de Alteriis. The Ischia debris avalanche: first clear submarine evidence in the Mediterranean of a volcanic island prehistorical collapse. *Terra Nova*, 18:202–209, 2006.
- [15] A. Argnani and C. Bonazzi. Malta escarpment fault zone offshore eastern Sicily: Plio-Quaternary tectonic evolution based on new multichannel seismic data. *Tectonics*, 24(TC4009), 2005.
- [16] D. Praeg, S. Ceramicola, R. Barbieri, V. Unnithan, and N. Wardell. Tectonically-driven mud volcanism since the late Pliocene on the Calabrian accretionary prism, central Mediterranean Sea. *Marine and Petroleum Geology*, 26:1849–1865, 2009.
- [17] D. Ridente, D. Di Bucci, U. Fracassi, F. Trincardi, and G. Valensise. Middle Pleistocene to Holocene activity of the Gondola Fault Zone (Southern Adriatic Foreland): deformation of a shear zone and seismotectonic implications. *Tectonophysics*, 453:110–121, 2008.
- [18] A. Argnani, M. Rovere, and C. Bonazzi. Tectonics of the Mattinata fault, offshore south Gargano (southern Adriatic Sea, Italy): Implications for active deformation and seismotectonics in the foreland of the Southern Apennines. *GSA Bulletin*, 121((9-10)):1421–1440, 2009.
- [19] G. Dalla Valle and F. Gamberi. Erosional sculpting of the Caprera confined deep-sea fan as a result of distal basin-spilling processes (eastern Sardinian margin, Tyrrhenian Sea). *Marine Geology*, 268:55–66, 2010.
- [20] S. Tinti, A. Maramai, and L. Graziani. The new catalogue of Italian tsunamis. 2004.
- [21] D. Minisini, F. Trincardi, and A. Asioli. Evidences of slope instability in the South Adriatic Margin. *Natural Hazards Earth System Sciences*, 6, 1, 1-20, 6:1–20, 2006.
- [22] D. Ridente, F. Fogliini, D. Minisini, F. Trincardi, and G. Verdicchio. Shelf-edge erosion, sediment failure and inception of the Bari Canyon on the Southwestern Adriatic Margin (Central Mediterranean). *Marine Geology*, 246:183–207, 2007.
- [23] F.L. Chiocci, C. Romagnoli, P. Tommasi, and A. Bosman. The Stromboli 2002 tsunamigenic submarine slide: Characteristics and possible failure mechanisms. *Journal of Geophysical Research*, 113(10.10), 2008.
- [24] C. Romagnoli, D. Casalbore, F.L. Chiocci, and A. Bosman. Offshore evidence of large-scale lateral collapse on the eastern flank of Stromboli, Italy, due to structurally-controlled, bi-lateral flank instability. *Marine Geology*, 262:1–13, 2009.

Monitoring Oil Spills at Sea with Optical Satellite Sensors: the PRIMI Project Optical Observation Module

F. Bignami¹, S. Colella¹, A. Pisano¹, R.H. Evans², R. Santoleri¹

1, Institute of Atmospheric Sciences and Climate, CNR, Roma, Italy

2, University of Miami, Rosenstiel School of Marine and Atmospheric Science, Miami, Florida

f.bignami@isac.cnr.it

Abstract

The PRIMI project funded by the Italian Space Agency (ASI) has implemented an observation and forecast system to monitor marine pollution from hydrocarbon oil spills (OS) in the Italian Seas. The system consists of four components, two of which for OS detection via multi-platform SAR and optical satellite imagery, an OS displacement forecast subsystem based on numerical circulation models and a central archive that provides WEB-GIS services to users. The system also provides meteorological, oceanographic and ship detection information. The Optical Observation Module, based on MODIS and MERIS imagery, is described here. The idea of combining wide swath optical observations with SAR monitoring arises from the necessity to overcome the SAR reduced coverage of the monitoring area. This can be done now, given the MODIS and MERIS higher spatial resolution with respect to older sensors (250-300 m vs. 1 km), which consents the identification of smaller spills deriving from illicit discharge at sea. The procedure to obtain identifiable spills in optical reflectance images involves removal of natural variability to enhance slick - clean water contrast, image segmentation/clustering and a set of criteria for the elimination of those features which look like spills (look-alikes). The final result is a classification of oil spill candidate regions by means of a score based on the above criteria.

1 Introduction

Illegal oil discharge continues to be a serious threat to the marine natural habitat, despite the remarkable reduction of occurrences resulting from the international commitment in marine environmental protection. In this framework, satellite remote sensing has proved to be an effective support in detecting these events, thus discouraging this bad practice. Indeed, since the launch of the first Euro-

pean Space Agency (ESA) Synthetic Aperture RADAR (SAR) ERS-1 satellite, many projects exploit SAR in oil spill (OS) detection. However, long revisit times and low spatial coverage, due to SAR high spatial resolution and consequent narrow swaths (typically of order 100 km [1]), call for a multi-platform SAR OS detection effort as well as OS monitoring via wider swath (typically of order 1000 km) platforms, i.e. optical sensor satellites. Optical OS detection is very recent (since 2000

see [2]), thanks to the increased spatial resolution of the new generation optical sensors, i.e. NASA MODIS (TERRA and AQUA; <http://modis.gsfc.nasa.gov>) platforms and ESA MERIS platform (<http://envisat.esa.int/instruments/meris/>). The 250 m and 300 m spatial resolution of some MODIS and all MERIS optical bands is now above typical illegal discharge slick dimensions (1-10 km), while the typical 1 km resolution of past sensors was practically useless in slick detection, if one excludes major disasters which do not need to be detected, since they become known by other means (mayday communications from board, news, etc.). In synthesis, SAR and optical platform observations have to be combined to optimize monitoring, which is hindered by low coverage and high revisit times in exclusively SAR observation systems and cloud cover in their optical counterparts. The PRIMI project (PRogetto pilota Inquinamento Marino da Idrocarburi, ASI funding, project PI: E-GEOS, Matera, Italy, scientific PI: CNR-ISAC UOS Rome, Italy [3]) has set up an oil spill monitoring system which, to our knowledge, for the first time integrates multi-platform SAR (ERS, ENVISAT, RADARSAT, ALOS, COSMO-SkyMed) and optical (MODIS TERRA, AQUA and MERIS) satellites into an Observation Module for OS detection in the seas around Italy (Ligurian, Tyrrhenian, Adriatic and Ionian Seas). Also, PRIMI utilizes the satellite observational information as an input to predict oil slick displacement and transformation via its Forecast Module. This consists of a set of numerical circulation models, i.e. the Mediterranean Forecasting System (MFS, [4]), regional higher resolution forecasting systems for the Adriatic [5] and Tyrrhenian [6] Seas and the Channel of Sicily

[7] and an oil dispersion and modification model stemming from the MEDSLIK model [8]. Finally, an Archive Module stores observational and forecast data and a WEB-GIS system is accessible to end users, to which oil spill detection reports are also sent. We describe here the PRIMI Optical Observation Module, developed at CNR-ISAC UOS Rome (Italy) and engineered by Flyby S.r.l. (Livorno, Italy), hereafter referred to as SSO_A (Advanced Optical Subsystem). SSO_A now replaces the PRIMI Preliminary Optical Subsystem which has been operational in the June 2008 - October 2009 period; oil spill detection was then visually performed by expert operators on MODIS L1B top of the atmosphere (TOA) radiance products. SSO_A has been operational until the project's end (Oct. 5, 2010), with OS detection being for the first time highly automated, though a final judgment on OS's detected by the SSO_A software was still left to an operator. SSO_A is now being refined offline, in making automatic OS - look-alike feature distinction more efficient and to attain full automation. Satellite data processing, the OS database used for the SSO_A development and validation cruise specifications are illustrated in section 2; custom image processing for automatic OS detection developed in SSO_A are described in section 3, together with preliminary validation cruise results for all PRIMI system components. Conclusions are given in section 4.

2 Materials and methods

2.1 Satellite data standard processing

SSO_A automatically downloads MODIS (TERRA and AQUA, swath width 2330 km) and MERIS (swath width 1150 km) imagery of the previous day, respectively from the NASA and ESA websites, as well as images of the same day, when available from ASI's National Multi-mission Center CNM, currently under development, and located in Matera (Italy). The subsystem selects all MODIS L0 (5 min satellite flight granules) and MERIS L1B products pertinent to the PRIMI coverage area, i.e. the seas around Italy. When CNM will be fully operational, it will replace the NASA and ESA sites as data sources, which will be used as a backup. Downloaded MODIS L0 and MERIS L1B files are then processed with NASA's SeaDAS v5.4 freeware (<http://oceancolor.gsfc.nasa.gov/seadas/help.html>) to obtain the a suite of remapped L2 MODIS products (see http://oceancolor.gsfc.nasa.gov/DOCS/MSL12/MSI12_prod.html), among which TOA reflectances (ρ_{TOA}) at 859 nm (Figure 1a). This product is then used for the OS detection subsequent steps. During the processing, a custom declouding procedure based on SST quality flags (the L2 product which gives the reliability of SST computation by SeaDAS at each pixel, depending on cloud presence or vicinity, reliability of atmospheric correction, etc.) is applied to the imagery. Also, images are destriped following Weinreb [9] with a prototype algorithm, which, though not fully satisfactory and thus under development, has proven adequate in strongly reducing errors in the OS detection steps.

2.2 Oil spill database

The development of both the Preliminary and Advanced PRIMI Optical Observation Subsystems relies on a number of MODIS and MERIS images of OS cases which were also observed in situ. These include a temporal suite of the Lebanon coastal spills caused by air raids on coastal power plants [10], some cases in the Italian seas (2002-2008) reported by the Italian Ministry of the Environment, for which remediation units were sent on the spot to perform cleanup duties, an OS off the Algerian coast (August 6-10, 2008) and five OS's visited by CNR's R/V Urania during the PRIMI cruise (see sections 2.3 and 3.4), i.e. a total of 63 images. The database is currently being updated, as new OS cases become known. OS regions were manually digitized in the images via ENVI's Region of Interest (ROI) tool (Figure 1b) and saved as OS pixel lat/lon text files, which were used in the development and testing of spectral and shape criteria and score tables for distinction between OS and look-alike features as detected by the clustering algorithm in each image (see Section 3.3). Finally, each OS scene in the images has been classified as high or low glint, depending on whether the a slick was in mirror-like reflection (high sun glint) conditions or not, the former occurring when the sun and satellite are on roughly the same plane containing a slick pixel at sea and on opposite sides of the pixel itself. Sun glint conditions were determined by finding a threshold of the glint angle α , given by (e.g.[11]):

$$\cos\alpha = \cos\theta_v \cos\theta_s - \sin\theta_v \sin\theta_s \cos\phi,$$

where θ_v and θ_s are the satellite and solar zenith angles and ϕ is the sun-satellite relative azimuth angle, as seen from an im-

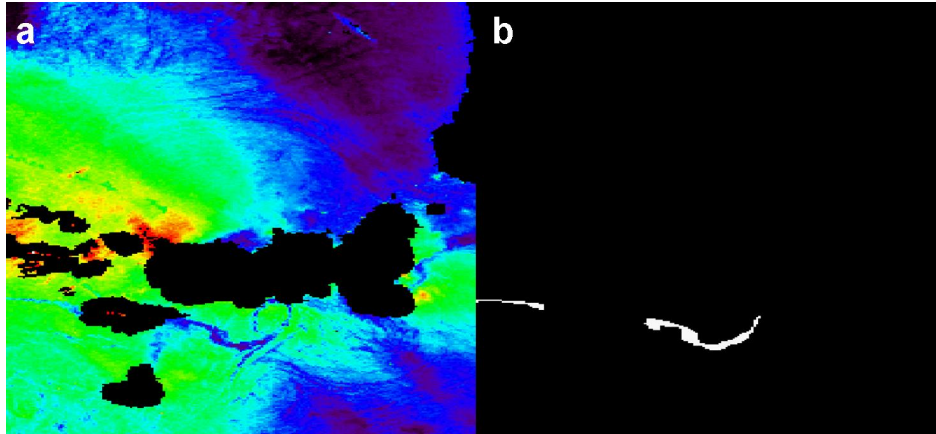


Figure 1: (a) MODIS AQUA, August 17 2005 12:15 UTC, TOA reflectance (rhot at 859 nm), low glint spill south of Elba island (northern Tyrrhenian Sea, slick in dark blue surrounded clean waters in green), clouds and land in black; (b) OS ROI (white) digitized with ENVI ROI tool.

age pixel. α thresholding has proven to be finer than the high glint standard MODIS flag (12-flags product, flag 04), because the former better separates illumination-view situations in which oil slicks in TOA reflectance images are brighter than surrounding water (positive contrast, typical of mirror reflection conditions) from those which are darker (negative contrast, low glint conditions). Indeed, some images, classified high glint by the MODIS flag 04, were seen to contain slicks both brighter and darker than surrounding water, indicating that the flag was not sufficiently discriminatory. High and low glint cases, as distinguished by α thresholding, have been treated separately in the development of the clustering and final detection steps of SSO_A, because of their opposite type of contrast with surrounding water.

2.3 Validation cruise

The PRIMI system was tested during a cruise [12] organized by CNR-ISAC on-board CNR R/V Urania and to which both PRIMI and non-PRIMI institutions have participated. The cruise took place in the seas around Sicily (Tyrrhenian, Ionian Seas and Sicily Channel; Figure 2), an area with high illegal hydrocarbon discharge frequency, as inferred from historical and PRIMI monitoring data. The main cruise objective was to visit oil slicks detected by the PRIMI SAR and Optical Observation Modules and whose displacement was predicted by the PRIMI Forecast Module, thus testing the system. Also, the cruise was dedicated to the hydrological and biogeochemical systematic sampling of the area (not described here). Besides the SAR and optical satellite imagery acquired for OS detection, the cruise dataset includes: (1) onboard RADAR sea surface roughness; (2) onboard LIDAR sea sur-

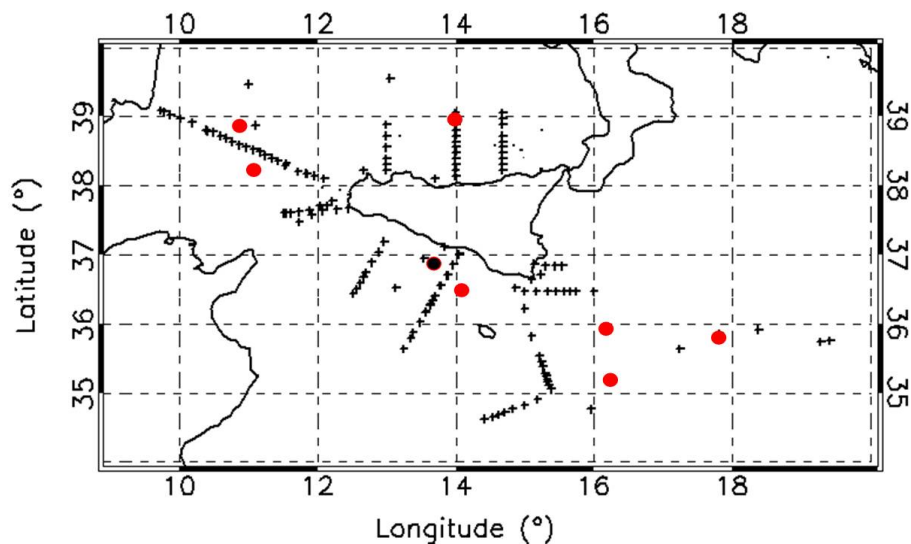


Figure 2: PRIMI cruise (Aug. 6 - Sep. 7 2009, R/V Urania) hydrological stations (black crosses) and visited OS's (red dots). Black dot: OS described in text.

face fluorescence and Raman attenuation time series; (3) polluted water samples; (4) ARGO, I-SPHERE and inert polyethylene drifting buoy trajectory and surface parameter data in correspondence of detected OS's; (5) SATLANTIC multispectral surface and water column radiation, for optical satellite algorithm validation; (6) nutrient, chlorophyll, Colored Dissolved Matter (CDOM), Dissolved Organic Carbon (DOC) data and (7) hydrographic data. The hydrological stations and the visited OS's are shown in Figure 2. A set of SAR ENVISAT ASAR, ERS-2 and COSMO-SkyMed acquisitions was planned before the cruise, in order to conceive the cruise track so as to maximize the probability of OS in situ validation and hydrological coverage. OS detection SAR reports were received on board, from the PRIMI opera-

tional site at ASI Matera (Italy), within two hours of acquisition (daytime images) or the following morning (nighttime images). After satellite detection, OS future positions were predicted in real time by the Forecast Module marine circulation and OS dispersion-transformation models and R/V Urania steamed towards the predicted OS location for visual detection and in situ sampling.

3 Results

3.1 Image custom atmospheric correction (“image flattening”) for oil spill detection

The basic idea for OS detection with SSO_A is to enhance OS contrast with respect to clean water as much as possi-

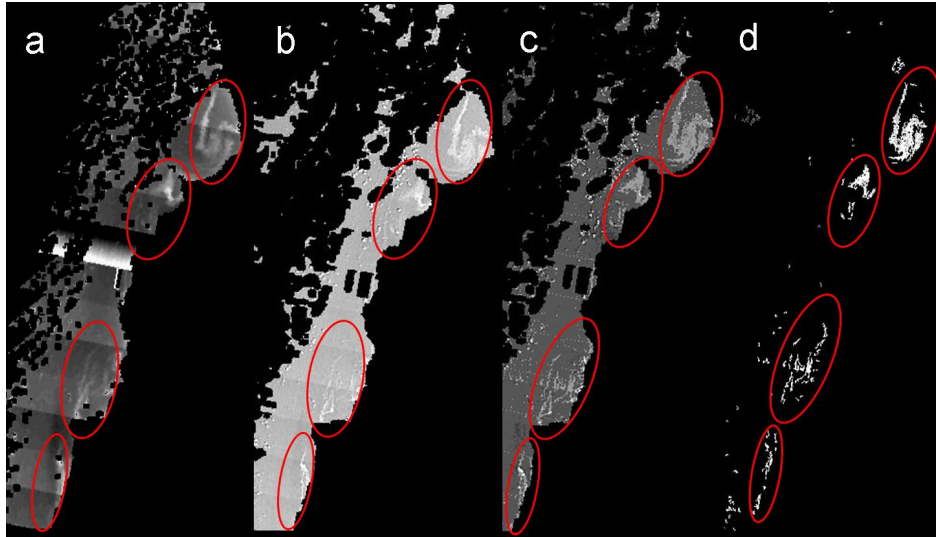


Figure 3: MODIS TERRA Aug. 1 2006 08:30 UTC, Lebanon coastal oil spill in high glint conditions (clouds and land in black). (a) rhot at 859 nm (slicks evidenced by red ellipses are not so sharply evidenced); (b) rhoeps-859 (“flattened sea” in grey and brighter/sharper slicks); (c) cluster matrix (different greys correspond to different reflectance mode values); (d) pruned cluster matrix ready for visual inspection: only OS candidates are left (in white).

ble in the MODIS L2 and MERIS L1B TOA reflectances rhot-nnn images (Figures 1 and 3a), before classifying high or low contrast surface structures as OS or look-alikes. Indeed, oil slicks in standard TOA reflectance images are often confused visually (and numerically) with analogous look-like oceanographic features such as chlorophyll filaments, etc. Moreover, atmospheric effects such as reflectance modulation due to aerosol patches can introduce further noise, thus further masking the slicks. Therefore, a procedure was devised, to “strip” each rhot-nnn image from the reflectances deriving from atmospheric (Rayleigh and aerosol scattering) and oceanic natural variability (chlorophyll, suspended matter), thus leaving a

smoother or flat “residual ocean” field in which oil are less liable to be confused with or masked by non-slick natural features. This is done by subtracting from rhot-nnn images the Rayleigh scattering and water-leaving reflectances of the same wavelength, as well as the signal from aerosol-sensitive rhot_555 reflectance normalized to the band under treatment. This eliminates surface and air column variability and produces what we call rhoeps-nnn or “flattened” TOA reflectances (Figure 3b). Empirically, rhoeps-nnn at 859 nm has given the best oil-water contrast enhancement and is the product used in the next OS detection steps.

3.2 Image clustering

The rhoeps-*nnn* “flattened” image is then treated with a mean shift algorithm [13, 14], a nonparametric clustering technique which does not require prior knowledge on cluster number and does not constrain cluster shape. The algorithm finds a set of reflectance values (modes) to which image pixels are assigned, thus segmenting the image into clusters. Each cluster is, in Euclidean space, in general formed by a set of disjointed regions. An example is given in Figure 3c. Regions are next classified as either oil slick or look-alike, as described in the following.

3.3 Look-alike elimination (cluster image pruning)

The clustered image of Figure 3c shows how some regions are patently not OS, e.g. the very large open sea dark grey region occupying most of the image, or the small whitish specks, which are cloud residuals. These too small or too large regions and those with “roundish” shape or “wrong” region-water contrast, i.e. brilliant (dark) regions in low (high) glint conditions, can be easily eliminated. The result of this region pruning process for the cluster matrix of Figure 3c is shown in Figure 3d. Unfortunately, the remaining regions are clearly not all OS and we define such regions as “OS candidates”. That is, to date, the mostly empirical effort to develop the parameters for look-alike pruning has revealed that there seem not to be neither geometrical nor spectral clear-cut selection criteria to distinguish OS’s from look-alikes, as is commonly believed. Region - water reflectance contrast may be used in visual/manual qualitative OS detection but is not sufficient for automatic de-

tection, to which PRIMI’s SSO_A is oriented, and does not assure that darker or more brilliant features are actually OS’s. This is due to the fact that oil spills are patchy and sometimes as small as residual cloud specks, and this was confirmed during the validation cruise (see section 3.4). Oil concentration on the surface, even within a small oil slick detected by a high resolution SAR image, may vary from virtual absence of hydrocarbon to a thin film to heavily polluted brown or black waters with floating hydrocarbon solid particles of variable dimensions. So, while SAR may classify also a thin film area as OS because it is based on surface roughness attenuation, an optical sensor may miss it because ocean color is only slightly altered with respect to clean water. Also, reflectance of a pixel within an OS is always an average resulting from a mix of the above pollution situations. Finally, the OS digitizing, declouding, destriping and flattening processes are not perfect and residuals of clouds or natural surface variability may still be present, which is the fundamental reason for which look-alike small white specks exist in Figure 3d. These facts and the results of the more consolidated research in SAR OS detection ([15] and references therein) induced us to re-analyze the OS candidate regions issuing from the above pruning process (Figure 3d) with an extended set of parameters and to define scores for each parameter applied to each OS candidate. These parameters involve reflectance histogram integrals of OS candidates and surrounding waters and have been devised in order to overcome ambiguities introduced by slick patchiness, which may bias region – water contrast computed with mean OS candidate reflectances single values. Instead, some of these “integral” parameters enable us to tell whether

a region is “statistically” darker or lighter than surrounding water. Scores for each parameter are computed by: (1) computing the parameter for all the certified OS’s in the OS database and plotting the parameter population histogram (x-axis: parameter value, y-axis number of OS’s in the database with that value), thus generating a sort of look-up table, to be updated as new OS cases are known; (2) computing the same parameter for a given OS candidate in the image under operational inspection; (3) assigning a score value from 0 to 1 to the latter OS candidate, depending on how populated is its parameter value in the look-up table. The set of parameters and the computation of single and cumulative scores, computed as a weighted linear combination of single scores, are still under development. However, even the present preliminary scores associated to OS candidates have allowed PRIMI SSO_A operators to better discriminate OS’s from look-alikes, in order to generate the PRIMI OS operational reports.

3.4 Validation cruise

We exemplify the OS in situ location effort during the Aug. 6 - Sep. 7, 2009 validation cruise onboard R/V *Urania* (see Section 2.3, Figure 3) by describing the sampling of a slick detected by the PRIMI SSO_A (MODIS TERRA image, Aug. 27 2009 10:00 UTC and SAR imagery Figures 4a, b (slick in blue ellipse), though partly under cloud. Upon detection, OS future positions were predicted in real time by the Forecast Module dispersion-transformation model (Figure 4c) and R/V *Urania* steamed towards the OS location on Aug. 27 morning, adjusting its course to the latest OS predicted positions. The OS was successfully located within a few nautical miles

of the predicted position (Figure 4c), photographed (Figure 4c, inset) and monitored with in situ RADAR and LIDAR (not shown, data analysis in progress). Polluted water samples were collected and heavy hydrocarbon concentrations were found in the samples. Also, a lagrangian drifter was deployed within the OS and the trajectory agreed with the GPS fixes of the slick being followed by the ship, in describing a north-westward drift, though the slick drift was seen to be more of a straight line, probably due to greater influence of the wind on the slick with respect to the drifter (Figure 4c). 8 OS’s were visited (see Figure 2c) out of a total of about 30 slicks detected by SAR in the area, some being also observed in MODIS or MERIS imagery when the sky was clear. In situ inspection revealed that in some cases the OS was only made of a thin hydrocarbon film, detected visually by iridescence and absence of capillary waves and instrumentally by roughness attenuation in the onboard RADAR signal and Raman signal depression in the LIDAR data. The three most polluted OS’s, i.e. those which contained thick, dark oil patches and floating solid hydrocarbon particles were chosen for drifter release. Patchiness was always found, both in lightly and heavily polluted sites. A more extensive description of the cruise results will be released in a forthcoming paper, as soon as all the ongoing data analyses will be concluded.

4 Summary and conclusions

We have described the PRIMI project’s Advanced Optical Observation Module (SSO_A), which makes use of MODIS L2 and MERIS L1B satellite TOA reflectance

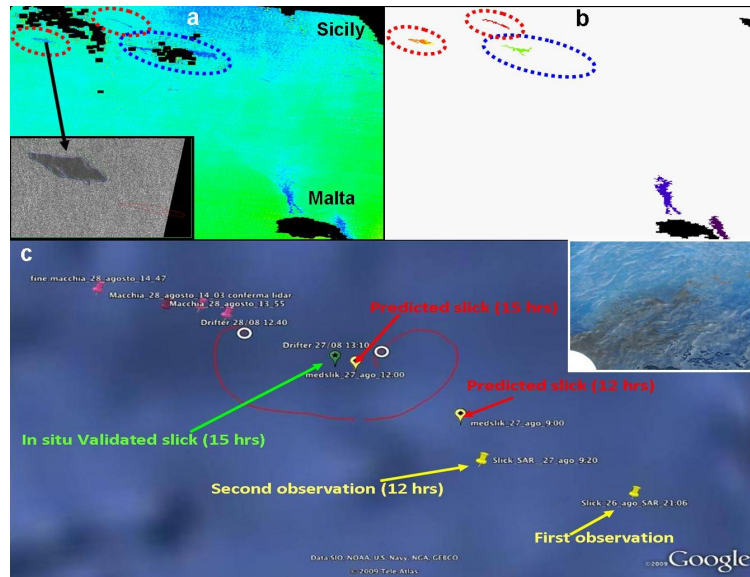


Figure 4: PRIMI cruise, OS of Aug. 26-27, 2009, Sicily Channel. (a) OS's detected by the PRIMI SSO_A (red ellipses: detected slicks; blue ellipse: in situ sampled slick) in MODIS TERRA rhoeps-859 image, Aug. 27 2009 10:00 UTC, inset: ENVISAT SAR image of a detected slick, Aug. 27 2009 9:20 UTC; (b) SSO_A OS candidate map; (c) SAR OS observation locations (yellow), Forecast Module prediction positions (red) and in situ location (green), drifter trajectory (red curve), final slick positions of Aug. 28 (tags at upper left), inset: one of the heavier oil slicks within the detected OS, as photographed from the ship.

imagery for oil spill detection, for the first time in a highly automated way. Images are first “flattened” to eliminate natural oceanic and atmospheric variability, in order to enhance slick-clean water contrast. Next, a clustering algorithm groups image pixels with similar reflectances into a set of clusters with common mode reflectance values. Cluster regions are then pruned by means of a first set of geometric and spectral parameters computed for each region and for water surrounding the region itself. These parameters have been devised and tested using PRIMI’s database of in situ certified OS cases, in which both

slicks and look-alikes are known. After pruning, most of obviously non-slick features (e.g. large regions) and look-alikes (e.g. slick-like regions with wrong region-water contrast with respect to glint situation) are eliminated. However, slick patchiness (verified in situ during the PRIMI cruise), residual natural variability after flattening, small residual clouds, etc., contribute to the impossibility to automatically eliminate all look-alikes with the above “clear-cut” pruning criterion. Therefore, a set of scores, to be assigned to OS candidates remaining after pruning, has been devised for a second set of distinction param-

eters and cumulative scores are computed as a linear combination of weighted single scores. Research for the PRIMI system development has been encouraged by the positive results of in the situ validation cruise, but calls for further work. A crucial point is to increase the number of certified cases in the OS database, in order to cover as many illumination-view situations as possible, so as to devise more robust pruning and score parameters, with the goal to fully automate the PRIMI SSO_A system.

5 Acknowledgments

We thank Dr. F. Nirchio for fruitful scientific discussion on look-alike elimination and score computation; Drs. M. de Dominicis, G. Coppini and N. Pinardi (INGV) for providing oil slick location and prediction positions; Dr. Mario Sprovieri (CNR-IAMC Naples) for hydrocarbon chemical analysis; all the PRIMI cruise participants and the R/V Urania crew. The PRIMI project is funded by the Italian Space Agency (ASI).

References

- [1] K.N. Topouzelis. Oil Spill Detection by SAR Images: Dark Formation Detection, Feature Extraction and Classification Algorithms. *Sensors*, 8:6642–6659, 2008.
- [2] C. Hu, F.E. Müller-Karger, C. Taylor, D. Myhre, B. Murch, and A.L. Odriozola. MODIS Detects Oil Spills in Lake Maracaibo, Venezuela. *EOS*, 84(33):313–319, 2003.
- [3] F. Nirchio, G.V. Pandiscia, G. Ruggieri, R. Santoleri, F. Tataranni, P. Trivero, N. Pinardi, A. Masini, G. Manzella, and C. Castellani. PRIMI (Pilot Project Marine Oil Pollution). *ISRSE 2009, 33rd International Symposium on Remote Sensing of environment Sustaining the Millennium Development Goals, May 4-8, 2009, Palazzo dei Congressi Stresa, Lago Maggiore, Italy, <http://isrse-33.jrc.ec.europa.eu/>, 2009.*
- [4] N. Pinardi, I. Allen, E. Demirov, P. De Mey, G. Korres, A. Lascaratos, P.Y. Le Traon, C. Maillard, and G. Manzella. The Mediterranean ocean forecasting system: first phase of implementation (1998–2001). *Annales Geophysicae*, 21:3–20, 2003.
- [5] P. Oddo, N. Pinardi, M. Zavatarelli, and A. Coluccelli. The Adriatic Basin Forecasting System. *Acta Adriatica*, 47 Suppl.:169–184, 2006.
- [6] A. Vetrano, E. Napolitano, R. Iacono, K. Schroeder, and G.P. Gasparini. Tyrrhenian Sea circulation and water mass fluxes in spring 2004: observations and model results. *Journal of Geophysical Research*, doi:10.1029/2009JC005680, 115(C06023):19, 2010.
- [7] S. Gabersek, R. Sorgente, S. Natale, A. Ribotti, A. Olita, M. Astraldi, , and M. Borghini. The Sicily Channel Regional Model forecasting system: initial boundary conditions sensitivity and case study evaluation. *Ocean Science*, 3:31–41, 2007.

- [8] R. Lardner, G. Zodiatis, D. Hayes, and N. Pinardi. Application of the MEDSLIK oil spill model to the Lebanese spill of July 2006. *European Group of Experts on satellite monitoring of sea based oil pollution. European Communities ISSN 1018-5593*, 2006.
- [9] M.P. Weinreb, R. Xie, J.H. Lienesch, and D.S. Crosby. Destriping GOES Images by Matching Empirical Distribution Functions. *Remote Sens. Environ.*, 29:185–195, 1989.
- [10] G. Coppini, M. De Dominicis, G. Zodiatis, R. Lardner, N. Pinardi, R. Santoleri, S. Colella, F. Bignami, D. R. Hayes, D. Soloviev, G. Georgiou, and G. Kallos. Hindcast of oil-spill pollution during the Lebanon crisis in the Eastern Mediterranean, July-August 2006. *Marine Pollution Bulletin*, doi:10.1016/j.marpolbul.2010.08.021, 2010.
- [11] L. Giglio, J. Descloitres, C.O. Justice, and Y.J. Kaufman. An Enhanced Contextual Fire Detection Algorithm for MODIS. *Rem. Sens. Env.*, 87:273–282, 2003.
- [12] R. Santoleri and the PRIMI Group. The PRIMI Project: August–September 2009 validation cruise on oil spill detection and fate. *Proceedings of SEASAR 2010, ESRIN, Frascati, Italy, 25-29 January 2010, in press*, 2010.
- [13] D. Comaniciu and P. Meer. Mean Shift: a robust approach toward feature space analysis. *IEEE Trans. Pattern Anal. Machine Intell.*, 24:603–619, 2002.
- [14] D. Comaniciu and P. Meer. Robust analysis of feature spaces: color image segmentation. *Proc. IEEE Conference on Computer Vision and Pattern Recognition, San Juan, Puerto Rico June 1997*, pages 750–755, 1997.
- [15] B. Fiscella, A. Giancaspro, F. Nirchio, P. Pavese, and P. Trivero. Oil spill monitoring in the Mediterranean sea using ERS SAR data. *2000 ERS-ENVISAT Symposium, October 16-20, 2000, Göteborg, Sweden*. http://earth.esrin.esa.it/pub/ESA_DOC/gothenburg/035nirch.pdf, 2001.

Sediment Distribution and Trace Metals Contamination in the Neretva Channel (Croatia)

S. Romano, F. Giglio, S. Albertazzi, M. Ravaioli

Institute of Marine Sciences, CNR, Bologna, Italy

stefania.romano@ismar.cnr.it

Abstract

The Neretva is the largest river of the eastern part of the Adriatic basin. Its catchment area is very broad and includes territories belonging to Bosnia, Herzegovina and, at the lowest reaches, Croatia. The river crosses areas exploited for agricultural, industrial and urban activities. Because of this, can become particularly severe given the location in karst area where erosion has already reached the geological base. The Neretva is characterized by a large amount of sediment that flows to the Adriatic sea into a narrow semi-enclosed basin, named Neretva Channel, located along the southernmost part of the Croatian coast. In order to contribute to the elevation of the distribution and the preservation potential of sedimentary deposits, the present study aims to trace the distribution of the Neretva River particle input toward the Adriatic Sea, in particular those associated to metal aggregates, and to follow their spatial vs. time distribution, using a suite of biogeochemical proxies like total and organic carbon, radiochemical data of $\delta^{13}\text{C}$ and distribution of some metals.

1 Introduction

Coastal areas are the places where the peculiarities of land-sea transition systems emerge more clearly, in terms of chemical, physical and biological changes, and where most human pressure occurs. Particles, which accumulate in marine sediments, originate from a combination of river discharge, runoff of agricultural soils, roads and urban settlements plus atmospheric dry and wet deposition. In these areas, the sediment composition is mainly controlled by local geology, but can also reflect anthropogenic discharge from industrial and urban activities, thus enhancing concentrations of both organic matter and metals. [1].

Eastern Adriatic coast, from Croatia to Albania, is a typical transgression environ-

ment formed during the Late Pleistocene-Holocene sea level rise by flooding of the pre-existing karstified surface [2], and it is characterized by several small rivers that form large estuaries. One of the biggest is that of the Neretva River (mean annual water flow $296 \text{ m}^3\text{s}^{-1}$), which is characterised by an estuary-type delta with a relatively large reclaimed alluvial plain.

At present, Neretva Delta is threatened by different planned activities such as road construction, urbanization, and hunting that may cause the release of contaminants into the water [3]. Over 90% of the soil of the area is exposed to water and wind erosion of varying intensity. The situation may be particularly severe in the karst area, where erosion has already reached the geological base.

In this context, biogeochemical proxies,

such as concentrations of bulk sedimentary organic carbon (C_{org}), total nitrogen (N), and their stable isotope compositions ($\delta^{13}\text{C}$), may provide information on sources and fate of sedimentary organic matter in aquatic sediments [4, 5, 6, 7]. The $\delta^{13}\text{C}$ and the N/C_{org} (atomic) ratio characterize the origin (marine vs. terrestrial) [8, 6] and the source of the organic materials. Although the C/N ratio has been more commonly used, the N/C ratio is the preferred parameter, since it behaves linearly in a mixing model [9, 10] and more reliably estimates the fraction of sedimentary organic carbon [11].

The present study aims to trace the spatial and time distribution of the particle inputs from Neretva River, to contribute in evaluating the distribution and the preservation potential of some metals associated with particles in the Neretva Channel.

2 Study area

The Neretva is one of the largest rivers of the eastern part of the Adriatic basin. It flows into the sea in the southern part of the Croatian coast close to Ploče, through a wide Delta (surface 12,000 ha). The river flows to narrow triangular-shaped semi-closed basin, called Neretva channel, bordered by the Croatian Coast on the North-East and by the Peljesac Peninsula on the South-West, while it is open toward the Adriatic Sea on the North-West (Figure 1). The Delta has undergone extensive land-reclamation works, and its previously twelve branches, became three in modern age. Marshes, several lakes and lagoons have disappeared and now the delta area suffers for the reduction of 90% of its surface due to irrigation, intense meteorological phenomena and increasing saline in-

gression that affect the life of animal and vegetal species of the area.

The river, 225 Km long, emerges in Zengora mountain in eastern Bosnia and Herzegovina, through canyons, cliffs and hollows in its upper and middle reaches it forces its way through the Dinaric Alps to spread downstream of the village of Pocitelj in Herzegovina over a vast wetland valley and then finally flows into the Adriatic Sea.

Its upper part, called Hutovo Blato, is in Bosnia-Herzegovina. Here the river cuts several canyons in Jurassic limestone and dolomite carbonate platform sequence. Then, the valley along the last thirty kilometers of the Neretva River spreads abruptly into an alluvial fan named "Neretvanske blatije" 20,000 ha wide, while in its lower reaches situated in the Republic of Croatia, the River branches creating a large delta. The riverbed is located on a very porous karst structure covered with sediment of low permeability.

The annual sediment discharge of the river is rather high (i.e., 3.6 tons in 2000), and can be considered similar to the sediment input of Po river (i.e., about 15.6 tons). The surficial currents, always oriented from SE to NW, are generally quite low (less than 10 cm·s⁻¹) and become slightly stronger during winter season.

3 Materials and methods

Study area, sampling locations and bathymetry are shown in Figure 1.

12 light box cores (subscript "BC", Figure 1) and 9 grab samples (subscript "G", Figure 1) were collected in May 2006 in order to sample both surficial and subsurficial sediments along SE-NW oriented transects. The BC short cores were radio-

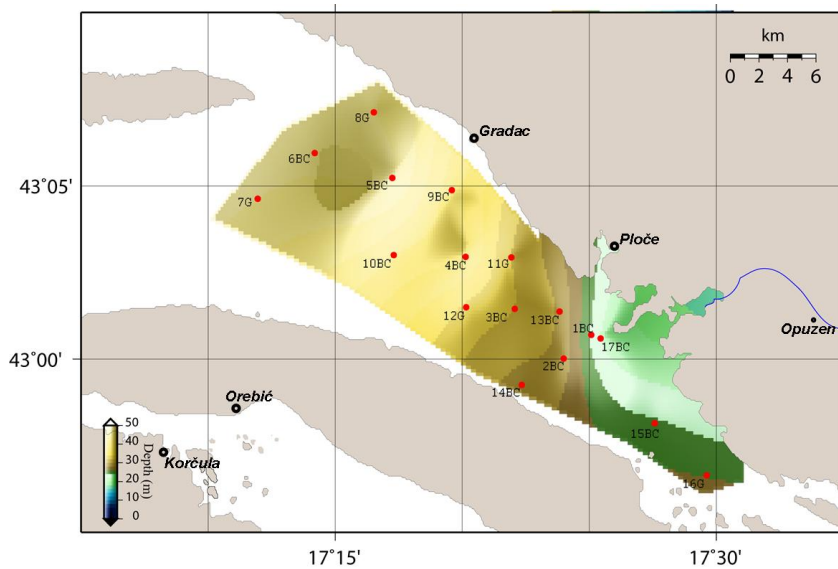


Figure 1: Study area and sampling location.

graphed and scanned for magnetic susceptibility. Then, the sediment was described for visual characteristics. Once the cores were opened, one half was stored as the historical archive and the other half was sub-sampled with a frequency of 2 centimeters for chemical and radiochemical analyses.

Before the analysis, sediments were dried at 60 °C in order to calculate their porosity according to Berner (1971), assuming a particle density of 2.5 g·cm⁻³. C_{org} and total carbon contents were determined using Fisons Elemental Analyser NA2000. In order to obtain organic carbon contents, the carbonate fraction was eliminated by pre-treatment with 1.5 M HCl. Stable isotopic analyses of C_{org} were carried out on the same samples by using a FINNIGAN Delta Plus mass spectrometer, that was directly coupled to the FISIONS NA2000 EA (see details in [7]).

Grain size analysis were carried out by wet sieving after a pre-treatment with H₂O₂, to separate sand from the finer fraction. Silt and Clay fractions were determined with X-ray Sedigraph.

¹³⁷Cs was measured by non-destructive gamma spectrometry [12, 13] using coaxial intrinsic germanium detectors (Ortec HPGc GMX-20195P and GEM-20200). ²¹⁰Pb was determined, by alpha counting its daughter ²¹⁰Po, assuming secular equilibrium between the two isotopes [13, 14]. For metals analysis an aliquot of wet sediment was leached with HNO₃ and H₂O₂ (10:3) under reflux [15]. This procedure allows to determine a fraction of metal associated to the surface of sediment particles or dissolved in the interstitial water. Cr, Ni and Pb concentrations were determined by Furnace Atomic Absorption Spectrophotometers, and the results reported on a dry weight of sediment.

The surficial samples data were analyzed for a correlation check through the Pearson correlation coefficient [16]. The analyses were performed to evaluate the proportionality between variables. STATISTICA software packages were used for the statistical analysis.

The spatial distribution of parameter were built by the gridding interpolation, method usually utilized by geoscientists to produces maps (The Generic Mapping Tools-free software, [17, 18]). A mask grid with no data was matched on a map grid to limit the computing only at the study area. A Mercator projection was applied on the grid map with isotropy grid spacing of 0.1 minutes.

4 Results and discussion

The cores radiography showed no evident inner sedimentary structures, but many of the samples seem to be mixed by bioturbation. The sediment is composed principally by silty-clay and seems to be quite similar all over the study area (Figure 1), coarser grain size increase with the radial distance from the river mouth. A sandy fraction was recognized only at the NW sites (station 7G). The C/N, $\delta^{13}\text{C}$ and Apparent Sediment Accumulation Rate (Figure 2a, 2b, 2d) showed similar areal distributions, very useful tools to trace the sediment sources and deposition patterns. Marine currents move particulate materials northward from the river mouth and, as expected, the sites close to the river inlet show a strong terrestrial input characterised by very low $\delta^{13}\text{C}$ values. On the contrary, at the farthest site, the marine input is strongly prevalent. The other stations show an increasing marine input moving northward, and the limit between marine and terrestrial sedimenta-

tion can be located around station 10BC. Hence, can assume that the particles are moved quickly by surficial currents but are released not so far from the river mouth and, in particular, in the area close to the coast.

However, its important to point out that our surficial sediment could represent a particular seasonal condition, and could be very different in other period. Moreover, the areal distribution of porosity (Figure 2c) shows a strange pattern with lower values close to the fluvial inlet, as expected, but also at the NW and NE of the coast in correspondence of the stations 9BC and 10BC. Together with the areal distribution of physical-chemical parameter, we tried to investigate the spatial and temporal distribution in the area of some inorganic contaminant (Cr, Ni and Pb) associates to the particles. We choose Cr, Ni and Pb, because these metals may represent both anthropogenic and natural source. The metal concentration-depth profiles are related both to the characteristics of the inputs and to sedimentation mechanisms, and could be occasionally affected by bioturbation. These latter determine sediment accumulation as the net result of deposition and resuspension. Usually, anthropogenic metal peak values are found in correspondence of periods of maximum inputs of these contaminants. However, biological mixing may disturb the record and redistribute the settled particles, leading to more uniform concentration profiles.

Figure 3 shows concentration-years profiles of box cores sampled along the direction of main sediment deposition, where, date were calculated according to Apparent Sediment Accumulation Rate (as shown in Figure 2d). Actually, these profiles do not account for any clear variation of concentration with depth and present similar

| | Cr ($\mu\text{g/g d.w.}$) | Ni ($\mu\text{g/g d.w.}$) | Pb ($\mu\text{g/g d.w.}$) |
|---------------------------------|-----------------------------|-----------------------------|-----------------------------|
| Average surficial concentration | 56.3 | 58.2 | 25.0 |
| Minimum | 26.9 | 28.7 | 4.5 |
| Maximum | 84.0 | 86.8 | 67.9 |
| BG | 45.0 | 51.8 | 24.0 |
| WA | 100 | 40.0 | 10.0 |
| LCB * | 100 | 70.0 | 40.0 |
| LCL* | 360 | 75.0 | 70.0 |
| ERL** | 81.0 | 20.9 | 46.7 |
| ERM** | 370 | 51.6 | 218 |
| ISQGs** | 52.3 | 15.9 | 30.2 |
| PEL** | 160.0 | 42.8 | 112.2 |

Mean metal concentrations pre-seventies (BG); World Average (WA): Forstner and Wittman (1984); * Italian Sediment Quality benchmark: APAT & ICRAM 2007; ** International Sediment Quality Guidelines: Long et al., 1995; Long et al., 1998; Grimwood & Dixon., 1997.

Table 1: Averaged metal concentration in surficial sediments; minimum and maximum values in cores and international benchmarks.

trends for the three metals. Core chronologies, based on ^{137}Cs and ^{210}Pb data, show that box cores represent approximately the last 50 years, and identify along the direction of main particles deposition a light peak in the end of 90s in 4BC and 13BC. On the contrary, 1BC, 9BC and 5BC do not show any clear variation downcore could suggest an input of material not related to the river, but it is also possible that there was a disturb of the signal intensity in the others samples.

In any case, the similar trends showed by Cr, Ni and Pb in the cores may suggest that the variations are linked to the change of physical proprieties (i.e. porosity, grain size...) downcore. This might be related to the changes in river transport occurred in the last 10 years during the post-war reconstruction of the area. Moreover, the low range of variation in concentration with time may also highlight, on a shorter time scale, the influence of seasonal currents on a shallow basin that could reprocess, move

and mix a large amount of sediment (N. Pinardi personal communication).

The Pearson correlation analysis (product-moment correlation r , [16]), applied on all data show a highly significant positive correlation ($p < 0.001$) between Cr and Ni, whereas highly significant negative correlations were observed between Cr and Ni with respect to both the total carbon and inorganic Carbon in turn, Pb did not show any significant correlation. On the other hand, sediment accumulation rates are significantly correlated with both $\delta^{13}\text{C}$ and C/N ratio.

This analysis could point out that Pb is affected by different mechanisms of transport and deposition than Cr and Ni. In particular, the source of Cr and Ni has not to be ascribed to the river but it might be linked to the coastal runoff in South Dalmatia coast. In fact, Cr and Ni levels are in the ranges of concentration reported for the soil of South Dalmatia [19]. Moreover, the comparison of the Pearson cor-

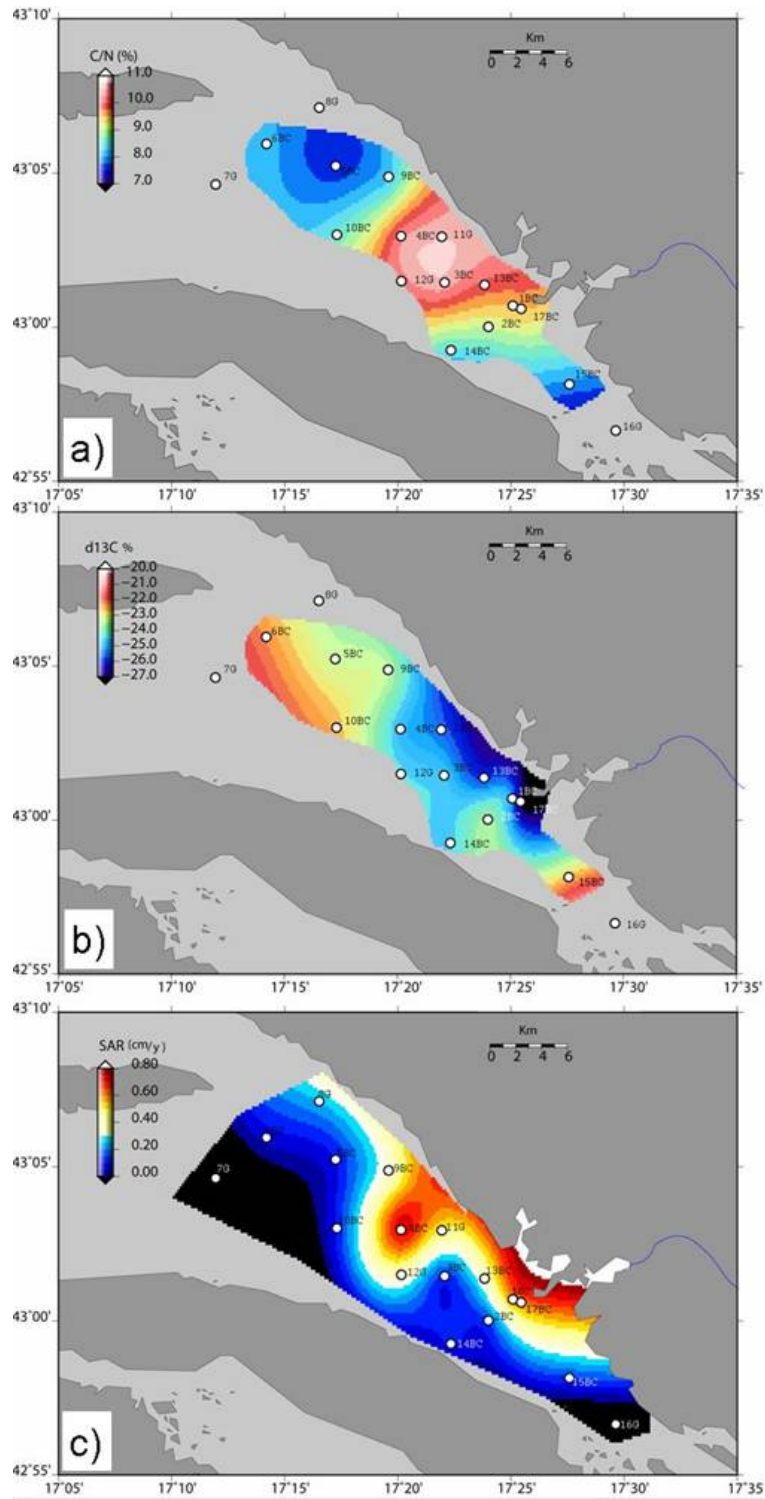
relation coefficient with the same parameter reported by other author [19] for the soil of the area at the Nord of the Neretva, shows a similar value ($r = 0.73$). Table 1 shows some preliminary result for metals concentrations in surficial sediment, with minimum and maximum values in cores. Some indications of potential contamination in present sediments may be obtained by comparing their concentration with pre-industrial levels and with some internationally recognised concentration benchmarks. In particular, the surficial concentrations were compared with Sediment Quality Guidelines: Threshold Effect Level (TEL), Effect Range Low (ERL), Probable Effect Level (PEL), Effect Range Median (ERM) [20]. Moreover other benchmarks (Base Chemical Level, LCB and Limit Chemical Level, LCL) derived for Italian coastal areas with similar geochemical characteristic, were used [21]. All these guidelines are screening tools to predict potential sediment toxicity, linking sediment concentrations of contaminants to any adverse biological effect resulting from exposure to various chemicals. Pb and Cr levels in surficial samples usually do not reach either PEL or ERM thresholds as well as the Italian benchmarks, with some exceptions. However the effect incidence for these samples can be considered low (8-30% for Pb and 2.9-21.1% for Cr [20]). The Ni surficial concentration at all stations exceeded both PEL and ERM guide-

lines but not the Italian benchmark. This means that these elements could cause adverse biological effect, although their levels are similar to natural soil concentrations (mean $84 \cdot g^{-1}$) in the area [19], and lower than the Italian benchmarks. In addition, the incidence of effect for exceeding ERM it is only 16.9 % [20] for Ni.

From a screening point of view, these results allow us to consider the Neretva Channel not contaminated by these three metals at time of sampling. On the other hand, a more reliable scenario is possible when the bottom sediment is reworked during winter season by storm or flood events and moved northward offshore along the Adriatic basin. Therefore, it will be necessary to repeat the sampling in other seasons in order to better evaluate the sedimentary conditions and the dynamic of the area.

5 Acknowledgement

Funds for this work were provided, in the framework of ADRICOSM-NERES (Neretva River Delta Environmental Requalification and Sustainable Development), by the Italian Ministry of Foreign Affairs. We are indebted with Frano Matic' of Institute of Oceanography and Fisheries, of Split Croatia for his help in sample collection, subsampling and handling on N/O BIOS and with professor Nadia Pinardi and INGV for kind collaboration.



1715

Figure 2: Areal distributions of a) C/N ratio, b) $\delta^{13}\text{C}$, and Apparent Sediment Accumulation Rate in the study area.

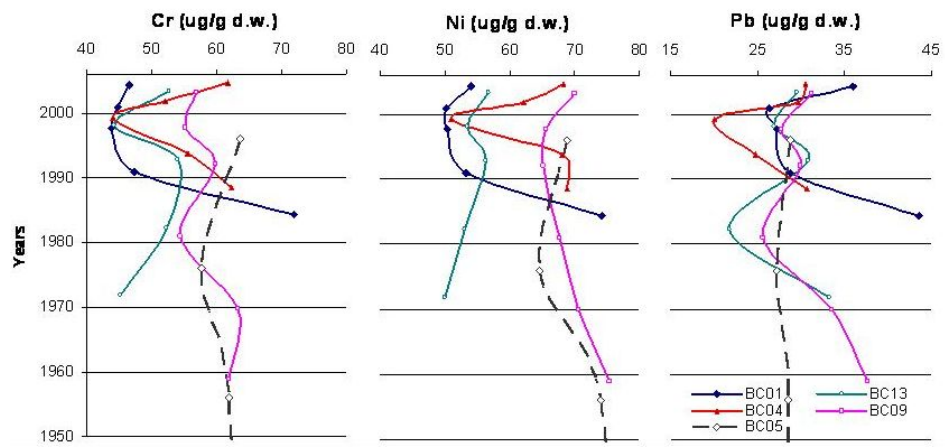


Figure 3: Metals concentration profiles in selected cores as function of time.

References

- [1] Z. Kljaković-Gašpić, D. Bogner, and I. Ujević. Trace metals (Cd, Pb, Cu, Zn and Ni) in sediment of the submarine pit Dragon ear (Soline Bay, Rogoznica, Croatia). *Environ Geol*, 58:751–760, 2009.
- [2] M. Surić, M. Juračić, N. Horvatinčić, and I. Krajcar Bronić. Late Pleistocene–Holocene sea-level changes and pattern of karstic coasts submersion — records from submerged speleothems along the Eastern Adriatic Coast (Croatia). *Marine Geology*, 214:163–175, 2005.
- [3] F. Calo and M. Parise. Waste management and problems of groundwater pollution in karst environments in the context of a post-conflict scenario: The case of Mostar (Bosnia Herzegovina). *Habitat International*, 33(1):63–72, 2009.
- [4] J.J. Middelburg and J. Nieuwenhuize. Carbon and nitrogen stable isotopes in suspended matter and sediments from the Schelde Estuary. *Marine Chemistry*, 60(3-4):217–225, 1998.
- [5] M.C. Graham, M.A. Eaves, J.G. Farmer, J. Dobson, and A.E. Fallick. A study of carbon and nitrogen stable isotope and elemental ratios as potential indicators of source and fate of organic matter in sediments of the Forth Estuary, Scotland. *Estuarine Coastal and Shelf Science*, 52(3):375–380, 2001.
- [6] N. Ogrinc, G. Fontolan, J. Faganeli, and S. Covelli. Carbon and nitrogen isotope compositions of organic matter in coastal marine sediments (the Gulf of Trieste, N Adriatic Sea): Indicators of sources and preservation. *Marine Chemistry*, 95:163–181, 2005.
- [7] T. Tesi, L. Langone, M.A. Goñi, S. Miserocchi, and F. Bertasi. Changes in the composition of organic matter from prodeltaic sediments after a large flood event (Po River, Italy). *Geochimica et Cosmochimica Acta*, 72:2100–2114, 2008.
- [8] R. Fichez, P. Dennis, M.F. Fontaine, and T.D. Jickells. Isotopic and biochemical composition of particulate organic matter in a shallow water estuary (Great Ouse, North Sea, England). *Marine Chemistry*, 43(1-4):263, 1993.
- [9] M.A. Goñi, M. J.Teixeir, and D.W.Perkley. Sources and distribution of organic matter in a river-dominated estuary (Winyah Bay, SC, USA). *Estuar. Coast. Shelf Sci.*, 57:1023–1048, 2003.
- [10] T. Tesi, S. Miserocchi, M.A. Goni, and L. Langone. Source, transport and fate of terrestrial organic carbon on the western Mediterranean Sea, Gulf of Lions, France. *Mar. Chem.*, 105:101–11, 2007.
- [11] E.M. Perdue and J.F. Koprivnjak. Using the C/N ratio to estimate terrigenous inputs of organic matter to aquatic environments. *Estuarine, Coastal and Shelf Science*, 73:65–72, 2007.

- [12] M. Frignani, L. Langone, M. Ravaioli, and A. Sticchi. Cronologia di sedimenti marini—Analisi di radionuclidi naturali ed artificiali mediante spettrometria gamma. *Rapporto Tecnico*, 24:32, 1991.
- [13] M. Frignani and L. Langone. Accumulation rates and ^{137}Cs distribution in sediments off the Po River delta and the Emilia-Romagna coast (northwestern Adriatic Sea, Italy). *Cont. Shelf Res.*, 11:525–542, 1991.
- [14] M. Frignani, L. Langone, S. Albertazzi, and M. Ravaioli. Cronologia dei sedimenti marini: Analisi di ^{210}Pb via ^{210}Po per spettrometria alfa. *Rapporto Tecnico*, 28, 1993.
- [15] L.G. Bellucci, M. Frignani, D. Paolucci, and M. Ravanelli. Distribution of heavy metals in sediments of the Venice Lagoon: the role of the industrial area. *Sci. Total Environ.*, 295:35–49, 2002.
- [16] K. Pearson. Mathematical Contributions to the Theory of Evolution. III. Regression, Heredity and Panmixia. *Philosophical Transactions of the Royal Society of London*, pages 253–318, 1896.
- [17] P. Wessel and W.H.F. Smith. Free Software Helps Map and Display Data. *EOS Trans., AGU*, 72(41):441, 1991.
- [18] P. Wessel and W.H.F. Smith. New, Improved Version of Generic Mapping Tools Released. *EOS Trans., AGU*, 79(47):579, 1998.
- [19] S. Miko, J. Halamić, Z. Peh, and L. Galović. Geochemical Baseline Mapping of Soils Developed on Diverse Bedrock from Two Regions in Croatia. *Geologia Croatica*, 54(1):53–118, 2001.
- [20] E.R. Long, D.D. MacDonald, S.L. Smith, and F.D. Calder. Incidence of adverse biological effects within ranges of chemical concentrations in marine and estuarine sediments. *Environmental Management*, 19:81–97, 1995.
- [21] APAT & ICRAM. Manuale per la movimentazione di sedimenti marini. <http://www.icram.org/nav2/movimentazioneidefondali.htm> & www.apat.gov.it/site/files/manualeSedimentiMarini.pdf, page 72, 2007.

Tracing Possible Offshore Sand Movement During Extreme Sea Storm Events: an Example from the Salerno Bay (Southern Tyrrhenian Sea)

V. Ferrante^{1,3}, F. Budillon¹, M. Iorio¹, C. Lubritto², M. Monaco³, E. Pugliese Carratelli³, D. Vicinanza⁴

1, Institute for Coastal Marine Environment, CNR, Napoli, Italy

2, Department of Environmental Sciences, Lab. CIRCE, Second University of Napoli, SUN, Caserta, Italy

3, CUGRI - University Research Consortium on Major Hazard - Naples and Salerno Napoli/Salerno, Italy

4, Department of Civil Engineering, Second University of Napoli, Aversa, Italy
eferrante@iol.it

Abstract

Current research on beach evolution is mainly focussed on processes which take place within the surf zone, i.e. the area where most of the breaking occurs. Sand movement outside this area is not easily traceable and therefore tends to be overlooked. However it has been widely reported that sand does move offshore during major sea storms and settles on the inner shelf, forming event layers at depths from which a return to the surf zone is unlikely under normal wave climate. The near-bottom hydrodynamics in this zone is dominated by the nonlinear interaction between waves and slowly varying currents, which results in a nested wave-current flow in the bottom boundary layer. The main purpose of the research activity proposed here is to learn more about the hydrodynamic processes that remove the sand from the littoral cell and release it at depth. The possibility that combined wave-current flows generate offshore shear stress at the seabed strong enough to cause the cross-shore mobilization of sand in the Salerno Bay (Southern Tyrrhenian Sea) should be taken into consideration. An integrated numerical model was used and implemented with real seafloor morphology and sediment parameters obtained from the inner shelf of the Salerno Bay, in order to provide a more realistic scenario of the impact of sea storms on the seabed. Results should also provide some further elements towards a better understanding of the marked shoreline retreat in the area over the last several decades.

1 Introduction

Sea storm current-waves interaction is recognized as being one of the most effective dynamics of sediment winnowing and deposition, able to drive sand beyond the

surf zone. Winter storm action induces sediment re-suspension from the seabed and drift in the bottom boundary layer (bbl) which may result on to the formation of graded sand layers lying on erosive surfaces mid-latitude shelves [1, 2, 3,

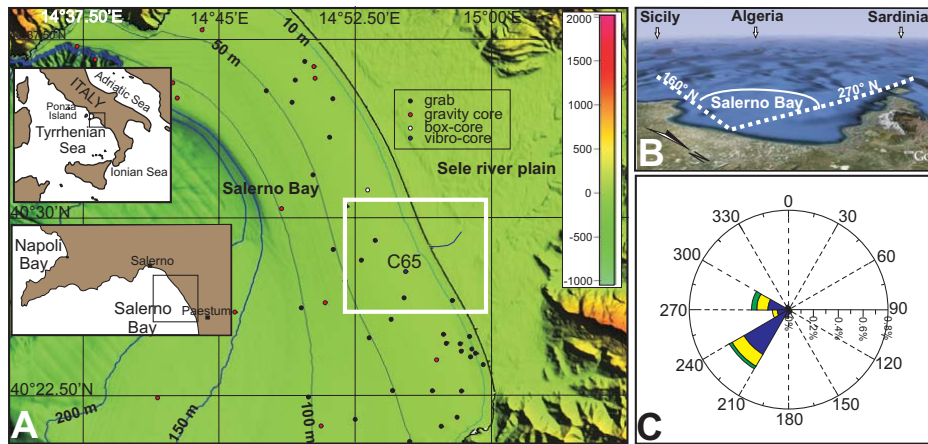


Figure 1: A) Study area (bathymetry and sediment samples from Carg mare Project) and core C65 site; B) wave exposure of the of the bay; C) wave climate.

4, 5]. The occurrence of sand layers in the stratigraphic record of lakes and off-shore settings can thus be considered evidence of past storminess (Andrade et al., 2004). Their formation and preservation is not common since it depends on various factors: the availability of sand from the coastal system, the burial rate offshore, the burrowing activity of benthic organisms, the seabed reworking due to subsequent storm recurrence [6, 7]. More recently a numerical model of sea storm events in the northern area of Salerno Bay proved that sand motion down to 50 m of depth could be due to wave-current interaction [8, 9]. This study aims to apply the same numerical approach to a different sector of the Salerno Bay (Figure 1), where the negative balance of sediments in the surf zone accounts for a significant retreat of the shoreline over the last several decades [10, 11].

2 Study area

2.1 Geological setting

The central sector of Salerno Bay is oriented to the southwest and bounds seaward the alluvial Plain of the River Sele and its tributaries (Figure 1). Well sorted sand spreads all along the coast and forms the submerged beach wedge down to 12 m of depth [12]; below it gives way to less sorted muddy fine sand [13]. The bay encloses a continental shelf of about 9 -20 km wide, with a seaward boundary of a sharp shelf break, 120 m deep in the northern sector and 180 m deep in the southern sector (Figure 1). Shelf gradient ranging between 0.6° and 1° is accounted for by the geometry of the Late Holocene marine wedge, which has been aggrading at different rates from the coast to the sea [5, 14]. The sedimentation rate on the outer shelf reaches about $100 \text{ cm}\cdot\text{ky}^{-1}$ over the last 2 ky [15]. Indeed about 2 m of marine sediment overlies the pumice deposit of the 79 A.D. Vesuvius

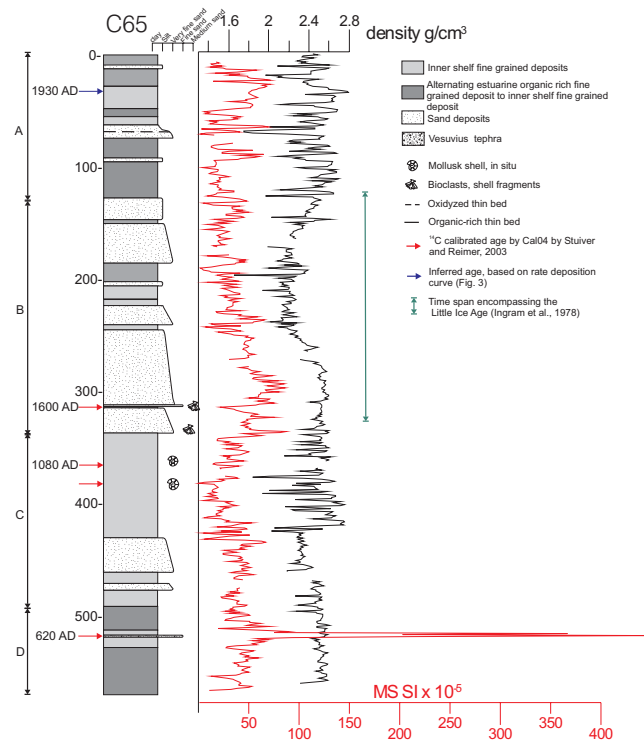


Figure 2: Lithostratigraphy of C65 core and petrophysical measurements (red curve is magnetic susceptibility, black curve is density).

eruption onto the outer shelf [16, 17]. No relevant sea level variations have been reported over this time span (0.4 ± 0.08 m below present day sea level, [18]). A normal progradation of the shoreline about 500 meters seaward was estimated during the late Holocene up to the Roman times [10], when the shoreline was located 500 m further inland with respect to that of the present day. From the 12th century up to the 18th century the progradation of the coast proceeded at a rate of 0.4 m/a, then up to 1954 A.D. at a rate of about 1,5 m/a in the central sector of the bay (Sele river mouth). Later on, a general tendency to the

retreat of about 0,28m/a has been evaluated based on aerial photo surveys [11]. The rate of erosion reached 8 m/y at the River Sele mouth between the '70s and '80s of the last century, and decreased to 2 m/y in the subsequent years (D'Argenio et al., this volume). The authors highlight that this process, besides the loss of sand from the foreshore has also caused the slope increase of the beach profile, the accumulation of pebbles along the shore and the erosion of the dune ridges in the backshore [11]. One of the main causes of such phenomena is the reduction in sediment yield from the River Sele over the last 50 y. The

river has a catchment area of about 2330 km² and has a mean water discharge of 69 m³/s [19]. The morphometric parameters of catchments rule out the possibility that the River Sele can produce hyperpycnal flows [20]. Besides, since the 1930's a dramatic decrease in sand yield has been observed at the river mouth due to a build up of dams in the middle stretch of the fluvial path. The central sector of the Salerno Bay is exposed to waves hitting from 180° N to 270° N (Figure 1). Wave data records were supplied by the wave buoy offshore Ponza Island operated by the Italian Sea Wave Measurement Network (Rete Ondametrica Nazionale, RON), which has been operating since July 1989. Three-hourly data set, which included significant spectral wave height (Hs), peak period (Ts), and wave direction (DD) were analyzed from July 1989 to December 2009. The extreme waves statistical analysis was carried out using the Peak Over Threshold method, according to the indications of Goda [21]. In order to solve the difference between the site of measurement and the actual site of this study, the offshore waves were transposed from Ponza Island to Salerno Bay at 115m depth isobaths using the geographical transformation. To estimate the direction of extreme wave events a threshold of three and six meters wave height was considered. According to Eagleson and Dean, [22] and based on statistical analysis of the last twenty years of wave event records, the depth of closure has been estimated at -10 m. Following the indication in Corsini et al. [23], a sea storm is a time series of sea states characterized by values of wave height, period and direction that vary within a given interval characterized by:

- wave height persistence over the threshold of 1.0 m for more than 12 consecutive hours,

- wave height decay below the threshold of 1.0 m for less than 6 consecutive hours,
- original direction belonging to a determinate angular sector ($\pm 30^\circ$ with respect to the initial direction).

Sea storms are typically characterized by values of wave height, period and direction that correspond to the peak intensity of the sea state sequence. For the Tyrrhenian Sea the minimum threshold is 2.0 m wave height and duration is 24 hours.

3 Methods and materials

3.1 Field data

Precise geological data, provided by the real stratigraphic and sedimentologic context of the inner shelf of the Salerno Bay was used to implement the model of coastal circulation.

C65 vibro-core, collected at 14 m of depth was analyzed and measured by its physical properties (magnetic susceptibility and density) at the IAMC CNR laboratory, in order to characterize event beds and tephra. ¹⁴C geochronological calibrations were obtained on Dentalium shells to evaluate the age and the rate of sediment aggradation throughout the core record (Figure 2).

The ¹⁴C analysis were carried out with an AMS system based on the 9SDH-2 Pelletron accelerator at CIRCE (Centre for Isotopic Research on Cultural and Environmental Heritage) of "Seconda Università di Napoli", Caserta (Italy).

Field data includes the submarine topography down to the 100 m isobath, the D₅₀ grain size of loose sediment, the occurrence of local rocky outcrops and plant colonization on the seabed. The data set was provided by the CARG project conducted

by IAMC over the last years (see Budillon et al., this volume).

3.2 Circulation model

The SHORECIRC program was used for the numerical simulation since it is considered one of the most reliable models to compute the variation of horizontal velocities of the nearshore circulation field in all three dimensions (and time). It was developed at the University of Delaware [24, 25], and successfully compared to data from the DUCK94 and Sandy Duck field experiments and with laboratory measurements [26]. A depth-integrated wave-averaged model was used to provide the full 3-D depiction of near shore circulation that was needed to find out sediment transport patterns in the study area.

3.3 Sediment transport model

When considering a non cohesive sediment, the individual sediment grains settle on the bottom due to their submerged weight and resist horizontal motion due to the presence of neighboring grains. The ratio of mobilizing (drag) and stabilizing (submerged weight) forces is of fundamental physical significance in fluid-sediment interaction for non cohesive sediment. Several empirical bed load transport formulas have been proposed for turbulent boundary layer flows [27]. The Meyer-Peter and Müller formula [28], is particularly popular in engineering literature. However, since it was originally developed using data obtained from steady flowing rivers with channels of negligible slope, its adoption for unsteady wave or combined wave-current turbulent boundary layer flows over an inclined bed is not straightforward. A conceptual model for bed-load transport

of sediment grains rolling or sliding along an inclined bottom has been proposed by Madsen et al. [29] and Madsen [30] as a physical interpretation of the purely empirical Meyer-Peter and Müller formula. The model is suited for the prediction of offshore sediment transport rate under sea storm events thus it serves the purpose of this study. The governing equation inserted in the model are presented below:

$$q(t) = w \cdot d \left\{ \frac{0.5 \cdot \rho \cdot f_{ow} \cdot [u^2(t) + v^2(t)]}{(\rho_z - \rho) \cdot g \cdot d} \right\}^3$$

where ρ is the fluid density, ρ^s is the bulk density of sediment, d is the mean sediment grain size, w is the fall velocity of sediment, f_{wc} is the combined wave-current friction factor, and u and v are the velocity components that result from the combination of high frequency (wave driven) and low-frequency (atmospheric and tide driven) currents. The method for computing f_{wc} suggested by Madsen [30], is essentially an iterative method that modifies the bottom boundary layer based on interaction with waves.

4 Results

4.1 Core stratigraphy and depositional rate at the beach-shelf boundary

The C65 vibro-core (40° 27.860' N, 14° 55.305' E) was collected in 2004, 2.6 km southwest of the Sele river mouth, 14 m below sea level, 1.2 km seaward of the depth of closure (Figure 1). It recovered 5.60 m of fine grained deposits interbedded with sandy, structure-less layers whose thickness varies from millimeters to decimeters (Figure 2, Table ??). A tephra layer,

| Sediment pattern | Depth range cm | Mixed estuarine –shelf pelite | Sand | Shelf pelite |
|------------------|----------------|-------------------------------|------|--------------|
| A | 0-125 | 60 % | 15% | 25% |
| B | 125–340 | 10% | 80 % | 10% |
| C | 340-490 | - | 28% | 72% |
| D | 490-560 | 70% | 10% | 20% |

Table 1: Lithologic patterns of C65 core are grouped in four sections. Percentages refer to the thickness.

| Depth (cm) | material | Radiocarbon age (BP) | Calendarial Age (AD) – one sigma | Lab code |
|------------|----------------------|----------------------|----------------------------------|----------|
| 312 – 313 | shell fragments | 752±40 | 1548 – 1651 | DSH1633 |
| 360 – 363 | dentalium shell | 1363±23 | 1043 – 1129 | DSH1634 |
| 380 – 381 | 2 turritellae shells | 1155±42 | 1242 – 1320 | DSH1631 |
| 516 – 519 | dentalium shell | 1836±42 | 576 - 666 | DSH1632 |

Delta R: 46±21

Table 2: Radiocarbon age and age calibrations on shells of C65 vibro-core (Cal04, [31]).

made up with lapilli and ash occurs 516 cm below the seafloor and settled owing to a historical eruption of the Vesuvius volcano (P. Petrosino and D. Insinga, personal communication), which stands at a distance of 58 km from the core site, in the NW direction. Within the fine-grained sediment, the estuarine-fluvial component was clearly identifiable because of its dark gray colour due to the high organic content, in contrast to marine fine-grained sediment that is varying shades of olive gray and has widespread shell fragments. Sand layers are quite homogeneous and do not show any particular structure, if not that of a normal gradation of the grain size. They are enclosed by sharp surfaces underneath and blend gradually upwards into pelite. Four main intervals can be identified from the top to the base, based on the occurrence and thickness of sandy layers versus pelite deposits: dentalium, turritellae and shell

fragments were found in situ in the olive gray pelite deposits and measured for radiocarbon age. Results are shown in Table 2. The calibration on the turritellae shell gave a suspicious and inconsistent value and was not given any further consideration.

The core consideration sediment dates back to 400 AD and thus encompasses a time record of about 1600 y. It is worth to noting that the core site has been always out of the closure depth over this time span, if we consider the shifting position of the shoreline through time, as reported by the authors (see introduction and references). Based on age calibrated depths, a depositional rate curve was interpolated (Figure 3).

Age calibration allowed the identification of the sediment deposited during the Little Ice Age (LIA, [32, 33]), which occurred from the middle of the 15th century

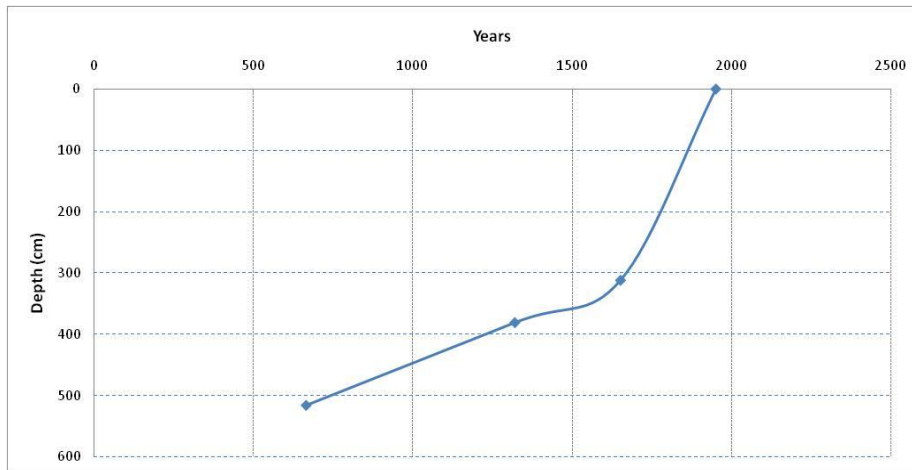


Figure 3: Mean sediment aggradation rate of the inner shelf at the core site, based on ^{14}C age calibrations of mollusk shells.

to the 19th century and was characterized by lower average temperatures and possibly by longer duration and more frequent exceptional winter storms than the present day [34, 35].

The time span of LIA coincides pretty well to the B interval of C65 core (Figure 2, Table 1), where an abrupt increase of sand occurs. Indeed, the base and the top of B interval date about 1600 – 1840 AD, based on interpolated values. Conversely, 1930 AD falls approximately in the uppermost 50 cm of the core, where fine grained sediment prevails, thus confirming the reduced bed load yield from the River Sele to the littoral cell, due to the dam construction.

4.2 Numerical simulation

The simulation was run moving from deep water conditions located at 100 m of depth and taking into account refraction-diffraction effects. The wave height used for the simulation was chosen at return pe-

riod $\text{Tr}=0.05$ ky ($H_s, \text{Tr}=7.75$ m, $T_s, \text{Tr}=12$ s) which assumes the value of $H=3.21$ m at the site of C65 (14 m of depth). This value is used as reference in the calculation of near bed wave orbital velocity at the same site. The circulation model simulation shows the formation of a crossshore current directed seawards with a direction 220° N (Figure 3). This current is generated by the interaction between two along-shore currents moving in opposite directions as shown in Figure 4. This crossshore current reaches the maximum velocity in proximity of the surf zone ($h=10$ m) and decreases offshore down to the depth of about 50 m. The 2DH mean value of current velocities near C65 sites are, $u_r=1.72$ $\text{m}\cdot\text{s}^{-1}$ and $u^*=1.05$ $\text{m}\cdot\text{s}^{-1}$ after 3 h, where u^* represents the shear velocity and u_r the steady current velocity.. The mentioned values remain constant for the rest of the simulation. This current coupled with oscillatory motion controlled wave and directed 230° N

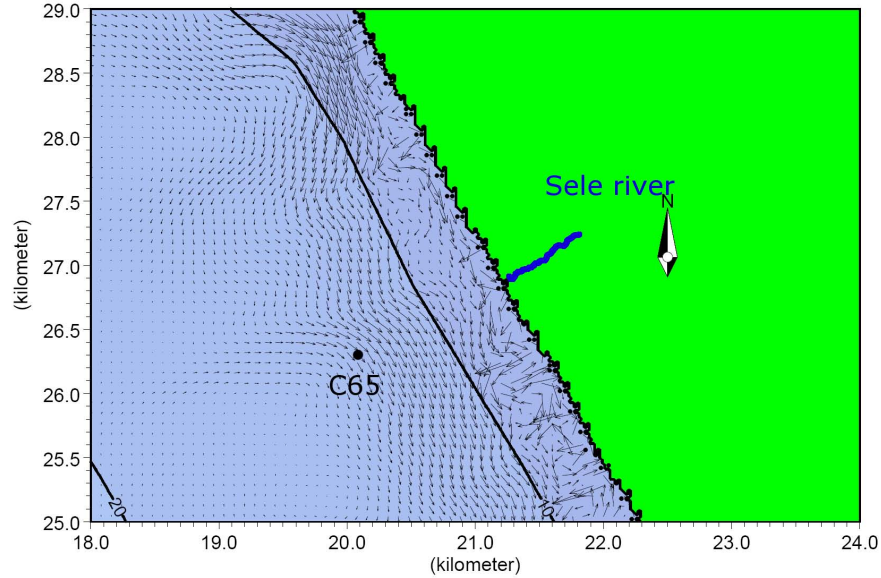


Figure 4: Numerical simulation of 2DH circulation off the Sele river mouth under sea storm conditions with a recurrence period T_r of 0.05 ky ($H_s, T_r=7.75$ m, $T_s, T_r=12$ s).

generates a nested current in the bbl that accounts for net fine sand transport down slope. It is worth noting that the direction of the net sediment transport is not the direction of the crossshore current but is obtained by:

$$\tan\theta_t = \frac{2}{3} \cdot \tan\theta_c$$

where θ_t is the direction of the net bed-load transport measured counter clockwise from the x axis, that in this case is 220° N [30] directed alongshore, as expected. Immediately outside the surf zone, the near bed current turns crossshore, since the oscillatory motion becomes predominant with respect to the currents, driven by radiation stresses (Figure 3). In Figure 5 the potential sediment transport rate for the investi-

gated area is represented. The colour map provides a visual scale to determine the rate of transport per cell width (cell width = 10 m). The combined wave current velocity is high enough to move sediment at the core site, and the resulting sediment transport direction is toward southeast, according to maximum wave induced orbital velocities and bottom currents. The potential net transport is directed offshore following current directions as shown in Figure 4. The depositional rate was numerically evaluated using the Lax-Wendroff morphological scheme, in order to appreciate the potential variation at the seabed during a typical Tyrrhenian Sea storm event. Results estimate that the potential sand aggradation at the seabed could reach 5 -10 cm for a single event, which is comparable to

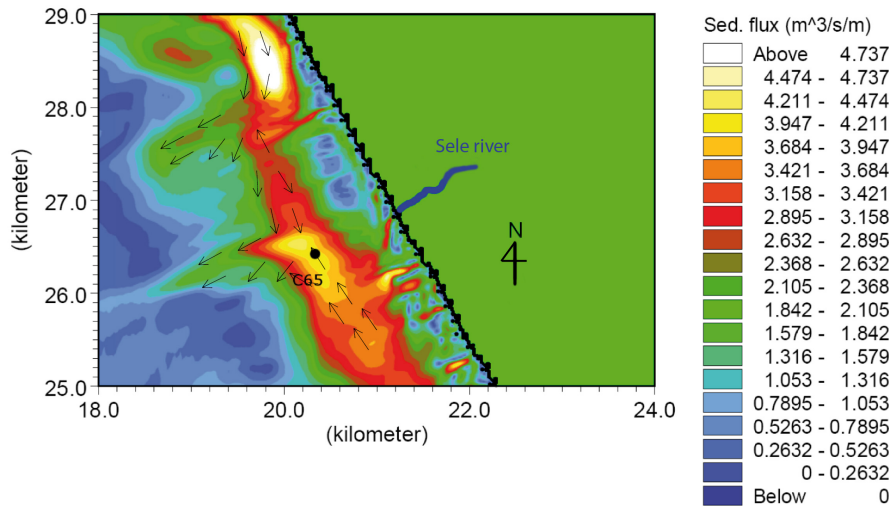


Figure 5: Mean sediment flux rate off Sele river mouth. Black arrows are the mean sediment flux direction.

the actual real thickness of sand layers in the uppermost core stratigraphic record.

5 Discussion

Age calibrations of cored sediment allowed us to infer a hypothetical frequency of sea storms that impacted the seabed at this site, during the last century. Namely, since the core site is 1.2 km distant from the closure depth over the last hundred years, it can be assumed that the sand layers which occur within the A section have been caused by sea storm events. Fluvial sand yield is negligible at this depth taking into account the type of river, the annual yield and the presence of dams since the last century. Three main events have been recorded over the last 0.15 ky, following the same criteria used in Budillon et al.[9]. Thus a major storm return frequency of 50 years is a

reliable value to implement the numerical model of sediment transport. The numerical simulations show that at the core site the cinematic condition at the seafloor is intense enough, after three hours, to start up and continue a net solid transport relative to fine and very fine sand particles (Figure 5). It is assumed that as the sea storm diminishes, the cinematic conditions decrease, u^*m slows down, and only the transport finest particles are transported farther seawards. Thus, a vertical and a horizontal sorting of grains could take place at the end of the process. The area where the potential transport rate is highest, as resulted from the numerical model, is located between a depth of 8 m to 15 m. The numerical simulation shows that u_m velocity at C65 site, where sand layers occur, is intense enough to transport sand over about 0.5 km during a 3 h time span (typical duration of a sea storm peak in the Southern Tyrrhe-

nian Sea), before settling down. This result is only indicative since u_m values change with depth and time following the typology of the sea storm. Since extreme events are generally accompanied by increasing and decreasing phases with significant wave heights that might uphold combined flows in the bbl, it is likely that much longer distances could be covered by sand particles during the whole storm event. It is worth noting that sediment transport during major sea storm events in this sector of the shelf, close to the foreshore (14 m of depth), may be due both to wave driven alongshore currents and combined flows in the bbl of the inner shelf. Indeed, the surf zone widens out to at least 9 m, under the effect of 7 m high waves. Sediment fluxes in the bbl mainly follow the littoral circulation patterns and move south-eastwards. If the numerical simulations proved the sand layers of A interval (Table 1, Figure 2) as possibly being deposited during sea storms, the sedimentation of sand layers several decimetres thick, as in B interval, is not easily understood. The marked increase of sand deposition since approximately 1600 AD, coinciding with the onset of the LIA, could be accounted for by two main factors:

- sea storm events might have been more frequent than at present and possibly longer lasting; on the contrary the possibility that higher waves or longer wave periods might have occurred is ruled out, owing to the geographical setting of the Mediterranean Sea
- the fluvial bedload to the sand bar at the river mouth and from here to the littoral cell might have been more consistent: as a consequence the quantity of sand transport by sea storm and therefore offshore sedimentation could have been higher than that of the present day.

6 Conclusion

In order to confirm the origin inferred to the sandy layers (sea storm deposition) found in the very recent stratigraphic record off the River Sele, a model of coastal circulation and sediment transport under sea-storm conditions was performed in the center of Salerno Bay. To implement the numerical simulations a hypothetical extreme sea storm was considered with a return period of 0.05 ky, a direction from 230° N, a significant wave heights of about 7.75m and a period T_s of about 12s. Results highlight that at the C65 site, 14 m below the sea level, 2DH current velocity reaches $1.75 \text{ m}\cdot\text{s}^{-1}$. The magnitude of the combined wave-current shear velocity at the same site reaches $1.05 \text{ m}\cdot\text{s}^{-1}$ and accounts for a potential sediment transport rate of $4\cdot 10^{-4} \text{ m}^3 \cdot \text{ms}^{-1}$. These values are compatible with the formation of sandy layers during an extreme sea storm and also accounts for their thickness. This study aims to explain the occurrence of sand layers in the inner shelf over the last 0,1ky, while the process that accounts for sand layers deposition during the LIA has been intentionally overlooked. Core litostratigraphy proves that the sand layers are thicker and more frequent over the time span correspondent to the LIA, if compared to those deposited during the ensuing and previous centuries. It can be assumed that the rapid progradation of the shore, the large yield of sand from the river's bedload and the different morphoclimatic conditions might have substantially affected the dynamics of the coastal environment.

7 Acknowledgment

C65 vibro-core was collected by Geolab srl as part of a submarine sand research activity directed by E. Cocco and E. Pugliese Carratelli and carried out on behalf of the Salerno Provincial Authority - Assessorato alle Politiche Ambientali [19]. Bathymet-

ric data was provided by Carg Project at 1:50000 scale [12]. We are grateful to Jacqueline Ashby for the English revision to the manuscript. This study was supported by a "Regione Campania, Assessorato Ricerca Scientifica, L.R. 5/2002" grant to F.B..

References

- [1] R.H. Dott and J. Bourgeois. Hummocky stratification: significance of its variable bedding sequence. *Geological Soc. Amer. Bull.*, 93:663–680, 1982.
- [2] W. Duke. Hummocky cross-stratification, tropical hurricanes, and intense winter storms. *Sedimentology*, 32:167–194, 1985.
- [3] A.W. Niedoroda, D.J.P. Swift, and J.A. Thorne. Modelling shelf storm beds: control of bed thickness and bedding sequence. in: *Shelf sandstone, shelf depositional sequence and petroleum accumulation: a symposium*, pages 15–39, 1989.
- [4] P. Myrow and J.B. Southard. Tempestite Deposition. *J. Sediment. Res.*, 66(5):875–887, 1996.
- [5] F. Budillon, C. Violante, A. Conforti, E. Esposito, et al. Event beds in the recent prodelta stratigraphic record of the small flood-prone Bonea stream (Amalfi Coast, Southern Italy). *Mar. Geol.*, 222-223:419–441, 2005.
- [6] R.A. Wheatcroft and D.E. Drake. Post-depositional alteration and preservation of sedimentary event layers on continental margins, I. The role of episodic sedimentation. *Marine Geology*, 199:123–137, 2003.
- [7] T.R. Keen, S.J. Bentley, W. Chad Vaughan, and C.A. Blain. The generation and preservation of multiple hurricane beds in the northern Gulf of Mexico. *Mar. Geol.*, 210:79–105, 2004.
- [8] F. Budillon, E. Esposito, M. Iorio, N. Pelosi, S. Porfido, and C. Violante. The geological record of storm events over the last 1000 years in the Salerno Bay (Southern Tyrrhenian Sea): new proxy evidences. *Advances in Geosciences (EGU)*, 2:123–130, 2005.
- [9] F. Budillon, D. Vicinanza, V. Ferrante, and M. Iorio. Sediment transport and deposition during extreme sea storm events at the Salerno Bay (Tyrrhenian Sea): comparison of field data with numerical model results. *Nat. Hazards Earth Syst. Sci.*, 6:839–852, 2006.

- [10] E. Cocco and M.T. de Magistris. Evoluzione storica e recente del litorale di Paestum, Golfo di Salerno. *Mem. Soc. Geol. It.*, 41:697–702, 1988.
- [11] G. D’Acunzi, T. De Pippo, C. Donadio, F. Peduto, et al. Studio dell’evoluzione della linea di costa della Piana del Sele (Campania) mediante l’uso della cartografia numerica. *Studi Costieri*, 14:55–67, 2008.
- [12] ISPRA. Carta Geologica d’Italia, scala 1:50000 Foglio 486 Foce del Sele. 2009.
- [13] E. Cocco, M.A. De Magistris, M.T. Efaicchio, and F. Boscaino. Geoenvironmental features of the Sele river plain littoral (Gulf of Salerno, Southern Italy). *Boll. Ocean. Teor. e Appl.*, 10(2-4):235–246, 1992.
- [14] M. Iorio, J. Iiddicoat, F. Budillon, P. Tiano, et al. Paleomagnetic secular variation time constraints on Late Neogene Geological events in slope sediment from the eastern Tyrrhenian Sea. In: Kneller (ed.) *External Controls on Deep-Water Depositional Systems*, SEPM Special Publication. 92:233–243, 2009.
- [15] M. Iorio, L. Sagnotti, A. Angelino, F. Budillon, et al. High-resolution petrophysical and paleomagnetic study of late-Holocene shelf sediments, Salerno Gulf, Tyrrhenian Sea. *Holocene*, 14(3):433–442, 2004.
- [16] M. Sacchi, F. Molisso, C. Violante, E. Esposito, et al. Insights into flood-dominated fan-deltas: very high-resolution seismic examples off the Amalfi cliffed coasts, eastern Tyrrhenian Sea. *The Geological Society, London*, 322:33–71, 2009.
- [17] D. Insinga, F. Molisso, C. Lubritto, M. Sacchi, et al. The proximal marine record of Somma–Vesuvius volcanic activity in the Naples and Salerno bays, Eastern Tyrrhenian Sea, during the last 3 kyr. *Journal of Volcanology and Geothermal Research*, 177(1):170–186, 2008.
- [18] F. Antonioli, G. Cremona, F. Immordino, C. Puglisi, et al. New data on the Holocene sea level rise in NW Sicily (Central Mediterranean Sea). *Global and Planetary Change*, 716:121–140, 2002.
- [19] CUGRI. Valutazione dell’apporto solido dei principali corsi d’acqua del golfo di Salerno by V. Bovolin within a research carried out under contract of the Salerno Provincial Authority - Assessorato alle Politiche Ambientali - ”Sistemazione del litorale salernitano, compresa la costa della città di Salerno”. page 303, 2004.
- [20] T. Mulder and J.P.M. Syvitski. Turbidity currents generated at river mouths during exceptional discharges to the world oceans. *The Journal of Geology*, 103:285–299, 1995.
- [21] Y. Goda. On the methodology of selecting design wave height. *21st International Coastal Engineering Conference, Amer. Soc. Civil Eng.*, pages 899–913, 1988.

- [22] P.S. Eagleson and R.G. Dean. Wave-induced motion of bottom sediment particles. *Jour. Hydraulics Div., Am. Soc. Civil Engrs*, 85(HY10):11–50, 1959.
- [23] S. Corsini, L. Franco, R. Inghilesi, and R. Piscopia. Atlante delle onde nei mari italiani. page 152, 2006.
- [24] U. Putrevu and I.A. Svendsen. Three-dimensional dispersion of momentum in wave-induced nearshore currents. *Eur. J. Mech. B/Fluids*, pages 83–101, 1999.
- [25] I.A. Svendsen and U. Putrevu. Nearshore mixing and dispersion. *Proc. Roy. Soc. Lond. A*, 445:561–576, 1994.
- [26] K.A. Haas and I.A. Svendsen. Laboratory measurements of the vertical structure of rip currents. *J. Geophys. Res.*, 107(C5):30–47, 2002.
- [27] A.J. Raudkivi. *Loose Boundary Hydraulics*, 3rd ed. page 538, 1990.
- [28] E. Meyer-Peter and R. Müller. Formulas for Bed-Load Transport. *Report on Second Meeting of International Association for Hydraulic Research*, pages 39–64, 1948.
- [29] O.S. Madsen, L.D. Wright, J.D. Boon, and T.A. Chisholm. Wind stress, bed roughness, and sediment suspension on the inner shelf during an extreme storm event. *Cont. Shelf Res.*, 13(11):1303–1324, 1993.
- [30] O. S. Madsen. Spectral wave-current bottom boundary layer flows. *Coastal Engineering, Proceedings, 24th International Conference, Coastal Engineering Research Council/ASCE*, page 384–398, 1994.
- [31] M. Stuiver and P.J.Reimer. Extended 14C data base and revised CALIB 3.0 14C age calibration program. *Radiocarbon*, 35:215–230, 1993.
- [32] M.J. Ingram, D.J. Underhill, and T.M.L. Wigley. Historical climatology. *Nature, Climatology Supplement*, 276:329–334, 1978.
- [33] R.S. Bradley and P.D. Jones. “Little Ice Age” summer temperature variations: their nature and relevance to recent global warming trends. *The Holocene*, 3:367–376, 1993.
- [34] H.H. Lamb. Climatic variations and changes in the wind and ocean circulation: the Little Ice Age in the Northeast Atlantic. *Quat. Res.*, 11:1–20, 1979.
- [35] S. Dawson, D.E. Smith, J. Jordan, and A.G. Dawson. Late Holocene coastal sand movements in the Outer Hebrides, N.W. Scotland. *Marine Geology*, 210:281–306, 2004.

Near Real Time Oil Spill Detection and Monitoring Using AVHRR Thermal Infrared Data

C.S.L. Grimaldi¹, D. Casciello², I. Coviello¹, T. Lacava¹, N. Pergola¹, V. Tramutoli³

1, Institute of Methodologies for Environmental Analysis, CNR, Potenza, Italy

2, ARPA Environmental Agency of Lombardia, U.O.Territorio ed Attività Produttive, Milano, Italy

3, Department of Environmental Engineering and Physics, University of Basilicata, Potenza, Italy

grimaldi@imaa.cnr.it

Abstract

Timely detection and continuously updated information are fundamental in reducing the ecological impact of the different sources of sea pollution. Data acquired by sensors aboard meteorological satellites, thanks to their high temporal resolution as well as to their delivery policy, can be profitably used for a near real time sea monitoring, provided that robust methodologies are implemented.

Recently, a new methodology for oil spill detection and monitoring, based on the general Robust Satellite Technique (RST) approach, has been proposed. This technique has shown, by using AVHRR Thermal Infrared (TIR) data, a good capability in automatically detecting, with high level of reliability, oil spill presence.

Achievements obtained by applying such a technique for the analysis of the spill occurred during the "Gulf War" off Kuwait and Saudi Arabia coasts in January 1991 will be shown in this paper. The results obtained by the proposed methodology will be discussed and analyzed also by comparison with those obtained by another AVHRR approach. Moreover RST exportability on different geographic areas as well as satellite systems (EOS/MODIS) will also be discussed. Obtained results seem to confirm the reliability of the proposed approach which promises to offer new economically sustainable opportunities for building a near real-time monitoring system for oil spill at global scale.

1 Introduction

Oil spills are one of the most dangerous sources of sea pollution. The main contribution to this kind of technological hazard comes from operational discharge from tankers (i.e. oil dumped during cleaning operations) representing 45% of total hydrocarbons marine pollution [1]. Satellite remote sensing might actually contribute

to mitigate oil spill environmental impact, provided that reliable and effective detection techniques are developed, and relevant information and products are timely delivered and shared.

Nowadays, the most preferred instruments for satellite oil spill detection are SAR (Synthetic Aperture Radar) sensors [2, 3, 4, 5], mainly thanks to their all-weather and all-day capabilities [6, 7], as well as to their

high spatial resolution. They are able to discriminate oil from clean water because oil presence dampens sea surface capillary waves that are the main cause of backscattering of microwave radiation originated by SAR systems. Hence, oil film can be detected as a dark spot in the bright image of the ocean collected by SARs. However, reliability in oil spill detection is limited by the presence of natural films or rain cells producing an oil spill similar signal (*look-alikes*) and by the influence of wind speed. Low wind, in fact, will not produce a sea surface roughness sufficient to make perceptible the oil/water contrast while very high speed wind will increase water roughness and corresponding scattered signal independently from oil spill presence: in detail, a wind speed between 1.5m/s and 6m/s is required for a reliable oil spill identification by SAR [6]. Moreover, the actual operational use of SAR sensors for a timely detection of oil spill at global scale is currently restricted by their revisit time (from several days to several weeks, depending on the latitude) and by their expensive costs. The present SAR revisit time limitation will be reduced when the dual COSMO-SkyMed mission will be fully deployed (expected for the 2010), and a SAR constellation of four satellites will guarantee a refresh time up to 12 hours [8]. Anyway, several open questions, regarding costs and effective global delivery policy of such data, still remain and might limit their full use in an operational context.

For the above mentioned reasons, passive optical sensors, on board meteorological satellites, may represent a suitable SAR alternative and an useful complement for oil spill detection and monitoring from space. Their high temporal resolution, in fact, (from several hours to a few minutes, depending on orbital and instrumental

characteristics of platforms/sensors) is adequate to monitor and mitigate, by a timely detection, oil spill hazard.

Reliable optical satellite techniques for an automatic oil spill detection in Infrared (IR) and Visible (VIS) spectral regions of the electromagnetic spectrum have been for long-time mostly missing. The ones up to now proposed are only able to localize the presence of an oil spill after an independent alert and often require the interactive intervention of an experienced operator [9, 10, 11, 12, 13, 14].

In particular, techniques working in the Middle (MIR) and Thermal (TIR) Infrared spectral regions [9, 10, 11] exploit oil and water different thermal inertia to detect oil spill. Oil thermal inertia, in fact, is lower than sea water one, so that oil polluted areas usually show higher brightness temperature in TIR images collected in daytime than sea water, the opposite during the night [6, 7]. Other techniques exploit the different reflectance of the two elements in the Visible and Near Infrared (NIR) regions [12, 13, 14]. The oil identification in this range is more difficult because of the not univocal oil spill spectral signature, that may change depending on several factors, as for example: sun/satellite geometry, sea surface roughness, oil thickness. As a consequence, in VIS and NIR bands oil spill often shows an ambiguous behaviour, appearing less or more reflecting than the sea water [15].

In latest times, an innovative technique, based on the general RST - Robust Satellite Techniques, [16, 17] - approach, originally named RAT - Robust AVHRR Technique - [18], has been proposed and applied [19, 20, 21, 22] to detect, automatically and timely, the presence of the oil spill over the sea, minimizing the "false-detections" possibly caused by spurious effects. TIR

data acquired by NOAA-AVHRR (National Oceanic and Atmospheric Administration - Advanced Very High Resolution Radiometer) in TIR channels 4 and 5 (respectively 10.3-11.3 μm and 11.4-12.4 μm) have been used. Thanks to its short revisit time (less than 6 hours, considering present NOAA satellites constellation), and low data acquisition cost, despite its relatively moderate spatial resolution (1.1 km at nadir), AVHRR data can be profitably used as far as a near real time oil spill monitoring and mitigation system is aimed at.

Achievements obtained by applying such a technique for the analysis of the spill occurred during the "Gulf War" off Kuwait and Saudi Arabia coasts in January 1991 will be shown in this paper. Results obtained by the proposed methodology will be discussed and analyzed also by comparison with those obtained by another AVHRR based approach. Besides, the possible advantages arising from the implementation of this techniques with data acquired by MODIS (Moderate Resolution Imaging Spectroradiometer) aboard the EOS (Earth Observing System) satellites, as well as by SEVIRI (Spinning Enhanced Visible and Infrared Imager) aboard MSG (Meteosat Second Generation) platform, will be also discussed.

2 Methodology

The RST approach exploits the analysis of long-term multi-temporal satellite records to obtain a former characterization of the measured signal, in terms of expected value and natural variability, providing then an identification of signal anomalies by an automatic, unsupervised change detection step. RST has already successfully found

application in other fields of environmental monitoring, like forest fires detection [23, 24, 25], flood mapping [26, 27, 28], monitoring of volcanic eruptions [29, 30, 31, 32, 33, 34], seismic areas [35, 36, 37, 38, 39, 40, 41, 42, 43], etc. Briefly, the technique is based on the computation, at pixel level, of the so-called Absolutely Local Index of Change of Environment (ALICE), defined as follows:

$$\otimes_V(r, t') = \frac{[V(r, t') - \mu_V(r)]}{\sigma_V(r)} \quad (1)$$

where μ_V and σ_V are, respectively, the temporal average and the standard deviation computed for the pixel centred at $r \equiv (x, y)$ coordinates, $V(r, t')$ is the satellite signal actually measured at the same pixel on the image at hand at the time $t = t'$. $\otimes_V(r, t')$ gives the excess of the current signal $V(r, t')$ compared with its historical mean value and weighted by its historical variability at each considered location. In general, the signal $V(r, t')$ is the measurement achieved in a single, specific spectral channel but it can also be a combination of different bands [18]. The robustness of this approach is intrinsic, because the higher is the variability $\sigma_V(r)$ of the signal, the harder will be to achieve high values of $\otimes_V(r, t')$ reducing, by this way, the problem of false alarms.

As above mentioned, thermal data may be useful for oil spill detection thanks to the thermal inertia contrast between oil and surrounding water. So that, the signal under investigation ($V(r, t')$) was the radiance measured in AVHRR TIR channels in which we expect to measure, in presence of spill, high values of the proposed indicator during daytime, the opposite during the night. To overcome possible limits related to year-to-year climatological changes and/or seasonal drifts,



Figure 1: “Gulf War” oil spill localization (WCMC, 1991).

oil spill detection was obtained by using the RETIRA (Robust Estimator of TIR Anomalies) index [36] where the measured signal $V(r, t')$ in Eq.1 is the difference $\Delta T_x(r, t') = T_x(r, t') - \langle T_x(t') \rangle$, between the current ($t = t$) signal value observed at location $r, T_x(r, t')$ and the spatial average $\langle T_x(t') \rangle$, computed in place, on the image at hand, considering only cloud-free pixels located over sea within the investigated area: with $x = 4, 5$ indicating the used AVHRR TIR channel (ch4 or ch5, respectively) [19, 20, 21]. Results obtained by using such an index:

$$\otimes_{\Delta T_x} = \frac{[\Delta T_x(r, t') - \mu_{\Delta T_x}(r)]}{\sigma_{\Delta T_x}(r)} \quad (2)$$

have shown its potential for a robust identification of oil spill presence.

3 Implementation

The accident which occurred during the “Gulf War” off Kuwait and Saudi Arabia coasts in January 1991, brought serious environmental damage to major portions of

the Middle East [44, 10]. The polluted area had an extension of 144 Km² south-east of Kuwait city (Figure 1). Because of cyclonic currents, the oil moved southward and began to accumulate on the North Coast of Saudi Arabia, endangering the fragile costal zones and mangrove forests and destroying wildlife habitats [44].

For the computation of the AVHRR reference fields, a historical data set of all AVHRR images available in a temporal range of ten years, from 1989 to 1999, covering the studied region, acquired during the same month (January) and in the same time range (10:30 - 11:30 GMT, LT = GMT + 3), have been processed. A Region Of Interest (ROI) of 512x512 pixels, centred at 32° LAT N, 52° LONG E, was extracted from each pass and re-projected in the same geographic projection. Thus, temporal average ($\mu_{\Delta T}(r)$) and standard deviation ($\sigma_{\Delta T}(r)$) were computed on this area, using the above constructed data-sets for AVHRR TIR channels 4 and 5.

By comparing each available (cloud free) AVHRR image of the studied event with

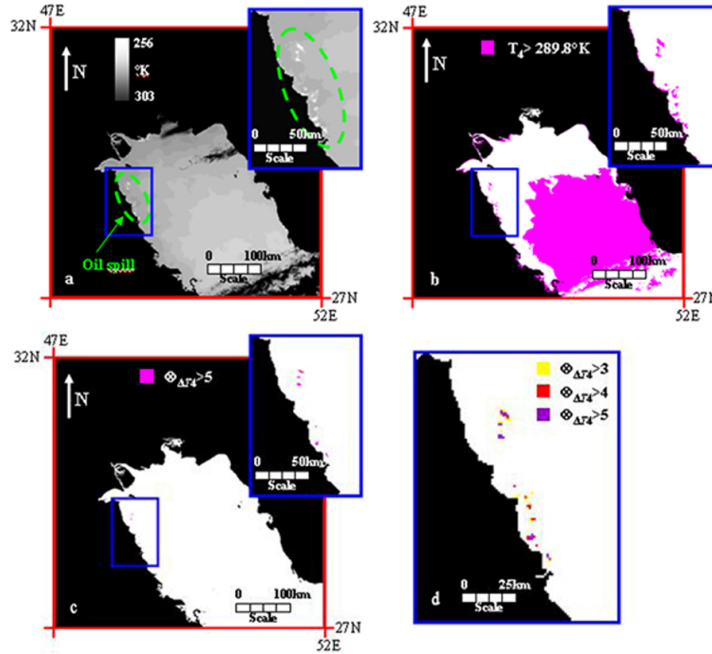


Figure 2: (a) AVHRR image (channel 4) of 24 January 1991 at 10.31 GMT (13.31 LT) in which oil spill area is highlighted by the green dotted circle. For this image a comparison between results achieved by Cross' technique (b) and RETIRA index (c), is shown. (d) Zoom of the area within the blue box where a detailed map of the oil spill structure is reported by exploiting different cutting levels of RETIRA index. Land is masked in black.

the relevant reference fields (at pixel level), the index defined by Eq. 2 have been computed and analysed.

Moreover, a comparison with results obtained by applying another, AVHRR-based, fixed threshold technique (i.e. Cross, 1992) has been carried out in order to better evaluate the improved reliability of the achieved results.

4 Results

In this section, RST results for the studied oil spill events are shown separately.

4.1 Persian Gulf oil spill event

RST achievements obtained analyzing Persian Gulf oil spill event are shown in Figures 2 and 3. In particular they are also compared with Cross' technique [9]. For the sake of brevity, only results obtained for two event images (i.e. 21 January at 10.31 GMT and 29 January at 11.24 GMT),

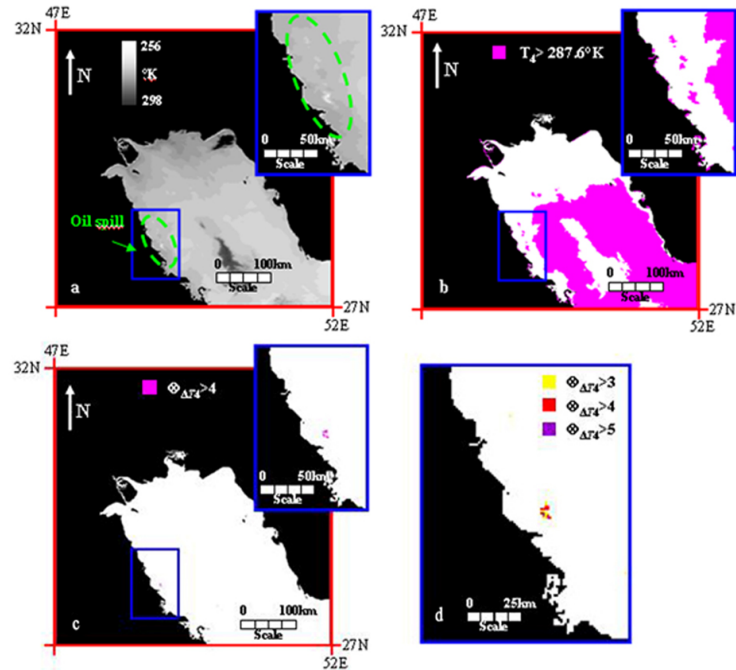


Figure 3: As Figure 2 for the AVHRR image of 29 January 1991 at 11.24 GMT (14.24 LT).

and only for AVHRR channel 4 are shown, as results achieved by using AVHRR channel 5 are very similar.

The analysis of these figures (where oil spill thickness and extension is described by anomalies of different relative intensities associated to different $\otimes_{\Delta T_x}$ values) confirms, first of all, that the oil spill had, as reported by the oil drift models achieved from in situ observations [45, 46], a southward motion along the Arabian coasts caused by the marine currents. Moreover, looking at Figure 2b and Figure 3b, it is possible to note the problems arising by using a fix threshold approach like the one proposed by Cross [9]: such a technique results ineffective in discriminating

oil spill areas because, besides polluted areas, large unaffected sea zones are also detected as polluted. This effect, mainly due to the normal thermodynamic of sea (thermocline, sea currents), reduces the reliability of such a technique. On the opposite, this problem does not affect the RST methodology: the impact of “site” effects are automatically reduced by the RST approach, which takes into account the “history” of each pixel of the scene. The proposed technique, in fact, detects oil spill presence only where polluted area have been independently documented by other sources [44, 45, 46], while no other pixels are identified as anomalous in the remaining part of the scene (which counts

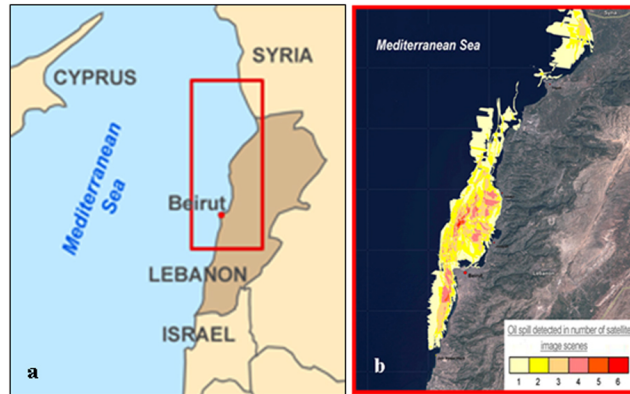


Figure 4: (a) Lebanon oil spill localization and (b) map of oil spill extent between 21 July and 10 August 2006 derived from several satellite images (IRS-P6, Spot-5, Envisat ASAR, Landsat -7 ETM, SRTM) and elaborated by DLR (DLR, 2006). Different colors (from light yellow to red) indicate the increasing number (from 1 to 6) of observations in which the respective area was covered by oil. Landsat archive scene was used as backdrop.

more than 80.000 sea pixels).

This indicates that the presence of oil spills is detected with a reliability of 100% over the full scene (i.e. no false alarms) by RST at high S/N levels ($\otimes_{\Delta T_4} > 5$ for the first image and > 4 for the second one). Such a signal to noise ratio means, in the RST context, that observed signal excess (i.e. $\Delta T_x(r, t') - \mu_{\Delta T_x}(r)$) is 5 (4) times higher (at least) than the historically observed local variability (i.e. $\sigma_{\Delta T_x}(r)$). Being the RETIRA index a standardized variable, values used for detection (i.e. 4 or 5) indicate the presence of signals with a very low probability of occurrence (i.e. statistically significant anomalies).

Another advantage of the RST approach is its potential use in a mapping phase. In fact, after a statistically based detection "for sure" (with no false alarms) at higher RETIRA values (at least ≥ 3 sigma), it is possible, zooming around the previous de-

tected anomalies, to use less selective index values (i.e. signal anomalies with lower intensities possibly associated to spills with different thickness/size and/or emulsion levels) for a better description of the size, shape and extent of the slick. In Figure 2d and Figure 3d, in fact, results obtained using RETIRA index $\otimes_{\Delta T_4}$ with different (lower) cutting levels are depicted in different colours. All the results confirm that the technique saves its detection capability also several days apart from the event, when the thermal contrast of polluted zones becomes less distinguishable due to the emulsion effect between oil and sea water and to the reduction of oil thickness (lower anomalies values in the image of 29 January are related to these phenomena). Moreover, although approximately one week has passed from the first release of oil into the sea, it should be noted that the total absence of false detections with

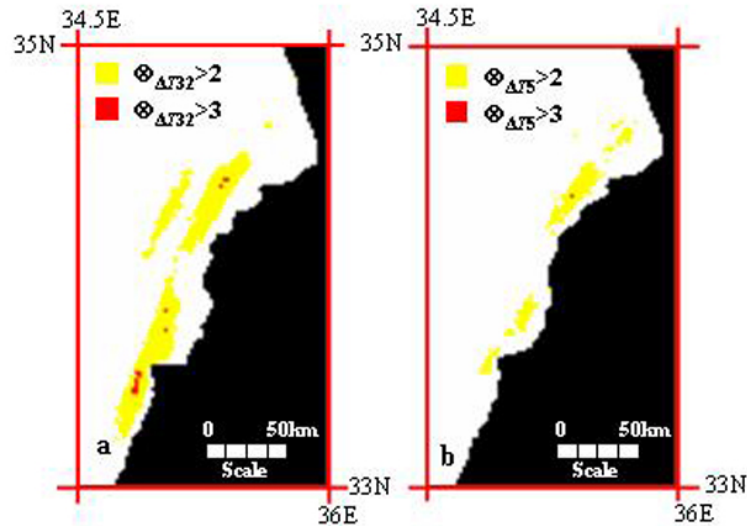


Figure 5: Oil spill mapping detected by RETIRA index on 28 July 2006 MODIS image at 10.30 GMT (a) and AVHRR image at 11.27 GMT (b). Land is masked in black.

RST is still confirmed.

The total independence of the RST technique from a specific satellite platform, allows for exporting it on different satellite systems. The proper application of such approach jointly to different satellite sensors aboard weather platforms will primarily benefit from an improved observational frequency. For example, the joint exploitation of both MODIS (Moderate Resolution Imaging Spectroradiometer) aboard EOS satellites, and AVHRR data allows for the opportunity to increase the observational frequency reducing the problem related to the cloud cover, that still represents the main limit of the proposed technique and, more in general, of all the methods using optical bands.

4.2 Lebanon oil spill event

In order to better assess and verify the reliability of the proposed approach and to also test RST exportability, another oil spill event, occurred in a different geographic area and temporal period, has been analyzed. To this aim, preliminary results obtained examining the oil spill event occurred during the “Lebanon War” in July 2006 are reported. In detail, on 13 and 15 July 2006, the oil-fuelled power plant of Jiyeh, located directly on the coastline, approximately 30 km south of Beirut, was hit by bombs. Part of the storage tanks caught fire and were burning for several days. Approximately 30,000 tons of heavy fuel oil was spilled into the Mediterranean Sea as a result of the blast [47] (Figure 4). Once computed the adequate reference fields for the month of July for both the sensors, following all the RST prescrip-

tions, a MODIS image of 28 July 2006, acquired at 10.30 GMT and an AVHRR scene acquired for the same day at 11.27 GMT have been studied. For completeness, results achieved by using longer wavelength channels (i.e. AVHRR channel 5 at 11.4–12.4 μm and MODIS channel 32 at 11.77–12.27 μm) will be shown.

In Figure 5, the structure of the detected oil spill is shown. Note as anomalous pixels have been identified in both MODIS (Figure 5a) and AVHRR images (Figure 5b) along the Lebanon coasts with similar distribution and extent. Moreover, the position and distribution of detected areas are in agreement with oil spill information reported by in situ observations (Figure 4) as well as with those reporting an oil spill drift toward North [47]. It is also possible to observe as the presence of oil spill is detected by RST, also in this case, with a reliability of 100% over the full scene (no false alarms) at a good S/N level ($\otimes_{\Delta T_5} > 3$ and $\otimes_{\Delta T_{32}} > 3$). The slight difference between the two maps is justifiable by the different view angles of the two sensors. In particular, over the investigated region, satellite zenith angles are significantly higher for AVHRR (44deg) than for MODIS (27deg), this makes: i) ground resolution cell size larger for AVHRR (about the double of the MODIS one), so that the signal coming from the same oil spill is spread over a wider area in the case of AVHRR, ii) atmospheric extinction more effective for AVHRR than MODIS, due to the different air masses crossed by the TIR signal [22]. Finally, the different acquisition times between two passes (about 1 hour apart) might have produced a further residual effect.

This study further confirms that the RETIRA index is intrinsically independent, for construction, on the observa-

tional/environmental conditions, because it is derived, at pixel level, on the base of the historical time series of homogeneous imagery. This circumstance, allows for a general application of this method at global scale, as seasonal and “site” effects are both taken into account by computation of historical values of the signal under investigation. This consideration is also supported by the results already obtained in previous works [19, 20, 21, 22], where test cases, characterized by different observing and natural conditions, were analyzed. Also for these events, in fact, same values of RETIRA index have been used to obtain similar results.

Although, as before mentioned, oil spill presence is always detected at statistically significant RETIRA values, the relative intensity of the anomalies may depend, as also this study demonstrates, on the specific characteristics of the spill (e.g. size, thickness, emulsion, etc.). However, a possible operational strategy may be designed for a fully automated implementation of the proposed methodology: looking first for pixel having very high RETIRA values (e.g. starting from the highest value on the scene) and then progressively lowering thresholds (up to RETIRA ≥ 3) as far as a “sure” detection occurs. A possible step forward is the possibility to exploit the better spatial resolution offered by MODIS VIS data (250m) for a more detailed mapping of the previously detected TIR anomalies.

A potential residual reliability problem that might affect the proposed approach could be related to the presence of ocean currents (warm currents in day-time or cold currents in night-time), which could produce an oil spill similar signal (i.e. look-alike). However, in our experience, these circumstances are very rare because, in order to be detected by RETIRA index, these

events have to be characterized by specific properties. In particular, they should be: i) occasional and sporadic events, having not specific seasonal/monthly periodicity or recurrence in the space-time domain because, if not, the proposed technique would recognize them as "normal" and not anomalous features, ii) particularly intense, in terms of thermal contrast, to produce a statistically significant (at least 3 sigma) deviation from the expected value measured in unperturbed conditions. Probably for these circumstances, in the cases so far analyzed, possible look-alikes of this nature have never caused false alarms.

5 Conclusions

In this paper, the timely detection and monitoring of oil spills by means of passive satellite sensors was treated. For this purpose, a technique, based on the general RST approach, is presented and discussed. The proposed method was able to detect, with high reliability, the polluted areas in different observational and environmental conditions. The detection was automatically performed (necessary condition for real-time application within an operational scenario) generating oil spill maps within minutes after acquisition time, and it was carried out using sole satellite data. Moreover, compared with traditional fix threshold techniques, RST approach has demonstrated to be fully unaffected (i.e. false alarm rate equal to zero) by local sea temperature dynamics. Additionally, the proposed technique is able to save oil spill detection capability also in the subsequent days of the event, when the increasing of emulsion effects may generally limit the efficiency of satellite-based detection schemes. This enhanced, once more, the

importance of using satellite data, especially those acquired from meteorological satellites which, despite their low-medium spatial resolution, may assure (in absence of cloud cover) high observational frequency.

Similar results have been obtained using both AVHRR and MODIS data independently, confirming RST exportability and reliability regardless of the used satellite system. For both sensors, in fact, RST detected oil spill presence with a reliability of 100% over the full scene (no false alarms) at good S/N levels and with a completely automated scheme. The investigation of RETIRA index at lower relative intensities allowed us to better map oil spills structure and extent achieving, also in this case, a good agreement of the two independent sensors.

The full integration of MODIS and AVHRR sensors will allow for more frequent observations (up to 3 hours starting from sensors having a maximum revisit time of 9 and 6 hours, respectively) of oil spill risk affected areas, increasing the sample rate of free clouds acquisitions.

In this context, SEVIRI (Spinning Enhanced and Visible Infrared Imager) on board MSG (Meteosat Second Generation), having 12 spectral channels (6 of them similar to AVHRR) and an observational frequency of 96 images per day, could guarantee an excellent opportunity. In fact, geostationary platforms can assure a reduction of observational noise (same view-angle, natural co-location of images, etc.), a timely detection and an effective continuous monitoring of oil spills. Results obtained so far encourage to investigate the possible implementation of the RST approach on MSG-SEVIRI because, despite the coarse spatial resolution of geostationary platforms (3-4 km), the very high

signal-to-noise ratios found for spilled areas by polar platforms will be further enhanced by the very low observational noise of geostationary platform making detection possible reliable and effective.

Finally, a synergic system, combining both the high spatial resolution information ensured by SAR (for detailed mapping of spill areas) and the high temporal resolu-

tion guaranteed by optical sensors aboard weather satellites (for timely detection), could represent an actually effective tool to manage oil spill hazard in near real time. Some efforts in this direction are in progress, in the framework of specific initiatives and research projects (e.g. ASI-PRIMI project) but present results still require a full validation and assessment.

References

- [1] ESA (European Space Agency). Oil pollution monitoring. 2004.
- [2] C. Brekke and A.H.S Solberg. Review on Oil spill detection by satellite remote sensing. *Remote Sensing of Environment*, (95):1–13, 2005.
- [3] A. Kostianoy, K. Litovchenko, O. Lavrova, M. Mityagina, T. Bocharova, S. Lebedev, S. Stanichny, D. Soloviev, A. Sirota, and O. Pichuzhkina. Operational Satellite Monitorino of Oil Spill Pollution in the Southeastern Baltic Sea: 18 Months Experience. *Environmental research, engineering and management*, 4(38):70–77, 2006.
- [4] G. Ferraro, A. Bernardini, M. David, S. Meyer-Roux, O. Muellenhoff, M. Perkovic, D. Tarchi, and K. Topouzelis. Towards an operational use of space imagery for oil pollution monitoring in the Mediterranean basin: A demonstration in the Adriatic Sea. *Marine pollution Bulletin*, (54):403–422, 2007.
- [5] M.N. Jha, J. Levy, and Y. Gao. Advances in Remote Sensing for Oil Spill Disaster Management: State-of-the-Art Sensor Technology for Oil spill Surveillance. *Sensors*, (8):236–255, 2008.
- [6] M.F. Fingas and C.E. Brown. Remote sensing of oil spills. *Sea Technology*, (38):37–46, 1997.
- [7] M.F. Fingas and C.E. Brown. A review of the status of advanced technologies for the detection of oil in and with ice. *Spill Science & Technology Bulletin*, (6):295–302, 2000.
- [8] ASI (Italian Space Agency). COSMO-SkyMed System Description & User Guide. 2007.
- [9] A.M. Cross. Monitoring marine oil pollution using AVHRR data: observation off coast of Kuwait and Saudi Arabia during January 1991. *International Journal of Remote Sensing*, (13):781–788, 1992.
- [10] W.Y. Tseng. Oil spill detection from NOAA-AVHRR imagery. *International Journal of Remote Sensing*, 16(18):3481–3482, 1995.

- [11] G. Borzelli, C. Ulivieri, A. Ciappa, G. Antonelli, and G. Laneve. A new perspective on oil slick detection from space by NOAA satellites. *International Journal of Remote Sensing*, (17):1279–1292, 1996.
- [12] C. Hu, F.E. Müller-Krager, C.J. Taylor, D. Myhre, B. Murch, and A.L. Odriozola. MODIS detects oil spills in Lake Maracaibo, Venezuela. *EOS, Transactions, American Geophysical Union*, 33(84):313–319, 2003.
- [13] F.M. Howari. Investigation of hydrocarbon pollution in the vicinity of United Arab Emirates coasts using visible and near infrared remote sensing data. *Journal of Coastal Research*, 4(20):1089–1095, 2004.
- [14] L. Shi, X. Zhang, G. Seielstand, C. Zhao, and M. He. Oil spill detection by MODIS images using Fuzzy Cluster and Texture Feature Extraction. *IEEE Oceans 07*, 2007.
- [15] Z. Otremba and J. Piskozub. Modelling of the optical contrast of an oil film on a sea surface. *Optics Express*, 9(8):411–416, 2001.
- [16] V. Tramutoli, V. Cuomo, C. Filizzola, N. Pergola, and C. Pietrapertosa. Assessing the potential of thermal infrared satellite surveys for monitoring seismically active areas: The case of Kocaeli (I'zmit) earthquake, August 17, 1999. *Remote Sensing of Environment*, (96):409–426, 2005.
- [17] V. Tramutoli. Robust Satellite Techniques (RST) for Natural and Environmental Hazards Monitoring and Mitigation: Theory and Applications. *Proceedings of Multitemp 2007*, DOI: 10.1109/MULTITEMP.2007.4293057, 2007.
- [18] V. Tramutoli. Robust AVHRR Techniques (RAT) for Environmental Monitoring: theory and applications. In *Earth Surface Remote Sensing II, Proceedings of SPIE*, 3496:101–113, 1998.
- [19] D. Casciello, C.S.L. Grimaldi, I. Coviello, T. Lacava, N. Pergola, and V. Tramutoli. A Robust Satellite Techniques for oil spill detection and monitoring in the optical range. In *Global Monitoring for Security and Stability (GMOSS), JRC Scientific and Technical Reports*, pages 294–305, 2007.
- [20] D. Casciello, T. Lacava, N. Pergola, and V. Tramutoli. Robust Satellite Techniques (RST) for Oil Spill Detection and Monitoring. *Proceedings of MultiTemp 2007*, DOI 10.1109/MULTITEMP.2007.4293040, 2007.
- [21] D. Casciello, T. Lacava, N. Pergola, and V. Tramutoli. Robust Satellite Techniques (RST) for oil spill detection and monitoring using AVHRR Thermal Infrared bands. *International Journal of Remote Sensing (in press)*, 2010.
- [22] C.S.L. Grimaldi, I. Coviello, T. Lacava, N. Pergola, and V. Tramutoli. Near real time oil spill detection and monitoring using satellite optical data. *Proceedings of IGARSS 2009, 13-17 July 2009, Cape Town, South Africa*, DOI: 10.1109/IGARSS.2009.5417590, 4:709–712, 2009.

- [23] V. Cuomo, R. Lasaponara, and V. Tramutoli. Evaluation of a new satellite-based method for forest fire detection. *International Journal of Remote Sensing*, (22):1799–1826, 2001.
- [24] G. Mazzeo, F. Marchese, C. Filizzola, N. Pergola, and V. Tramutoli. A Multi-temporal Robust Satellite Technique (RST) for forest fire detection. *Proceedings of Multitemp 2007, Digital Object Identifier 10.1109/MULTITEMP.2007*, 2007.
- [25] G. Baldassarre, G. Benigno, R. Corrado, I. Coviello, C. Filizzola, T. Lacava, F. Marchese, G. Mazzeo, R. Paciello, N. Pergola, F. Sannazzaro, S. Serio, , and V. Tramutoli. Assessment of the Robust Satellite Technique (RST) in real time detection of summer fires. *Proceedings of Multitemp 2009, Fifth International Workshop on the Analysis of Multitemporal Remote Sensing Images, 28-30 July, Mystic, Connecticut, USA*, pages 216–223, 2009.
- [26] T. Lacava, V. Cuomo, E. Di Leo, N. Pergola, F. Romano, and V. Tramutoli. Improving Soil Wetness Variations Monitoring From Passive Microwave Satellite Data: The Case Of April 2000 Hungary Flood. *Remote Sensing of Environment*, 96(2):135–148, 2005.
- [27] T. Lacava, E.V. Di Leo, N. Pergola, and V. Tramutoli. Space-time soil wetness monitoring by a multi-temporal microwave satellite records analysis. *Physics and Chemistry of the Earth*, (31):1274–1283, 2006.
- [28] T. Lacava, N. Pergola, F. Sannazzaro, and V. Tramutoli. Improving flood monitoring by RAT (Robust AVHRR Technique) approach: the case of April 2000 Hungary flood. *International Journal of Remote Sensing*, DOI: 10.1080/01431160902942902, 31(8):2043 – 2046, 2010.
- [29] N. Pergola, V. Tramutoli, T. Lacava, and C. Pietrapertosa. Robust satellite techniques for monitoring volcanic eruptions. *Annals of Geophysics*, (45):167–177, 2001.
- [30] N. Pergola, V. Tramutoli, and F. Marchese. Automated detection of thermal features of active volcanoes by means of Infrared AVHRR records. *Remote Sensing of Environment*, (93):311–327, 2004.
- [31] N. Pergola, V. Tramutoli, I. Scaffidi, T. Lacava, and F. Marchese. Improving volcanic ash clouds detection by a robust satellite technique. *Remote Sensing of Environment*, (90):1–22, 2004.
- [32] N. Pergola, G. D’Angelo, M. Lisi, F. Marchese, G. Mazzeo, and V. Tramutoli. Time domain analysis of robust satellite techniques (RST) for near real-time monitoring of active volcanoes and thermal precursor identification. *Physics and Chemistry of the Earth*, 34(6-7):380–385, 2009.

- [33] A. Bonfiglio, M. Macchiato, N. Pergola, C. Pietrapertosa, and V. Tramutoli. AVHRR Automated detection of volcanic clouds. *International Journal of Remote Sensing*, 26(1):9–27, 2005.
- [34] C. Filizzola, T. Lacava, F. Marchese, N. Pergola, I. Scaffidi, and V. Tramutoli. Assessing RAT (Robust AVHRR Techniques) performances for volcanic ash cloud detection and monitoring in near realtime: The 2002 eruption of Mt. Etna (Italy). *Remote Sensing Environment*, (107):440–454, 2007.
- [35] V. Tramutoli, G. Di Bello, N. Pergola, and S. Piscitelli. Robust satellite techniques for remote sensing of seismically active areas. *Annals of Geophysics*, 44(2):295–312, 2001.
- [36] V. Tramutoli. Robust Satellites Techniques (RST) for natural and environmental hazards monitoring and mitigation: ten years and applications. *The 9th International Symposium on Physical Measurements and Signatures in Remote Sensing, Beijing (China)*, 36:792–795, 2005.
- [37] G. Di Bello, C. Filizzola, T. Lacava, F. Marchese, N. Pergola, C. Pietrapertosa, S. Piscitelli, I. Scaffidi, and V. Tramutoli. Robust Satellite Techniques for Volcanic and Seismic Hazards Monitoring. *Annals of Geophysics*, (47):49–64, 2004.
- [38] C. Filizzola, N. Pergola, C. Pietrapertosa, and V. Tramutoli. Robust satellite techniques for seismically active areas monitoring: a sensitivity analysis on September 7, 1999 Athens’s earthquake. *Physics And Chemistry Of The Earth*, (29):517–527, 2004.
- [39] R. Corrado, R. Caputo, C. Filizzola, N. Pergola, C. Pietrapertosa, and V. Tramutoli. Seismically active area monitoring by robust TIR satellite techniques: a sensitivity analysis on low magnitude earthquakes in Greece and Turkey. *Natural Hazards and Earth System Sciences*, (5):101–108, 2005.
- [40] N. Genzano, C. Aliano, C. Filizzola, N. Pergola, and V. Tramutoli. A robust satellite technique for monitoring seismically active areas: The case of Bhuj-Gujarat earthquake. *Tectonophysics*, (431):197–210, 2007.
- [41] N. Genzano, C. Aliano, R. Corrado, C. Filizzola, M. Lisi, G. Mazzeo, R. Paciello, N. Pergola, and V. Tramutoli. RST analysis of MSG-SEVIRI TIR radiances at the time of the Abruzzo 6 April 2009 earthquake. *Natural Hazards and Earth System Sciences*, 9:2073–2084, 2009.
- [42] C. Aliano, R. Corrado, C. Filizzola, N. Pergola, and V. Tramutoli. Robust satellite techniques (RST) for the thermal monitoring of earthquake prone areas: the case of Umbria-Marche October, 1997 seismic events. *Annals of Geophysics*, (51):451–459, 2008.

- [43] C. Aliano, R. Corrado, C. Filizzola, N. Genzano, N. Pergola, and V. Tramutoli. TIR Satellite Techniques for monitoring Earthquake active regions: limits, main achievements and perspectives. *Annals of Geophysics*, (51):303–317, 2008.
- [44] WCMC (World Conservation Monitoring Centre). Gulf war environmental information service: impact on the marine environment. 1991.
- [45] P. Daniel and J. Potevin. A numerical study of movements of an oil slick on the sea surface in the Persian Gulf from 25 January 1991 to 1 February 1991. *Proceedings of the First Thematic Conference on Remote Sensing for Marine and Coastal Environments, ERIM*, pages 249–260, 1992.
- [46] R. Proctor, R.A. Flather, and A.J. Elliott. Modelling tides and surface drift in the Arabian Gulf application to the Gulf oil spill. *Continental Shelf Research*, 14(5):531–545, 1994.
- [47] UNEP (United Nations Environment Programme). Environmental Update No. 01-Lebanon Crisis -27 July 2006. 2006.

Tsunami Early Warning System: Deep Sea Measurements in the Source Area

L. Pignagnoli¹, F. Chieric^{1,2}, P. Favali³, L. Beranzoli³, D. Embriaco⁴, S. Monna³, F. D'Oriano^{1,5}, N. Zitellini¹

1, Institute of Marine Sciences, CNR, Bologna, Italy

2, IRA-INAF, BO (affiliazione non presente, segnalare)

3, National Institute of Geophysics and Volcanology, Roma, Italy

4, National Institute of Geophysics and Volcanology, Portovenere (SP), Italy

5, Department of Geo-Environmental and Earth Sciences, University of Bologna, Bologna, Italy

luca.pignagnoli@bo.ismar.cnr.it

Abstract

In the framework of the EU project NEAREST, a new Tsunami Early Warning System (TEWS), able to operate in tsunami generation areas, was developed and installed in the Gulf of Cadiz. The TEWS is based on the abyssal station GEOSTAR, placed above a major tsunamigenic structure, and on three seismic centres of Portugal, Spain and Morocco. The core of the system is a tsunami detector installed onboard of GEOSTAR. The tsunami detector communicates with a surface buoy through a dual acoustic link. The buoy is connected to land stations via satellite link. The system was designed for near-field conditions and successfully operated from August 2007 to August 2008, 100 km SW of Cabo de Sao Vicente (Portugal). A new mission started on November 11th, 2009 in the same location. The tsunami detection is based either on pressure events either on seismic events. The bottom pressure data are analysed in real-time at the seafloor by a new tsunami detection algorithm, which can recognize tsunami waves as small as one centimetre. At the same time it was developed a new theoretical approach to account for tsunami generation in compressible water and in presence of a porous sediment. This model showed that hydro-acoustic waves, travelling much faster than the tsunami, are caused by the seafloor motion. These waves can propagate outside the generation area and are characterised by a modulation carrying valuable information on the seafloor motion, which can be recovered from their first arrival.

1 Introduction

Tsunami waves are dangerous and potentially destructive waves generated by different mechanisms, as submarine earthquakes, sub-aerial and submarine landslides, volcanic eruptions, meteorite impacts or moving barometric variation.

Among these mechanisms, the most common is due to earthquake as reported by the catalogues [1, 2, 3]. Tsunamis can travel long distances with low attenuation, at speed depending on water depth. The disastrous Sumatra event on December 26th, 2004 [4] and the event of Samoa Islands on September 29th, 2009 are recent examples

of the tsunami threat. As a consequence of those tragedies, the development of reliable Tsunami Early Warning System (TEWS) received a strong impulse both from scientific and civil institutions.

A TEWS is presently based on a seismic trigger and on the direct measurement of the anomalous wave in deep sea or, alternatively, on the observation of its effect in the vicinity of the shore. The current systems are based on bottom pressure recorder and seismic sensors network, as DART and DART II [5], DONET [6] and GITEWS [7]. The common feature of these TEWS is the presence of the pressure sensors, used to monitor the pressure perturbations at depth, including travelling tsunami waves [8]. In this case the tsunami signal has to be identified among other pressure perturbations, which can have greater amplitudes and that are caused by various effects as barometric pressure changes, wind waves, tides, boats travelling nearby the sensor location, sea floor acceleration due to seismic events, salinity and temperature variations, and marine currents. All these effects are considered as noise and have to be filtered out to obtain a detailed measurement of the tsunami wave.

When tsunami waves are generated by sources far from the coast these TEWS should operate with good results, but when the tsunamigenic sources are located near the coast they show strong limitations because of the very short time allowed to issue an effective warning. Unfortunately, the highly populated coasts of the Mediterranean are all characterized by a similar condition. To minimize the elapsed time between generation and identification of the tsunami wave, NEAREST project (<http://nearest.bo.ismar.cnr.it>) proposed to monitor directly the potential tsunamigenic structures. This poses the problem of the

tsunami wave detection in near field condition where, in addition to the effects mentioned above, the tsunami signal is masked by dynamics and kinematics effects induced by sea floor motion.

We choose the Gulf of Cadiz as a test region for the Tsunami Warning System able to operate in generation area, because this region is characterised by well confined potential tsunamigenic sources [8]. In the framework of NEAREST, a prototype of a new instrument, called "tsunameter", specifically designed to operate well in near-field conditions has been developed and installed above a major tsunamigenic structure, off the Gulf of Cadiz, at water depth of 3200m. The tsunameter is installed onboard the abyssal station GEOSTAR developed by INGV through previous EU funding. The station communicates with a surface buoy through a dual acoustic link: the buoy is connected to land stations via satellite link. This system operated from August 2007 to August 2008 offshore Cabo de Sao Vicente (Gulf of Cadiz) and a new mission started in the same region on November 2009. The need to better understand the tsunami generation process favoured the development of a new conceptual model taking into account water compressibility and the presence of porous seabed [9].

2 Tsunameter Components and Characteristics

The tsunameter is made by a set of devices, bottom pressure sensor, accelerometers, seismometer connected to a processing unit hosted onboard of GEOSTAR. The tsunameter is in charge of the data process-

ing and of the identification of the tsunami wave, if present. In addition, the tsunameter communicates in a two-way mode by mean of a surface buoy, through a dual acoustic link. The surface buoy is connected to control land stations thanks to a satellite dual link. Figure 1a shows the tsunameter communication scheme. The seafloor station is designed to operate in three different ways:

1. Mission mode: two periodic messages are sent to the surface buoy every 6 hours containing, respectively, the sensors status and sampled data.
2. Event mode: it is triggered by a seismic or pressure event, the data relevant for the warning purpose are sent to the surface buoy.
3. Idle mode: a power saving mode during which the station can be reconfigured and restarted.

The data acquired by the tsunameter are real-time processed at the sea-floor by dedicated algorithms and are cross-checked in order to send a tsunami warning message. In particular the tsunami detection procedure is based on a double check on both

pressure and seismic events. The seismic data are processed using a Short Term Average over Long Term Average (STA/LTA) algorithm. The bottom pressure data are analysed using the new tsunami detection algorithm developed within NEAREST and composed by a chain of different filters. Each filter can be included or excluded by the processing routine. The application of this filtering cascade to the bottom pressure time series reduces the dynamical range of the sea level perturbations, from about 1-3 meters of equivalent water to few centimetres, obtaining tsunami detection sensibility better than 1cm. Finally, the filtered bottom pressure data are matched against an appropriate tsunami amplitude threshold. Once exceeded a warning message is issued.

More details about the GEOSTAR abyssal station is given in Figure 2: inset a) shows a picture of the station with the upper module MODUS that guide the GEOSTAR during the deployment, while inset b) shows a scheme of the real time communication from sea floor to the land stations.

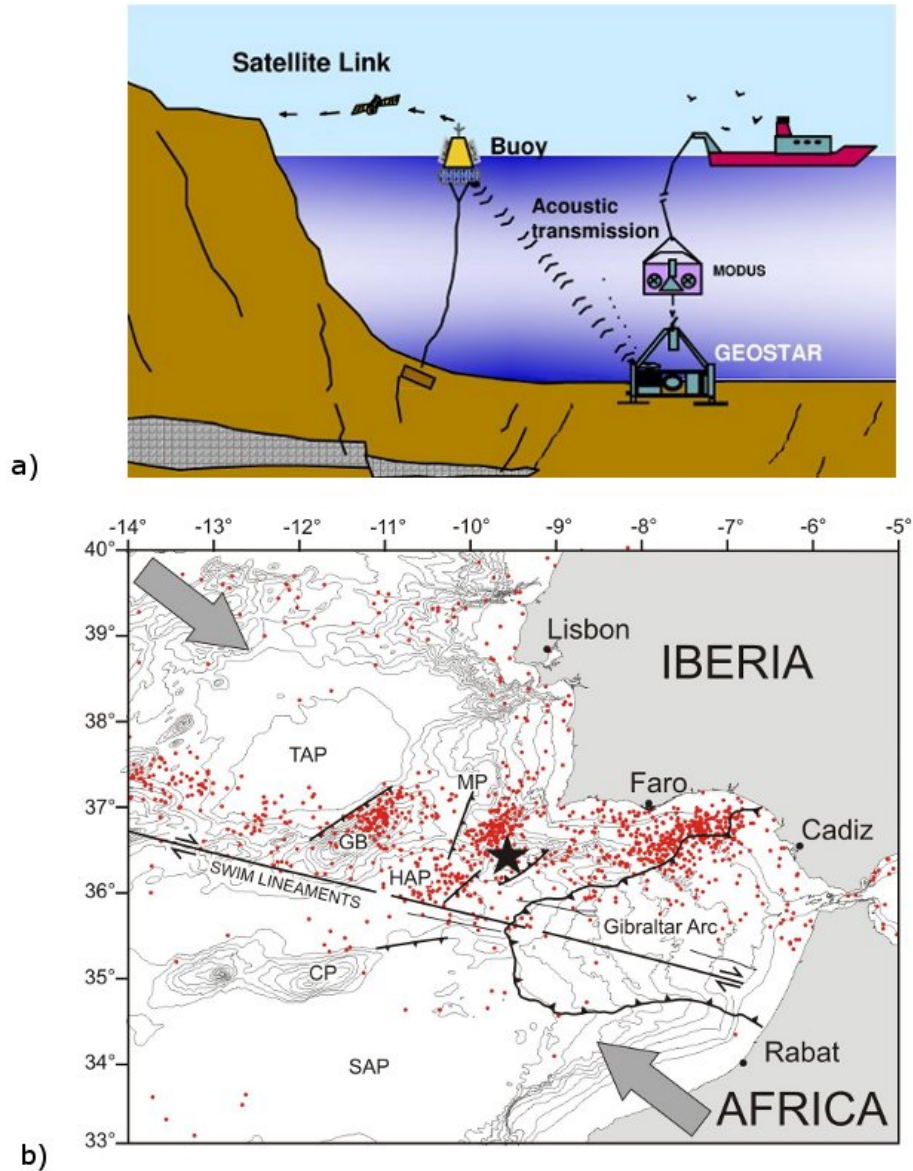
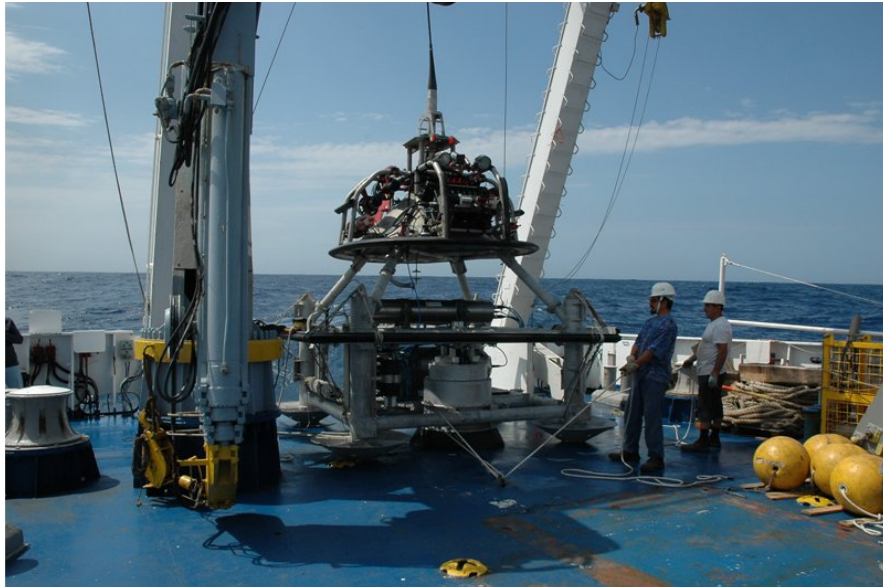
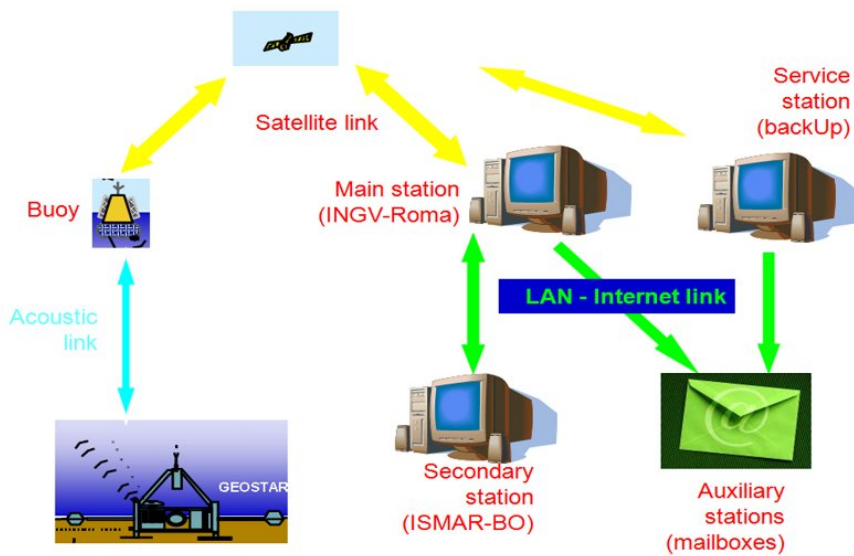


Figure 1: Inset a): Communication scheme of the tsunameter. Inset b): Gulf of Cadiz morpho-tectonic map. Contour line every 500m from GEBCO digital Atlas; Black star: GEOSTAR Location; Grey arrows: relative movement direction between Africa and Iberia plates; TAP: Tagus Abyssal Plain; HAP: Horseshoe Abyssal Plain; SAP: Seine Abyssal plain; GB: Gorringe Bank; MP: Marques de Pombal Structure; Swim Lineaments from [10] representing the probable modern plate boundary between Africa and Iberia; black line with triangles: major thrust fault present in the area.



a)

Near real time Communication scheme



b)

Figure 2: Inset a): Picture of GEOSTAR with the upper module MODUS. Inset b): Tsunameter real time communication scheme.

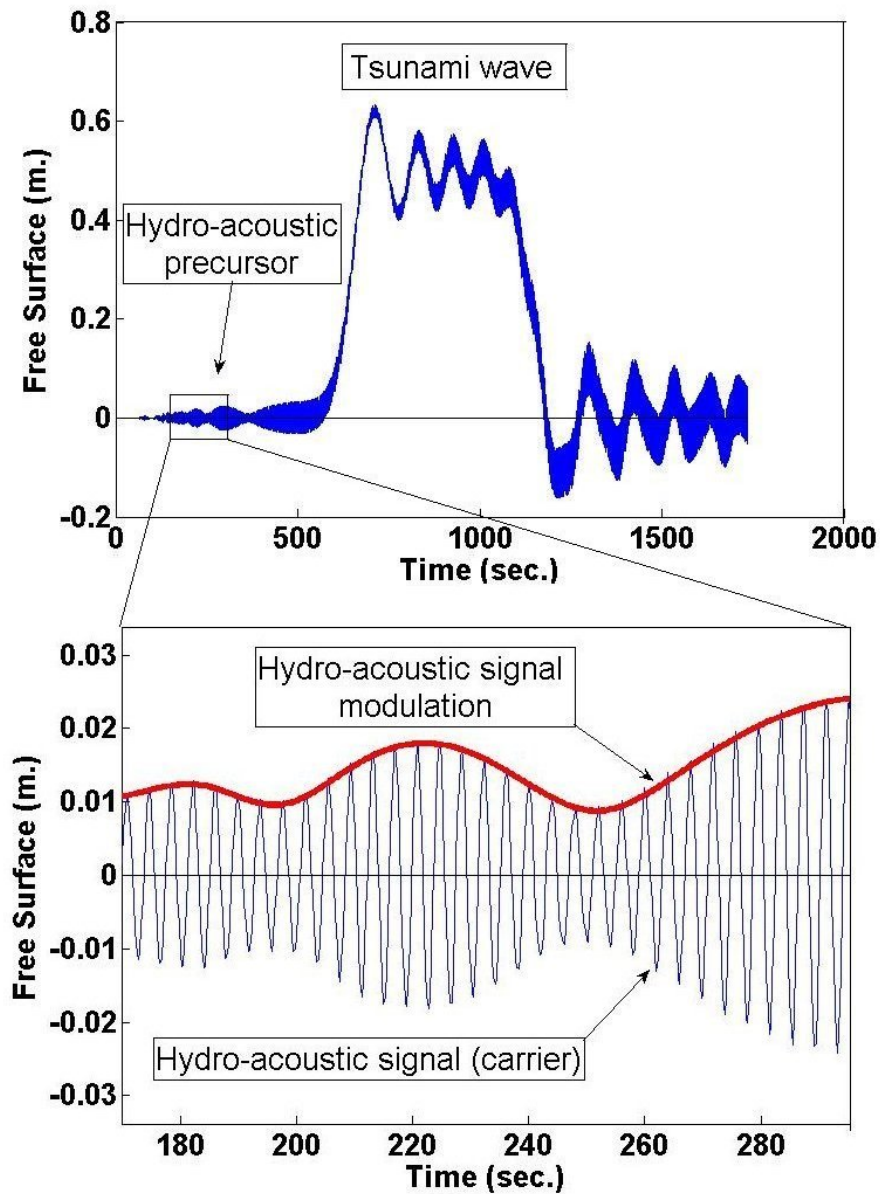


Figure 3: The upper inset represents the free-surface plots at fixed observation point located at 100 km from the source, while the lower inset is the zoom of the first part of the acoustic signal with its modulation.

3 NEAREST pilot experiment in the gulf of Cadiz

The SW Iberia is a tsunami prone area as testified by the 1755 Lisbon earthquake which caused a devastating tsunami affecting all the cities facing the Gulf of Cadiz and reaching the coasts of Great Britain and Caribbean islands. This region is situated at the Eastern end of the Atlantic Eurasia-Africa plate boundary with convergence rate of $4 \text{ mm}\cdot\text{y}^{-1}$ [11] and has seismic activity concentrated along a belt going from the Gibraltar Strait to the Azores. The geological structures of this area were studied and mapped in the framework of NEAREST and during the previous EU project BIGSETS and the ESF project SWIM. It is now well established that the main tsunamigenic tectonic sources are located between the long ESE-WNW strike-slip faults, the SWIM lineaments showed in Figure 1b [10] and the Iberian coastline. In the framework of NEAREST, a prototype of the tsunameter described in the previous paragraph was installed on-board of the multi-parametric observatory GEOSTAR and successfully deployed offshore Cabo de Sao Vicente. The station was placed above an active, potentially tsunamigenic structure, the Marques de Pombal Structure [12, 13] at a depth of 3200 m. on August 25th 2007. The system operated for one year. The bottom pressure signal was processed by the new tsunami detection algorithm.

Recently, on November 11th 2009, the abyssal station, with the tsunameter on-board, was deployed again in the same region where it is presently operating.

4 Future perspectives for hydro-acoustic precursor?

A challenging and very promising frontier for scientific research in the field of the Tsunami Early Warning is the "hunt" for a potential tsunami precursor. Starting from the pioneering work of Peltier and Hines [14] and passing through the work of Artru et al. [15] many attempts have been made to find the possible tsunami precursors induced in the atmosphere, while a first attempt to look for a hydro-acoustic precursor in the water column was made by Okal et al. [3], who proposed to use the T-waves for tsunami warning purpose. These waves are the high-frequency acoustic signal caused by the earthquake and channelled in the seawater by SOFAR wave guide.

More recently, Chierici et al. [9] developed a theoretical work concerning tsunami generation taking into account the water compressibility and the effect of a porous sea bed. They showed that modulated hydro-acoustic waves are generated in the water layer by the sea-floor motion. The presence of the porous sediment acts as a "natural" low pass filter and allows the hydro-acoustic waves to propagate up-slope and outside the generation area with low attenuation. The main and surprising feature of these waves is their modulation, which carries information on the seafloor motion and source parameters. The existence of these waves was firstly observed during the Tokachi-Oki 2003 event [16], when two pressure sensors, located within the generation area, detected an hydro-acoustic signal generated by the seafloor motion induced by the earthquake. The model of Chierici et al. correctly reproduces the

measured frequency and amplitude of the signal. These acoustic waves travel with speed at least seven time greater than the tsunami waves well preceding its arrival. Information about the source parameters, for instance the sea floor motion velocity, the source extension and the source displacement may be extracted from the very first pulses of the modulation. Thanks to these results the modulation of these acoustic waves may act as a “hydro-acoustic tsunami precursor” and could be integrated in a new generation of Tsunami Early Warning System. Figure 3 shows an example of this hydro-acoustic signal, obtained using the model developed by [9]. The upper inset represents the water surface disturbance for a fixed observation point at 100 km distance from the source. The lower inset shows the hydro-acoustic precursors and its modulation characterised by its pulses.

5 Conclusions

In the framework of EU project NEAREST, a new tsunameter designed to operate in a generation area was developed and installed off the Gulf of Cadiz, where successfully worked for one year. The system has been recently redeployed at the same site. The tsunameter is able to take into account the dynamical and kinematical effects due to the sea floor motion biasing the

tsunami signal measurements and identification.

A key role in the development of a future and more effective Tsunami Early Warning System designed for near-field conditions, could be played by potential tsunami precursors. On behalf of NEAREST project Chierici et al. found, in a theoretical work, that modulated waves, which are induced in the water column by the sea floor motion, might be regarded as “hydro-acoustic tsunami precursors”. These waves travel at speed much greater than the tsunami wave, propagating outside the generation area with low attenuation and carrying relevant information on the sea floor motion. The measurement and analysis, in a real ocean environment, of this hydro-acoustic signals is the needed step in order to validate the use of this acoustic signal for tsunami early warning purpose.

6 Acknowledgments

This work was supported by the Commission of the European Communities under contract 037110 - GOCE (NEAREST Project), under contract 036851 - GOCE (ESONET-NoE and ESONET-LiDO Demo Mission) and by the Italian MIUR (PRIN project 2007). A particular thanks to Dr. Rita Maria Riccioni for many helpful discussions and manuscript revision.

References

- [1] E. Boschi, E. Guidoboni, G. Ferrari, G. Valensise, and P. Gasperini. Catalogue of the strong earthquakes in Italy from 461 BC to 1990. 1997.
- [2] NGDC Tsunami Catalog. web site: <http://www.ngdc.noaa.gov/hazard/tsu.db.shtml>. 2009.

- [3] E.A. Okal, P.J. Alasset, O. Hyvernaud, and F. Schindele. The deficient T waves of tsunami earthquakes. *Geophys. J. Int.l*, 152(2):416–432, 2003.
- [4] C. Lomnitz and S. Nilsen-Hofseth. The indian ocean disaster: Tsunami physics and early warning dilemmas. *EOS Trans. AGU*, 86:65–70, 2005.
- [5] C. Meinig, S.E. Stalin, A.I. Nakamura, F. Gonzalez, , and H.G. Milburn. Technology Developments in Real-Time Tsunami Measuring, Monitoring and Forecasting. *In Oceans 2005 MTS/IEEE, September 2005, Washington, D.C.*, 2005.
- [6] K. Kawaguchi, K. Hirata, T. Nishida, S. Obana, and H. Mikada. A new approach for mobile and expandable real time deep seafloor observation -Adaptable Observation System. *IEEE Journal of Oceanic Engineering*, 27:182–192, 2002.
- [7] A. Rudloff, J. Lauterjung, U. Muench, and S. Tinti. Preface ”The GITEWS Project (German-Indonesian Tsunami Early Warning System)”. *Nat Haz. & Earth Sysst Sciences*, 9(4):1381–1382, 2009.
- [8] J.H. Filloux. Tsunami recorded on the open ocean floor. *J. Phys. Oceanogr.*, 13:783–796, 1982.
- [9] F. Chierici, L. Pignagnoli, , and D. Embriaco. Modeling of the hydroacoustic signal and tsunami wave generated by seafloor motion including a porous seabed. *J. Geophys. Res.*, 115:C03015, 2010.
- [10] N. Zitellini, E. Gràcia, L. Matias, P. Terrinha, M.A. Abreu, G. De Alteriis, J.P. Henriet, J.J. Dañobeitia, D.G. Masson, T. Mulder, R. Ramella, L. Somoza, and S. Diez. The Quest for the Africa-Eurasia plate boundary West of the Strait of Gibraltar. *EPSL*, 208:13–50, 2009.
- [11] C. DeMets, R.G. Gordon, D.F. Argus, and S. Stein. Effect of recent revisions to the geomagnetic reversal time scale on estimates of current plate motions. *Geophysical Research Letters*, 21:2191–2194, 1994.
- [12] N. Zitellini, L. A. Mendes, D. Cordoba, J. Danobeitia, R. Nicolich, G. Pellis, and al. Source of 1755 Lisbon earthquake and tsunami investigated. *EOS Trans. Am. Geophys. Union*, 82(26):285, 2001.
- [13] N. Zitellini, M. Rovere, P. Terrinha, F. Chierici, L. Matias, and Bigset Team. Neogene through Quaternary Tectonic reactivation of SW Iberian Passive Margin. *Pure Appl. Geophys.*, 161:565–585, 2004.
- [14] W.R. Peltier and C.O. Hines. On the possible detection of tsunamis by a monitoring of the ionosphere. *Journal of Geophysical Research*, 81:1995–2000, 1976.
- [15] J. Artru, V. Ducic, H. Kanamori, P. Lognonné, and M. Murakami. Ionospheric detection of gravity waves induced by tsunamis. *Geophy. J. Int*, 106:840–848, 2005.

- [16] M. Nosov, S. Kolesov, A. Denisova, A. Alekseev, and B. Levin. On the near-bottom pressure variations in the region of the 2003 Tokachi-Oki tsunami source. *Oceanology*, 47(1):26–32, 2007.

The Hindcast of Historical Storms in the Mediterranean Sea

L. Bertotti, L. Cavaleri
Institute of Marine Sciences, CNR, Venezia, Italy
luciana.bertotti@ismar.cnr.it

Abstract

The recent availability of an archive of the past meteorological data since 1957 and of highly sophisticated and powerful computers and numerical models allows to reconstruct with pretty good accuracy all the events of the last half a century. In this paper we focus, as examples, on two historical storms, namely a mistral one in the Western Mediterranean that almost sank a ship with 800 passengers on board, and the one in the Adriatic Sea associated to the event that led to the floods and destruction happened in Florence and Venice in particular, but more in general on the Central and North-Eastern Italy.

1 The potential at disposal

The present availability of large computer power and of sophisticated meteorological and wave forecast models, together with the archive of meteorological data, allows to reconstruct with optimal accuracy any event of the last half a century. The archive of meteo data, presently available at the European Centre for Medium-Range Weather Forecasts (ECMWF, Reading, U.K.) has been made possible thanks to the extensive project ERA-40 [1], aimed at a self-consistent reconstruction of the meteorological and wave situations after 1957. While the resolutions used for ERA-40, both meteorological and wave ones, are not sufficient for a reliable hindcast in enclosed seas, as it is the case of the Mediterranean Sea, the large archive built for the purpose offers the basic information to analyse with much higher resolution, practically the one presently available, any specific event of these 50+ years. The purpose of this paper is to provide two

examples of such a hindcast. In particular we focus on two storms, both noticeable for different reasons. The first one is a mistral storm in the Western Mediterranean that caused heavy damage to a large cruise ship, forcing it to send a rescue call and to stay for many hours in a very difficult situation. The second one is the historical storm that led to the flooding of Florence and Venice in 1966. Here we focus on its oceanographic aspect, and in particular on the wave and surge conditions present at the time on the Adriatic Sea.

2 The 2005 mistral storm in the Western Mediterranean

2.1 The fact

On February 14, 2005 the cruise ship “Voyager” en route from Tunis to Barcelona came across a severe Mistral storm. The

storm was from the northern sector, with a very intense and gusty wind, typical of the situation. Waves were then estimated at about ten metre significant wave height. From what derived from later reports, at a certain moment the ship was hit by one or more high waves that broke the windows of the control deck, well high above the floating line. The consequent flooding of the ship control system brought her to a halt, forcing the crew to send out a distress call. One of the reports about the call shows well the terrible conditions the ship was in: *“Battered by storm.*

A high wave smashing through the windows of the bridge and damaging electronics is thought to have caused the power cut. The distress call from the ship said it was taking on water and was in ‘terrible condition’, UK coastguards reported.

They received the message just after 0900 GMT on Monday, via the Gimi.

The French coastguards told the BBC that the ship was not on fire and not in danger of sinking.

Most of the passengers ...” After many hours the crew managed to restart one of the engines and she slowly made her way to the closest harbour in Sardinia.

2.2 Analysis of the storm

At the time ECMWF was using the operation T511 meteorological model, corresponding to about 40 km resolution. A direct inspection of the forecast fields clearly shows that the storm had been well forecast. However, due to the underestimate of the surface wind fields typical of the enclosed basins, also the derived significant wave heights H_s were as expected underestimated. See Cavaleri and Bertotti [2] for a thorough discussion on the subject. For a better analysis Bertotti and Cava-

leri ([3], henceforth referred to as BC1) analysed the storm with higher resolution. They carried out a series of short (12 hours) forecasts at T799 resolution (about 25 km) starting at 12 hour interval from the available analyses. Assembling all the forecasts together provided a uninterrupted sequence of higher resolution wind fields at three hour interval, suitable for the following wave evaluation. At this aim they used the WAM model [4] at 0.25 degree resolution. A second hindcast was done using the COAMPS winds, a high-resolution model used at the Fleet Numerical Meteorology and Oceanography Center (FNMOC, Monterey, California, USA). Figure 1 shows the hindcast wave conditions at 09 UTC of February 14 forced by the ECMWF wind fields. The ellipse indicate the area of the accident.

A good example of the quality of the hindcasts is given in Figure 2 where the modelled H_s along the marked cross section (ground track of the Jason-1 altimeter) are compared with the corresponding measured values. We note that more to the South the two hindcasts diverge (as specified, ECMWF somehow anticipated the storm), but all the results are consistent where our present interest is focused. During the model runs not only the integrated wave values, but also the full 2D spectra were saved in the area of interest to be later used for the extreme analysis.

2.3 Statistics

Some of the various reports from onboard the ship referred to waves up to 14 m high. A direct use of the standard Rayleigh distribution quickly shows that, given the local conditions, such wave height had to be quite common. In any case a 14 m high waves could not damage the ship at the

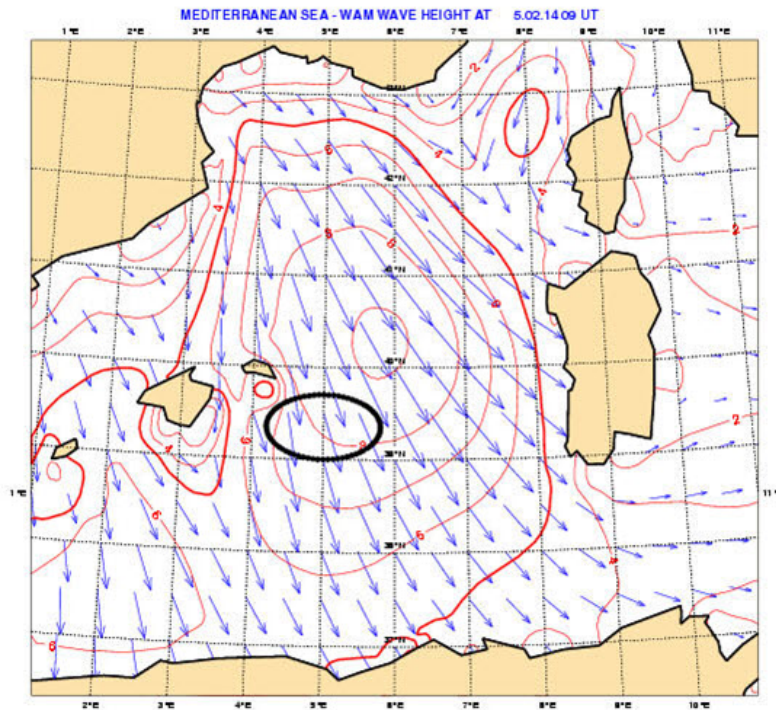


Figure 1: Wave field at 09 UTC 14 February 2005. The area is the Western Mediterranean Sea. Isolines at 1 m interval. Arrows show significant wave height and mean direction. The ellipse shows the approximate position of the cruiser "Voyager" at the time of the accident (after BC1). Calibrated ECMWF T799 wind fields have been used.

height where the control room is located. Bertotti and Cavaleri ([5], henceforth referred to as BC2) hypothesised that indeed it was a 14 m crest that hit the ship, and moved therefore to analyse the corresponding probability. At this aim, apart from the linear theory, they considered the Tayfun distribution [6]. The related results are shown in Table 1.

Focusing for the time being on the first four lines, we see that a 14 m crest is extremely unlikely, as easily guessed, when considering the linear theory, but coming into the real of the, although remote, possibilities

when we base our considerations on the Tayfun distribution. Indeed, if in the area of 10 m Hs, an encounter every 14 days is something to take into account.

However, things get much worse when we consider the possible highly nonlinear effects. [7] explored the modulational instability in a random sea based on the nonlinear Schrödinger equation (NLS), showing that this could indeed lead to much higher wave and crest heights. The implications are summarised in the lower two lines of Table 1 where we see that, if in a 10 m Hs sea (the data at disposal are not sufficient

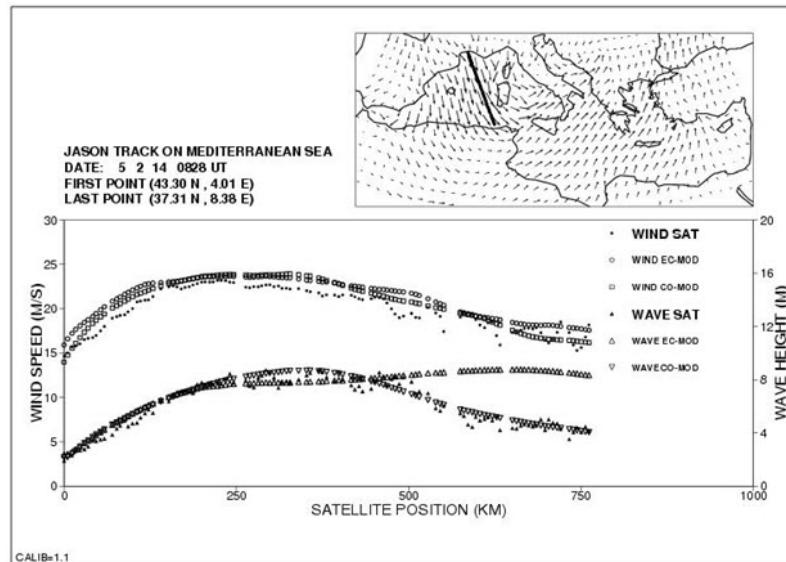


Figure 2: Comparison between Jason altimeter wind speeds and wave heights and corresponding model results. EC-MOD = ECMWF and CO-MOD = COAMPS. The ground track and the overall wind field are shown in the smaller upper right figure (after BC2).

for the 8 m H_s estimate), a 14 m crest encounter is to be expected on the average every 20 hours.

3 The 1966 storm in the Adriatic Sea

3.1 The fact and the idea

In early November 1966 the northern part of Italy was hit by a very severe southeasterly storm. More than 130 persons lost their lives and, although for different reasons, the two top art treasured cities, Florence and Venice, suffered tremendous damage. In the former one this was caused by an unprecedented overflow of the Arno river. In Venice the problems were associated with the high level the sea reached

in the lagoon, flooding more than 90% of the town at a level exceeding any previous record by more than 40 cm. The peak level was 1.94 metre above the nominal sea level. In a town whose pavement is on average one metre above it, this meant that large part of the town was under one metre of water (1.20 m in San Marco square).

At the time there was practically no forecast of what was about to happen. The question naturally arises if the lack of forecast of the 1966 storm has to be associated to the lack of data as compared to the ones present today, or to the lack of computer power and the related highly sophisticated meteorological models we enjoy today. We formulated the question in a slightly different way: should we have had at disposal in 1966 the present hardware and software, but still only the data of the time, how good

| theory | H_s (m) | Probability | N waves | Time |
|--------|-----------|------------------------|-----------------------|--------------|
| linear | 8 | 0.23×10^{-10} | 0.44×10^{11} | 10,000 years |
| linear | 10 | 0.15×10^{-6} | 0.65×10^7 | 3 years |
| Tayfun | 8 | 0.45×10^{-7} | 0.22×10^8 | 7 years |
| Tayfun | 10 | 10^{-5} | 10^5 | 14 days |
| NLS | 8 | - | - | - |
| NLS | 10 | 0.17×10^{-3} | 6000 | 20 hours |

Table 1: Encounter probability of a 14 m high wave crest for different significant wave heights H_s and according to different theories. Tayfun is second order theory, NLS is modulational instability based on nonlinear Schrödinger equation. N is the average number of waves ($=1/\text{probability}$) between two encounters. Time is the corresponding elapsed time. Based on the wave conditions present at the time and location of the "Voyager" accident. The available data do not cover the case NLS-8.

would our forecast have been? Implicit in this question is the argument that, if the reply will be positive, i.e. our forecasts would have been good, in similar conditions a fortiori one could expect today a good forecast.

3.2 The analysis

We have analysed (hindcast) the storm, starting from 20 days before the event, with T511 spectral resolution (~ 40 km spatial one), i.e. the resolution of the operational ECMWF meteorological model at the time we did our experiments [8]. However, we were mainly interested in the forecast, and, emulating the forecasters of the time, but with the modern software and hardware, starting from October 29 we issued a forecast every 12 hours, i.e. at 12 (UTC) of Oct 29, 00 Oct 30, 12 Oct 30, 00 Nov 01, and so on till Nov 04. From each forecast we extracted the sequence of wind fields to drive the marine side of our experiments. We have used two marine models, respectively for waves and for circulation (that includes surge). For waves we used WAM [4] with 1/12 degree resolution. The nar-

row opening at the southern end, Otranto, of the Adriatic Sea and the focus of interest on its northern section allowed us to consider for waves only this sea. On the contrary for circulation we were forced to consider the whole Mediterranean Sea as the tidal conditions at Otranto are an important boundary condition. For this we have used SHYFEM [9], a finite element model that allows a denser mesh in the northern part of the basin (and in the Venice lagoon), where we expect the higher surface gradients.

The peak wind and wave conditions reached in the Adriatic Sea on November 4 are shown in Figure 3. In front of Venice 28 m/s wind speed was present, leading to the big flood that affected the town and the whole lagoon. The flood was further enhanced by the heavy wave conditions, 10 m significant wave height in the Adriatic, 8 m in front of Venice, that contributed to pile up the water against the Venice defences. Detailed maps of the sequential situations in the whole basin are available. However, in this study the most interesting result was the predictability of the storm. This is most evident in the time history of the sea level in Venice. No record is available from the

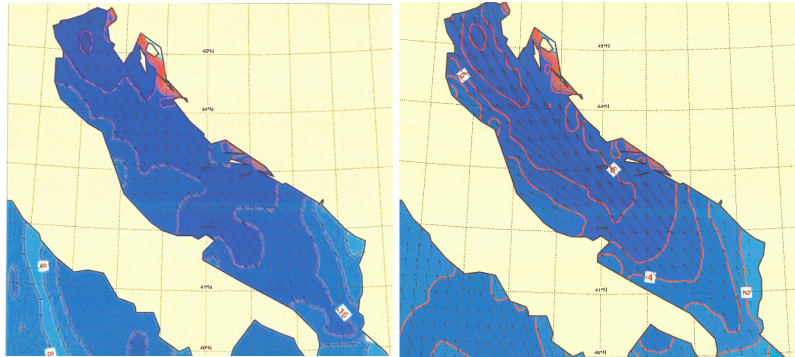


Figure 3: Wind (left) and wave (right) conditions in the Adriatic Sea, East of Italy, at the peak of the storm of November 4, 1966. Isotachs at 4 m/sec intervals. Isolines of wave heights at 1 metre intervals. Peak conditions in front of Venice (upper-left part of the sea) were $28 \text{ m}\cdot\text{s}^{-1}$ and 8 m respectively. A T511 resolution of the ECMWF meteorological model has been used.

coast as all the instruments were destroyed by the storm.

The time history of the surface level at one location represents the sum of the perfectly predictable astronomical tide (the spring tide excursion is about one metre in the Northern Adriatic) and of the meteorological component, i.e. the oscillations of the basin surface related to the wind and atmospheric pressure distributions. Note that in the case of November 4, 1966 event the resulting sea level, maximum at 1.94 metre above the nominal sea level, was in practice due only to the surge, the astronomical tide at the nominal time of the peak being only +0.12 metre.

The results of the surge analysis are given in Figure 4, where we compare the recorded time history of the sea level versus the analysis and the forecasts we issued, during this study, on the base of the data available one day, two days, and so on till six days before the storm. We see that with the present tools it would have been possible to forecast the storm, and the

flood, up to six days in advance. The implications for all the practical activities and possible defences are obvious.

4 Discussion and conclusions

In the case of the November 4, 1966 event our experiments have shown the predictability of the storm till at least six days in advance. This is not a unique result. Not shown in this paper, we have carried out the same sequence of experiments also for another strong storm, although certainly not as severe as the 1966 one, peaked on December 22, 1979. Our results are very similar to the ones for the 1966 case, i.e. both the surge and the wave conditions were well predicted till six days in advance.

This strongly suggests that, should similar events happen today, we should be able to provide forecasts at least as good as the ones shown in the previous section. We purposely say “at least” because the

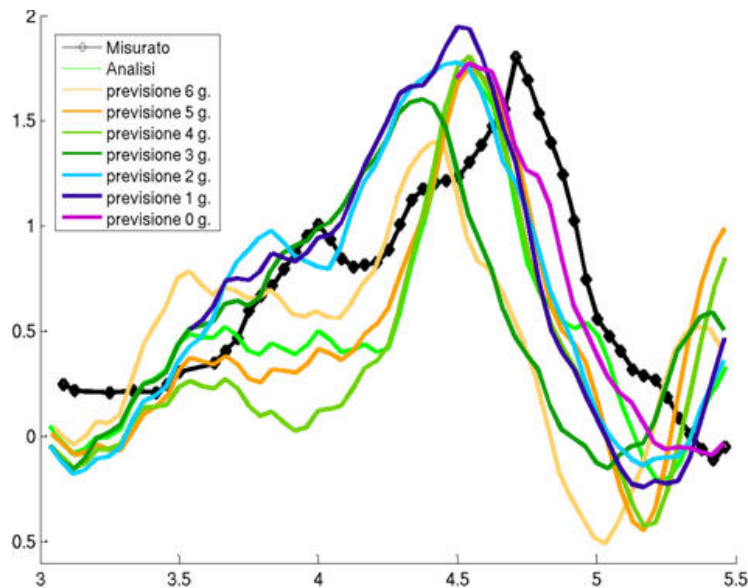


Figure 4: Time series of the meteorological surge (metres) during the November 1966 days. The curves show respectively measured data, the analysis (hindcast) and the forecasts issued, a posteriori, at different days before the storm.

enormous volume of information presently available is expected to lead to more accurate analysis and tendency, hence to better forecasts.

More in general, and as we have seen with

the 2005 storm in the Western Mediterranean, we have presently the capability to analyse in detail any meteorological event happened during the last 50+ years.

References

- [1] S.M. Uppala, P.W. Kallberg, A.J. Simmons, U. Andrae, V. da Costa Bechtold, M. Fiorino, J.K. Gibson, J. Haseler, A. Hernandez, G.A. Kelly, X. Li, K. Onogi, S. Saarinen, N. Sokka, R.P. Allan, E. Andersson, K. Arpe, M.A. Balmaseda, A.C.M. Beljaars, L. van de Berg, and J. Bidlot. The ERA-40 Reanalysis. *Quart. J. Roy. Meteorol. Soc.*, 131:2961–3012, 2005.
- [2] L. Cavaleri and L. Bertotti. The improvement of modelled wind and wave fields with increasing resolution. *Ocean Engineering*, 33(5-6):553–565, 2006.
- [3] L. Bertotti and L. Cavaleri. Analysis of the Voyager storm. *Ocean Engineering*, 35(1):1–5, 2008.

- [4] G.J. Komen, L. Cavaleri, M. Donelan, K. Hasselmann, S. Hasselmann, and P.A.E.M. Janssen. . *Dynamics and Modelling of Ocean Waves*, page 532, 1994.
- [5] L. Bertotti and L. Cavaleri. The predictability of the “Voyager” accident. *Nat. Hazards Earth Syst. Sci*, 8:533–537, 2008.
- [6] M.A. Tayfun. Narrow-band nonlinear sea waves. *J. Geoph. Res.*, 85:1548–1552, 1980.
- [7] M. Onorato, A.R. Osborne, M. Serio, L. Cavaleri, C. Brandini, and C.T. Stansberg. Extreme waves modulational instability and second order theory: wave flume experiments on irregular waves. *J. Mech: B Fluids*, 25(5):586–601, 2006.
- [8] A. Simmons and A. Hollingsworth. Some aspects of the improvement in skill of numerical weather prediction. *Q. J. Roy. Meteor. Soc.*, 128:647–677, 2002.
- [9] G. Umgiesser, D. Melaku Canu, A. Cucco, and C. Solidoro. A finite element model for the Venice lagoon. Development, set up, calibration and validation. *Journal of Marine Systems*, 51:123–145, 2004.

Dissolved and Particulate Concentrations of Lead in the Mediterranean Sea

M. Del Core¹, M. Sprovieri², D. Salvagio Manta²

1, Institute for Coastal Marine Environment, CNR, Napoli, Italy

2, Institute for Coastal Marine Environment, CNR, Capo Granitola (TP), Italy
mariannadelcore@iamc.cnr.it

Abstract

Dissolved Pb concentrations in the Mediterranean Sea Seawater samples were collected in the Mediterranean Sea during the TRANSMED (summer 2007) and SESAME-IT4 (spring 2008) oceanographic cruises for analysis of trace elements in dissolved phase. Lead concentrations generally range between 0,05 and 1 nmol·l⁻¹, close to those recorded in the world ocean, without evidence of scavenging behaviour along the water column. Very high contents of dissolved Pb (about one order of magnitude higher than those measured in the other stations) were detected along the entire water column in three sampling sites localise in the Gulf of Lyon (NW Mediterranean) and SE Spain as possible response to inputs from the Rhone and Ebro rivers. These results suggest a key role played by polluted rivers on the chemistry of the Mediterranean seawater.

1 Introduction

The distribution of many dissolved trace metals (TMs) in seawater has been accurately determined for most of the open ocean. Conversely, few studies were carried out in the Mediterranean sea [1, 2, 3, 4, 5, 6, 7]. They generally show higher surface TMs concentrations when compared to the ocean seawater. This contribution presents a unprecedented survey carried out during two oceanographic cruises TRANSMED (May-July 2007) and SESAME-IT4 (March-April 2008) of dissolved Pb concentrations [Pbd] in the Mediterranean sea and offers an intriguing picture of the effective impact of anthropic inputs at regional scale on the biogeochemistry of this element.

Actually, the bio-geochemical cycles of Pb at global scale is considered to have

been significantly affected by anthropic inputs since the beginning of the Industrial Revolution and successive inception of consuming alkyllead gasoline. The atmosphere is considered the main pathway for Pb transport to the ocean [8, 9] and therefore, the success of antipollution international regulations planned to reduce Pb levels at systemic scale can be reliably checked by verifying effective decrease of this element in seawater [8, 10]. Closeness of the Mediterranean to the highly industrialised area of the western country renders this basin an excellent potential monitor of the effects of human activity on the biogeochemical cycles of Pb in seawater.

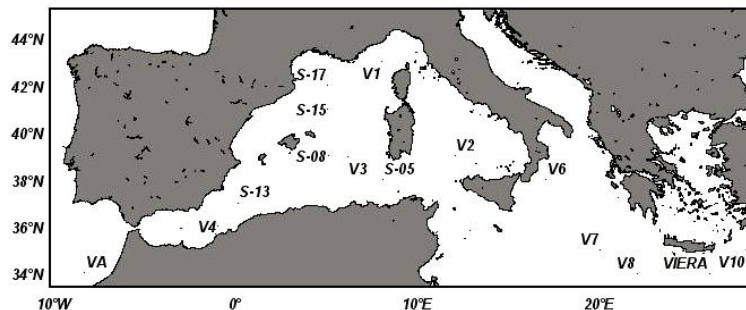


Figure 1: Sampling stations of the TRANSMED (V) and SESAME (S) cruises.

2 Sampling and analysis

Seawater samples were collected in the Mediterranean sea during two oceanographic cruises, TRANSMED (May-July 2007) and SESAME-IT4 (March-April 2008). During the first cruise, a total of 120 seawater samples were collected from the entire water column at 10 sampling stations. During the SESAME cruise, 93 seawater samples were collected from the entire water column in 5 stations (S-05, S08, S-13, S-15 and S-17) in the Western Mediterranean (Figure 1). Sampling procedures and analytical methods used to measure dissolved trace metals concentrations in seawater are reported in details in Schelfo Handbook [11] and Poikane [12].

3 Results and discussion

Vertical profiles of dissolved Pb are shown in Figures 2 and 3. In the Alboran Sea, [Pbd] at the surface shows a maximum ($\sim 4,25 \text{ nmol}\cdot\text{l}^{-1}$) possibly due to the contribution of Atlantic water flowing through Gibraltar significantly enriched of TMs by mixing with Spanish coastal waters. Then, along its flow through the Sicily Channel

and towards the eastern basin, the surface water masses record a constant decreasing trend in [Pbd] (0.55 to $0.17 \text{ nmol}\cdot\text{l}^{-1}$). Conversely, although surface [Pbd] decreases from Gibraltar also following its northeastward, values from the Gulf of Lion and also in the SW area of the basin are extremely high (particularly in the S-17 stations where [Pbd] is $\sim 5,15 \text{ nmol}\cdot\text{l}^{-1}$) and suggest significant influence of terrestrial inputs from the close lands. The distribution of [Pbd] in the surface waters reported in Figure 4 clearly evidence an evident asymmetric pattern between eastern and western basin with the latter significantly affected by regional river inputs from highly industrialised lands. [Pbd] in the intermediate waters (the Levantine Intermediate Water [namely LIW] flowing in the Mediterranean from east to west at a depth of 150-600 m) are generally undistinguishable from the surface water (ranging between 0.05 and $0,4 \text{ nmol}\cdot\text{l}^{-1}$) also in the formation area in the Levantine basin where possible effects of inputs from lands may produce enhanced levels of this element as effect of anthropic pollution. Once again, dissolved [Pb] in the LIW in the Lion Gulf (Figure 4) and SW area of the basin are still high ($3,3-9,0 \text{ nmol}\cdot\text{l}^{-1}$) when

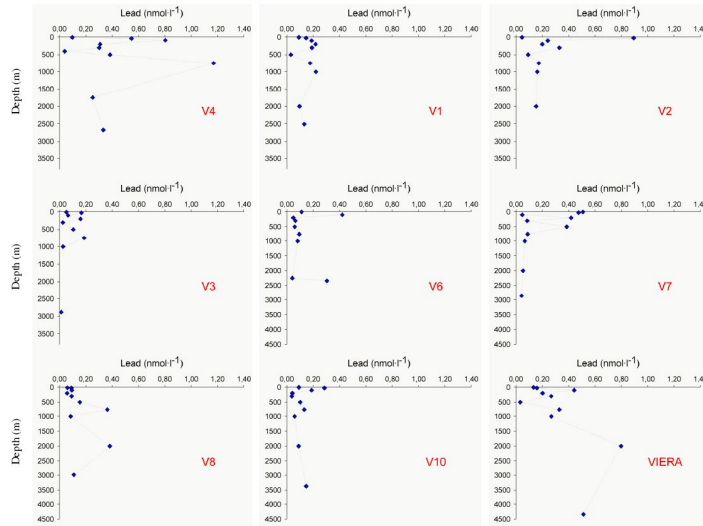


Figure 2: Vertical distribution of dissolved [Pbd] ($\text{nmol}\cdot\text{l}^{-1}$) in the TRANSMED stations.

compared to those recorded in the same water mass in the rest of the basin. Particularly in the S-15 station, where the surface [Pbd] range between 0,11 and 0,33 $\text{nmol}\cdot\text{l}^{-1}$, an evident increase was detected also at 300-600 m depth (5,0- 9,17 $\text{nmol}\cdot\text{l}^{-1}$). Finally, the deep waters (Figure 4), but of the enriched waters of the Gulf of Lion (4,3 and 13,8 $\text{nmol}\cdot\text{l}^{-1}$) show very low values in the entire basin. Permanence of an asymmetric pattern of [Pbd] distribution between eastern and western basin testify a significant effect of the kinetic dissolution of particulate with consequent release of Pb in dissolved phase. Actually, as reported by [13] fast dissolution effects of Pb-enriched particulate were measured in the Mediterranean area and could coherently explain the effect of homogenization

in [Pbd] between surface and deep waters recorded in the western area.

4 Conclusions

The presented distribution patterns of dissolved [Pb] in Mediterranean seawaters show an important impact of anthropic inputs, mainly in the western part of the basin where 1-2 times higher values were recorded. Inputs from the Rhone and Ebro rivers appears the most important sources of dissolved [Pb] in that area. Kinetic effects on the dissolution mechanisms of particulate associated to significant release of Pb in the dissolved phase seem to play a key role in the distribution of that element at basin scale.

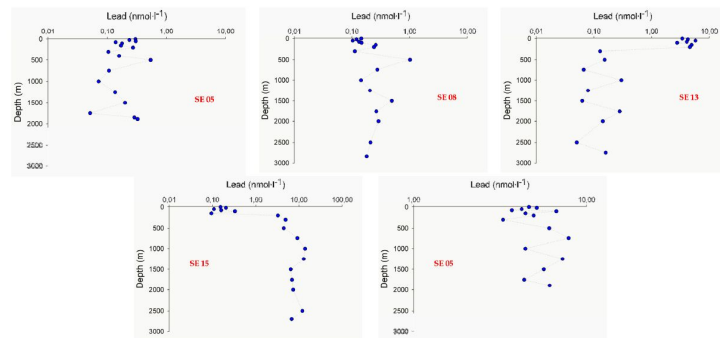


Figure 3: Vertical distribution of dissolved [Pbd] ($\text{nmol}\cdot\text{l}^{-1}$) in the SESAME stations.

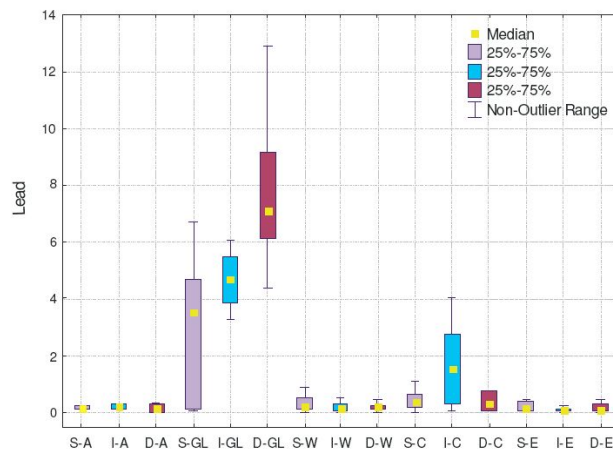


Figure 4: Box whiskers plot for [Pbd] dissolved concentrations in surface (S-A), intermediate(I-A) and deep(D-A) waters at the Atlantic station; for surface (S-GL), intermediate(I-GL) and deep(D-GL) waters in the Gulf of Lyon; for surface (S-W), intermediate(I-W) and deep(D-W) waters in the Western Mediterranean Sea; surface (S-C), intermediate (I-C) and deep(D-C) waters in the Sicily Channel and surface (S-E), intermediate(I-E) and deep(D-E) waters in the Eastern Mediterranean Sea.

References

- [1] G.Copin-Montegut, P.Courau, and E. Nicolas. Distribution and transfer of trace elements in the Western Mediterranean. *Mar. Chem.*, 18(2-4):189–195, 1986.
- [2] E.A. Boyle, S.D. Hapnick, X.X. Bai, and A.Spivack. Trace metal enrichment in the Mediterranean Sea. *Earth Planet. Sci. Lett.*, 74:405–419, 1985.
- [3] P.J. Statham, J.D. Burton, and D.J. Hydes. Cd and Mn in the Alboran Sea and adjacent North Atlantic: geochemical implications for the Mediterranean. *Nature*, 313:565–567, 1985.
- [4] A.Van Geen, P. Rosener, and E. Boyle. Entrainment of trace metal enriched Atlantic shelf water in the inflow to the Mediterranean Sea. *Nature*, 331:423–426, 1988.
- [5] N.H. Morley, J.D. Burton, S.P.C. Tankere, and J.M. Martin. Distribution and behaviour of some dissolved trace metals in the western Mediterranean Sea. *Deep-Sea Research II*, 44(3-4):675–691, 1997.
- [6] J.H.Martin, S.E. Fitzwater, R.M. Gordon, C.N. Hunter, and S.J.Tanner. Iron, primary production and carbon–nitrogen flux studies during the JGOFS North Atlantic Bloom Experiment. *Deep-Sea Res.*, 40:115–134, 1993.
- [7] N.H. Morley, P.J. Statham, and J.D. Burton. Dissolved trace metals in the south-western Indian Ocean. *Deep-Sea Research I*, 40:1043–1062, 1993.
- [8] C. Migon, L. Alleman, N. Leblond, and E. Nicolas. Evolution of atmospheric lead over the north-western mediterranean between 1986 and 1992. *Atmospheric Environment*, 27, 1993.
- [9] V. Sandroni and C. Migon. Significance of trace metal medium-range transport in the western Mediterranean. *Sci. of the total Environment.*, 196:83–89, 1997.
- [10] E. Nicolas, C. Migon, and L. Alleman. Heavy metal concentrations and Pb evolution from 1986 to 1992 in the north-western Mediterranean Sea. *Wat. Pollut. Res.*, 30:279–286, 1993.
- [11] Schelfo. A practical handbook for trace metal and ancillary analyses. *University of California, Environmental Toxicology, Special Publication March 1997 Written and Compiled by Genine*, 1997.
- [12] R. Poikane, J. Cartensen, I. Dahllof, and J. Aigars. Distribution pattern of particulate trace metals in the water column and nepheloid layer of the Gulf of Riga. *Chemosphere*, 60:216–225, 2005.
- [13] C. Guieu, R. Chester, M. Nimmo, J.-M. Martin, and S. Guerzoni. Atmospheric input of dissolved and particulate metal to the northwestern Mediterranean. *Deep-Sea Research II*, 44(3-4):655–674, 1996.

Styles and Nature of Submarine Volcanism: the Tyrrhenian Sea Case History

M. Marani, F. Gamberi, V. Ferrante, M. Rovere
Institute of Marine Sciences, CNR, Bologna, Italy
michael.marani@bo.ismar.cnr.it

Abstract

Volcanism at subducting plate boundaries represents about 25% of the Earth's magma production. Rollback of ancient, dense oceanic slabs ultimately leads to the generation of magmatism and new lithosphere in back arc basin spreading environments. Thus, subduction zones are characterised by the development of large volcanic edifices both in island arc and backarc basin environments hosting 80% of the currently active volcanoes of the planet. Much of the volcanism occurs in the submarine environment.

Submarine volcanic landforms have been shown to result, in part, from processes similar to those commonly observed in terrestrial volcanic settings. All land-based lava flow morphologies have been recognized in the marine environment, while the products of explosive eruption styles have been documented even from the deep ocean at 2000 metres water depth. However, submarine conditions dictate the development of landforms that are absent from terrestrial counterparts such as the ubiquitous pillow or tube lavas. Landforms typical to the submarine environment are low aspect ratio flat top volcanic seamounts and volcanic terraces.

The development of submarine volcanism and associated processes has been revealed by the increasing coverage worldwide of swath bathymetry. A similar mapping effort has been undertaken in the Tyrrhenian Sea, a young oceanic backarc basin characterised by active arc volcanoes, where the primary morphologies submarine volcanism are well preserved.

1 Introduction

Submarine volcanic landforms have been shown to result, in part, from processes similar to those commonly observed in terrestrial volcanic settings. All land-based lava flow morphologies have been recognized in the marine environment, while the products of the range of explosive eruption styles have been documented even from the deep ocean at >3000 metres water depth [1]. However, submarine conditions dictate the development of unique lava flow

morphologies and landforms that are absent from terrestrial counterparts. Higher lava viscosity or lower extrusion rates at the seafloor give rise to the ubiquitous pillow or tube lavas that form small edifices and ridges, observed in all submarine geological settings, and also in the fossil record [2]. Landforms typical only to the submarine environment are low aspect ratio flat top volcanic seamounts, the origin and modes of formation of which are much less understood. In part explained by the faster cooling rates, varying eruption styles and

greater pressure ranges of the marine ambient [3, 4], much data is lacking in terms of the controlling parameters due to the impossibility of directly observing their formation.

Volcanism at subducting plate boundaries represents about 25% of the Earth's magma production [5], mainly developed within the volcanic arc environment. Convergent settings characterised by the subduction of ancient, dense oceanic lithosphere result in an extensional volcanic island arc due to the rollback of the oceanic slab and, ultimately, to the generation of further magmatism and new lithosphere in back arc basin (BAB) spreading environments. Thus, subduction zones are characterised by the development of large volcanic edifices both in island arc and backarc basin environments hosting 80% of the currently active volcanoes of the planet [6].

Much of the volcanism occurs in the submarine environment. This has been shown to be true by the increasing coverage worldwide of high resolution swath bathymetry and reflectivity data targeting the development of submarine volcanism and associated processes. Recent examples include innovative studies of the morphology of submerged volcanoes carried out in the Mariana arc and in the submerged sectors of Hawaii [7, 8, 9].

The use of swath bathymetric mapping as a remote sensing tool, augmented by steadily increasing ground truthing by means of sampling and video coverage, has profoundly increased our knowledge about the unique characters of submarine volcanism, concerning both edifice morphology and the structural instability of volcanic constructs inherent to the underwater environment. A similar mapping effort has been undertaken in the Tyrrhenian Sea [10], a young backarc basin characterised by ac-

tive arc volcanoes, where the primary morphologies of submarine arc and backarc volcanoes are preserved, and can thus contribute to the understanding of submarine volcanic processes.

In particular, a full-ocean-depth EM12 multibeam system was utilised for seafloor mapping and reflectivity. Swaths in the Tyrrhenian were planned at 20% overlap to generate complete coverage; they were complemented by gravity, magnetic and reflection seismic data acquisition. In successive research campaigns, high resolution MAKII depp-tow sidescan sonar, digital TV visual observations and extensive seafloor sampling augmented knowledge and ground-truthed the morphological data.

2 Setting

The Tyrrhenian Sea, bordered to the east and south by the Apenninic-Maghrebides mountain belt and to the west by the passive Sardinian margin, formed as a consequence of rifting and backarc extension of the Alpine/Apennine suture above the north-westerly subducting Ionian oceanic slab, [11]. An eastwards migration of crustal thinning and oceanic accretion affected the Tyrrhenian area since lower-mid Miocene (~15 Myr). E-W directed rifting in the northern Tyrrhenian and along the western margin of Sardinia [12, 11] marks the initial opening of the Tyrrhenian basin leading to the formation of oceanic domains and associated volcanism in the Southern Tyrrhenian. First, production of oceanic crust occurred westward, during the Pliocene spreading of the Vavilov basin (4.3-2.6 Myr), where the large centrally located Vavilov volcano developed [11]. A subsequent change

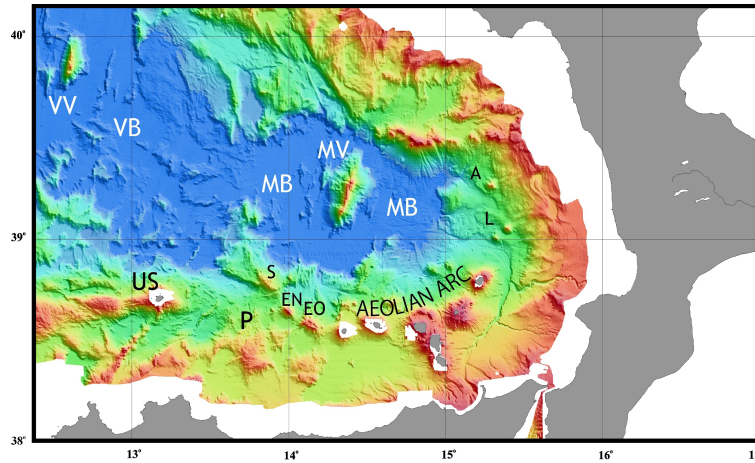


Figure 1: Shaded relief bathymetry (illum. from NW) of the central-southern Tyrrhenian Sea with features discussed in the text: MB and VB, Marsili Basin and Vavilov Basin respectively, Vavilov volcano (VV) and Marsili volcano (MV). Also labeled are the submerged arc volcanoes: Sisifo (S), Enarete (EN), Eolo (EO), Lametini (L) and Alcione.

to ESE-directed extensional stress in Late Pliocene-Quaternary resulted in the emplacement of basaltic crust southeastwards, generating the Marsili backarc basin (2 Myr) also containing a large axial volcano, Marsili seamount, [11, 13, 14]. The eastwards migration of backarc basin development and active volcanism is induced by the rollback of the Ionian subducting plate. In step with backarc basin development, the subduction-related island arc volcanism of the southern Tyrrhenian basin migrated from west to south-east, from Sardinia (32-13 Ma) to the currently active Aeolian island arc, developing the present-day arc/backarc configuration of the southern Tyrrhenian region (Figure 1). The Aeolian arc consists of seven islands and a number of submarine volcanoes west and northeast of the emergent arc. Available chronological data [15] show that the beginning of activity took place in the Quaternary (\sim 1-

1.3 Ma) at Sisifo seamount and Filicudi. From \sim 0.8 Ma to the Present, dominantly shoshonitic and calcalkaline lavas, mainly consisting of basalts and basaltic andesites to rhyolites, were erupted in the different submarine and emerged edifices. Numerous studies have been recently focussed on the submerged flanks of Stromboli Island [16, 17, 18, 19, 20] but are not discussed in this paper. The northeastern submerged portion of the arc, positioned on the Calabrian margin, consists of isolated cones and the large, Palinuro volcanic complex. To the west of the emergent islands a number of submerged arc volcanoes are located on the Sicilian margin. The following discussion will describe the morphology of several of the most outstanding submarine arc volcanoes, substantially analysing their origin and their present makeup in terms of edifice stability. Subsequently, the large, axially located backarc volcanoes, Marsili

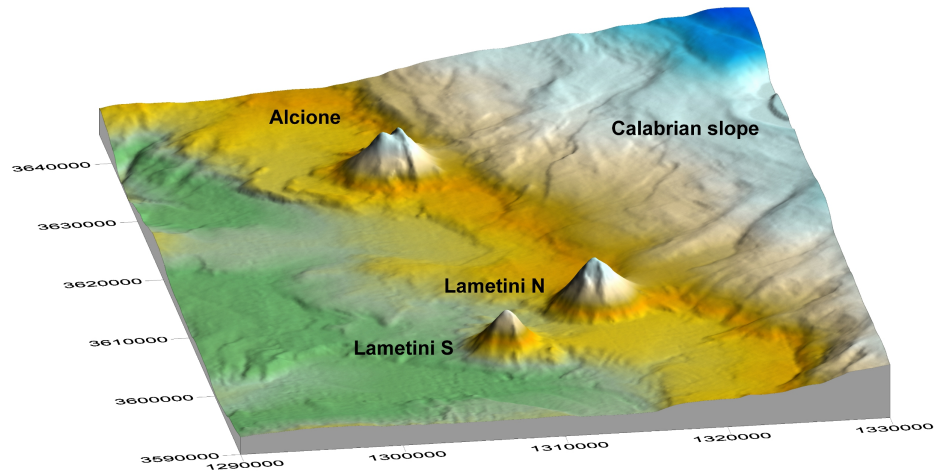


Figure 2: Colour-coded relief bathymetry (illum from N) of the Calabrian slope and the location of the submerged eastern Aeolian arc volcanoes. Note the position of Alcione and the Lametini volcanoes on the slope bench.

and Vavilov, will be illustrated.

3 The submerged aeolian arc

3.1 Northeastern Arc Volcanoes

Three volcanoes, Alcione and the twin cones of the Lametini seamounts (Figure 2), lie in the Calabrian slope delimited by the Palinuro volcanic complex to the north and Stromboli Island to the south. The volcanoes develop in the westerly deepening Calabrian lower slope at a depth in the order of 2000 m. At this depth, the slope gradient decreases to form a relatively lower gradient bench, the Lametini-Alcione flat, on which the volcanoes arise.

3.1.1 Alcione

Dredge hauls indicate a calc-alkaline basaltic composition for the seamount [15]. Measurement of the height of the volcano is dependant on the sloping bench on which it is situated. Summit heights vary from 900 m to 1200 m for the eastern summit and from 825 m to 1125 m for the western one determined on whether the heights are taken from the eastern base of the volcano or from the deeper western base of the volcano respectively. This ~1000 m high volcano is a textbook example of primary edifice gravitational instability. The general conical shape is entirely dissected by NNW-SSE trending, 100 m relief arcuate scarp (Figure 3) that displaces downwards the western (seaward) half of the edifice. The top of the volcano is characterised by two summit areas: an eastern summit, directly flanked by the scarp, elongated along the scarp trend and a western coni-

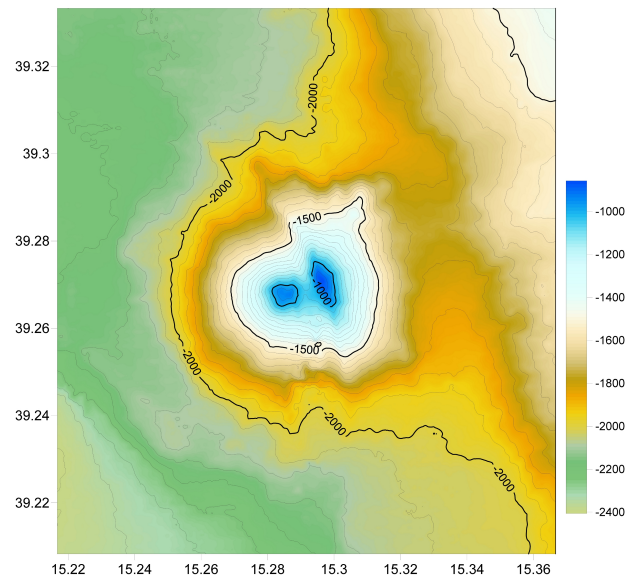


Figure 3: Alcione volcano colour-coded relief (illum from E). Note the scarp cutting across the edifice. For discussion refer to text.

cal summit, located about 800 m from the scarp and 75 m deeper than the former. The distinguishing morphological features of Alcione are to some extent similar to analogue models involving basement fault activation beneath a volcanic edifice [21] or differential flank creep and spreading [22]. A third possibility is the growth of a younger cone (the western part of Alcione) within the arcuate scar of a previous sector collapse that dissected a former edifice.

3.1.2 Local structure of Alcione region

A summary analysis of the basement structure around the volcano furnishes an indication to verify which, if any, of the above-mentioned processes are or were active on Alcione. Surrounding seafloor morphology shows a steep, 15 km long,

N-S trending, 400m high scarp located at the base-of-slope to the east of Alcione. A second, shorter N-S directed scarp is interrupted at the northern flank of the volcano (Figure 4). To the west, a series of NW-SE trending, 200 m high scarps delimit the flat bench on which the volcano develops. Finally, two positive relief belts with arcuate trends develop between the volcano and the western delimiting scarps.

If the scarps are the surface expression of a fault system, the volcano could be located in the relay ramp area linking two faults. Deformation directly related to basement fault activation can be ruled out because no fault follows the arcuate trend of the Alcione scarp. E-W seismic profiles crossing the edifice show seismic basement dropping ~600 m, from 2400 m depth East of the volcano to 3000 m depth west of it and sediment fill increasing from ~400 m to

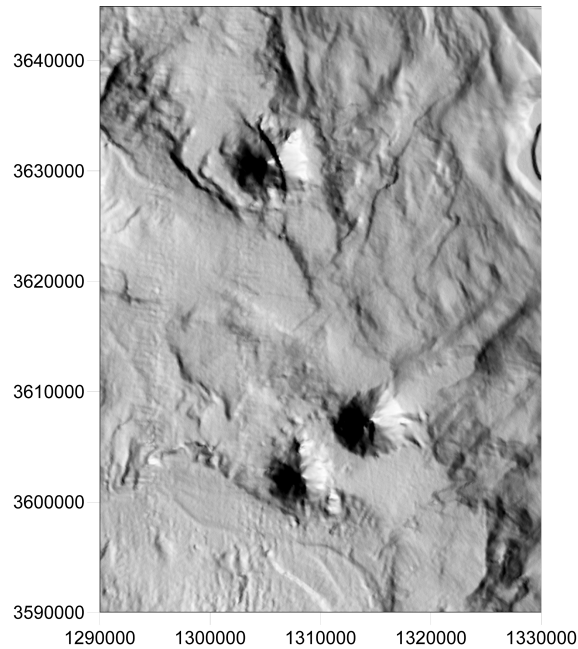


Figure 4: Shaded relief of the Alcione – Lametini region displaying the principal fault scarps that dissect the region and the main depositional architecture.

~700 m across the drop. The seismic signal beneath the volcano is obscured but it is reasonable to assume the existence of a fault system in this position. Flank creep due to differential spreading of the western portion of Alcione is a possible mechanism to explain the Alcione structure considering the E-W asymmetry of the volcano base, the basement drop beneath it and the thicker sediment pile to its west. Spreading or creep should be towards WSW, perpendicular to the edifice cutting scarp with a deep-seated decollement plane probably located within weaker sedimentary material. However, the arcuate positive elements at the western base of the volcano may be the evidence of the deposits due to a more rapid and catastrophic failure, affecting a whole flank portion of the for-

mer Alcione edifice. The arcuate scarp of Alcione, in this scenario, would represent the remnant scarp of this failure while the eastern portion of the volcano, a younger cone, nested within the failed flank.

3.1.3 Lametini seamounts

The two conical edifices of the Lametini seamounts are located 20 km due south of Alcione on the same gently sloping bench area (Figure 3). They are aligned in a NE-SW direction 3 km apart. The NE volcano (LamN) is larger than the SW one (LamS). Dredge samples from LamN [15] recovered basalts. Both volcanoes display E-W asymmetry due to the sloping bench, LamN having heights between 1300 m and

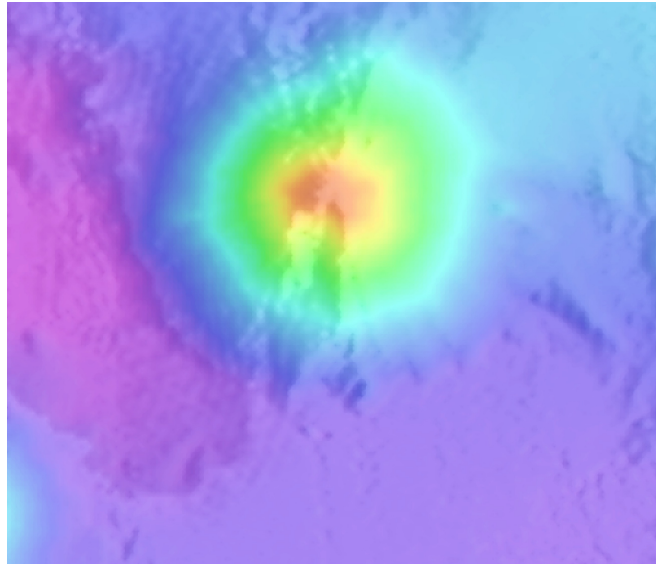


Figure 5: Largest Lametini cone (LamN in text). Colour-coded relief (illum from E). Note the large surficial scar affecting the southern flank of the cone and the positive relief at its base, possibly representing the proximal portion of the failed material.

900 m and LamS between 850 m and 650 m measured along the western and eastern flanks respectively. Apart from its size, a distinctive characteristic of LamN, is a prominent slide scar on its western flank (Figure 5). It initiates as a 600 wide scar at the summit and broadens to 1500 m at the base of the edifice. Scarp walls are in the order of 100/150 metres high at the top, diminishing downwards. Interestingly, a feature with positive relief, within the lower part of the scar, from 1600 m depth to the base of the cone at 2100 m, possibly represents the proximal portion of the slide material still lying on the volcano flanks. There is no indication, however, of slide deposits on the adjacent seafloor, at the base of the volcano.

3.1.4 Local structure of the Lametini region

Although scarce, seismic data in the Lametini region indicate variations in basement depth, which could be related to the location and alignment of the two volcanoes. Basement depth, in fact, is 2800 m north of the cones, dropping to 3250 m south of them. Available data however preclude any accurate estimate of the direction of the structure affecting the basement. As to the slide scar on LamN, the feature is most probably related to a mass-wasting event along a shallow-seated detachment plane, evidence of gravitational instability due to the sloping ($\sim 15^\circ$) flanks of the volcano and not associated to any form of deep-seated source.

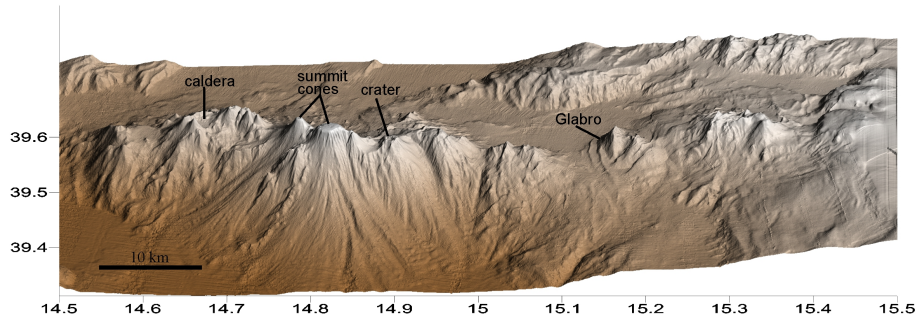


Figure 6: Perspective shaded relief of the Palinuro Volcanic Complex (PVC), with main features described in text labeled.

3.2 Palinuro

Palinuro is made up of basalts and basaltic andesites and has been dated to 0.35 Ma [15]. The composite Palinuro volcanic complex (PVC) stretches E-W for 50 km. It stands between the mid Calabrian slope at 1600 m water depth to its north and the deep Marsili basin (3400 m depth) to its south. The PVC delimits the north-western extent of Aeolian arc volcanism. At least six single volcanic edifices can be recognised along the PVC (Figure 6), their bases coalescing to form a near continuous volcanic ridge. Shallow water depths characterise the central portion of the PVC, with two volcanoes between $14^{\circ}45'$ and $14^{\circ}50'$ reaching 175 m and 70 m depths. They display flat tops, mostly due to emersion during glacial times. To the west of the two shallower volcanoes, clusters of small cones surround a depressed area ($14^{\circ}40'$ - $14^{\circ}45'$) bordered by an arcuate northwestern ridge and smooth slope. This morphology could be related to a caldera-forming gravitational collapse event of a pre-existing volcanic edifice, followed by the creation of resurgent domes; the lin-

ear scarp bordered by the smooth slope could be the sole remainder of the original volcano flank (Figure 7). The domes of the caldera region are the site of extensive hydrothermal activity, similar to other hydrothermal areas in the Tyrrhenian arc region [23, 24, 25]. To the east, adjacent to the central area ($14^{\circ}50'$ - $15^{\circ}00'$), a series of smaller cones develop, mostly exhibiting horseshoe morphology and cratered summits (Figure 8).

Further east, the PVC is affected by tectonic structures that are very prominent in the morphology of the last volcano, Glabro (centred on $15^{\circ}10'$), isolated from the PVC by a narrow moat. This easternmost volcano of the PVC has outstanding morphology (Figure 9). No samples are available for Glabro. The volcano is dissected by a series of arcuate fault scarps into two separate parts characterised by N-S elongated, linear summit zones. Very steep internal scarps delimit the western (830 m water depth) and eastern (870 m water depth) summit portions of Glabro, separated by a 1.8 km wide saddle lying at a water depth of 1100 m. The western portion of Glabro is larger, higher and has

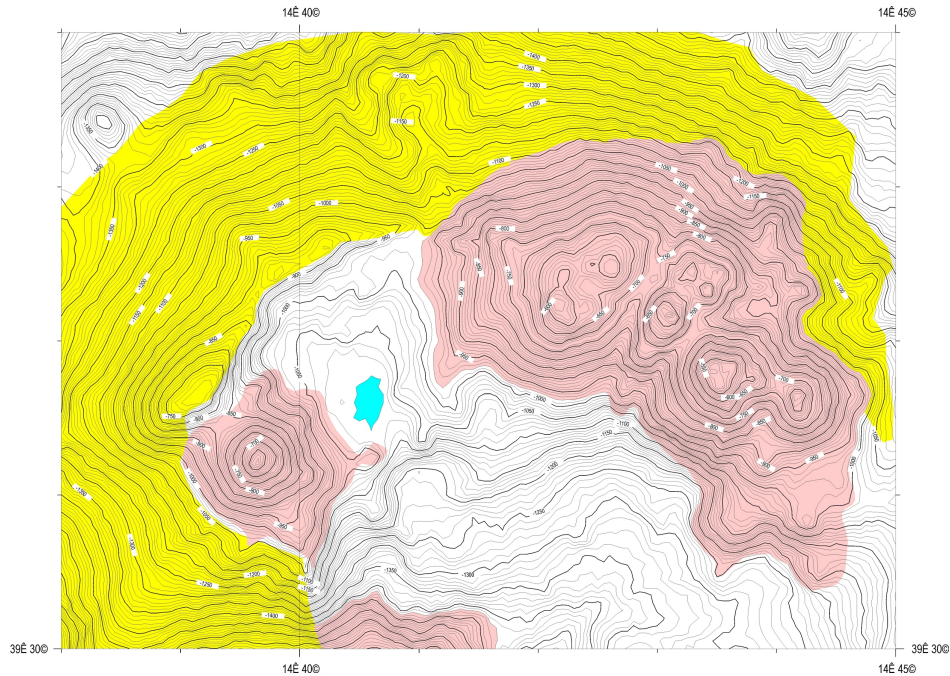


Figure 7: Bathymetry of the Western caldera region of Palinuro. In yellow the interpreted original flanks of the volcanic edifice prior to collapse, in pink the late stage resurgent domes.

a shape very similar to a smooth-flanked elongated cone split vertically into half. The flanks of the smaller, eastern portion are morphologically irregular, and its resulting shape is more complex. Surrounding perimeter faults also characterise the adjacent seafloor of Glabro, two intersecting the seafloor to the west of the edifice and one to the east. The faults that have dissected Glabro, both the internal and perimeter features, have two distinctive properties. Firstly, all scarps are arcuate but with trends that fall into the N-S quadrant, elements with cross-cutting attributes are in fact lacking. Secondly, all the faults affect solely the area contiguous to the volcano, conspicuously diminishing in height

until terminating at the immediate external perimeter of the edifice. These elements lead to the conclusion that the observed volcano-tectonics is intimately linked to, and the surface expression of the destabilising processes that have affected Glabro. With regard to the processes at the origin of destabilisation, a first possibility is a thorough dissection of the volcano by normal faulting. A problem with this assumption is that since the faults are linked only to the volcano, some other process must have been at work to focus the faulting. A more credible process is directional gravitational spreading towards the E-NE. In effect, some of the elements characterising Glabro seem to have development close

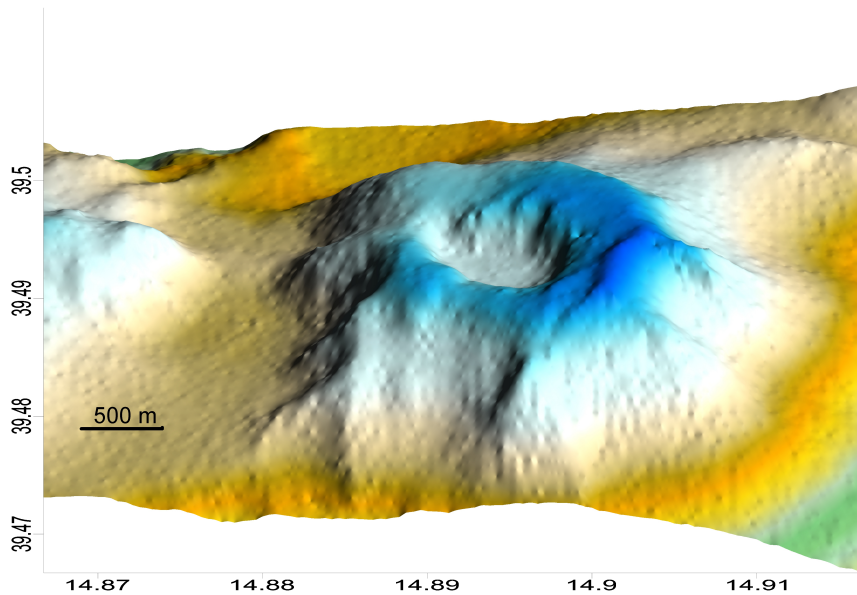


Figure 8: Cratered volcano. The volcano is a small cone characterised by an asymmetric crater located at a minimum water depth of 500 m). Crater walls have a maximum height of 290 m, diminishing to 180 m at its western rim. The floor of the crater is at 130 m above the base of the volcano.

to the morphological characteristics of volcanic spreading described by analogue and numerical modelling results [26, 27]. In the spreading case, the western scarps could be the surface expression of compression due to a slide surface underlying the entire edifice, probably initiating at the inward facing eastern fault. Movement along the decollement surface would cause destabilisation and dissection of the volcano summit, originating the two steep inward-facing collapse scarps delimiting the two sum-

mit areas, developing as the flanks of a central leaf graben.

3.2.1 Western Arc Volcanoes

Located on the seaward portion of the Cefalù basin, and west of the Island of Alicudi, the submerged portion of the western Aeolian arc is aligned in a NW direction and consists of Eolo and Enarete seamounts and the volcanic range comprising Sisifo seamount. Eolo, Enarete and

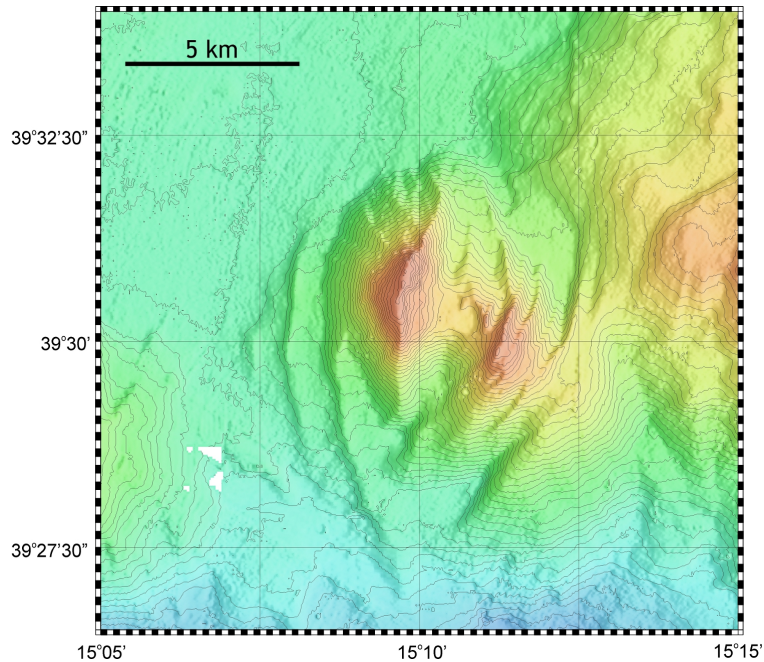


Figure 9: Glabro Volcano. Colour-coded relief (illum. from E) with bathymetry at 25 m contour interval. Glabro is made up of two summit areas bounded by striking internal and perimeter scarps. Note the diminishing throw of perimeter scarps away from the volcano. See text for discussion.

the Islands of Filicudi and Alicudi are positioned at the northern margin of the Cefalu basin (Figure 10), flanking the 1500 m deep, flat-lying seafloor of the basin and bounded by a 500 m to 1000 m seawards-facing scarp to the north.

3.2.2 Eolo

This volcano is located 20 km due west of Alicudi Island. The volcano is generally characterised by irregular flanks, and a wide, 3 km by 2 km, relatively flat summit area, ~800 m deep, elongated in a NW-SE direction. The flat summit is roughly square shaped and bounded by linear highs (75 to 125 m high) on 3 sides except to

the SW. In this latter side, the southwestern portion of the summit area terminates at a 300 m deep scarp surrounded by 3 small cones (350 m, 250 m and 175 m high) which thus form a closed depression. Dredge hauls from Eolo have included basalts, dacites and rhyolites, dated between 0.85-0.77 Ma [15]. The more silica-rich rocks characterise the small cones that surround the southwestern depression, suggesting a second episode of volcanism and cone emplacement following gravitational collapse of this flank of Eolo. The wide irregular base area of Eolo does not seem proportional to its present morphology. A conjecture could interpret the flat lying summit surrounded by delimiting highs as

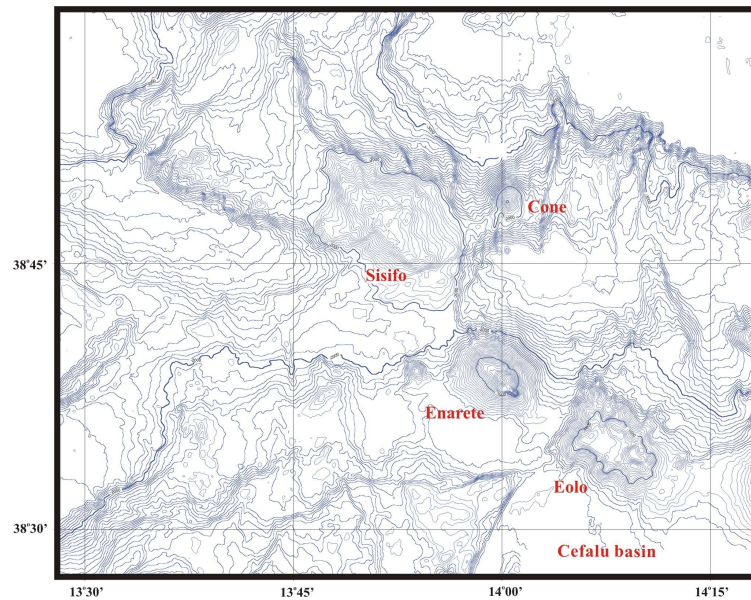


Figure 10: Bathymetry (interval 50m) of the western submerged Aeolian arc. Features discussed in text are labeled.

a filled caldera, implying the destruction of a previously larger edifice.

3.2.3 Enarete

It lies 10 km to the NW of Eolo. This volcano, from which basalt rocks, dated 0.78-0.67 Ma, were dredged [15], has the morphology of a near perfect cone, slightly elongated with NW-SE trend (Figure 10). It is asymmetric in height, ranging between 1700 m and 1450 m, given that its northern flank terminates at greater depth. About 3 km west from the base of Enarete, a small, 500 m high cone rises from the flat seafloor (Figure 10). NW of Enarete lies the complex and irregular morphology of Sisifo seamount which lies upon a WNW-ESE directed, 40 km long ridge. Made up of basalts and trachytes, dated 1.3-0.9 Ma, this edifice holds the oldest age data so far

available for the Aeolian Arc. Younger volcanism, however, has been active in the region as shown by the morphological expression of a regular 1000 m high, conical volcano (located north of Enarete, at the southeastern margin of the Sisifo ridge).

4 Backarc volcanoes

4.1 Marsili

Marsili volcano rises 3000 metres from the Marsili basin seafloor to a minimum depth of 489 metres. It is elongated ~ 60 km NNE-SSW with mean width of 16 km. A narrow, 1 km wide linear region of lower gradient, approximately bounded by the 1000 metre isobath, marks the summit rift zone that stretches 20 km along the main axis of the volcano. On the lower flanks

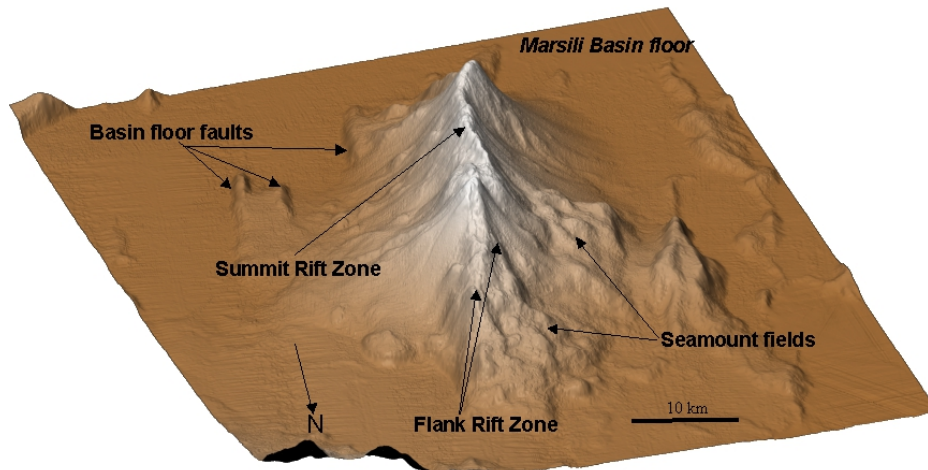


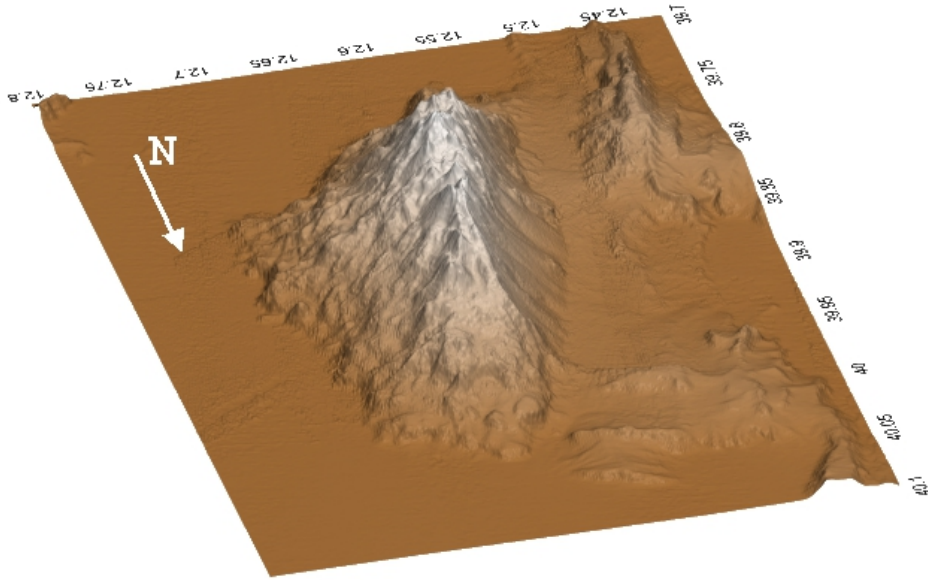
Figure 11: Perspective shaded relief of Marsili volcano. Main features are labeled.

of the volcano, particularly to the NW and SE, numerous seamounts develop while the adjacent basin areas to the west and to the east of the Marsili edifice are characterised by large fault scarps (Figure 11). The volcano summit axis zone and tip regions are characterised by the development of linear structures arranged in segments generated mainly by the alignment of narrow, linear cone ridges, or by the linear arrangement of several circular-based cones [13]. Segment locations show that the central portion of the volcano is the main site of stress release and ensuing volcanic activity. These features, along with other morphological characteristics of the volcano and adjacent regional geology, led [13] to interpret Marsili volcano as a super-inflated spreading ridge, constructed due to robust volcanism during the last 0.7 Ma. Rock samples dredged from the volcano have allowed the interpretation of the geodynamic significance

of the Marsili volcano in relation to the subduction environment of the Tyrrhenian back-arc [13, 28].

4.2 Vavilov

Vavilov volcano has a length of ~ 30 km, elongated in a N-S direction with a maximum width of ~ 14 km. It rises 2800 m from the flat Vavilov basin floor 3600 m deep to minimum water depth of 800m. Vavilov is a mature volcano, its formation occurring at the time of oceanisation of the Vavilov backarc basin at about 3Ma [29]. The summit area, however, seems to have been subsequently active at 0.4 to 0.1Ma [30]. The overall morphology of Vavilov volcano is dominated by the strong asymmetry between its eastern and western flanks (Figure 12). While the eastern flank, dipping on average 15° , displays irregular “volcanic” topography due to small cones,



magma vents are at the origin of the volcanoes. The vents are essentially unique, as shown by the variations of geochemical signatures of the products between adjacent volcanoes, and may tap portions of a heterogeneous mantle beneath the arc. A probable exception is the Palinuro volcanic complex. Although complicated by a range of volcanic morphologies, its linearity given by the uninterrupted merging of its vents could be indicative of the stability of magma supply along a major crustal discontinuity. Moreover, its trend and location, together with it being the limit of arc volcanism in this sector, are distinctive characters that differentiate Palinuro from the other submerged Aeolian volcanoes, and make it more similar to the two major backarc seamounts.

Backarc volcanoes of the Tyrrhenian are characteristically large reaching relatively shallow water depths (500-800 m) with bases at ~3500 m water depth. Both Marsili and Vavilov display satellite cones and terraces on their flanks, and relatively lower gradient summits characterised by a series of cones. Vavilov displays a more subdued topography probably due to sediment draping, but nevertheless shows the development of similar features described

for Marsili.

A variety of instability processes have affected several of the described volcanoes. In the arc sectors, these processes are linked to the ubiquitous basement faults that underlie the volcano. This framework could favour gravitational spreading, which causes the most outstanding morphological transformation in the arc. It may be incipient in the case of Alcione and in a mature stage in the case of Glabro.

If these two examples represent the end members of the spreading case, it follows that this process takes place by slow movement along the sliding surface, demonstrated by the development of the two cone summits on Alcione and the integrity, albeit disjointed, of the Glabro edifice. On the contrary to deep-seated spreading, the northern Lametini seamount displays a relatively large flank slide scar, most probably related to the failure along a slide surface limited to the edifice and due to the high gradient of the flanks. This type of instability evolves within a much more restricted time frame than that of gravitational spreading. Vavilov volcano is the most representative candidate for this style of "instantaneous" gravitational instability.

References

- [1] L. Head, J.W. and Wilson. Deep submarine pyroclastic eruptions: theory and predicted landforms and deposits. *Volcanol. Geotherm. Res.*, 121:155–193, 2003.
- [2] T.K.P. Gregg and J.H. Fink. Quantification of lava flow morphology through analog experiments. *Geology*, (23):73–76, 1995.
- [3] D.A. Clague, J.G. Moore, and J.R. Reynolds. Formation of submarine flat-topped volcanic cones in Hawai'i. *Bull. Volcanol.*, (62):214–223, 2000.
- [4] N.T. Bridges. Ambient effects on basalt and rhyolite lavas under Venusian, subaerial and subaqueous conditions. *Jour. Geophys. Res.*, 102: E4:9243–9255, 1997.

- [5] H. Sigurdsson. Encyclopedia of Volcanoes. pages 1–1417, 2000.
- [6] D. Chester. Volcanoes and Society. pages 1–351, 1993.
- [7] S.H. Bloomer, R.J. Stern, and N.C. Smoot. Physical volcano-logy of the submarine Mariana and Volcano arcs. *Bull.of Volcanol.*, (51):210–22, 1989.
- [8] E.A. Parfitt, T.K.P. Gregg, and D.K. Smith. A comparison between subaerial and submarine eruptions at Kilauea volcano, Hawaii: implications for the thermal viability of feeder dikes. *J. Volcanol.Geoth. Res.*, (113):213–242, 2002.
- [9] T.K.P. Gregg and D.K. Smith. investigations of the Puna Ridge, Hawaii: relations of lava flow morphologies and underlying slopes. *J. Volcanol. Geoth. Res.*, 126:63–77, 2003.
- [10] M. Marani, F. Gamberi, and E. Bonatti. From seafloor to deep mantle: architecture of the Tyrrhenian backarc basin. *Memorie Descrittive Della Carta Geologica d'Italia*, 64:1–194, 2004.
- [11] K.A. Kastens et al. The geological evolution of the Tyrrhenian Sea: an introduction to the scientific results of ODP Leg 107. *Proc. Ocean Drill. Program Sci. Results*, 107:3–26, 1990.
- [12] N. Zitellini, F. Trincardi, M. Marani, and A. Fabbri. Neogene tectonics of the northern Tyrrhenian Sea. *Giornale di geologia*, 48:24–40, 1986.
- [13] M.P. Marani, T. Trua, et al. Thermal constriction and slab tearing at the origin of a superinflated spreading ridge: Marsili volcano (Tyrrhenian Sea,. *Journal of Geophysical Research*, 107:doi: 10.10, 2002.
- [14] L. Cocchi, F. Caratori Tontini, F. Muccini, M. P. Marani, G. Bortoluzzi, and C. Carmisciano. Chronology of the transition from a spreading ridge to an accretional seamount in the Marsili backarc basin (Tyrrhenian Sea). *Terra Nova*, 21:368–374, 2009.
- [15] L. Beccaluva, G. Gabbianelli, F. Lucchini, P.L. Rossi, and C. Savelli. Petrology and K/Ar ages of volcanics dredged from the Aeolian seamounts: implications for geodynamic evolution of the Southern Tyrrhenian basin. *Earth and Planetary Science Letters*, 74:187–208, 1985.
- [16] M.P. Marani, M Gamberi, F. and. Rosi, A. Bertagnini, and A. Di Roberto. Deep-sea deposits of the Stromboli 30 december 2002 landslide. pages 157–170, 2008.
- [17] M.P. Marani, M Gamberi, F. and. Rosi, A. Bertagnini, and A. Di Roberto. Subaqueous density flow processes and deposits of an island volcano landslide (Stromboli Island, Italy). *Sedimentology*, 56:1488–1504, 2009.

- [18] A. Di Roberto, M. Rosi, A. Bertagnini, M.P. Marani, et al. Deep water gravity core from the Marsili Basin (Tyrrhenian Sea) records Pleistocenic–Holocenic explosive events and instability of the Aeolian Archipelago, (Italy). *Journal of Volcanology and Geothermal Research*, 177:133–144, 2008.
- [19] A. Di Roberto, A. Bertagnini, M. Pompilio, F. Gamberi, et al. Newly Discovered Submarine Flank Eruption at Stromboli Volcano (Aeolian Islands, Italy). *Geophysical Research Letters*, 35:L16310, 2008.
- [20] A. Tibaldi, C. Corazzato, M. Marani, and F. Gamberi. Subaerial-submarine evidence of structures feeding magma to Stromboli Volcano, Italy, and relations with edifice flank failure and cree. *Tectonophysics*, 469:112–136, 2009.
- [21] N. Vidal and O. Merle. Reactivation of basement faults beneath volcanoes: a new model of flank collapse. *J. Volcanol. Geotherm. Res.*, (99):9–26, 2000.
- [22] T.R. Walter and V.R. Troll. Experiments on rift zone evolution in unstable volcanic edifices. *J. Volcanol. Geotherm. Res.*, (127):107–120, 2003.
- [23] M. Marani, F. Gamberi, and C. Savelli. Shallow-Water Polymetallic Sulfide Deposits In The Aeolian Island Arc. *Geology*, 25:815–818, 1997.
- [24] M.P. Marani, F. Gamberi, R.A. Binns, and J.M. Parr. Results from recent seabed sampling of hydrothermal deposits in the south Tyrrhenian Sea. *Mineral Deposits: Processes to Processing*, 719:547–550, 1999.
- [25] F. Gamberi, M. Marani, and C. Savelli. Tectonic, Volcanic and Hydrothermal Features of a Submarine Portion Of The Aeolian Arc (Tyrrhenian Sea). *Marine Geology*, 140:167–181, 1997.
- [26] O. Merle and A. Borgia. Scaled experiments of volcanic spreading. *J. Geophys. Res.*, 101: B6:13805–1381, 1996.
- [27] B. Van Wyk de Vries and R. Matela. Styles of volcano-induced deformation: numerical models of substratum flexure, spreading and extrusion. *J. Volcanol. Geotherm. Res.*, 81:1–18, 1998.
- [28] T. Trua, G. Serri, and M.P. Marani. Geochemical features and geodynamic significance of the southern Tyrrhenian backarc basin. *Geological Society of America, Special Paper*, 418:221–233, 2007.
- [29] K.A. Kastens et al. ODP Leg 107 in the Tyrrhenian Sea: Insight into passive margin and backarc basin evolution. *Geol. Soc. Am. Bull.*, 100:1140–1156, 1988.
- [30] C. Robin, P. Colantoni, M. Gennesseaux, and J.P. Rehault. Vavilov seamount: a mildly alkaline Quaternary volcano in the Tyrrhenian Sea. *Mar. Geology*, 78:125–136, 1987.

Cliff Instability at Tremiti Archipelago with Particular Reference to San Nicola Island (Southern Italy)

R. Pagliarulo

Research Institute for Geo-Hydrological Protection, CNR, Bari, Italy
r.pagliarulo@ba.irpi.cnr.it

Abstract

The cliffs of the Tremiti Islands, which are located in the Adriatic Sea in the North of the Apulian coastline (Southern Italy), are affected by severe instability processes. From the geological point of view, the Tremiti Islands are made of a sequence of bioclastic limestone, dolomitic limestone, calcilutite and calcarenite, with the age ranging from Paleocene to Middle Pliocene. These rocks are covered by a calcareous crust and loess deposits (Upper Pleistocene- Holocene). The structural set up of the major islands of the Tremiti (San Nicola and San Domino) is controlled by predominant NE-SW and E-W fault systems, which mark the coastlines of the islands. Along the cliffs, severe erosive processes are produced by different factors, as the climate and sea actions, and the effects of these processes are worsened by the seismic activity which affects the evolution of the cliff stability with time. These processes are mainly represented by block topplings, slidings and rockfalls. This study has represented the background for the engineering design in the stabilization works of the cliffs below.

1 Introduction

Due to severe climate contexts, islands are frequently involved in coastal instability processes, which are mainly represented by erosion and landsliding, that produce scenarios of active coastal evolution [1, 2, 3]. If such processes are characterised by high evolution rates they may expose the social and economic life of the islands to a risk. This is the case of the Tremiti archipelago (Adriatic Sea, Southern Italy) which represents a typical context where weathering and erosional processes along with deep landslide phenomena act on carbonatic rocks that are morphologically and structurally controlled by the geodynamic

evolution. Remarkable cultural heritage buildings lying on these islands are nowadays at risk due to the rapid evolution of erosion processes, rockfalls and mass movements occurring along the rock cliffs delimiting the island coasts. At present, such processes are inducing a narrowing of some portions of the islands with a negative impact on the preservation of the cultural heritage and in general on the future socio-economic life of the islands.

This paper describes some of the results of an original study about the Tremiti Islands, carried out within a research project (1997-2002) supported by the Italian National Research Council (CNR), which is aimed at defining the geological and geotechnical

incidences on the evolution of some archaeological sites. The study performed on the Tremiti islands has firstly been focused to field surveys in order to define both a detailed geological setup of the islands, as there were very few previous data about this topic, and the geomorphological processes, such as erosion and landslide processes, which are currently active. Therefore, the outcropping geological sequences have been described taking into account the new geodynamic interpretations of the whole area. Then, the mineralogical and petrographical features of the lithotypes have been analysed in order to understand the role of the physical and mechanical behaviour of these rock materials on their susceptibility to erosion and landslide and to predict the evolution of the same processes. The geological, geomorphological and geotechnical study has been aimed at discussing the factors controlling the erosional and landslide phenomena and identifying the areas with a high instability hazard. As a consequence, the main interest has been addressed to the island of San Nicola where the most remarkable examples of cultural heritage are located. [4].

The archipelago of the Tremiti Islands, located in the Adriatic Sea, about 22 km north of the Apulian coastline, is formed of four islands: San Domino, San Nicola, Caprara and the smallest Cretaccio. Another small island, Pianosa ($\sim 0,1 \text{ km}^2$), which is far away from the others, also belongs to the Tremiti municipality administration. San Domino is the most developed island from the touristic point of view and is also the biggest of the archipelago (2 km^2 surface area). San Domino has been inhabited since the 2nd millennium BC and was subsequently visited by the Greeks and Romans [5]. In the year 1000 it was chosen as a hermitage by the Benedictine monks

who later left the island and settled in San Nicola that is the most populated island. It is the site of a Monastery and the Abbey of Santa Maria [6]. The island of Caprara is deserted and the island of Cretaccio is a major block of rock, and thus uninhabited.

2 Structural set-up and geological outlines

The Tremiti archipelago represents the top of a E-W and NW-SW elongated structural high, along regional strike-slip fault alignments [7, 8]. It shows a gentle ($10^\circ \div 20^\circ$) SE vergent monoclinial setting. Within the complex geodynamic structures of the Mediterranean area the Tremiti archipelago belongs to the Adria microplate and in particular is located at the northern side of the Apulian foreland, (Figure 1). [9]). Deep seismic reflection data from Italian lithospheric exploration project CROP (Section M-13, [10]) show the huge positive Tremiti rose with two major right strike-slip faults (NE-SW) defined north and south by the EW fault zone [11]. This structure is interpreted as the antithetic structure of the Mattinata fault in the Gargano Promontory [12]. Subordinate dip-slip faults are associated with variable orientation from NS to WNW and ESE. Slight folds show NE-SW and WNW-ESE trends. A mesostructural study has been carried out by [13]. These analyses show joints and tension cracks with N-E and N-S trends, parallel to the local orientation of the coastline. The fault systems which have been observed are still seismically active [14, 15, 16]. In fact, since 1600 the Gargano region has been affected by several seismic events. Most of these events occurred offshore, therefore their epicentre, especially for the old-

est ones, is uncertain. Three important seismic sequences occurred between 1986 and 1990. In 1986 the first seismic sequence (body wave magnitude $m_b = 4.2$) was recorded 50 km North of the Tremiti Archipelago and subsequently a second one occurred in 1988 NNE off the Gargano Promontory ($m_b = 5.3$). In 1989 another earthquake was recorded with the epicentre at the Tremiti Islands ($m_b = 4.7$) [15]. It is not already clear which are the local effects of seismicity but in the particular geological setting examined the seismic stress may also result in important co-seismic effects, such as the weakening of the rock masses along the joint systems.

From the geological point of view the Tremiti Archipelago consists of a discontinuous sequence of carbonatic marine sediments, ranging from Late Paleocene - Early Eocene to Middle - Late Pliocene, overlain by late Pleistocene and Holocene discontinuous continental deposits (Figure 2).

Being a gentle SE-dipping slightly folded monocline structure, the older formation outcrops at the San Domino island. The thickness of the Bue Marino Formation, which is the oldest one, is about 60 m and the age is Late Paleocene [17]. In transgression on these deposits there is the Caprara Formation which has a maximum thickness of 25 m. The age of this Formation is attributed to Early Eocene. A continuity of sedimentation characterises the contact between the Caprara Formation and the San Domino Formation which outcrops widely at San Domino, Caprara and Cretaccio islands, in accordance with the framework of the Tremiti islands. The total thickness of San Domino Formation is about 200 m and it includes different lithofacies: stratified yellow-greenish dolomites, calcitic dolomites, doloarenites,

recrystallized dolomitic calcarenites, whitish Nummulites biocalcarenes and biocalcilitites sometimes dolomitized, biostromal banks and breccias in the upper levels referable to Middle-Late Eocene. This formation is overlain by the Cretaccio Formation through a transgressive surface. This is the most widespread unit both in the islands and in the sea floors among them. The lower member is made up of well stratified yellow - greenish and yellow - reddish glauconitic laminate doloarenites, which pass upwards to marly biocalcilitites, yellow - whitish fossiliferous marls, yellow - whitish and occasionally greyish calcisiltites containing yellow limonite clasts. In these deposits soft sediment structures are clearly visible, probably due to liquefaction phenomena triggered by seismic activity. The total thickness of the formation is about 150 m and the age is referred to Middle Miocene. The Cretaccio Formation is overlain by the San Nicola Formation which outcrops at San Nicola island and is about 35 m thick. It consists of hard recrystallised and fractured dolomitic calcarenites [18]. These formations are mainly affected by the erosion and landsliding processes described in the following sections. The succession ends with whitish - yellow calcareous travertinoid crusts referable to Middle - Late Pliocene. The whole succession of continental deposits of the Upper Pleistocene and Holocene can be observed at San Domino. At the base there are well cemented conglomerates with reddish sandy - silty matrix, followed by 2 m thick marly limestones and red marl horizon, which is overlain by eolian deposits that are interbedded by carbonate crusts.

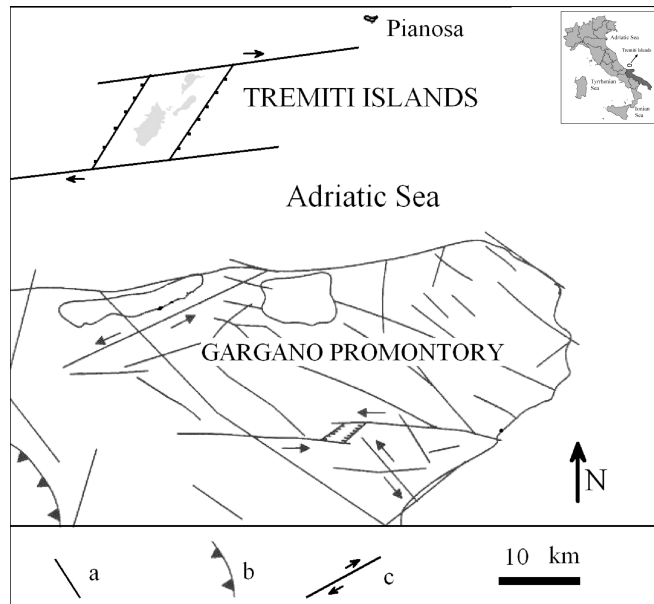


Figure 1: Schematic structural setting of the Tremiti Islands and the Gargano Promontory (the area of the islands is not in scale) with evidences of extensive strike-slip and normal faulting and block rotation. a) Main faults; b) Apenninic thrust front; c) faults with a prevailing strike-slip movements, (after [13], modified).

3 Geomorphological features

The Tremiti Archipelago is characterised by a slightly rough morphology with a landscape having steep slopes and subtabular tops gently SE dipping due to the monoclinal structure. Locally, slight anticline fold structures dislocated by faults can be noticed, the most important of which is located in San Domino island at Poggio del Romito, the highest relief of the Tremiti islands. The coastal morphology is characterized by high rock cliffs (up to about 60 m high at San Nicola) and low relief flat coasts with gently dipping convex slopes. In the areas where the Eocene and Pliocene formations outcrop, the cliffs are

approximately sub-vertical with overhanging blocks; slope angles ranging between 50° and 75° instead characterise the cliffs in the Miocene strata of San Nicola island. The flat coast sectors are slightly indented and contains large pocket beaches. The only one sandy beach, Cala delle Arene, is located at San Domino. Where the Paleogene formations outcrop, the coastline is articulated in caps and promontories, inlets, small bays and sea caves, arches and stacks. Inlets, small bays and sea caves are mainly located along faults and joint systems. Arches and stacks, related to the main fault trends, are produced by wave action, although, locally, notches are not visible. Where Miocene and Pliocene deposits outcrop, due to the rapid recession

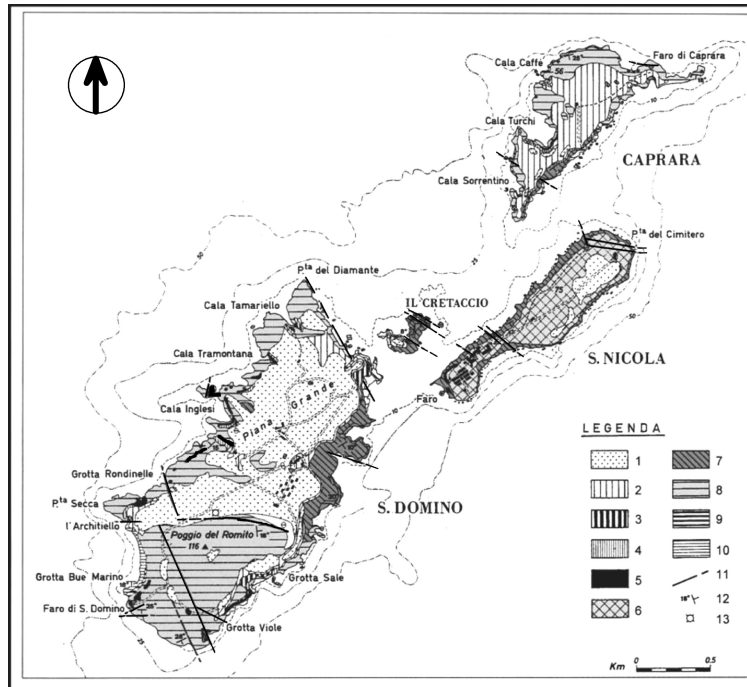


Figure 2: Geological sketch of the Tremiti Islands (after [17], modified): 1) Brown loess (late Pleistocene- Holocene); 2) Calcareous crust (late- middle Pleistocene); 3) Yellowish loess (middle- late Pleistocene); 4) Loess and reddish gravels (middle Pleistocene); 5) Conglomerates and marly limestones (middle Pleistocene); 6) San Nicola Fm (middle late Pliocene); 7) Cretaccio Fm (Aquitanian- Tortonian); 8) San Domino (middle-late Eocene); 9) Caprara Fm (early Eocene); 10) Bue Marino Fm (Paleocene); 11) Faults; 12) Bedding attitudes; 13) Borehole Tremiti 1.

of the cliffs, the coastline is more regular and large sea caves, inlets and other landforms due to erosive phenomena are less frequent, [19]. Karst processes have mainly produced superficial landform characterised by either joints enlarging by solution or joints filled with residual materials. In the Tremiti Islands groundwater is not present and there is no evidence of karst drainage in the caves.

4 Erosional and weathering processes

The evolution of the coastal morphology of the Tremiti Islands is mainly related to mass movements and selective erosion processes which are at present very active.

The weathering processes of the rock materials forming the cliffs are related to the climatic conditions [3]. The climate at the Tremiti Islands is typically Mediterranean and is therefore characterized by an an-

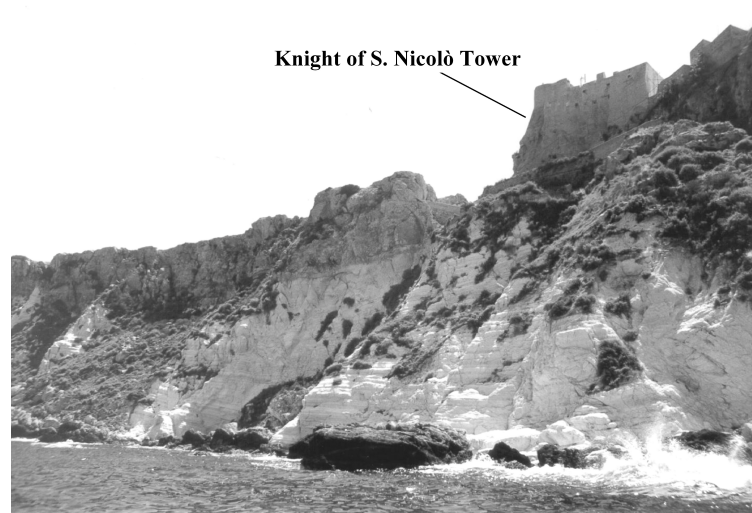


Figure 3: The N-W coast of San Nicola: the Cretaccio Fm with the overlying San Nicola Formation. Selective erosion between limestone and calcilutite can be seen in the upper part while intense sea erosive processes are visible at the foot of the cliff.

nual trend of temperatures with mild winters and warm and dry summers. The minimum values of the temperature are recorded in January (9.2°C) while the maximum values occur in August (29°C) with peaks reaching up to 38°C . The rainfalls are concentrated in the autumn - winter term ($\sim 476\text{ mm}\cdot\text{yr}^{-1}$ on average) and the wind regime is characterised by predominant winds coming from the 2nd and 4th quadrant. Sea conditions are stable during summer time while rough seas and strong storms are frequent in the period autumn-winter. These storms are mainly responsible for the erosion processes of the rock cliffs, [20, 1]. The impact force of rainfall water, the rain infiltration and the wind erosion remove fine particles from the rock matrix, mainly along either the exposed calcarenite joints (San Nicola Formation) or the calcisiltite and calcilutite (Cretaccio Formation) cliff surfaces. In

particular, the Cretaccio Formation is characterised by a high susceptibility to erosion due to a weak cement and a fine grain size. In fact, flaking, pulverization and disaggregation of cement, cracking and dissolution weaken the levels composed of finer particles and make them more friable. This, frequently, causes overhanging calcarenite blocks due to selective erosion at the contact between the calcarenite and calcilutite levels. Moreover, cyclic wetting - drying processes induces weathering within the most shallow portions of the rocks belonging to Cretaccio and S. Nicola formations [21]. The disintegration of rock resulting from alternate wetting and drying causes the growth of salt crystals, [3]. The sea spray action, particularly active during strong storms, contributes to the chemical and salt weathering and to the general degradation of the rock cliff surfaces. The effects of all these pro-

cesses give rise to a layer of external rock material which is weaker and more erodible. Thermic stresses are also particularly effective on the calcarenitic levels.

The above described processes have a larger impact on the coast sectors characterised by high cliffs, as in San Nicola island, where weak and porous marly calcisiltites are overlain by stiff calcareous and dolomitic rock masses [22, 19].

5 Mechanisms of coastal landsliding

The instability processes observed along the coasts of the Tremiti islands are characterised by different mechanisms. At San Domino and Caprara the more diffuse collapse mechanism is represented by rockfalls of small to medium size overhanging rock blocks, which is induced by the gradual undercutting either at the cliff foot, due to the sea erosion at the notch level, (Figure 3), [23]), or at higher levels due to selective erosion phenomena. In particular, these phenomena occur in the Paleogene formations after large sea storms, heavy rainfalls and seismic shocks. Tensile failures are frequent along the sides of the top of the islands due to either stress release or concentration of tensile stresses (Figure 4); as a consequence, this induces toppling or sliding of large dislocated blocks [24, 2, 25, 21].

The instability processes at San Nicola island are particularly evident and the failure mechanisms of the rock slopes are complex. Landslides mainly occur as rockfalls, topplings and retrogressive slides. All along the coasts of the island, large fractures often start to develop within the weaker Miocene calcilutite and calcisiltite

and are characterised by a retrogressive evolution [26]. In particular, the deformation processes induce tension stresses at the top of the overlying Pliocene dolomitic calcarenite, which is stiffer. As a consequence, cracks and fractures develop due to the exceeding of the tensile strength of the same rock material. These tension cracks delimit blocks on the top of the slopes which are susceptible of toppling [27].

Rockfalls and topples are also frequent along both the costal sectors adjacent to the Abbey of Santa Maria and are generally produced by either the selective erosion at the contact between the two formations or the action of the climatic agents along the rock joint surfaces (Figure 5). Due to the progression of such processes, nowadays the current profile of the cliffs at both sides of the Abbey is aligned with that of the walls of the monumental structure, thus inducing high risk for this important historical building.

Along the southern coast of San Nicola island, i.e. the harbour area, rockfalls, topples and block slidings can be observed. In particular, block slidings are presumably induced by the rain infiltration within the dip-slope joints which causes the reduction of the shear strength of the joints due to weathering of the rock surfaces.

A geomechanical characterization of the intact rock and of the joints has been carried out at San Nicola island in order to estimate the main physical behaviour of the two main rock materials [28]. Erosion at the sea level and the weathering of the exposed joint surfaces are some of the most important processes which induce the general or partial collapse of the cliffs [4].

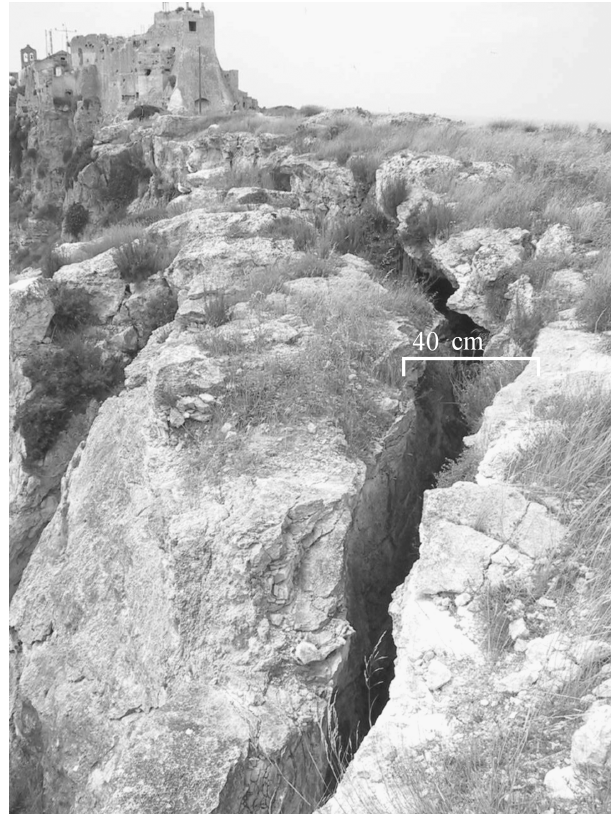


Figure 4: Tensile failure within the upper rigid formation at San Nicola. In the background the fortress with the tower of San Nicolò.

6 Conclusive remarks

An integrated study involving geostructural, geomorphological and geomechanical analysis has been carried out in order to investigate the instability processes which severely affect the cliffs of the island of San Nicola, above which the S. Maria Abbey was built, and the factors controlling them. Field surveys have shown that the geomorphological evolution of the Tremiti Islands is significantly influenced by weathering and subaerial processes. The morphology of the islands is related to both the geo-

dynamic evolution and the climatic conditions of the area at the regional scale and the resulting landforms are dynamically evolving according to the current morphogenetic processes. In particular, the coastal morphology results from the combined actions of tectonics, sea wave action, wind erosion and rain infiltration. The lithology of the outcropping rocks, which are weak and erodible, is a predisposing factor for different instability processes, such as weathering, erosion and deep landslide processes. Therefore, the environmental

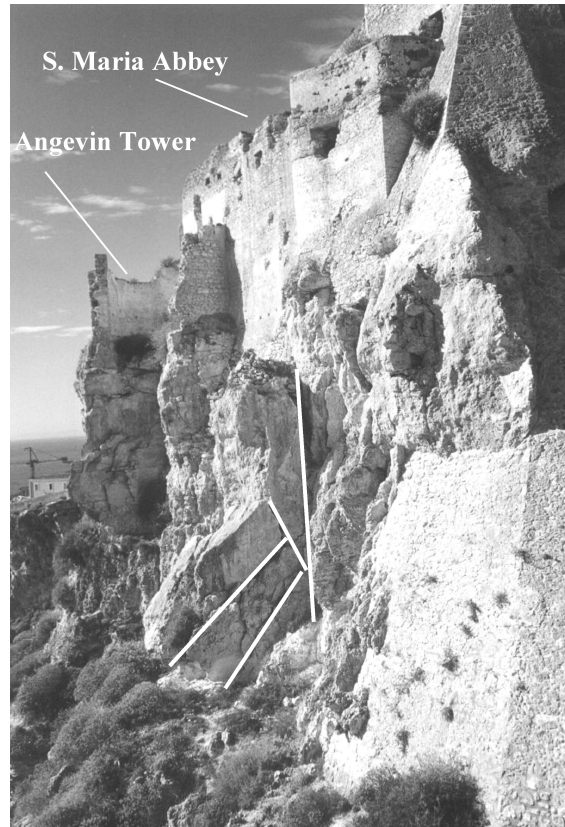


Figure 5: Large rock blocks, delimited by white lines, prone to topple on the South-Eastern cliff of San Nicola island. A close-up of the Angevin tower partially collapsed and the external wall of the fortress aligned with the cliff edge.

factors produce a gradual weakening of the rock masses in the long term, making them prone to selective erosion and landsliding phenomena, which are favoured by the presence of an intensely fractured dolomitic calcarenitic formation overlying a weaker calcisiltitic and calcilitic formation. Different kinds of failure mechanisms have been observed at San Nicola island, according to the particular geological setting, such as rockfalls, topplings and lateral spreads with retrogressive evo-

lution. Locally, the presence of artificial and natural rock blocks and debris at the foot of the cliffs represents an effective protection structure to the wave attack during storms. The salt weathering along with the rain infiltration causes chemical degradation of the most external portions of the rocks. The wind erosion is particularly effective on the friable and low cemented calcarenites and biomicrites of the San Nicola Formation. This frequently causes isolated overhanging calcarenite blocks prone

to fall. In the eastern side of the island few cases of rock sliding along dip-slope bedding planes have been noticed. At San Domino and Caprara islands, medium-size block rockfalls due to both undercutting processes, mainly at the notch level, and the detachment of overhanging blocks are widespread.

References

- [1] A.S. Trenhaile. Modelling the role of weathering on shore platform development. *Geomorphology*, 94:24–39, 2008.
- [2] T. Sunamura. Geomorphology of rocky coasts. *Wiley, New York*, page 302, 1992.
- [3] W.J. Stephenson and R.M. Kirk. Development of shore platforms on Kaikoura Peninsula, South Island, New Zealand II: The role of subaerial weathering. *Geomorphology*, 32(1-2):43–56, 2000.
- [4] P. Lollino and R. Pagliarulo. The interplay of erosion, instability processes and cultural heritage at S. Nicola island (Tremiti Archipelago, Southern Italy). *Geografia Fisica e Dinamica Quaternaria*, 31(2):161–169, 2008.
- [5] F. Delli Muti. *Le Isole Tremiti*. Ed. Marietti. 1965.
- [6] C.B. McCledon. The church of S. Maria di Tremiti and its significance for the history of Romanesque architecture. *The Journal of the Society of Architectural Historians*, 43(1):5–19, 1984.
- [7] D. Ridente and F. Trincardi. Eustatic and tectonic control on deposition and lateral variability of Quaternary regressive sequences in the Adriatic basin (Italy). *Marine Geology*, 184:273–293, 2002.
- [8] R. Gambini and M. Tozzi. Tertiary geodynamic evolution of the Southern Adria microplate. *Terra Nova*, 8:593–602, 1996.
- [9] C. Doglioni, M. Tropeano, F. Mongelli, and P. Pieri. Middle–Late Pleistocene uplift of Puglia: an anomaly in the apenninic foreland. *Memorie Società Geologica Italiana*, 51:101–117, 1996.
- [10] I.R. Finetti and A. Del Ben. Crustal tectono-stratigraphic setting of Adriatic Sea from new CROP seismic data. CROP Project, 1 Deep Seismic Exploration of the central Mediterranean and Italy (Atlases in Geosciences) Elsevier (Finetti I.R. Editor). 1:519–547, 2005.
- [11] C. Nicolai and R. Gambini. Structural architecture of the Adria platform-and-basin system. *Bollettino Società Geologica Italiana*, 7:21–37, 2007.
- [12] C.M. Brankman and A. Aydin. Uplift and contractional deformation along a segmented strike-slip fault system: the Gargano Promontory, southern Italy. *Journal of Structural Geology*, 26:807–824, 2004.

- [13] G.F. Andriani, N. Walsh, and R. Pagliarulo. The influence of the geological setting on the morphogenetic evolution of the Tremiti Archipelago (Apulia, Southeastern Italy). *Natural Hazards and Earth System Sciences*, 5:29–41, 2005.
- [14] A. Argnani, G. Bortoluzzi, P. Favali, F. Frugoni, M. Gasperini, M. Ligi, M. Marani, G. Mattiotti, and G. Mele. Foreland tectonics in the Southern Adriatic Sea. *Memorie Società Geologica Italiana*, 48:573–578, 1994.
- [15] P. Favali, R. Funiciello, G. Mattiotti, G. Mele, and F. Salvini. An active margin across the Adriatic Sea (Central Mediterranean Sea). *Tectonophysics*, 219:109–117, 1993.
- [16] C. Montone and R. Funiciello. Elementi di tettonica trascorrente alle Isole Tremiti (Puglia). *Rendiconto Società Geologica Italiana*, 12:7–12, 1989.
- [17] R. Selli. Isole Tremiti e Pianosa in Note Illustrative della Carta Geologica d'Italia, F° 156 San Marco in Lamis. *Serv. Geol. d'Italia, Roma*, pages 49–64, 1971.
- [18] V. Cotecchia, A. Guerricchio, and G. Melidoro. Geologia e processi di demolizione costiera dell'isola di S. Nicola (Tremiti). Atti I Conv. Gruppo Naz. Geol. Appl. Geologia Applicata e Idrogeologia. 30(I):491–507, 1995.
- [19] G.F. Andriani and A. Guerricchio. Caratteri litostratigrafico-tessiturali e geomeccanici delle rocce affioranti nell'isola di San Nicola (Isole Tremiti). *Geologia Applicata e Idrogeologia*, 31:87–105, 1996.
- [20] A.S. Trenhaile. The geomorphology of rock coasts. Oxford Univ. Press. page 388, 1987.
- [21] A.S. Trenhaile. Coastal Dynamics and Landforms. Oxford Univ. Press. page 366, 1997.
- [22] V. Cotecchia. Geotechnical vulnerability and geological evolution of the Middle Adriatic coastal environment. *Rivista Italiana di Geotecnica*, 33(3):46–55, 1999.
- [23] R.J. Allison and O.J. Kimber. Modelling failure to explain rock slopes change along the Isle of Purbeck coast (UK). *Earth Surface Processes and Landforms*, 23(8):731–750, 1998.
- [24] T. Sunamura. Mechanisms of shore platform formation on the southern coast of the Izu Peninsula. *Japan Journal of Geology*, 86(2):211–222, 1978.
- [25] T. Sunamura. Rock control in coastal geomorphic processes. *Transaction, Japanese Geomorphological Union*, 15(3):253–272, 1994.
- [26] R.J. Allison and D. Brusden. Some mudslides movement pattern. *Earth Surface Processes and Landforms*, 15:297–311, 1990.

- [27] O.J. Kimber, R.J. Allison, and N. Cox. Mechanisms of failure and slope development in rock masses. *Transaction of the Institute of British Geographers*, 23(3):353–370, 1998.
- [28] V. Cotecchia, P. Lollino, and R. Mastromattei. Analisi dei processi demolitori naturali e di taluni interventi mirati alla riduzione del rischio ed al restauro monumentale delle Isole Tremiti. VI Ciclo di Conferenze di Meccanica ed Ingegneria delle Rocce (MIR), Torino. pages 145–172, 1998.

Earthquakes-Induced Environmental Effects in Coastal Area: Some Example in Calabria and Sicily (Southern Italy)

S. Porfido¹, E. Esposito¹, C. Violante¹, F. Molisso¹, M. Sacchi¹, E. Spiga²

¹, Institute for Coastal Marine Environment, CNR, Napoli, Italy

², Geologist, ES OR Campania n.85, Avellino, Italy

sabina.porfido@iamc.cnr.it

Abstract

The Messina Strait, between Calabria and Sicily's Coast, is one of the most seismically active areas of the Southern Italy. Since 1783, there have been 7 earthquakes with M ranging between 6.0 and 7.2. They have produced wide damages and induced numerous and spectacular coseismic environmental effects (primary and secondary effects) overall along the coast where the impact was particularly catastrophic. These earthquakes caused several changes in elevation, landslides and settlements, relevant landslides (the 1783 event triggered in Scilla, along the cliff of the M. Pacì a huge rock avalanche of 5 Mm^3 in the areal and 3 Mm^3 in the submarine zone, generating a disastrous tsunamis), ground fractures (Capo V. area, during the 1905 seismic event; in Messina, Reggio C., Villa S. Giovanni, during the 1908 event); liquefaction phenomena (Messina, Ganzirri and Reggio C., 1908 event), and catastrophic tsunamis (5 induced by the 1783 events, other 2 by 1905 and 1908 events).

The run-up observed ranging from few centimeters to tens of metres: the highest tsunami wave was about 16 m in Scilla (Feb. 6, 1783 tsunami), 13 m in Pellaro (1908 event) and 1,30 m along the Calabrian coast (1905 tsunami). Finally, it is important to consider the seismically induced effects with the aim to reduce the future risk for the population living along the coast and the potential damage to structures and natural environment, through a more precise estimate of their type, size and distribution, according to the new macroseismic scale ESI2007.

1 Introduction

The seismicity of the Calabria and Sicily regions and in particular of the Messina Strait is strictly connected with the Siculo-Calabrian rift zone, one of the most seismically active areas of the Italian peninsula, characterized by several seismogenic sources (ITHACA) capable of producing earthquakes with $M \geq 7$ and intensity values $I \geq X$ both on the MCS scale (CPTI04)

and on the new macroseismic scale ESI 2007 [1]. The historical seismicity occurred in this area, is well documented and shows a very high-recurrence of large events with at least 34 earthquakes with $VII \leq I \leq XI$ on the MCS scale; nine events with $I = X-XI$ in the last 2000 years, five of which in the last 225 years and two in XX century (Table 1 and Figure 1). The Siculo-Calabrian seismic belt includes the largest earthquakes which have

occurred in southern Italy in the last six centuries as the 1693 earthquakes, the 1783 seismic sequence, the 1905 Calabria earthquake and the 1908 Messina - Reggio Calabria earthquake. These earthquakes produced wide damage on the urban design and triggered spectacular coseismic environmental effects along the coastal area.

2 Methodology

According to the original definition of macroseismic Intensity (MCS, MM, MSK, EMS Scales) the assessment degrees can be defined as a classification of earthquake induced effects on human, manmade structures and natural environment. Although geological effects were included in the traditional macroseismic scales, later on they have been disregarded by the seismologists dealing with intensity estimates. It was probably due to their inner complexity and variability requiring specific skills and knowledge. Specific studies on earthquake induced ground effects have offered new evidence that coseismic environmental effects provide precious information on the earthquake size and its intensity field, complementing the traditional damage-based macroseismic scale ([1] and references therein).

The Environmental Seismic Intensity Scale (ESI2007 Scale) is a new earthquake intensity scale only based on the effects triggered by the earthquake in the natural environment. The ESI2007 Scale follows the same basic structure as any other 12 degree scale, such as the MCS, MM, MSK etc. It is based on the observation of the environmental features, such as surface faulting, subsidence, uplift (primary effects) and liquefaction, ground crack, slope movement, hydrological changes, tsunami (secondary

effects). As the traditional macroseismic scales, the ESI2007 Scale is a tool to assess both epicentral (I_0) and local (II) intensities. The epicentral (I_0) intensity is defined as the intensity of shaking at epicenter; several techniques can be applied to assess I_0 : according to Postpischl (1985) I_0 is "the value of the closed isoseismal line having the highest degree and including at least 3 different data points". Starting from intensity VII, the ESI2007 scale considers surface faulting parameters and total area of distribution of secondary effects as diagnostic element for I_0 assessment. According to this approach, ranges of surface faulting parameters (primary effects) and typical extents of total area of secondary effects for each intensity degree, have been defined [1].

These studies attempt at reconstructing the coseismic effects on the basis of a careful review of contemporary documents (i.e. documentary sources, historical and technical reports, expert investigations, diaries, historical books, iconographic material and newspapers) and on the most recent scientific literature. In this perspective, the environmental effects of three of the most ruinous earthquakes, of the last three centuries, in the area of the Messina Strait are analyzed according to the new macroseismic scale ESI 2007 (Environmental Seismic Intensity, [1]): the 1783 Calabrian seismic sequence, (I = XI MCS, M 6.91-7.2), the September 8, 1905, Calabria event (I = XI MCS, M 7.06-7.9), and the December 28, 1908 Messina - Reggio Calabria event (I = XI MCS, M 7.24-7.32).

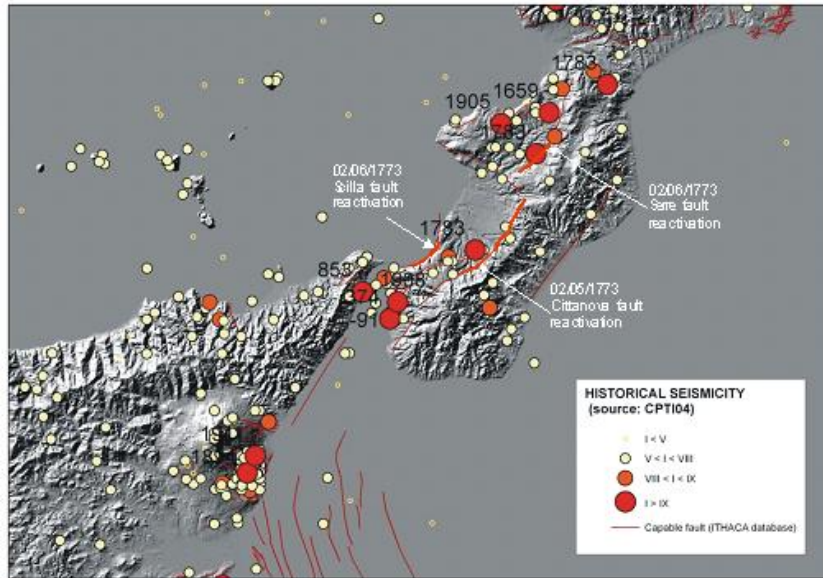


Figure 1: Historical earthquakes occurred in the last 2000 years in the Siculo-Calabrian Rift. Red bold line indicate active faults (according to CPTI04 and ITHACA database).

3 The 1783 seismic sequence

The 1783 Calabrian seismic sequence was characterized by a three years long sequence and five main shocks generated by individual fault segments of regional WNW-ESE trends.

The 1783 multiple event started at the beginning of February and went on until the end of March, reaching a maximum release of energy on March 28 with assessed macroseismic magnitude $M=6.9$ (CPTI04). More than 30,000 lives were lost and 200 localities were completely destroyed by the February 5 main shock; the epicentral area ($I_0 = XI$ MCS) was located on the Gioia Tauro plain, at the western foot of the northern Aspromonte mountain. The shock produced spectacular ground effects,

both primary and secondary, such as tectonic deformations, ground fractures, liquefaction phenomena, tsunamis, hydrological changes and diffuse landslides of large size, which in most cases dammed the rivers creating more than 200 new temporary lakes. The second shock, occurred on February 6, struck the coast between Scilla and Palmi and induced the large Monte Paci-Campallà rock avalanche from the sea-cliff west of Scilla, generated a disastrous tsunami (Figure 2, run-up of 16 m), that affected the coast for a total length of 40 km, from Bagnara to Villa San Giovanni and from Torre Faro to Messina, causing more than 1500 casualties in Scilla [2, 3, 4].

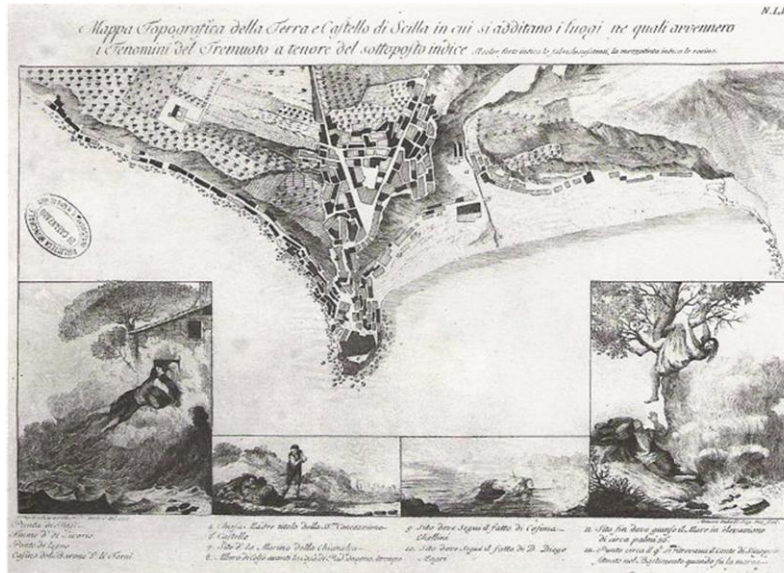
Recently a dynamic numerical modelling by FDM code FLAC 6.0 was performed by [5], to back-analyse the landslide occurred

| | | | | |
|---|-------------|--------------------|------|------|
| 374 | | Southern Calabria | 9.5 | 6.30 |
| 853 | 08 31 | Messina | 9.5 | 6.30 |
| 1169 | 02 04 07 | Eastern Sicily | 10.0 | 6.60 |
| 1184 | 05 24 | Crati Valley | 9.0 | 6.00 |
| 1509 | 02 25 22 20 | Southern Calabria | 8.0 | 5.57 |
| 1626 | 04 04 12 45 | Girifalco | 9.0 | 6.08 |
| 1638 | 03 27 15 05 | Calabria | 11.0 | 7.00 |
| 1638 | 06 08 09 45 | Crotonese | 9.5 | 6.60 |
| 1659 | 11 05 22 15 | Central Calabria | 10.0 | 6.50 |
| 1693 | 01 11 13 30 | Eastern Sicily | 11.0 | 7.41 |
| 1743 | 02 20 16 30 | Southern Ionio | 9.5 | 6.90 |
| 1767 | 07 14 01 05 | Cosentino | 8.5 | 5.83 |
| 1783 | 02 05 12 | Calabria | 11.0 | 6.91 |
| 1783 | 02 06 00 20 | Southern Calabria | 8.5 | 5.94 |
| 1783 | 02 07 13 10 | Calabria | 10.5 | 6.59 |
| 1783 | 03 01 01 40 | Central Calabria | 9.0 | 5.92 |
| 1783 | 03 28 18 55 | Calabria | 10.0 | 6.94 |
| 1786 | 03 10 14 10 | North-East. Sicily | 9.0 | 6.02 |
| 1791 | 10 13 01 20 | Central Calabria | 9.0 | 5.92 |
| 1818 | 02 20 18 15 | Catanese | 9.0 | 6.00 |
| 1823 | 03 05 16 37 | Northern Sicily | 8.5 | 5.87 |
| 1832 | 03 08 18 30 | Crotonese | 9.5 | 6.48 |
| 1835 | 10 12 22 35 | Cosentino | 9.0 | 5.91 |
| 1836 | 04 25 00 20 | Northern Calabria | 9.0 | 6.16 |
| 1854 | 02 12 17 50 | Cosentino | 9.5 | 6.15 |
| 1870 | 10 04 16 5 | Cosentino | 9.5 | 6.16 |
| 1894 | 11 16 17 52 | Southern Calabria | 8.5 | 6.05 |
| 1905 | 09 08 01 43 | Calabria | 11.0 | 7.06 |
| 1907 | 10 23 20 28 | Southern Calabria | 8.5 | 5.93 |
| 1908 | 12 28 04 20 | Southern Calabria | 11.0 | 7.24 |
| 1909 | 07 01 06 24 | Calabro- Messinese | 8.0 | 5.55 |
| 1947 | 05 11 06 32 | Central Calabria | 8.0 | 5.71 |
| 1978 | 03 11 19 20 | Southern Calabria | 8.0 | 5.36 |
| 1978 | 04 15 23 33 | Patti Gulf | 9.0 | 6.06 |
| The largest earthquakes occurred in the Calabria an Sicily in the last 2000ys | | | | |

Table 1: List of the largest earthquakes occurred in Southern Italy in the last 2000 years ($I \geq VIII$ MCS, CPTI04).

in Scilla during the 1783 seismic sequence, the results of modeling show a post-seismic trigger of the rock-avalanche, related to the second main shock of the 1783 events. From February 7 to March 28, three main shocks took place with epicenters migrating northwards from Mesima Valley to Catanzaro. The last one caused severe damage along both the Tyrrhenian and Ionian coasts. The cumulative effects of all these earthquakes was devastating, more than 380 villages were damaged, 180 were totally destroyed. From a seismogenic point of view the 1783 sequence can be related to the active fault segments present in southern Calabria [6, 7, 8, 9, 10], combin-

ing geological, morphological and seismological data have been identified three of the most significant fault segments generating the 1783 sequences for a total length of ca.100 km. The amount of surface faulting (rupture length and maximum displacement and the minimum total area distribution of secondary effects 11.000 km² (Figure 3) indicate $I_0 = XI$ on ESI 2007 scale, in good agreement with I_0 resulting from MCS scale.



Mappa topografica della terra e castello di Scilla in cui si additano i luoghi ne quali avvennero i fenomeni del terremoto... (Schiantarelli, 1784)

Figure 2: Historical drawing illustrating the tsunamis triggered by the February 6, 1783 event along the Scilla coast (Schiantarelli, 1784).

4 The 1905 Southern Calabria earthquake

On September 8, 1905 a large earthquake with estimate Magnitudes ranging from $M \approx 7.0$ to $M \approx 7.9$ and MCS intensity XI occurred in the the Capo Vaticano peninsula (Calabria). Several Authors identified different epicenters both inland, near to Vibo Valentia, and offshore not far from the coastline, suggesting as capable faults the Vibo and Capo Vaticano normal fault segments [9]. This earthquake extensively ruined several villages located in the northern part of the Capo Vaticano peninsula within an area that suffered a MCS intensity greater than IX, causing the death of 557 people.

The event induced a great number of effects on the environment in a wide area [11, 12, 10, 13]: large landslides, accompanied by several cracks and fractures (Aiello Calabro, Martirano, Gero carne, Cirò, Conidoni, Acri etc) and liquefaction features occurred in several places within the epicentral area (Tropea, Aman tea, Seminara, Rosarno etc), hydrological variation (changes in flow and in the temperature of springs and rivers) were also observed over the entire Calabria region both in the near field (Piscopio, Curinga, Martirano, Rosarno etc.) and far field (Orsomarso, Cetraro etc). This event also generated a tsunami (Sieberg-Ambraseys Int. 4) that inundated the whole northern coast of the peninsula from Vibo to Tro-

pea with an estimated height of waves of about 1-2 m, the anomalous waves were observed also in Scalea, Ischia, Civitavecchia, Naples and Messina with a run-up of few cm, [14] and moreover submarine telephone cable 12 km East from Vulcano Island was cut (Figure 4). On the basis of all the collected data it was possible to estimate the total area distribution of secondary effects, about 15,000 km² and assess the ESI 2007 intensities values $I_0 = X$ (Figure 5) in agreement with the equivalent MCS assessment (CPTI04).

5 The 1908 Southern Calabria-Messina earthquake

The December 28, 1908 Southern Calabria-Messina earthquake ($I = XI$ MCS, $M 7.2$) is one of the strongest seismic events that struck Italy during the XXth century and the most ruinous in terms of casualties (at least 80,000). The epicentre was located at sea in the Messina Straits. The impact of the earthquake was particularly catastrophic in Reggio Calabria and Messina, damages have been more intense and widespread along the Calabrian coast, between south of Reggio Calabria and south-west of Scilla. In Sicily the most damaged area was the coast from its easternmost tip to south of Messina. Some minutes after the earthquake, a destructive tsunami (Sieberg-Ambraseys Int.6) inundated both sides of the Strait, with a run-up that rose above 10-13 meters in some places (Sant'Alessio, Pellaro), killing at least 2,000 people, with maximum on-land water penetration of 600 m in Pellaro and 700 m in Catania [15]. More than 100 environmental effects were catalogued

among them, particularly relevant were the changes in elevation along both sides of the Strait, partly due to the settlement of loose sediments and artificial filling (e.g., Messina and Reggio Calabria harbor areas), and partly ascribed to landslides and tectonic slip. Liquefaction was reported in the areas of Messina, Pantano (lake Ganzirri) and Reggio Calabria. Portions of the coast were lost, especially on the Calabrian side, most of them eroded by the tsunami. The most relevant ground cracks were reported in Messina, Reggio Calabria and at San Procopio near Sant'Eufemia in Calabria (4-5 km long, according to [16]). Landslides and rockfalls occurred in many Sicilian and Calabrian localities (especially between Reggio C. and Bagnara C.). A submarine telephone cable between Gallico (in Calabria) and Gazzi (in Sicily) was cut likely by a slide. In both the regions ground collapses and also several hydrological anomalies occurred: springs flow-rate and elevation changes, water temperature variations and gas emissions [17]. The obtained database allows a comprehensive view of ground coseismic environmental effects [17], giving also the possibility to apply the ESI 2007 environmental intensity scale in order to corroborate the intensity evaluation of the earthquake. It is readily evident that, apart from the huge tsunami wave, in agreement with a submarine location of the epicentral area, coseismic environmental effects appear to be modest with respect to the effects reported for earthquakes of similar magnitude occurred in the same region (i.e., 1783 Calabrian and 1905 earthquakes) in this case the epicentral intensity based on the ESI 2007 scale $I_0 = X$ is slightly lower than the corresponding MCS $I_0 = XI$.

6 Discussion and conclusion

The contemporary documents analyzed, include descriptions of environmental coseismic phenomena effects associated with the earthquakes, becoming more and more scientifically accurate with time. In this study, this wealth of knowledge is reviewed for a set of chosen events, to scrutiny the practical applicability of the ESI2007 scale in order to: (a) reassess the epicentral intensities (I_0) for three historical events in the same region, and (b) contribute to reduce the future risk from environmental effects, through a more precise estimate of their type, size and distribution in the earthquake-prone areas.

The review of the effects on the natural environment triggered by these three catastrophic earthquakes, through the last three centuries, has allowed estimation of epicentral intensity values independently from the damage effects on the man made structures.

The ESI 2007 epicentral intensity (I_0) values, are based essentially on primary effects and in particular on the length of surface faulting, as the maximum offset is generally not available. The actual surface rupture length is not readily provided by historical information. At best, only its most prominent part is reported. However, the total rupture can be inferred, based on the distribution of ground ruptures interpretable as coseismic faulting and the characteristics of the macroseismic field.

The earthquakes analysed here share the

same epicentral intensity (X and XI ESI 2007 scale) in good agreement with the corresponding MCS XI values. Similarly, the total area distributions of secondary effects have provided I_0 values consistent with these estimates, when the primary effects are not available.

The comparison between ESI scale and MCS scale intensities has shown a difference for the 1905 and 1908 events, where maximum ESI intensity is one degree lower than the corresponding MCS ones, according to the concentrated areal distribution of the ground effects occurred. The use of Earthquake Environmental Effects for intensity assessment recently promoted by the ESI 2007 scale provide an added value to traditional intensity evaluations being applicable also in not inhabited areas and not afflicted by saturation of all diagnostic effects even for the greatest earthquakes, improving the intensity evaluations based on the classical macroseismic scales. In addition, some environmental morphogenetic effects (either primary and secondary) can be stored in the palaeoseismological record, allowing to expand the time window for seismic hazard assessment up to tens of thousands of years [18, 19]. Finally, it is important to consider the seismically induced effects with the aim to reduce the risk for the population living along the coast and the potential damage to structures and natural environment, through a more precise estimate of their type, size and distribution, especially in Calabria and Sicily regions characterized by a very high level of seismicity.

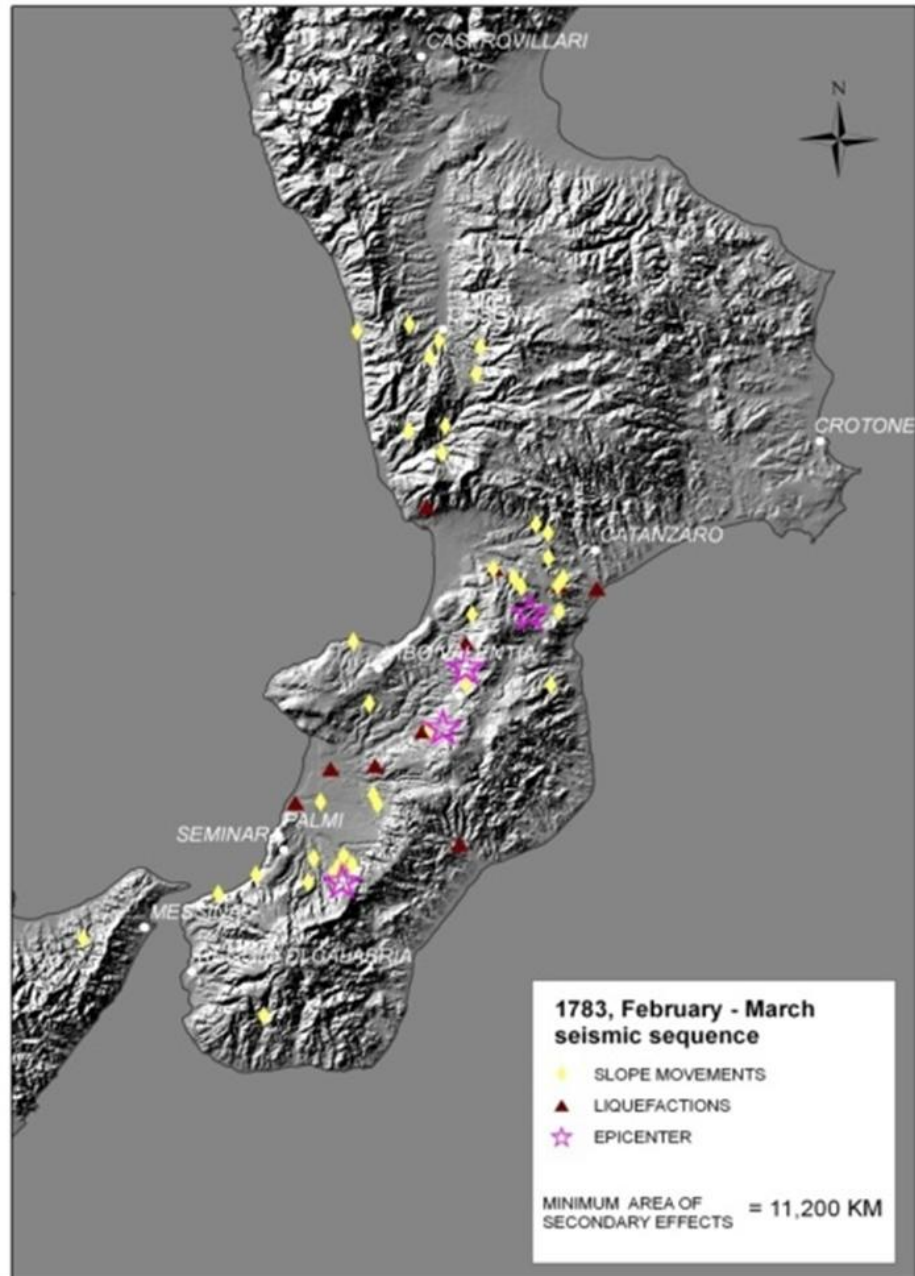


Figure 3: The February-March 1783 seismic sequences: epicenters and the most important secondary effects distribution: slope movements, liquefactions and hydrological changes (minimum area of secondary effects 11.200 km²).

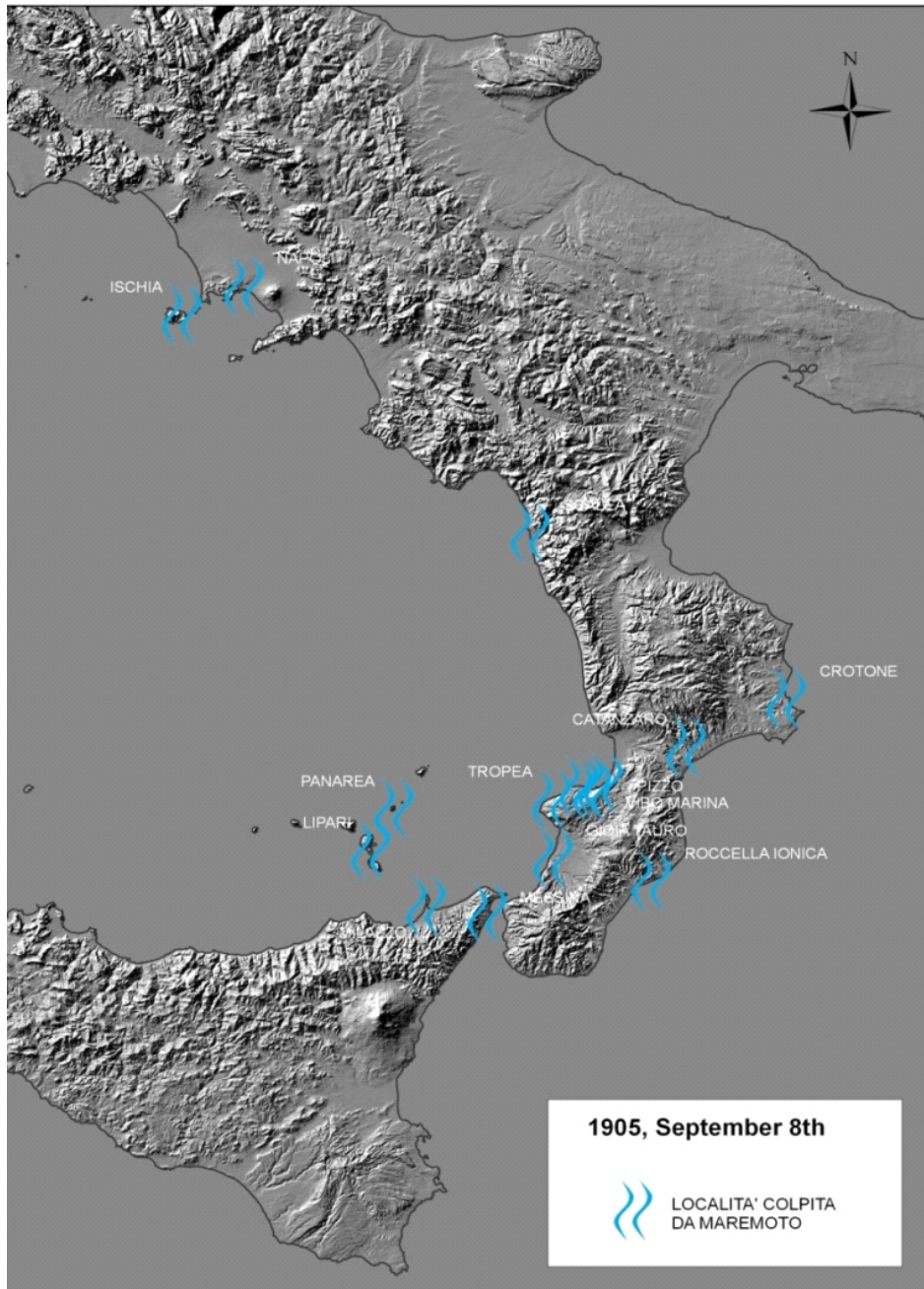


Figure 4: The 1905 Southern Calabria earthquake: general map of the localities hit by tsunamis.

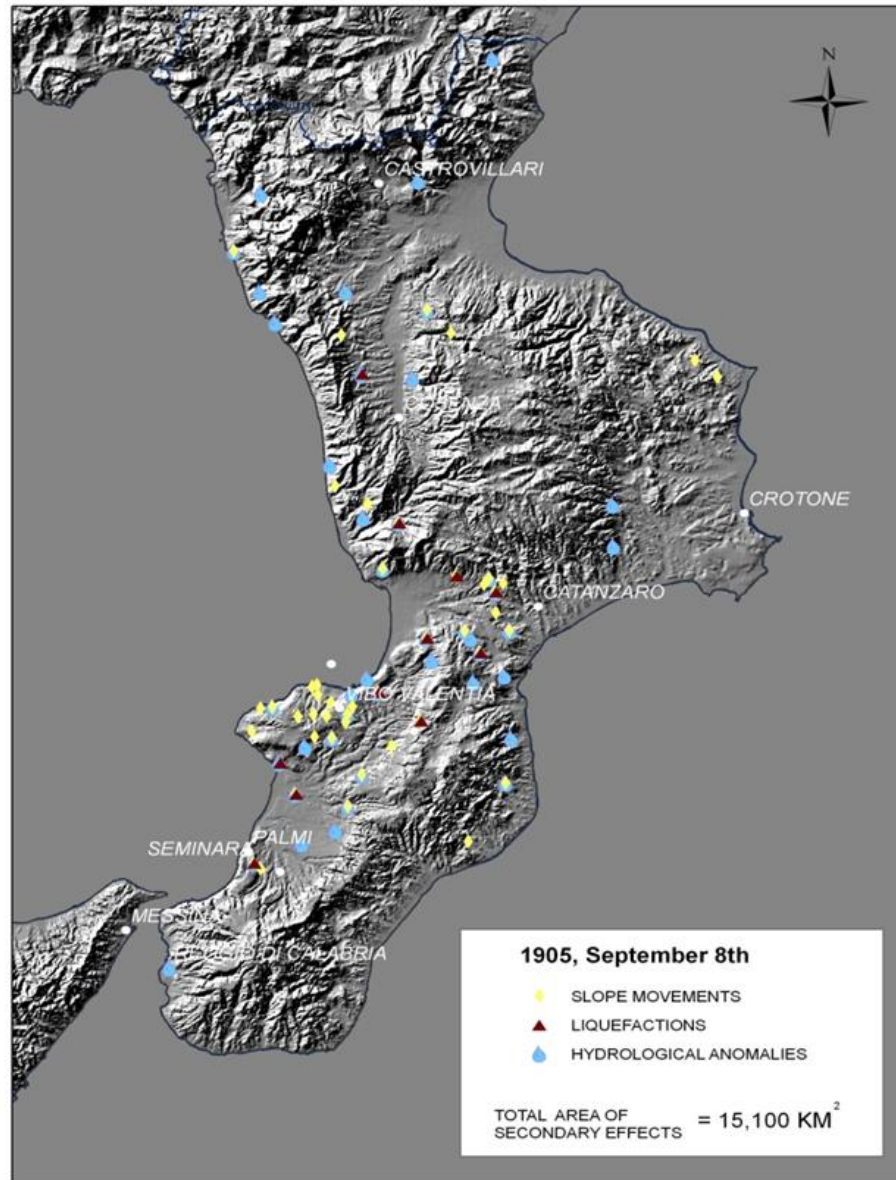


Figure 5: The 1905 Southern Calabria: sites of ground effects: slope movements, liquefactions and hydrological changes (total area of secondary effects 15.000 km²).

References

- [1] A.M. Michetti, E. Esposito, L. Guerrieri, S. Porfido, L. Serva, R. Tatevossian, E. Vittori, F. Audemard, T. Azuma, J. Clague, V. Comerci, A. Gurbinar, J. Mc Calpin, B. Mohammadioun, N.A. Morner, Y. Ota, and E. Roghozin. Intensity Scale ESI 2007. *Mem. Des. Carta Geologica d'Italia*, 74:1–53, 2007.
- [2] A. Minasi. Continuazione ed appendice sopra i tremuoti descritti nella relazione colla data di Scilla de 30 settembre 1783, con altro che accadde in progresso, Messina. 1785.
- [3] M. Sarconi. Istoria de' fenomeni del tremuoto avvenuto nelle Calabrie e nel Valdemone nell'anno 1783. 1784.
- [4] G. Vivenzio. Historia de' Tremuoti avvenuti nella Provincia della Calabria ulteriore e nella Città di Messina nell'anno 1783 e di quanto nella Calabria fu fatto per lo suo risorgimento fino al 1787 preceduta da una Teoria Istoria Gen. De'Tremuoti. 1-2, 1778.
- [5] F. Bozzano, E. Esposito, L. Lenti, S. Martino and A. Montagna, A. Paciello, and S. Porfido. Numerical modelling of earthquake-induced rock landslides: the 1783 Scilla case-history (Southern Italy). *Fifth Int. Conf. on Recent Advances in Geotech. Eart. Eng., San Diego California*, 2010.
- [6] V. Cotecchia, A. Guerricchio, and G. Melidoro. The geomorphogenetic crisis friggere by the 1783 earthquake in Calabria (southern Italy). *Proc. of the Int. Symp. On Engineering geology problems in seismic areas. IAEG*, 6:245–304, 1986.
- [7] E. Jacques, C. Monaco, P. Tapponier, L. Tortorici, and T. Winter. Faulting and earthquake triggering during the 1783 Calabria seismic sequence. *Geophys. J.*, 147:499–516., 2001.
- [8] P. Galli and V. Bosi. Paleoseismology along the Cittanova fault: Implications for seismotectonics and earthquake recurrence in Calabria (southern Italy). *Journ. Geophys. Res.*, 107(1-19), 2002.
- [9] S. Catalano, C. De Guidi, C. Monaco, G. Tortorici, and L. Tortorici. Active faulting and seismicity along the Siculo-Calabrian Rift Zone (Southern Italy). *Tectonophysics*, 453:177–195, 2008.
- [10] S. Porfido, E. Esposito, L. Guerrieri, and L. Serva. Terremoti storici ed effetti ambientali nell'area dello stretto. Proceedings of the congress: Cento anni dopo il terremoto del 1908- ISPRA -12-13 Nov., 2008 Messina-Villa San Giovanni. 2008.
- [11] M. Baratta. Il grande terremoto calabro dell'8 settembre 1905. *Atti Soc. Toscana di Sc. Nat.* XXII:57–80, 1906.

- [12] G. Chiodo and M. Sorriso-Valvo. Frane sismo-indotte: casistica e fenomeni innescati dal terremoto dell'8 settembre 1905. 2006.
- [13] A. Tertulliani and L. Cucci. Fenomeni associati al terremoto della Calabria dell'8 settembre 1905. *Quaderni di geofisica*, 60, 2008.
- [14] S. Tinti. Il maremoto del 1905 nel Golfo di Sant'Eufemia. *In 8 settembre 1905 terremoto in Calabria a cura di Guerra & Savaglio*, 2006.
- [15] P. Di Manna, A.M. Blumetti, V. Comerci, L. Guerrieri, L. Serva, and E. Vittori. The 1908 tsunami effects along the Messina Straits (Southern Italy): a contribution for predicting inundation scenarios. *Geophysical Res. Ab. EGU*, 2009.
- [16] M. Baratta. La catastrophe sismica calabro-messinese (28 dicembre 1908). *Soc. Geografica. Ital.*, 1910.
- [17] V. Comerci, A. M. Blumetti, E. Brustia, P. Di Manna, E. Esposito, D. Fiorenza, L. Guerrieri, S. Porfido, L. Serva, and E. Vittori. One century after the 1908 Southern Calabria - Messina earthquake (southern Italy): a review of the geological effects. *Geoph. Res. Ab. EGU*, 10, 2008.
- [18] L. Guerrieri, R. Tatevossian, E. Vittori, V. Comerci, E. Esposito, A.M. Michetti, S. Porfido, and L. Serva. Earthquake Environmental Effects (EEE) and Intensity Assessment: THE INQUA SCALE PROJECT. *Boll. Soc. Geol. Italiana*, 126, 2007.
- [19] S. Porfido, E. Esposito, L. Guerrieri, E. Vittori, G. Tranfaglia, and R. Pece. Seismically induced ground effects of the 1805, 1930 and 1980 earthquakes in the Southern Apennines, Italy. *Boll. Soc. Geol. It.*, 126(2):333–346, 2007.

Statistical Trend Analysis and Extreme Distribution of Significant Wave Height in the Period 1958-1999 along the Italian Seas

M. Sclavo¹, S. Carniel¹, G. Martucci²

1, Institute of Marine Sciences, CNR, Venezia, Italy

2, National University of Ireland, Galway, Ireland

mauro.sclavo@ismar.cnr.it

Abstract

The study aims at performing a climatological and statistical analysis of the wave fields around the Italian coasts. The research on long - term wave series and on extreme events has been increasingly motivated by environmental sciences due to the numerous applications, aiming at better understanding of such events and devise actions to prevent their consequences in terms of damages to infrastructures and persons. The study presents a statistical analysis of sea states timeseries derived using the wave model WAM forced by the ERA-40 dataset in selected areas near the Italian coasts. For the period 1-Jan-1958 to 31-Dec-1999 the analysis yields: (i) the existence of a negative trend in the annual- and winter-averaged sea state heights; (ii) the existence of a turning-point in late 70's in the annual-averaged trend of sea state heights at a site in the Northern Adriatic Sea; (iii) the overall absence of a significant trend in the annual-averaged mean durations of sea states over thresholds; (iv) the assessment of the extreme values on a time-scale of thousand years. The analysis uses two methods to obtain samples of extremes from the independent sea states: the r-largest annual maxima and the peak-over-threshold. The two methods show statistical differences in retrieving the return values and more generally in describing the significant wave field. The study shows the existence of decadal negative trends in the significant wave heights and by this it conveys useful information on the wave climatology of the Italian seas during the second half of the 20th century.

1 Introduction

This study aims at performing a climatological and statistical analysis of the wave fields in the Northern Adriatic Sea. In oceanography- as well as in meteorology - climate can be described by the mean type, frequency and intensity of weather events occurring during a climatological period of time. In the same way the mean values of a timeseries are used to assess the exis-

tence of a trend over a climatological time interval, the sample of the timeseries extremes is used to determine the probability of extreme events to occur at fixed return periods. The study of extreme events has been increasingly motivated by environmental sciences due to the numerous applications, aiming at better understanding extreme events and devise actions to prevent their consequences in terms of damages to infrastructures and persons. One

major commitment to improve this understanding should be on reducing the uncertainty related to their assessment. The statistical analysis of the extreme waves is used by coastal engineers to assess the risk of damages to offshore constructions or by oceanographers and modellers to calculate trends in the past and future wave fields [1], also based on different emission scenarios [2]. Depending on the method and criteria to sample the extremes from a timeseries, different results can be obtained by applying the same statistical analysis on the different samples. Depending on the method and on the average value of the extremes, a specific event can be regarded as to be an actual risk for the environment or not. The hitherto extreme wave analysis allows extracting the independent and identically-distributed data from climatological timeseries and to use them for applications of two methods such as the “peak over threshold” (POT) and the r largest annual maxima which are amongst the best techniques to select the extreme from large datasets and to provide robust estimates of the extreme values at future return periods (see [3, 4]). The present analysis will focus on trends of the mean wave significant heights on selected locations in the Adriatic Sea during the second half of the 20th century. The statistical differences in the extremes using the two methods will be used to assess which technique can provide the best return values for the selected return periods.

2 Data setup and calibration

WAM is an advanced third generation model developed in the late 80s and presently one of the most widely used and

tested by the scientific community [5]. It calculates directional spectra from which integrated values such as significant wave height, mean wave direction and frequency can be derived.

Since July 1992 the European Centre for Medium-Range Weather Forecasts (ECMWF) has been running WAM forced by a meteorological model. The re-analysis project ERA-40, completed in 2003, is a re-run from mid 1957 to 2002 of a fixed version of ECMWF atmospheric analysis system, including WAM, at a resolution of about 125 km. It uses all available observations to constraint the analysis and has a temporal resolution of 6 hours.

Results from WAM forced by the ERA-40 wind fields were considered covering the whole Mediterranean basin. Output wave parameters fields (Significant Wave Height and direction) were then stored every 6 hours. The wave dataset (further named “ERA-40”) was obtained extracting the relevant information at selected points of the WAM output grid in the Adriatic Sea.

As highlighted by previous studies (see e.g. [6]), a possible underestimate of the wind speed components due to a lack of resolving small, sharp scale features in the wind pattern, may also affect the WAM-computed values of significant wave height. The ERA-40 wind fields may be suffering from a possible underestimation, especially in enclosed areas nevertheless, since this dataset constitutes one of the most advanced product when dealing with long-term series, we tried to overcome these drawbacks by comparing, for the overlapping years, the ERA-40 results with time-series calibrated by satellite data, as described in Cavaleri and Sclavo [7].

Cavaleri and Sclavo [7] presented a study in which the WAM output wave fields (0.5° grid resolution) from July 1st 1992 to June

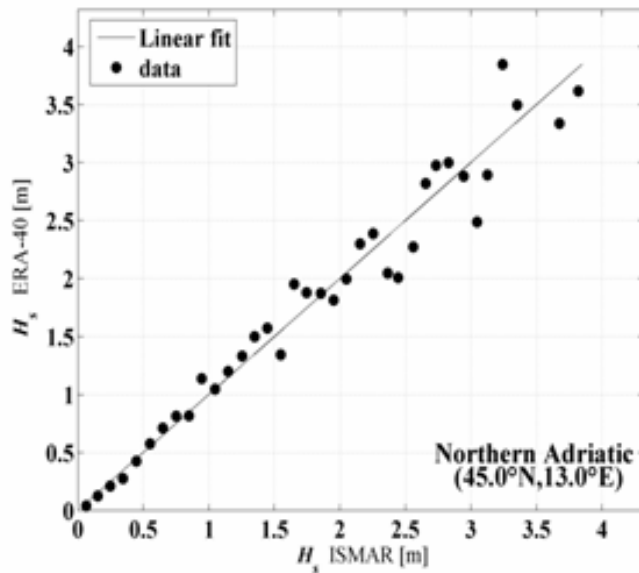


Figure 1: Calibrated ERA-40 significant wave height vs. ISMAR significant wave height. Data in the graphics have been averaged over a height-span of 0.1 m.

30th 2002 have been calibrated for several points in the Mediterranean Sea, following two successive validation-calibration steps. First, the ERS1-2 and the Topex/Poseidon satellites wave data have been validated using the wave dataset provided by the Italian Buoy Network then the WAM model data have been calibrated by comparison with satellite data, and finally tested for correlation with other observational data. In the present work, a similar procedure has been applied, ensuring for the period from 1992 to 2002, a good-quality wave height timeseries in the Adriatic Sea that in the following will be named as “ISMAR”.

The ERA-40 has been calibrated as well, with the procedure described in the following, on some representative geographical sites in the Northern Adriatic Sea, se-

lected among the available WAM output grid points. The wave timeseries spans a 42 year period from from 01-Jan-1958 to 31-Dec-1999. The overlapping period between the ERA-40 and ISMAR calibrated timeseries is 7.5 years, from 1992 to 1999. At each selected position the two timeseries have been linearly fitted to retrieve the calibration factor a and the intercept c using the linear relation $H(\text{ISMAR})=a \cdot H(\text{ERA40})+c$. Table 1 shows the values of parameters a and c for the considered points. Once calibrated, the two timeseries are in good agreement during the overlapping time interval. In Figure 1 are shown the results of the comparison at a representative site located in the Northern Adriatic. The calibrated ERA-40 timeseries has then been processed retain-

| Coordinates | slope “a” | intercept “c” |
|-----------------|-----------|---------------|
| 44.50°N,12.50°E | 1.132 | 0.575 |
| 44.00°N,13.00°E | 2.329 | -0.011 |
| 44.50°N,13.00°E | 2.401 | 0.051 |
| 45.00°N,13.00°E | 1.655 | 0.027 |
| 45.50°N,13.00°E | 1.066 | -0.053 |
| 41.00°N,13.50°E | 1.510 | 0.184 |
| 44.50°N,13.50°E | 2.006 | 0.083 |
| 44.50°N,14.00°E | 2.389 | 0.043 |
| 42.50°N,14.50°E | 2.002 | 0.487 |
| 42.50°N,15.50°E | 2.193 | -0.029 |
| 41.00°N,17.50°E | 1.287 | 0.353 |

Table 1: Slope and intercept values of linear wave timeseries calibration.

ing only independent wave events, selected on the basis of their autocorrelation coefficient, for which a value less than 0.1 was considered adequate to ensure the independence among the events.

3 Methodology of statistical analysis

The identification of the best probability distribution $F(h)$ fitting the sampled independent data allows the determination of the extreme waves return values and re-

turn periods. Two methods are used for sampling the extremes from iid data: the r largest annual maxima (rmax) and the “peak over threshold” (POT) method. The first is a selection of the largest r maxima ($r = 5$) during each year throughout the time-series. The second method, widely used, makes use of a threshold to select records from a dataset. The POT method increases the available information by using more data than the r largest peaks per year. However, in practical applications the results are quite sensitive to the criteria adopted for peak selection.

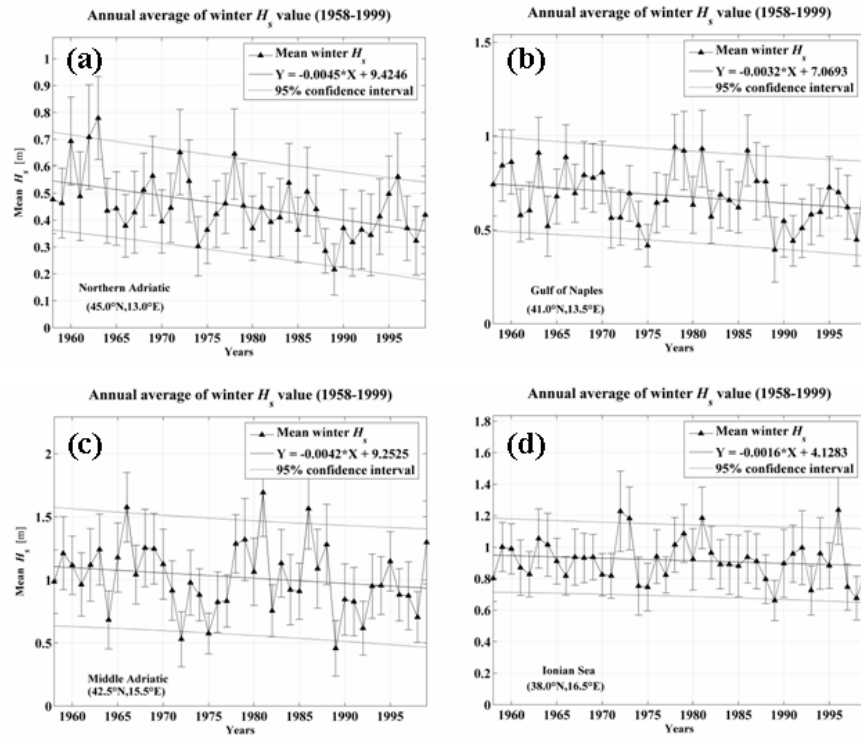


Figure 2: From (a) to (d), at four different geographical sites, the winter-averaged significant wave height values through the 1958-1999. The straight solid line represents the linear regression of the timeseries with 95%-confidence intervals (thin lines). Error bars values have amplitude equal to two times the significant wave height standard deviations.

A statistical analysis of the ERA40 wave timeseries has been performed to provide information about the annual winter averaged significant wave height, the significance of trends during the 42-years period and the total number of wave events. The annual number of sea states, the annual- and the winter-averaged wave height and the statistical significance of their trends in the Northern Adriatic Sea are presented in the following chapters. The POT and the r_{max} determined extreme waves are then discussed.

4 Results

The determination of a trend in the ERA-40 timeseries is relevant when assessing the H_s future scenarios. For the northern area, the point (45.0°N, 13.0°E) has been selected. A linear fitting (Figure 2) shows the trend of the mean significant wave height value along the period of the ERA-40 timeseries, obtained as an average over the winter period (December to February), i.e. when most of the sea storms occur. All sea states (all heights and direc-

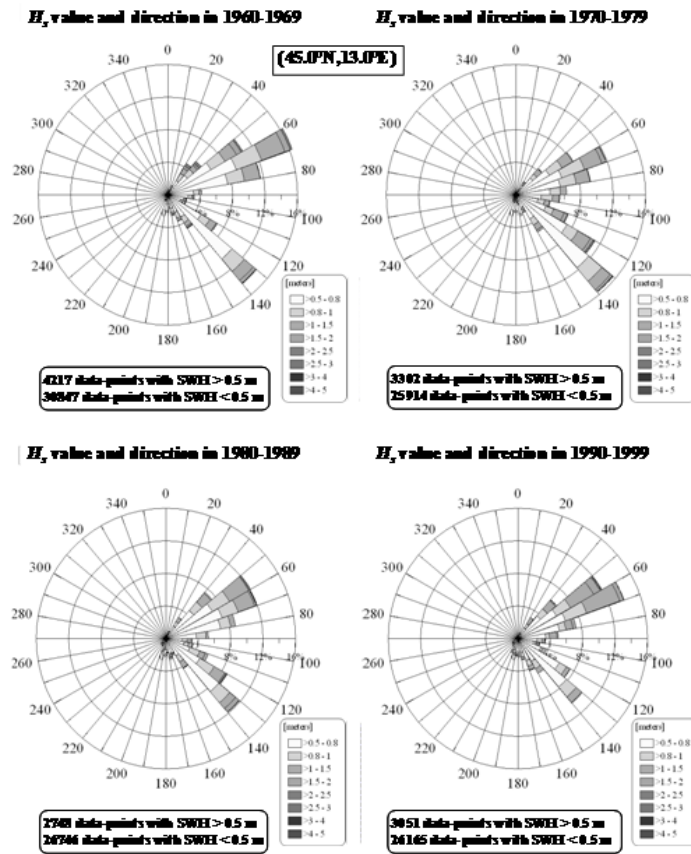


Figure 3: Decennial rose diagrams from 1960 to 1999 of significant wave heights and relative frequencies of occurrence at (45.0°N, 13.0°E).

tions) have been considered for the analysis that shows a clear negative trend in all the computed linear fits. In the Adriatic Sea, trend's slopes through the 42 years are negative being 4.5×10^{-3} m year⁻¹ and 4.2×10^{-3} m year⁻¹ for Northern and Middle Adriatic, respectively. A Student's t test has been used to assess the statistical significance of all trends. Trends in Figure 2 are in agreement with the overall negative trends in winter averaged wave height values found by other authors over

the Mediterranean Sea and with the trends of the annual averaged values. The wave occurrences and heights have been statistically analyzed at representative sites in the Northern Adriatic. This area, embedding the Venice lagoon and its coastal surroundings, is of particular interest due to the delicate equilibrium of its ecosystem that calls for a better understanding and mitigation of the wave impact (for a more complete picture on the effects of Bora winds on physical and

bio-geochemical properties of the northern Adriatic, see for instance [8]).

For the point in front of the Venetian coast (45.0°N, 13.0°E), Figure 3 shows the height, occurrences and incoming direction of the significant wave heights divided in four decades (1960-69, 1970-79, 1980-89 and 1990-99). Data have been sampled using a threshold set at 0.5 meters. Throughout the first three decades a general decrease in wave occurrences does happen in correspondence of both the incoming directions of Bora (north-easterly, down-sloping wind) and Sirocco (Mediterranean south-easterly wind). On the contrary, a moderate increase appears for the Bora data from 1990 to 1999; during the same period, the Sirocco component continues to decrease.

Figure 4 shows the total number of wave events and annual-averaged values for sea states with wave height higher than 0.5 m coming from the Bora sector (0 N to 90 degrees N) are shown. The timeseries in both panels of Figure 4 can split into two sub-series with a turning-point around 1989. This break-point is showing a change in the derived trends that can not be related to the introduction of satellite data (that dates back to early '80s). On the other hand, benefiting from long-term simulations dealing with climate dynamics in the ocean and atmosphere, this signal could be related to the Eastern Mediterranean Transient, which effects on the Adriatic sea have not yet been thoroughly investigated by the scientific community.

The comparison between POT and r max methods aims at defining which method can provide, for fixed return periods, the best estimation of the return values with the least statistical error. The set of cumulative probability distributions generally employed for the extreme data analysis are the

Weibull (2 or 3 parameters), Fréchet, Gumbel or the Lognormal distributions. Since a Lognormal distribution can be represented by a Weibull distribution with one parameter set to a fixed value, a linear least squares based algorithm has been implemented, which selects automatically the best fitting distribution amongst the Weibull, Fréchet and Gumbel (see[9]).

A threshold fixed at the 75th percentile of the ordered dataset and a value $r = 5$ are used for the application of the POT and the r max methods, respectively.

A comparison between the two methods is shown in Figure 5. The two methods provide closer estimations for return periods longer than 100 years. For small return periods, the return values are larger using the rmax method and this is due to inclusion of smaller wave heights selected by the POT 75th percentile threshold. The r max method, on the other hand, selects only the highest waves from the dataset that makes it a good candidate to provide more conservative extreme return values.

Qualitatively, for return periods shorter than 100 years, the rmax method provides more realistic return values, despite a larger statistical error. When considering larger return periods (more than 100 years), the POT method gives return values comparable with the ones computed by rmax, but with a smaller statistical error. This is explained by the fact that the differences between the two methods are larger for small return periods when extreme return values strongly depend on the source dataset. For large return periods, the POT dependence on source dataset becomes feeble and the method provides better extreme return values with a smaller standard deviation.

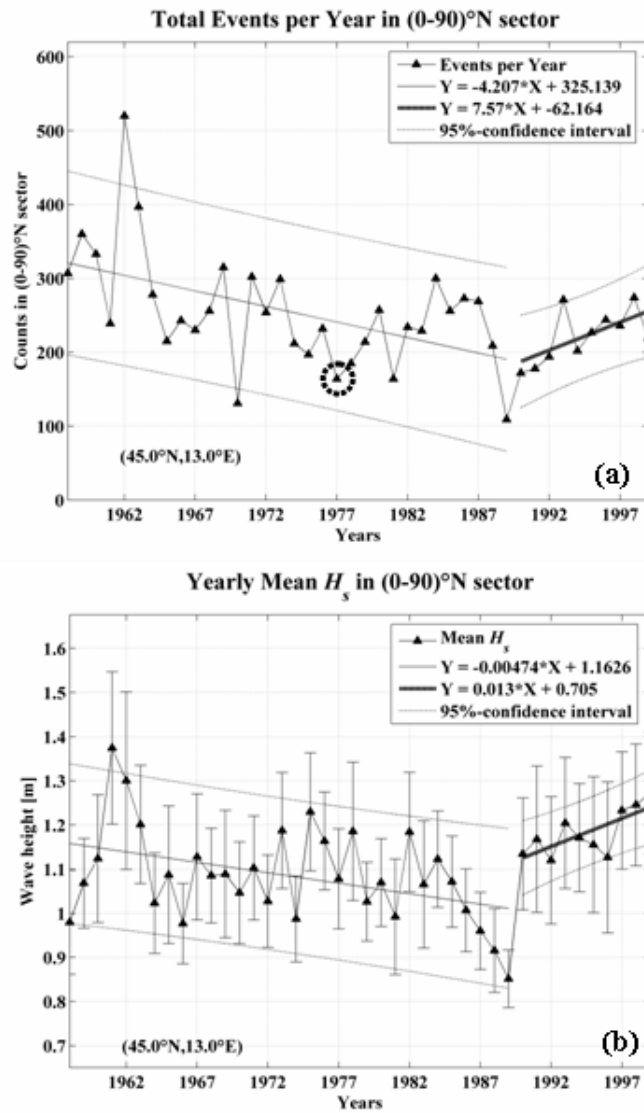


Figure 4: Panel (a) and panel (b) show, for the period 1958-1999, respectively, the annual total number of sea-states and the mean annual significant wave height values in the sector of [0-90°N] incoming wave direction. Two linear fits for each panel display the trends over the year ranges 1958-1989 and 1990-1999. Thin lines around the regression lines indicates the 95%-confidence intervals. Error bars on panel (b) have amplitude equal to two times the annual standard deviations.

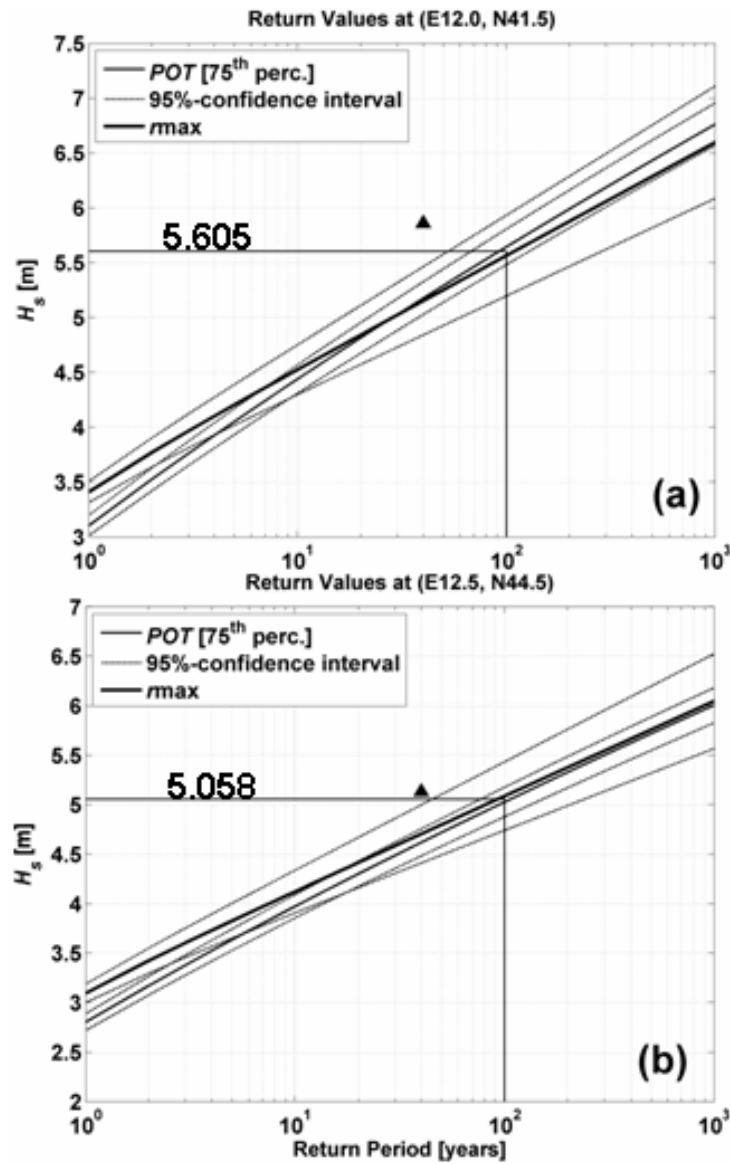


Figure 5: From 1 to 1000 years, the solid lines show the return values [m] obtained using the POT (thin) with threshold 75th percentile and the rmax (thick) with 5 annual maxima. Thin lines show the 95% confidence intervals.

5 Conclusions

The first part of this study was dedicated to determine trends and statistical significances during the period from January 1958 to December 1999 for the ERA-40 wave timeseries, a calibration of WAM model outputs produced using the ERA-40 forcings. The investigated wave parameters were the significant wave height values (averaged over the winter season and over all the incoming directions); the total number of sea states characterised by a certain significant wave height for all the incoming directions (and particularly for the North-Eastern sector); the averaged mean duration and probability of threshold exceedance; the return periods of extreme waves and their duration of exceedance.

The statistical analysis showed that, during the second half of the 20th century winter averaged significant wave height had a statistically significant negative trend. An investigation of the existing relation between the observed decrease in the total number of occurrences and in the annual averaged values of wave height, was car-

ried out through the period from 1960 to 1999, in the Northern Adriatic area. The results showed a clear negative trend during the first three decades opposite to a reverse positive trend starting with a turning-point at the beginning of the last decade.

In the last part of the work we compared two methods to compute extreme values, the POT and the r max. The presented case showed differences in the computed extreme return values especially for return periods less than 100 years. In this range, the return values determined by POT were systematically smaller than the ones determined by the r max. For return periods less than 100 years, the POT method can provide extreme return values closer to those computed by r max and with a smaller statistical error.

6 Acknowledgements

This activity was supported by the VECTOR-FISR Project and the EC FP7/2007-2013 under grant agreement n° 242284 (Project FIELD_AC).

References

- [1] P. Lionello, S. Cogo, M.B. Galati, and A. Sanna. The Mediterranean surface wave climate inferred from future scenario simulations. *Global Planet Change*, 63:152–162, 2008.
- [2] N. Nakicenovic, J. Alcamo, G. Davis, et al. Special Report on Emissions Scenarios, a Special Report of Working Group III of the IPCC. page 599, 2000.
- [3] E. Simiu and N.A. Heckert. Extreme wind distribution tails: A “peaks-over-threshold” approach. *J. Struct. Eng.*, 122:539–547, 1996.
- [4] R.L. Smith. Extreme value theory based on the r largest annual events. *J. Hydrol.*, 86:27–43, 1987.
- [5] G.J. Komen, L. Cavaleri, M. Donelan, K. Hasselmann, et al. Dynamics and Modelling of Ocean Waves. page 536, 1994.

- [6] R.P. Signell, S. Carniel, L. Cavaleri, J. Chiggiato, et al. Assessment of wind quality for oceanographic modelling in semi-enclosed basins. *Journal of Marine Systems*, 53:217–233, 2005.
- [7] L. Cavaleri and M. Sclavo. The Calibration of Wind and Wave Model Data in the Mediterranean Sea. 53:613–627, 2006.
- [8] A. Boldrin, S. Carniel, M. Giani, M. Marini, et al. The effect of Bora wind on physical and bio-chemical properties of stratified waters in the Northern Adriatic. *Journal of Geophysical Research Ocean*, 114, 2009.
- [9] Y. Goda. Statistical Analysis of Extreme Waves. Part III of. Random Seas and Design of Maritime Structures. page 443, 1997.

Pseudo-3D Seismic Tomography Approach on a Tuff Cliff in the Sorrento Peninsula, Italy

V. Di Fiore¹, A. Rapolla², A. Angelino¹, F.P. Buonocunto¹, G. Cavuoto^{3,1}, A.G. Cicchella¹, E. D'Aniello², D. Tarallo²

1, Institute for Coastal Marine Environment, CNR, Napoli, Italy

2, Department of Earth Sciences, University of Napoli "Federico II", Napoli, Italy

3, Institute of Environmental Geology and Geoengineering, CNR, Roma, Italy

vincenzo.difiore@cnr.it

Abstract

The studied area is located in the Sorrento Peninsula, a major Quaternary morphostructural unit of the western flank of Southern Apennines. The peninsula forms a narrow and elevated mountain range that separates two major embayments of the eastern Tyrrhenian margin and is characterized generally by a carbonate bedrock capped by pyroclastic deposits (i.e. "Campania Ignimbrite"), originated from the Campi Flegrei volcanic district. The occurrence of steep slopes and the high relief energy of the area, along with the marine erosion at the base of the coastal cliff creates favourable conditions for the occurrence of a generalized instability of the slopes that is manifested by tuff rock falls as prevailing landslide phenomena. Prediction of such landslides type is difficult if not accompanied by accurate hydrogeologic and geotechnical monitoring and assessment. Often, the presence of pervasive fracturing and cavities in tuff deposit can cause instability and rock falls. Because of 2D-3D cliff effect, we don't apply the standard seismic acquisition geometry. Therefore, we applied a particular seismic geometry to detect this specific site. A non linear seismic inversion was used to obtain 2D models. They allowed to build a pseudo 3D Vp/Vs ratio. The 3D Vp/Vs ratio pseudosection showed anomaly zones in the investigated rock. We identified an area with a low Vp/Vs value that we associate with a medium having a lower porosity or in dryer condition respect to the surrounding material.

1 Introduction

This study shows the results of a 2D tomographic investigation carried out on a tuff cliff located in the city on Piano di Sorrento in the Sorrento Peninsula. The Sorrento Peninsula is a morphostructural unit placed on the western part of the southern Apennines composed of carbonatic substrate covered by flyschoid and pyroclastic deposits (Ignimbrite Campana auct) and a morphology of characterized by high

and low relief and with a coastal perimeter composed of very high and steep cliff. In the studied area, sub-vertical cliff, tuff deposits discontinuities and marine erosion conditions facilitate the triggering of landslides such as rock falls and gravity instability that characterise mainly the high sector of the cliff made of variable thickness of incoherent pyroclastic deposits and anthropic material. The prediction of these gravity phenomena appears very difficult due to the unknown physical features of

the tuff deposits that characterize several coastal areas of the Campania Coast with subvertical to vertical cliff.

In this particular geomorphologic setting, a non-destructive investigation (geophysical investigation) in order to characterize the geometry as well as the degree of fracturing of the rock pile, allows to define a preliminary model to evaluate the stability condition.

In such context a new acquisition technique has been tested in order to overcome the logistic difficulties that usually concern these areas. In fact the acquisition geometry has been defined with the vertical and horizontal geophones located along the subvertical cliff while the source is positioned on the cliff's top.

2 Geological and morphological data

The Sorrento Peninsula is located in the inner sector of the Southern Apennines (Figure 1) fold-and-thrust belt which is the result of Miocene to Early/Middle Pleistocene deformation of Mesozoic to Tertiary carbonate platforms and carbonate and/or siliciclastic slope to basinal domains [1]. In the studied area, the resulting chain is a pile of thrust-units unconformably overlain by synorogenic siliciclastic deposits, Late Tertiary in age, and alloctonous tectonic slides of internal units stacked from the west to the east during the Miocene-Pliocene tectonic phases (Sicilide unit Auct.: AdB Sarno, 2003, [2]).

The Pleistocene deposits outcropping in Penisola are characterized by alluvial, coluvial deposits, variable in thickness, with a prevalent carbonate component and pyroclastic fall deposits related to the Cam-

panian Ignimbrite (CI) eruption [3] and Post-Ignimbrite (PI) deposits[2]. Holocene deposits are made up of few meters of incoherent and humific material derived from recent eluvial deposits and former sedimentary and pyroclastic deposits. The Pliocene and Quaternary events generated "apenninic" NE-SW and "antiapenninic" NW-SE system faults which are widespread and cause the blockfaulting phenomena and formation of several graben-like structures. These structural features characterise the Peninsula perimeter with a sub-vertical to vertical rocky shore mainly controlled by NE trending faults while the morphology of the internal sector shows a high to low relief creating horst-and-graben structures [4]. Subsequently, some of these have been ("Sorrento Graben") filled by the CI (39 Ka: [5]) and PI deposits [2].

The unit rocks, forming the high escarpments which confine the Sorrento graben to NE and SW (i.e. Montechiaro and Punta del Capo highs), can be related to a upper Cretaceous succession of shallow marine limestones, with very subordinate dolomitic beds referable the Santonian-Aptian interval (cfr. Calcari a radiolitidi unit (RTD): ISPRA., 2005). The Miocene cover is well preserved only in the western portion of the peninsula (De Blasio, 1981), which is the less elevated sector of the ridge and are locally affected by landslides and rock falls events correlated to rocks weathering and to a pervasive jointing.

The central sector of Sorrento graben is a low gradient, subplanar, topographic surface located at the foot of the carbonate reliefs, filled by CI deposits and is dissected by incised valleys, orthogonal to the coastline, with very low hierarchical order. The CI is a gray, poorly to moderately welded, trachytic ignimbrite sheet.

The tuff shows a gray-purple colour, with red flames, in which are visible large gray pumice, well-rounded and lithic fragments. It is characterized by the typical vertical columnar jointing, as well as subhorizontal discontinuities associated with textural changes and different degrees of cementation linked to lithological changes and vertical fractures linked to tectonic history of the area (Figure 2d). The tuff unit is preceded by a pumice-rich sandy horizon between 30 to 50 cm thick, with a well-stratified pumice sharp edges. The CI deposits outcropping in valleys and at several points above the plain, including the sides of the relief of St. Angelo-Casarlano and the town of Piano di Sorrento (S. Liborio, Villa Pagliano, neighbourhood Atigliana, Mortora-Carotto, Lavinola valley, Trasaella, S. Agata) up to an altitude of about 160 mt above sea level.

At the town of Piano di Sorrento, the edge of the plain towards the sea is characterized by sub-vertical cliffs, carved into the CI tuff, developed for about 5 km and with a coastal platform submerged with low angle ($\leq 10\%$) (morphotype A1: [6]). The tuff cliff is often affected by several traces of human activities such as caves and small hollows of building materials, active up to the 1950s, which develop mainly near the outlets downstream at the base of tuff cliff. The coastal forms of the Sorrento Peninsula can be classified in four cliff-types according to the lithological and structural condition of the coast [7]. Limestones cliff, which outcrops mainly along the coast from Castellammare di Stabia to Meta di Sorrento (Figure 2a) and is usually vertical, opening on the toe of a slope modelled by frost-weathering during the wurmian glaciation. The structural cliff, quite vertical, is a fault-plane and outcrops from Naples area to Massa Lubrense, Praiano,

and Salerno area (Figure 2b). The cliff of pyroclastic rocks, always vertical, is surmounted by a large terrace, coinciding with natural deposition at the top-surface of the pyroclastic rocks, which near Sorrento village match a maximum height of 50 mt. (Figure 2c). Finally, the cliff in flysch shows a slope of about 35deg and opens on the bottom of a versant which bears the traces of the solifluxion which happened during the damp Wurm. This versant is still instable as proved by the numerous landslides small terraces (Figure 2e).

The stratigraphy has heavy implications on the distribution and type of landslides in the studied area, correlated to lithological and structural characteristics, as well as the degradation of surface outcropping units. Therefore, gravitational phenomena within the Sorrento graben can be classified into:

- Roto-translative slides and earth-flows that affect the pyroclastic layer on carbonate or flysch reliefs;
- collapses and rockfalls on the steep side of the limestone highs;
- collapses and landslides along the anthropogenic or natural cuts, on the riverbanks in the valleys and in the upper ignimbrite cliffs where there are variable thickness of pyroclastic and anthropic deposits;
- topples of the outer portions of the tuff cliff.

3 Data acquisition and analysis

The studied area is a cliff 42 m high composed of tuff materials covered by a 6 m thick layer of incoherent anthropic deposits and pyroclastic products. The cliff has been interested by different rock falls

events whose cumulus is still evident on the cliff foot.

In order to obtain a 2D P and S wave velocity model, five seismic profiles located on 10 m long rays semicircle distribution designed on the top cliff have been acquired (Figure 3).

10 Hz vertical and horizontal geophone were located along the cliff at a distance of 5-6 m from the beach (Figure 4). The energy source used was a 10 kg sledge hammer and the shots were executed along the 10 m long semicircle ray defined on the summit of the cliff. The shot interval was established at 0.5m for a total of 20 shots for each profile and a 24 bit with 24 channels seismograph was used.

Data were processed using a Non-linear Least Squares [8] inversion technique, while the ray tracing was obtained through the Finite Difference Calculation [9]. The RMS error shows from the results was always lower than 1 ms.

The Finite Difference Calculation of travel time is an accurate method used in numerous application, as tomographic inversion, to increase computing speed.

Assuming a velocity structure as sampled discrete points in two dimensional space, with equal horizontal and vertical spacing, Vidale [9] computed two travel time equations, the first for nearly flat wavefronts (1) and the second for strongly curved wavefronts (2).

$$t_3 = t_0 + \sqrt{2(hs)^2 - (t_2 - t_1) \cdot (t_2 - t_1)}, \quad (1)$$

where t_3 is the travel time between point C1 and point source A, t_0 is travel time of zero in A, t_1 is the travel time between point B1 and point source A, t_2 is the travel time between point B2 and point source A,

h is the mesh spacing and s the slowness (inverse of velocity).

$$t_3 = t_s + s \cdot \sqrt{(xs + h)^2 + (z + h) \cdot (z - h)} \quad (2)$$

where t_s is the origin time for the virtual source point, lied at the center of the curvature of the circular wavefronts, xs is the x-coordinate of the virtual source point, zs is the z-coordinate of the virtual source point [9].

In the same way, the solution for the other three corners is calculated from the times of their neighbors. Solution will progress increasing radius around the source point.

To ray tracing, the essential aim is to find the minimum travel time between source and receiver for each source-receiver pair [8].

We use a Non-Linear Least Squares Method approach, because a Jacobian matrix, used for linear method, requires ray-path, that can not be calculated without a velocity model.

The iterative solution of a non-linear Least Squares matrix require five fundamental step [8]:

1. Calculation of theoretical value Y_0 for initial model $X_0: Y_0(Z) = Y(Z, X_0)$.
2. Calculation residual (dY) between theoretical value Y_0 and observed value Y .
3. Correction for $X(dY)$: $((AT)A) dX = (AT) dY$
4. Calculation of new estimate for X_1 .
5. Return to step 1 until solution stabilization, when residual error is acceptable. $(AT) =$ Transpose matrix of A

Finally, a 3D pseudo reconstruction in terms of V_p/V_s ratio was performed understanding the lateral development of the anomalies. The 3D reconstruction is carried out by cubic spline interpolation.

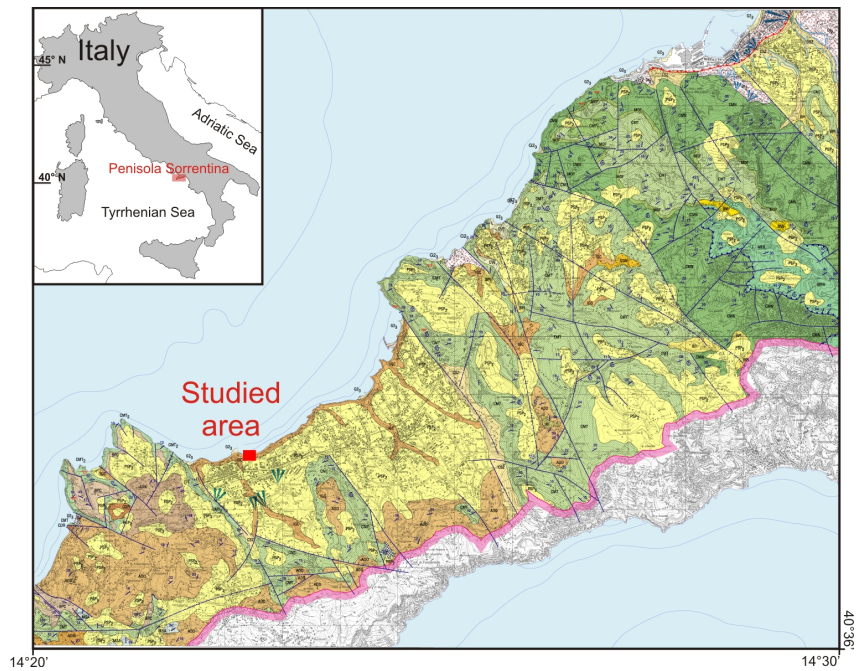


Figure 1: Geological Map 1:25.000: Foglio 466 sez. III Sorrento. Legend: Volcaniclastic Undifferentiated deposits (Post-Ignimbrite campana formation). PSP2: Sin and post 79d.c pyroclastites. IGC: Ignimbrite Campana Formation (upper Pleistocene); PTM: Tramonti pyroclastites (upper Pleistocene). Depositi continentali e di transizione. Dt2: slope deposits (Olocene); CSZ: Scanzano conglomerates (upper Pleistocene); CVE: Vico Equense alluvial fan deposits (upper Pleistocene); CGN: Gragnano conglomerates (upper Pleistocene); BPI: Pimonte Breccia (upper Pleistocene); BMF: Monte Faito Breccia. Monte Faito Unit. MFR: Monte Faito limestones (Santonian-Barremian). Sicile Complex Unit. MFA: Sant'Arcangelo Formation (Lower Eocene –Paleocene); Ac: calcareous-marly member (Miocene ?-Oligocene); Av: argillitic member (Miocene ?-Oligocene). Monti Lattari Unit: BPC: Punta del Capo Breccia (upper tortonian); ADD: Deserto sandstones (lower Tortonian); ADM Marciano sandstones Serravallian?); ADN: Nerano sandstones (Serravallian); CDR: Recommone calcarenites (Serravallian ?-Burdigalian?); CMT: Meta limestones (Santonian-Aptian); CMT2 Breccia and conglomerates limestones member (Santonian); MOF: Faito Orbitolina marls (Aptian); CMN: Moiano limestones (Aptian – Berriasian).



Figure 2: The edge of Marechiaro relief characterized by sub-vertical cliffs, carved into the “Calcarei a radiolitidi”. Unit show favourable conditions for the occurrence of a generalized instability phenomena manifested by tuff rock falls with cumulus evident on the cliff foot; b) Structural limestone cliff with evidence of “ancient rock falls” (dashed red line); c) CI tuff cliff in northern side of Piano di Sorrento affected by several traces of human activities such as caves and small hollows of building materials; d) A detail of the typical vertical columnar jointing and fractures (yellow lines) affected the CI Uni. Red lines are evidences of crosscutting or parallel discontinuity to bedding which affected the tuff mass; e) Cliff in flysch shows a slope of about 20deg-35deg near Massalubrense.

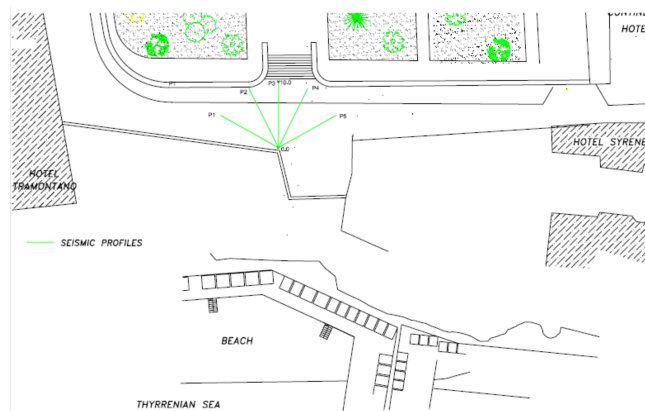


Figure 3: Field geometry map reporting seismic profiles location.



Figure 4: Sections showing V_p (A-E), V_s (F-K) and V_p/V_s ratio (I-O) for the studied area.

4 Results and Conclusion

Figure 5 shows the 2D tomograms obtained for the P and S wave velocity field and the V_p/V_s ratio. The P wave velocity is variable from 300 m/sec, for the pyroclastic and incoherent deposits that lie on the first 6 m starting from the ground level, to 1800 m/sec in correspondence of the tuff deposits. The S wave velocity presents values variable from 90m/sec to 700 m/sec for respectively pyroclastic incoherent deposits and tuff bedrock.

Figures 5A to E show the P wave velocity field. It is evident an increase in velocity with the depth except for the profile C where a negative velocity anomaly appears. The same trend is shown for the S wave velocity profiles (Figures 5F-K).

Figures 5I-O reports the V_p/V_s -ratio derived from the velocity measurements.

Because many rocks with different states of fracturing, pore pressure, fluid saturation, and partial melt affect seismic velocities,

the interpretation of seismic velocity is often nonunique (i.e. the single interpretation of the P and S wave velocity field doesn't show any significant anomaly). Therefore, it is useful to consider velocity ratios to differentiate between the different physical effects in the medium. Moos and Zoback [10] show that fluid saturated fractures decrease both V_p - and V_s -velocities, while it increases the V_p/V_s -ratio.

These anomalies we believe that are representative of the different conditions of the rock mass.

In this case, particularly interesting appears the low value of V_p/V_s ratio (Figure 5 L-M) localized between 30 and 36 m elevation that could be associated with a medium having a lower porosity or in dryer condition respect to the surrounding material that have relative high value V_p/V_s ratio.

The first and the other sections (Figure 5I) show a guided waves effect probably generated from the relative high degree

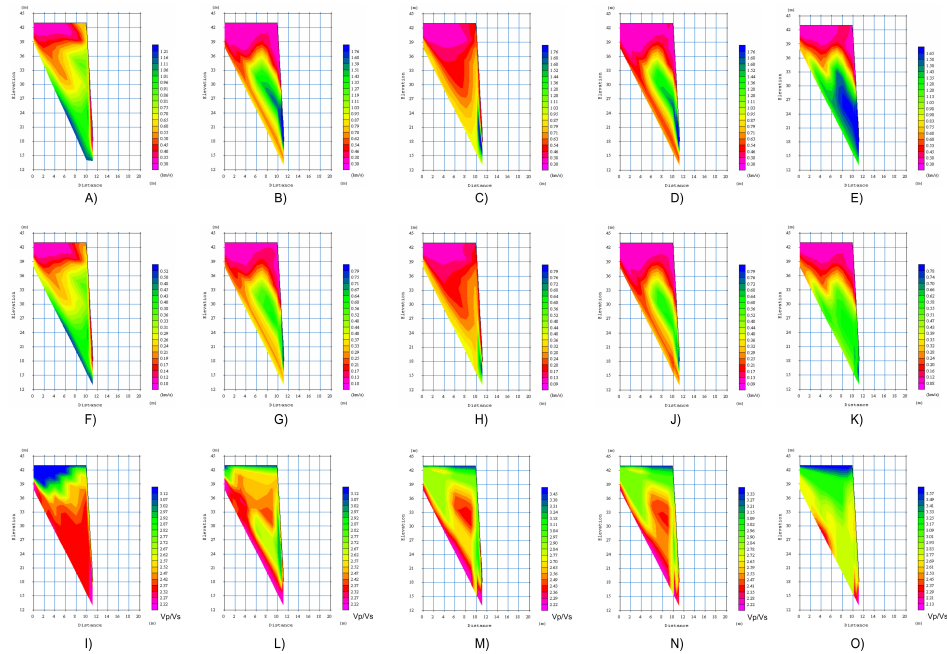


Figure 5: Sections showing V_p (A-E), V_s (F-K) and V_p/V_s ratio (I-O) for the studied area.

of weathering and/or from arrangement of planar discontinuity which affected the tuff mass (crosscutting or parallel to bedding). Figure 6 reports the 3D model of the V_p/V_s ratio obtained by non linear cubic spline interpolation. The discontinuities detected isolate blocks evident on the slices going from 30 to 36 m but their extension is wider compared to the 2D representation. In fact, the low anomaly is wider in the central zone of the investigated area where seems to have a shape similar to a ring and de-

creases its extension at the top and bottom slices. Our opinion is that these defects, or discontinuities, may be related to localized fracture with a relative increase in local water inflow which decrease the mechanic continuity of the rock, leading to key block weathering and failure. Because the technique used in this work was very able to detect the discontinuity in cliff rock, we can propose it in other areas at different scale and lithology also.

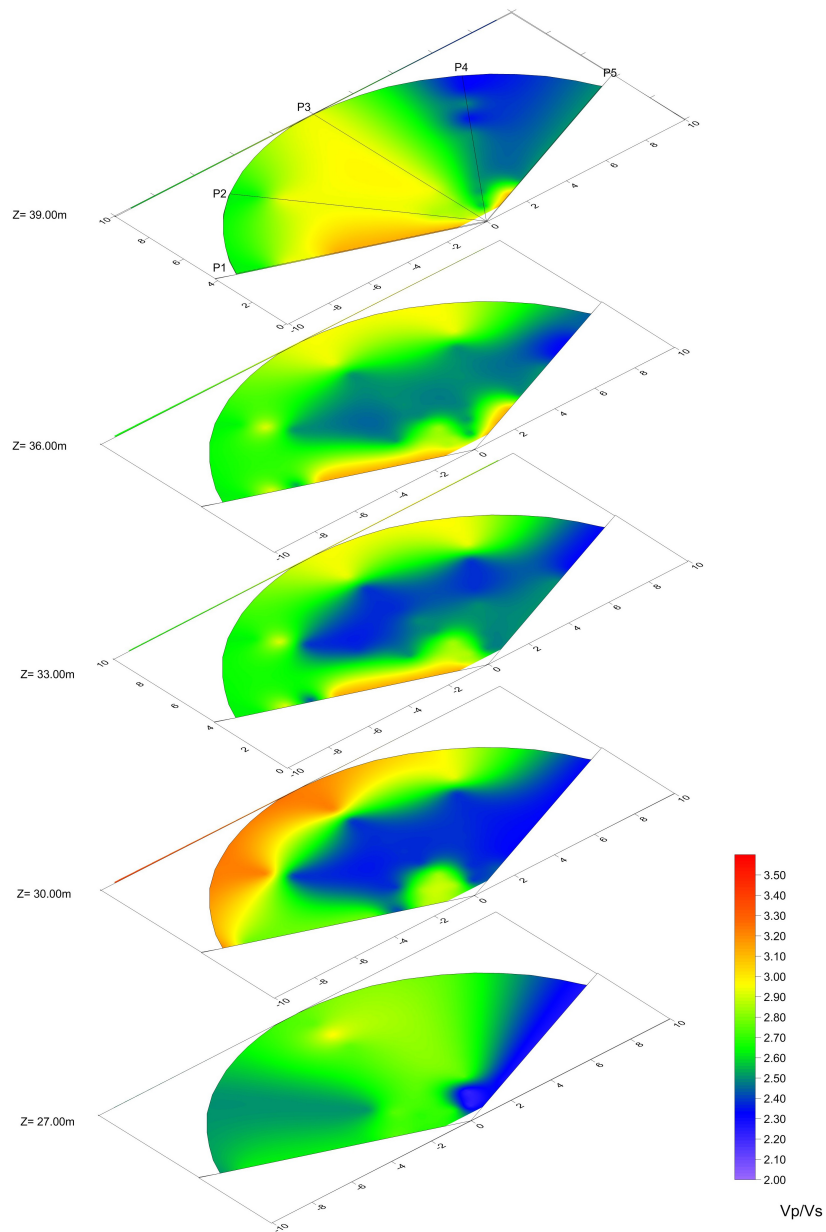


Figure 6: 3D reconstruction of the V_p/V_s ratio. the blue area defines a low V_p/V_s ratio value localized between 30 and 36m elevation.

References

- [1] E. Patacca and P. Scandone. Geology of the Southern Apennines. *Boll. Soc. Geol. It.*, page 75, 2007.
- [2] Autorità di Bacino Regionale del Sarno - Regione Campania - ARPA. Carta Geologica regionale in scala 1:25.000 “Progetto CARG”: Foglio 466 sez. III “Sorrento”. 41, 2003.
- [3] P. Di Girolamo, M.R. Ghiara, L. Lirer, R. Munno, G. Rolandi, and D. Stanzione. Vulcanologia e petrologia dei Campi Flegrei. *Mem. Soc. Geol. It.*, 41:1005–1014, 1984.
- [4] A. Milia and M. Torrente. Tettonica della penisola Sorrentina (margine peritirrenico campano). *Boll. Soc. Geol. It.*, 116:487–502, 1997.
- [5] B. De Vivo and G. Rolandi. Mt Somma - Vesuvius and volcanism of the Campanian Plain. *Mineralogy and Petrology*, 73(1-3):233, 2001.
- [6] T. De Pippo, M. Pennetta, F. Terlizzi, and A. Valente. Principali tipi di falesia nella Penisola Sorrentina e nell’Isola di Capri: caratteri e lineamenti morfoevolutivi. *Boll. Soc. Geol. It.*, 126:181–189, 2007.
- [7] L. Brancaccio. Genesi e caratteri delle forme costiere nella Penisola Sorrentina. *Boll. Soc. Natur.*, 77:247–274, 1968.
- [8] G.J. Berryman. Lecture notes on: Nonlinear inversion and tomography. 1991.
- [9] J.E. Vidale and D.V. Helmberger. Elastic finite-difference modelling of the 1971 San Fernando, Ca. earthquake. *Bull. Seism. Soc. Am.*, 78:122–142, 1988.
- [10] D. Moos and M.D. Zoback. In situ studies of velocity in fractured crystalline rocks. *J. Geophys. Res.*, 88:2345– 2358, 1983.